



**Graduate School in Civil Engineering and Architecture**

**University of Pavia, Italy**

DICAr - Department of Civil Engineering and Architecture

**TOOLS AND STRATEGIES FOR COMBINED  
LOCAL AND GLOBAL SEISMIC VULNERABILITY  
ASSESSMENT OF URM STRUCTURES**

A Thesis Submitted in Partial Fulfilment of the Requirements  
for the Degree of Doctor of Philosophy in

**CIVIL ENGINEERING AND ARCHITECTURE**

*Candidate:*

**Umberto Tomassetti**

*Supervisors:*

Prof. Andrea Penna - University of Pavia, Italy

Dr. Francesco Graziotti - University of Pavia, Italy

September, 2018

Signature of author.....  
University of Pavia, Italy  
Department of Civil Engineering and Architecture, DICAr  
September, 2018

Certified by.....  
Andrea Penna  
University of Pavia, Italy  
Associate Professor of Structural Engineering  
Thesis Supervisor

Accepted by.....  
Ferdinando Auricchio  
Full Professor of Mechanics of Solids  
Coordinator of the Doctoral School, DICAr

## Thesis Supervisors

.....  
Andrea Penna  
Associate Professor of Structural Engineering  
Department of Civil Engineering and Architecture, DICAr  
University of Pavia, Italy

.....  
Francesco Graziotti  
Assistant Professor of Structural Engineering  
Department of Civil Engineering and Architecture, DICAr  
University of Pavia, Italy





# TOOLS AND STRATEGIES FOR COMBINED LOCAL AND GLOBAL SEISMIC VULNERABILITY ASSESSMENT OF URM STRUCTURES

by

Umberto Tomassetti

Submitted to the Department of Civil Engineering and Architecture on September 28, 2018  
in partial fulfilment of the requirements for the degree of  
*Doctor of Philosophy in Civil Engineering and Architecture*

## **Abstract**

Recent seismic events have provoked an increasing interest in understanding as well as predicting the risk associated with future earthquakes. An initial step in any reliable definition of the seismic vulnerability of a region is understanding properly the structural behaviour of its building stock. While the state of knowledge regarding the behaviour of unreinforced masonry (URM) building typologies commonly encountered in historically seismic prone regions is comparatively advanced; there exists large URM building stocks in several parts of the world composed of structural typologies whose earthquake response is virtually unknown. With increasing cases of induced seismicity, a proper understanding of the seismic behaviour of such structural typologies (also often designed with no particular consideration for lateral loads) has become of paramount importance and can be reliably achieved only by large scale experimental campaigns. In this context, the first part of this dissertation constitutes of multi-scale experimental activities on Dutch structures: ranging from characterisation tests to dynamic tests on full scale components and buildings. In particular, incremental dynamic tests were performed on: single leaf and cavity walls in the out-of-plane (OOP) direction, a full scale two-storey cavity wall house and also a one-storey roof sub-structure of the tested house. Such experiments allowed the study of their structural response at both local as well as global scales and at various levels of intensity. In the second part of this dissertation, light computational models capable of capturing the dynamic OOP response of walls, roof substructures, chimneys and parapets were developed. These models were calibrated with the performed dynamic experiments as well as other experimental tests in literature. Innovative aspects of these models include the focus placed on developing and testing various damping models to capture the energy dissipation involved in their rocking response. In the third and final part of the dissertation, emphasis was placed on the potential risk associated with the development of local mechanisms in walls and non-structural components. The numerical models developed in the second part were implemented to evaluate the seismic vulnerability associated with non-structural components especially in an induced seismic activity scenario. Fragility curves are then provided considering different building and non-structural component configurations, including their initial state to be undamaged or already damaged. Guidelines are also provided on the choice of appropriate intensity measures as well as engineering demand parameters to be used. This dissertation in its entirety attempts to take a significant step forward in the development of robust yet light computational models having few but sufficient degree of freedoms capable of assessing simultaneously the performance of URM structures both globally and locally.



## Table of Contents

<b>Introduction</b> .....	1
References.....	5
<b>1. Out-of-plane shaking table tests on URM single leaf and cavity walls</b> .....	7
1.1. Introduction.....	7
1.2. Characterisation of the masonry specimens.....	9
1.2.1. Specimen construction and geometric characterization.....	9
1.2.2. Mechanical characterization of the materials.....	11
1.3. Test set-up and dynamic loading sequence.....	12
1.3.1. Test set-up.....	12
1.3.2. Instrumentation and data acquisition.....	13
1.3.3. Dynamic input motion.....	14
1.3.4. Testing Programme.....	15
1.4. Test results.....	17
1.4.1. Dynamic identification.....	17
1.4.2. Deformed shapes.....	18
1.4.3. Damage patterns and failure mechanisms.....	19
1.4.4. Specimen F- $\Delta$ relationships.....	22
1.4.5. Specimen's acceleration capacity.....	24
1.4.6. Energy dissipation.....	25
1.4.6.1. The classical rocking theory.....	25
1.4.6.2. Experimental computation of the coefficient of restitution.....	26
1.4.6.3. Experimental computation of the damping ratio.....	29
1.4. Conclusions.....	30
1.5. Acknowledgments.....	31
1.5. References.....	31
<b>2. Shaking table test on a full-scale URM cavity wall building</b> .....	35
2.1. Introduction.....	35
2.2. Specimen Characteristics.....	36
2.2.1. Geometry of the specimen.....	37
2.2.2. Building construction details.....	39
2.2.3. Mechanical properties of materials.....	40
2.3. Testing protocol and instrumentation.....	42
2.3.1. Input signals.....	42
2.3.2. Testing protocol.....	43
2.3.3. Instrumentation.....	44
2.4. Test results.....	45
2.4.1. Shaking table performance.....	46
2.4.2. Damage evolution.....	46
2.4.3. Deformed shapes.....	50
2.4.4. Hysteretic responses.....	51

---

2.4.5. Response of the roof structure.....	53
2.4.6. Identification of the specimen damage limit states.....	56
2.4.7. Derivation of EDPs according to the specimen performance.....	59
2.5. Conclusions.....	61
2.6. Acknowledgments.....	62
2.7. References.....	62
<b>3. Two-way bending OOP collapse of a full-scale URM building tested on a shake table.</b>	<b>65</b>
3.1. Introduction.....	65
3.2. Specimen Characteristics.....	66
3.2.1. Geometry of the specimen and construction details.....	66
3.2.3. Mechanical properties of materials.....	69
3.3. Testing protocol and instrumentation.....	71
3.3.1. Input signals.....	71
3.3.2. Testing protocol.....	72
3.3.3. Instrumentation.....	73
3.4. Test results.....	74
3.4.1. Shake table performance.....	74
3.4.2. Damage evolution and identification of damage states.....	75
3.4.3. Analysis of the dynamic behaviour of the structure.....	81
3.4.4. Performance of building furniture.....	82
3.4.5. Hysteretic response.....	82
3.4.6. Response of the roof structure.....	84
3.4.7. Two way bending out-of-plane collapse.....	86
3.4.8. Building's performance in terms of common EDP parameters.....	89
3.5. Conclusions.....	93
3.6. Acknowledgments.....	94
3.7. References.....	94
<b>4. Modelling one-way out-of-plane response of single leaf and cavity walls.....</b>	<b>97</b>
4.1. Introduction.....	97
4.2. One-way bending out-of-plane response of single leaf walls.....	99
4.2.1. Static force-displacement relationship.....	99
4.2.2. Dynamic behaviour.....	101
4.2.3. Energy dissipation.....	102
4.3. One-way bending out-of-plane response of cavity walls.....	106
4.3.1. Static force-displacement relationship.....	106
4.3.2. Dynamic behaviour and energy dissipation.....	108
4.4. The proposed numerical model.....	108
4.4.1. The reference experimental campaign.....	109
4.4.2. The assumed force-displacement relationship.....	109
4.4.3. The numerical model.....	110
4.4.4. The calibration approach.....	111
4.5. Comparison with experimental results.....	113
4.5.1. Simulation of the dynamic response of single leaf specimens.....	113
4.5.2. Simulation of the dynamic response of cavity wall specimens.....	116
4.5.3. Summary of the results.....	119
4.5.4. Selection of the most appropriate damping model.....	121
4.6. Conclusions.....	122

4.7. Acknowledgments.....	123
4.8. References.....	123
<b>5. Modelling rocking response via equivalent viscous damping.....</b>	<b>125</b>
5.1. Introduction.....	125
5.2. Rigid body SDOF equation of motion.....	127
5.3. Force-displacement relationship.....	128
5.4. Energy dissipation in the OOP response of masonry structures.....	129
5.4.1. The coefficient of restitution.....	129
5.4.2. The equivalent viscous damping.....	130
5.4.3. Equivalence between the damping models.....	131
5.5. Implemented SDOF model.....	133
5.6. Derivation of the equivalence.....	134
5.7. Validation of the proposed EVD relationships.....	139
5.7.1. Comparison with experimental results.....	139
5.7.2. Comparison at overturning condition via IDA analysis.....	141
5.8. Conclusions.....	142
5.9. Acknowledgments.....	143
5.10. References.....	143
<b>6. Vulnerability of timber roofs supported by unreinforced masonry gables.....</b>	<b>147</b>
6.1. Introduction.....	147
6.2. Description of the roof structure.....	148
6.3. Experimental seismic performance.....	149
6.4. Modelling the dynamic response of roof substructures.....	152
6.4.1. Diaphragm modelling.....	153
6.4.2. URM gable modelling.....	155
6.4.3. Implemented numerical model.....	155
6.5. Comparison with experimental results.....	156
6.6. Vulnerability of roof structures.....	158
6.6.1. Primary SDOF (URM building's response).....	159
6.6.2. Secondary SDOF (Roofs' response).....	160
6.6.3. Employed accelerograms and response of primary SDOFs.....	161
6.6.4. Results of NLTH analysis.....	162
6.6.5. Fragility curves of roof structures.....	163
6.7. Conclusions.....	168
6.8. Acknowledgments.....	169
6.9. References.....	169
<b>7. Probabilistic seismic assessment of URM chimneys and parapets.....</b>	<b>173</b>
7.1. Introduction.....	173
7.2. Modelling the dynamic response of parapets and chimneys.....	175
7.2.1. Equation of motion.....	175
7.2.2. Force-displacement relationship.....	176
7.2.3. Energy dissipation.....	177
7.2.4. The numerical model.....	178
7.3. Simulation of the experimental response of parapets and chimneys.....	178
7.3.1. Reference experimental campaigns.....	178
7.3.2. Calibration of parapet responses.....	179
7.3.3. Calibration of chimney responses.....	181

---

7.4. Seismic vulnerability of parapet and chimney.....	184
7.4.1. Primary SDOF (URM building's response) .....	186
7.4.2. Secondary SDOF (Roof building's response) .....	186
7.4.3. Employed accelerograms and response of primary and secondary SDOFs	187
7.4.4. Adopted intensity measures.....	188
7.4.5. Geometries and modelling parameters.....	189
7.4.6. Analyses results.....	190
7.4.7. Floor rocking spectra.....	192
7.4.8. Fragility curves.....	193
7.8.4.1 Analysis of the different IMs efficiency.....	194
7.8.4.2 Proposed fragility curves for parapets .....	196
7.8.4.3 Proposed fragility curves for chimneys.....	200
7.4.9. Relationship between global and local damage.....	203
7.4.10. Comparison with empirical fragility functions.....	205
7.5. Conclusions.....	206
7.6. Acknowledgments.....	207
7.7. References.....	207
<b>Conclusions</b> .....	<b>211</b>
<b>Future developments</b> .....	<b>216</b>

## Introduction

The environmental, economic and social impact of recent earthquakes on countries and local communities have promoted an increasing interest on understanding and predicting the seismic risk associated with future events. A reliable definition of this risk, quantified in expected injuries, casualties and financial losses in a given period of time, is strictly dependent on the adopted hazard, exposure, fragility and consequence models and it might help decision-makers towards its mitigation. Within this context, fragility models might be the most familiar ones for structural engineers.

In the last two decades, indeed, these needs in addition with the advent of performance based earthquake engineering (PBEE) have encouraged a growing characterisation of the seismic performance of structures under different levels of earthquake intensity in order to consider not only life safety but also the functionality of the building as a whole. In order to assess economic losses, focus was placed on a better evaluation of structural damage as well as damage to equipment, contents and consequently business or activities interruption, with additional consideration given to more frequent events at lower intensity. Failure mechanisms and collapse of both structural and non-structural elements were furthermore studied to assess the amount of potential falling debris and provide probability of injury or death to people that are hit by them.

These studies rely, in the vast majority of cases, on different typologies of numerical models which have been opportunely developed and calibrated to study the phenomenon under consideration. The reliability of these models depends on the level of knowledge of the seismic behaviour of the structural typology under study and adopted modelling approach and assumptions. Laboratory and *in-situ* experimentations of structures or components as well as characterisation of materials representing a solid benchmark for these numerical models may significantly reduce the epistemic uncertainty related to these simulations by allowing for the development of more robust fragility models.

This applies *a fortiori* in the case of Groningen, an area in the northern Netherlands not naturally prone to tectonic earthquakes, in which, not designed for lateral loads, local structures were exposed to seismic events induced by reservoir depletion due to natural gas extraction. The local building stock was mainly composed of unreinforced masonry (URM) structures, with the majority of residential terraced houses structures, which are subject of study of this thesis work.

The seismic performance of these structures built with the construction technique of cavity walls, slender piers and very specific regional details was rather unknown and very limited information was available on the seismic behaviour of buildings with similar characteristics. Furthermore, literature currently lacks information on the effect of low-magnitude and short-duration induced earthquake signals on buildings. This limited knowledge is at odds with the need of estimating acceptable risk level for the local population expressed in terms of “Local Personal Risk” of buildings, defined as the annual probability of fatality for a hypothetical person continuously present inside or

within 5 metres of a building [1]. This required a robust estimate of the collapse probability of structural and non-structural elements within, which implied consideration of uncertainties higher than those associated with initial damage states.

These motivations called for a large experimental research effort aimed specifically at evaluating the vulnerability of the building stock, whose specific focus was on URM buildings.

The known out-of-plane (OOP) vulnerability of URM walls in addition with the lack of information on the OOP performance of cavity walls led to the decision of performing experimental shake table tests on one-way-bending [2] and two-way-bending [3] excited single leaf and cavity wall specimens. The former experimental campaign has foreseen dynamic testing of three cavity wall panels with different tie distributions (inner calcium silicate brick wall and outer clay brick wall) and one single-leaf wall constructed using calcium silicate brick masonry. The experimental arrangement allowed the specimens to be tested under different input signals and loading conditions, inducing an out-of-plane one-way bending action in the walls. The observed failure mechanisms, the energy dissipation involved in the exhibited rocking behaviour as well as the capability of the ties system of coupling the response of the two leaves in cavity wall specimens are presented and discussed in Chapter 1 [2].

The seismic performance of URM cavity wall terraced houses as a whole was characterised up to the collapse condition with two full-scale shake table tests presented in Chapter 2 and Chapter 3.

Chapter 2 investigates the dynamic response, along the weak direction, of a two-storey full scale URM building representing the end-unit of a terraced house, built with cavity walls and without any particular seismic design or detailing. In the tested specimen, indeed, the loadbearing masonry was composed of 100mm thick calcium silicate bricks, sustaining two reinforced concrete floors. A pitched timber roof was supported by two gable walls. The veneer was made of clay bricks connected to the inner masonry by means of metallic ties, as seen in common construction practice. An incremental dynamic test was carried out up to the near-collapse limit state of the specimen, adopting input signals consistent with the characteristics of induced seismicity ground motions. The test was stopped in order to prevent a global collapse of the specimen that could have caused damage to the laboratory facilities.

The need of characterising its collapse mechanism led to the decision of performing a further test on a one-storey full-scale URM structure which was meant to represent second-storey and roof of the first specimen. The input motions were floor acceleration response histories of the previously tested two-storey specimen. An incremental dynamic test, with vertical and horizontal inputs, was in this case carried out up to explicit collapse of some of its bearing elements. A two-way bending out-of-plane (OOP) collapse of a loadbearing wall was observed and described in Chapter 3 [4].

The observed flexibility and the wish of estimating potential consequences of a roof mechanism in terms of collapsed volume called for their characterisation up to collapse condition with a further full-scale shake table test on a roof substructure. Results, failure mechanism and comparison between performances of all tested roof configurations are presented and discussed in Chapter 6.

Furthermore, the experimental programme included also *in-situ* mechanical characterization tests [5] and laboratory tests, such as: characterization tests on bricks, mortar and small masonry assemblies; in-plane cyclic shear-compression tests [6] and



three more full-scale shake table tests on different URM building typologies [7][8][9][10].

This large experimental campaign was followed by an intense modelling effort characterised by different approaches according to the specific goal of the study. URM structures, indeed, have been modelled in literature with a multitude of different computational strategies. For example, micro-modelling was adopted to interpret the results of *in situ* shove tests, laboratory direct shear tests with the goal of deriving possible correlation as well as studying the role of dilatancy [11]. The Applied Element Method (AEM) approach was, instead, employed to develop and calibrate numerical models of specific building typologies in order to assess failure mechanism and amount of collapsed debris [12][13]. Multi degree of freedom (MDOF) models based on a macroelement approach [14][15] were adopted to derive fragility functions for specific buildings [16]. Light computational models such as SDOF systems, calibrated on more refined models, were adopted to perform cloud analysis and consequently derive fragility functions for all the addressed building typologies [1].

Within this framework, in view of the encouraging results of both experimental tests on full-scale URM houses and modelling activities regarding the vulnerability and overall performance of URM buildings exposed to induced earthquakes, emphasis shifted on the potential risk associated with the development of local mechanisms in walls or in non-structural components. Part of the thesis work, thus, consisted in developing light computational models for the assessment of the seismic performance of OOP behaviour of URM walls, roof substructures and URM secondary elements such as chimneys and parapets. Damage and collapse involving these elements located in positions where highest ground motion amplification is expected have been largely documented.

Chapter 4 [17] presents a single-degree-of-freedom (SDOF) numerical model for the analysis of the dynamic OOP behaviour of URM walls or portion of walls. It takes into account both the linear and the non-linear rocking response phase of URM walls. The numerical model was developed to capture the experimental dynamic response of both single leaf and cavity wall specimens subjected to a pure one-way bending action with both top and bottom end supports of the wall moving simultaneously (Chapter 1, [2]). A detailed investigation into the force-displacement relationships characterising both wall typologies has been carried out in order to provide reliable parameters for the simulation of their dynamic behaviour. Particular emphasis was placed on the energy dissipation involved in the rocking mechanism. While it is generally modelled by means of the coefficient of restitution, assuming that the overall reduction of energy is concentrated at the instant of the impact, the work proposes the adoption of velocity dependant equivalent viscous damping (EVD) forces. Different typologies of EVD models have been proposed and compared in order to identify the most appropriate one to capture the dependency of the damping phenomenon on the oscillation amplitude and subsequently the system frequency.

Their effectiveness in simulating the experimental rocking response called for a comparison with a coefficient of restitution approach and the characterisation of the most appropriate damping ratio value to be associated with a specific wall configuration. Both damping approaches are presented and compared on the study of free rocking responses in Chapter 5. A relationship linking damping ratio and slenderness angle via coefficient of restitution is derived and proved against experimental responses and large sets of natural ground motions.

A further SDOF numerical model for the analysis of timber roofs supported by URM gables is presented and calibrated against several experimental responses in Chapter 6. The SDOF system is composed of two springs in parallel: a bi-linear elastic one for the simulation of the typical non-linear rocking behaviour of the masonry gables and an elastoplastic one with two hardening branches for simulating the highly dissipative timber diaphragm hysteretic behaviour. This numerical model was then used to perform large sets of analyses in order to assess the vulnerability of these architectural elements. The influence of the whole building characteristics (*e.g.* number of storeys and structure strength) on the seismic performance of this roof typology was also investigated. Fragility curves for the different damage states are finally proposed.

A probabilistic seismic assessment of non-structural masonry components such as parapets and chimneys was carried out in Chapter 7. These elements are free standing components located above the perimeter walls or the roofline, subjected, hence, to the highest amplification of ground motion during an earthquake. Their damage and collapse may represent a significant hazard for building occupants and pedestrians, as well as, losses in terms of building repair cost. For these reasons a SDOF model was presented and calibrated on several experimental dynamic tests on parapets and chimneys. The model was then adopted to assess the vulnerability of opportunely selected secondary elements placed on top of different primary structure and roof configurations. The buildings differ in terms of number of storeys and structure lateral strength. The SDOFs presented in Chapter 6 were used to simulate the responses of primary structures and roofs when subjected to a large set of natural ground motions. Their acceleration output was used as acceleration input for chimneys and parapets. Overturning fragility curves were obtained from the cloud results. Moreover, focus was also placed in establishing which intensity measure resulted as the most efficient one and how the median collapse intensity was affected by the characteristics of the primary structure. The numerical fragility functions were finally compared with empirical ones.

## References

- [1] H. Crowley, B. Polidoro, R. Pinho, and J. van Elk, "Framework for Developing Fragility and Consequence Models for Local Personal Risk," *Earthq. Spectra*, vol. 33, no. 4, pp. 1325–1345, 2017.
- [2] F. Graziotti, U. Tomassetti, A. Penna, and G. Magenes, "Out-of-plane shaking table tests on URM single leaf and cavity walls," *Eng. Struct.*, vol. 125, 2016.
- [3] F. Graziotti, U. Tomassetti, S. Sharma, L. Grottoli, and G. Magenes, "Experimental response of URM single leaf and cavity walls in out-of-plane two-way bending generated by seismic excitation," *Constr. Build. Mater.*, vol. (in press), 2018.
- [4] U. Tomassetti *et al.*, "Two-way bending out-of-plane collapse of a full-scale URM building tested on a shake table," *Bull. Earthq. Eng.*, vol. (in press), 2018.
- [5] M. Tondelli, F. Graziotti, A. Rossi, and G. Magenes, "Characterization of masonry materials in the Groningen area by means of in-situ and laboratory testing," *Tech. Report, Eucentre, Pavia, Italy.*, 2015.
- [6] F. Graziotti, A. Rossi, M. Mandirola, A. Penna, and G. Magenes, "Experimental characterisation of calcium-silicate brick masonry for seismic assessment," in *Proceedings of the 16th International Brick and Block Masonry Conference*, 2016, pp. 1619–1627.
- [7] S. Kallioras *et al.*, "Experimental seismic performance of a full-scale unreinforced clay-masonry building with flexible timber diaphragms," *Eng. Struct.*, vol. 161, no. November 2017, pp. 231–249, Apr. 2018.
- [8] S. Kallioras, A. A. Correia, F. Graziotti, A. Penna, and G. Magenes, "Experimental seismic performance of an unreinforced clay-masonry building with chimneys up to collapse conditions," *V. e Giardini*, no. (to be submitted), 2018.
- [9] M. Miglietta *et al.*, "Shake-table test on a cavity-wall building with flexible diaphragms," *Tech. Report, EUCENTRE, Pavia, Italy.*, 2018.
- [10] F. Graziotti, A. Penna, and G. Magenes, "A comprehensive in situ and laboratory testing programme supporting seismic risk analysis of URM buildings subjected to induced earthquakes," *Bull. Earthq. Eng.*, Sep. 2018.
- [11] G. Andreotti, F. Graziotti, and G. Magenes, "Detailed micro-modelling of the direct shear tests of brick masonry specimens: The role of dilatancy," *Eng. Struct.*, vol. 168, pp. 929–949, 2018.
- [12] D. Malomo, R. Pinho, and A. Penna, "Using the applied element method for modelling calcium silicate brick masonry subjected to in-plane cyclic loading," *Earthq. Eng. Struct. Dyn.*, vol. 47, no. 7, pp. 1610–1630, 2018.
- [13] D. Malomo, R. Pinho, and A. Penna, "Using the Applied Element Method to simulate the dynamic response of full-scale URM houses tested to collapse or near-collapse conditions," in *16th European Conference on Earthquake Engineering*, 2018.
- [14] S. Lagomarsino, A. Penna, A. Galasco, and S. Cattari, "TREMURI program: An equivalent frame model for the nonlinear seismic analysis of masonry buildings," *Eng. Struct.*, vol. 56, pp. 1787–1799, 2013.
- [15] A. Penna, S. Lagomarsino, and A. Galasco, "A nonlinear macroelement model for the seismic analysis of masonry buildings," *Earthq. Eng. Struct. Dyn.*, vol. 43, pp. 159–179, 2014.
- [16] S. Kallioras, F. Graziotti, and A. Penna, "Numerical assessment of the dynamic response of a URM terraced house exposed to induced seismicity," *Bull. Earthq. Eng.*, vol. (accepted), 2018.
- [17] U. Tomassetti, F. Graziotti, A. Penna, and G. Magenes, "Modelling one-way out-of-plane response

of single-leaf and cavity walls,” *Eng. Struct.*, vol. 167, pp. 241–255, Jul. 2018.

## 1. Out-of-plane shaking table tests on URM single leaf and cavity walls

Graziotti F., Tomassetti U., Penna A., Magenes G. Out-of-plane shaking table tests on URM single leaf and cavity walls, *Engineering Structures*, 2016 125, 455-470.

**Abstract.** Damage observations from recent seismic events have confirmed that the activation of out-of-plane local mechanisms is one of the major causes of structural collapse in unreinforced masonry buildings. Particularly vulnerable are cavity walls commonly used in residential building in regions such as Central and Northern Europe, Australia, New Zealand, China and several other countries. Usually, the inner leaf has a load-bearing function, carrying vertical loads transmitted by floors and roof while the outer leaf, having only aesthetic and insulation functions, is lightly loaded. The two leaves are typically connected by means of metallic ties. The high out-of-plane vulnerability, which may prevent the exploitation of the global capacity associated with the in-plane capacity of the structural walls, is mainly due to the high slenderness of the masonry leaves and the lack, or ineffectiveness, of ties between leaves. Often ties are too widely spaced and/or heavily degraded. Despite the complexity of the composite behaviour of such a construction typology, no dynamic tests on cavity walls are reported in current literature. For this reason, four out-of-plane shaking table tests were conducted on full-scale unreinforced masonry assemblies of three cavity wall panels with different tie distributions (inner calcium silicate brick wall and outer clay brick wall) and one single-leaf wall constructed using calcium silicate brick masonry. The experimental arrangement allowed the specimens to be tested under different input signals and loading conditions, inducing an out-of-plane one-way bending action in the walls. The research is aimed at understanding the seismic behaviour of cavity walls, their failure mechanisms and how they are affected by boundary conditions and degree of connection between the two leaves. The paper describes the main experimental results, including deformed shapes, damage patterns, force-displacement relationships, and the capacities in term of acceleration sustained by the specimens. Additionally, the energy dissipation involved in the mechanism has been investigated in terms of coefficient of restitution and damping ratio. All the processed data are freely available upon request (see <http://www.eucentre.it/nam-project>).

### 1.1. Introduction

Over the last decades, observations of damage caused by major earthquake events have shown that the structural collapse in unreinforced masonry (URM) buildings is very often associated with the activation of out-of-plane overturning mechanisms, rather than the

attainment of maximum stress in structural elements: such overturning mechanisms are activated by the loss of equilibrium in masonry portions due to out-of-plane (OOP) actions. This behaviour is often associated with the lack of good connections to adjacent perpendicular walls and floors (e.g. [1-3]). Cavity wall buildings are particularly vulnerable to out-of-plane actions due to the walls being both slender and lightly loaded, which prevents the development of their full in-plane strength capacity. Cavity construction is a form of wall construction where a cavity is left between the two leaves of bricks. Sometimes insulating material is inserted in the cavity. The external leaf of a cavity wall is often a brick veneer wall without any load bearing function, whereas the internal leaf is a load-bearing wall, carrying the vertical loads transmitted by the floors and roof. It is common for the inner leaf to be constructed with different materials than the outer leaf. In several European countries, an example of this solution is to have the inner wall made of calcium silicate bricks/blocks, whereas the outer wall uses clay bricks. Leaves on either side of a cavity wall are typically connected by regularly spaced metal cavity ties, which can vary in material, shape and spacing. Because of their relatively light weight, good thermal insulation properties and effective protection against driving rain, cavity walls are widely used in Central and Northern Europe countries, especially for residential constructions. Experience on the seismic behavior of cavity walls is quite limited, and mostly related to earthquakes which have occurred in Australia (Newcastle, 1989) and New Zealand (Christchurch sequence, 2010-2011).

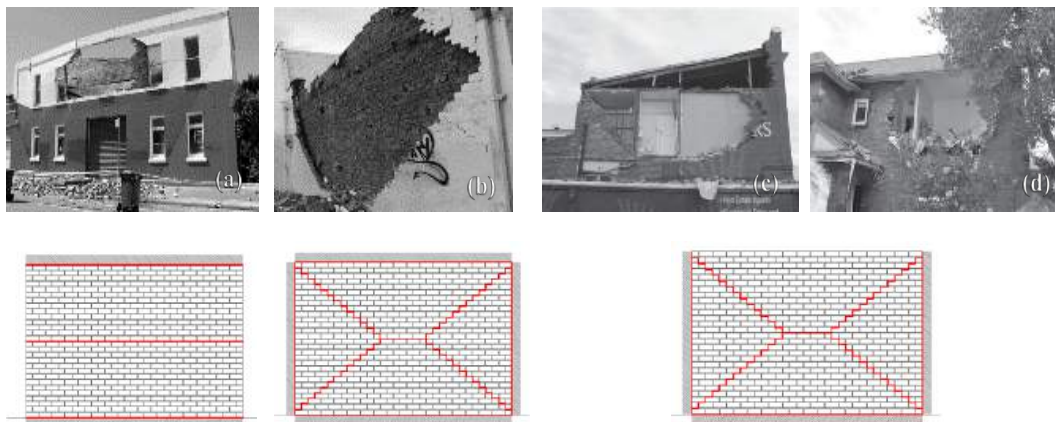


**Figure 1.1 One-way bending failure (a), two-way failure (b), top portion cantilever wall failure (c, d) (adapted from Dizhur *et al.*, 2011).**

Dizhur and Ingham [4] noted three primary types of out-of-plane wall failures in cavity wall buildings following the Christchurch earthquakes: (i) vertical (or one-way) bending of the wall (7% of the cases), which tended to occur in longer walls or walls without side supports; (ii) two-way bending (57% of the cases), which required support of at least one vertical edge of a wall and (iii) top portion cantilever type failure with the entire top section of a wall or building façade collapsing, mainly due to a lack of top horizontal restraint. The OOP failures may affect the entire wall (both leaves), especially in front façades or upper storey walls of many two-storey buildings, or otherwise may affect the external leaf only. This high vulnerability is mostly due to the slenderness of the masonry leaves and the lack or inefficiency of anchoring systems between leaves. The leaf

connections (ties) are often too widely spaced and embedded in weak mortar, which results in the pull-out of the anchoring systems. Corrosion of ties has also been repeatedly reported as strongly affecting their effectiveness [2-5]. In addition, another primary cause of failure observed in cavity wall buildings is the lack of appropriate wall-to-diaphragm and wall-to-floor connections. The seismic OOP assessment of solid walls with top support has been already the subject of significant experimental investigations (among others [6-11]) and the theoretical modelling of such response was also carried out resorting to rigid-body idealizations. Very little experimental research, instead, has been carried on the seismic behaviour of cavity walls. In particular, no dynamic tests on cavity walls are presently available in the literature.

This paper presents experimental results which were obtained as a part of a wider research project aimed at assessing the vulnerability of URM buildings in the Groningen (the Netherlands) region, which in the last two decades has been exposed to induced seismicity [12]. Currently, very limited data are available on the seismic response of construction typologies specific to Dutch practice. The project, started in 2014, aims at investigating the performance of structural components, assemblies and systems typical of building typologies present in the Groningen area. The experimental campaign includes in situ mechanical characterization tests and laboratory tests such as characterization tests on bricks, mortar and small masonry assemblies, in-plane cyclic shear-compression and dynamic out-of-plane tests on full-scale masonry piers. Shaking table tests on full-scale masonry house specimens have also been performed at the laboratory of EUCENTRE Pavia. The experimental campaign aims to be a solid reference for the development of reliable numerical models to be used in fragility curves development and in the assessment of the seismic risk.

This paper describes out-of-plane shaking table tests on full-scale masonry assemblies. Three specimens represented different cavity wall configurations with different tie distributions, and one was a single-leaf wall specimen. The test set-up was constructed in order to induce OOP one-way bending behaviour in the specimens. The effect of vertical edge boundary conditions, reported also in earthquake damage observations (*e.g.* two way bending, see Figure 1b ), was deliberately not considered, as a first approach to the problem, and the horizontal double-fixed boundary conditions were designed in order to be always known in every testing phase. This allowed for a reduction of the unknowns and a simplification of the problem to the advantage of the subsequent interpretation and possible use of the data for model calibration.

Section 1.2 of the paper provides information on the specimen geometry and their material characterization. Section 1.3 provides a detailed description of the test-setup and the observed testing programme. The test results including deformed shapes, failure mechanisms, damage patterns, energy dissipation and other specific features of the observed dynamic behaviour are presented in Section 1.4. Part of such information is also reported in Tomassetti *et al.* [13].

## **1.2. Characterisation of the masonry specimens**

### **1.2.1. Specimen construction and geometric characterization**

Under controlled laboratory conditions, professional masons built the specimens in accordance with Dutch practices common in the years 1970-1980. The specimens were composed of one single leaf wall made of Calcium Silicate (CS) bricks and three cavity

wall panels with an inner CS brick wall (density  $1835 \text{ kg/m}^3$ ) and an outer clay brick wall (density  $1950 \text{ kg/m}^3$ ), with an 80 mm air gap. The two masonry leaves were approximately 2750 mm high,  $h$ , 1450 mm wide,  $w$ , and 102 mm thick,  $t$ . The sizes of the bricks were respectively  $212 \times 102 \times 71$  for the CS bricks and  $211 \times 100 \times 50$  for the clay bricks. The mortar bed-joints were nominally 10 mm thick in both walls. The specimens differed in terms of the applied vertical overburden pressure,  $\sigma_v$  (0.1 and 0.3 MPa), and number of ties, which were chosen according to code prescriptions and common masonry practices (2 and 4 ties/ $\text{m}^2$ , see Figure 2). These levels of imposed overburden pressure could be considered representative of a loadbearing wall located at the second and first storeys respectively, of a classical two storeys residential building. They are not meant to represent upper or lower bounds, but rather common values that can be often found in real buildings. L shape steel ties with a diameter of 3.1 mm and 200 mm long were inserted in the mortar bed-joints during the laying of the bricks to connect the two masonry leaves (see detail in Figure 2). Tests on pull-out strength of this specific coupling system were performed by Messali *et al.* [14] at TU Delft. Those researchers found that the pull-in and pull-out strengths of the “zigzag” tie extremity embedded in clay masonry specimens, considering an overburden pressure of 0.3 MPa, resulted higher than the strengths associated with the hook extremity embedded in CS specimens and subjected to the same imposed pressure. The average pull-out and push-in strengths recorded for CS specimens were approximately 1.46 kN and -1.09 kN, respectively. Moreover, the tensile ultimate capacity of the steel anchors was approximately 4.3 kN. Table 1.1 identifies the specimens, their geometry, tie configuration and the applied overburden pressure.

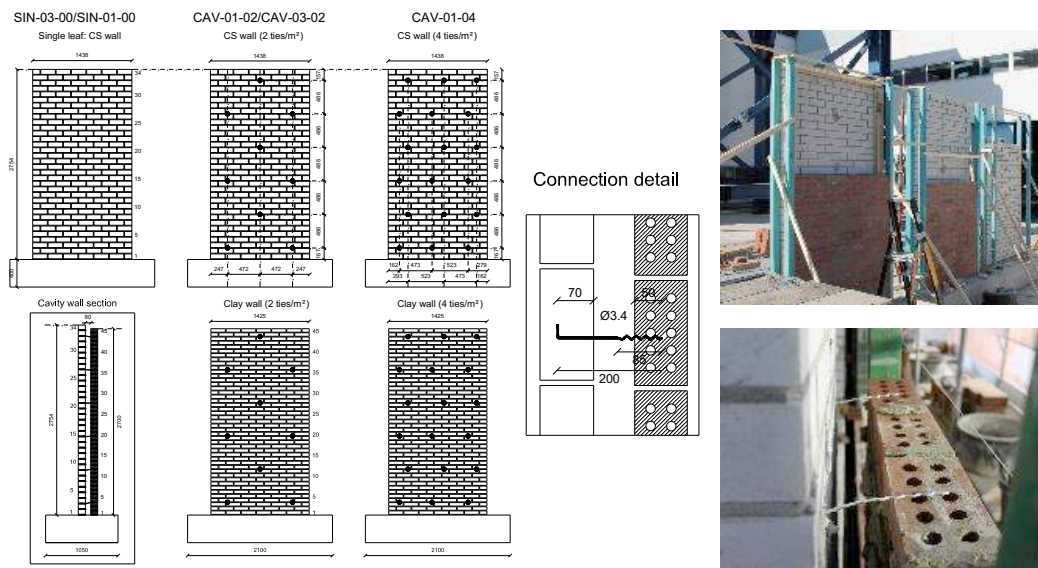


**Figure 1.2 Specimens geometry and construction details.**

Even if the scope of the present tests was envisaging idealized boundary conditions, the specimens could be somehow representative of a single storey vertically spanning cavity wall between two RC slabs and separating two tall windows; the floor system, usually, lies only on the inner CS wall, while the outer wall is continuous over the full height of the building. Moreover, often there is no physical connection at the diaphragm level



between the floor system and the outer clay wall. A full-scale house specimen with these specific construction details has been tested on the shake table at the EUCENTRE laboratory in Pavia, and will be the subject of a future publication.

**Table 1.1 Characteristics of test specimens**

Specimen ID	Wall Type	$w$	$t$	$h$	$\sigma_v$	Ties/m <sup>2</sup>
		[mm]	[mm]	[mm]	[MPa]	
SIN_03_00	Single CS leaf wall*	1438	102	2754	0.3	-
SIN_01_00	Single CS leaf wall*	1438	102	2754	0.1	-
CAV_01_02	CS inner wall	1438	102	2754	0.1	2
	Clay outer wall	1425	100	2700	0	
CAV_03_02	CS inner wall	1438	102	2754	0.3	2
	Clay outer wall	1425	100	2700	0	
CAV_01_04	CS inner wall	1438	102	2754	0.1	4
	Clay outer wall	1425	100	2700	0	

### 1.2.2. Mechanical characterization of the materials

A detailed overview of the experimental test campaign on material samples and masonry wallettes performed at the laboratory of the Department of Civil Engineering and Architecture of the University of Pavia is provided in Graziotti *et al.* [15]. Table 1.2 summarises experimental mean values, standard deviations (*St.Dev.*) and coefficients of variation (*C.o.V.*) for the investigated mechanical parameters, namely compressive strength ( $f_m$ ), Young's Modulus in compression ( $E$ ) and the flexural tensile strength ( $f_w$ ) of masonry perpendicular to bedjoints. The first two parameters were determined on masonry specimens according to EN 1052-1 [16], while the last one by means of the bond wrench tests as per EN 1052-5 [17]. Moreover, the mortar's compressive ( $f_c$ ) and flexural strength ( $f_t$ ) values were determined according to EN 1015-11 [18] and shown in Table 1.2 (shaded cells).

It can be appreciated how the CS masonry is characterized by a lower compression strength but a higher tensile (bond) strength compared to the clay brick masonry. In general, the mechanical characteristics of clay masonry resulted to have a dispersion higher than the one of CS masonry. This may be possibly related to the higher scatter in the properties of the components used for the clay brick masonry and to the lower bond developed between mortar and clay bricks.

**Table 1.2 Results of characterization tests on mortar and masonry specimens.**

	Calcium Silicate					Clay				
	$f_c$	$f_t$	$f_m$	$f_w$	$E$	$f_c$	$f_t$	$f_m$	$f_w$	$E$
<b>Mean [MPa]</b>	6.77	2.77	6.20	0.238	3256	6.09	2.03	11.32	0.158	5760
<b>St.Dev. [MPa]</b>	0.88	0.25	0.41	0.039	641	1.16	0.47	1.31	0.092	1613
<b>C.o.V. [%]</b>	13.0	9.0	7.0	16.3	20.0	19.0	23.0	12.0	58.2	28.0

### 1.3. Test set-up and dynamic loading sequence

#### 1.3.1. Test set-up

The test set-up was installed on a uni-directional shake table and oriented to excite the specimens in OOP one-way bending. Figure 3 shows some pictures of the test setup. Frame A, designed to be rigid, ensured that the dynamic input motion was transferred from the table to the top of the wall with negligible amplification. The specimens were anchored through the foundation to the shake table by means of steel bolts. The CS wall (representing the load-bearing wall in a real structure) was vertically loaded to the desired initial axial stress value through a steel beam pulled down by means of two steel rods in series with two springs (as shown in Figure 4). The connection between frame A and the beam on top of the specimen consisted of a pair of steel braces with mechanical hinges at one end (Figure 3c).

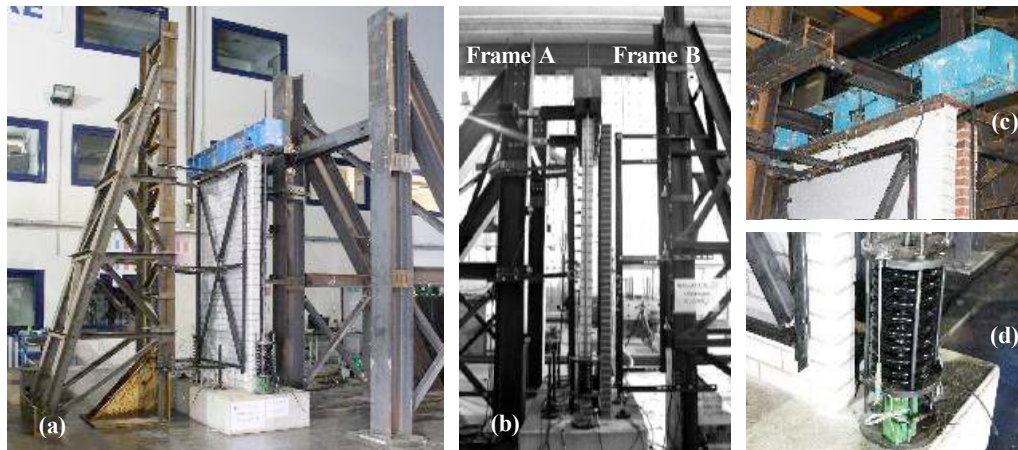


**Figure 1.3 Specimens geometry and details: general view (a,b), top boundary condition (c) and spring system (d).**

The braces were rigidly connected to the specimen top beam by means of steel plates in order to avoid any relative rotation. The hinge system allowed for the uplift of the wall whilst simultaneously transferring the horizontal dynamic input of the shake table to the top of the specimen. The resulting static configuration of the inner wall was that of double fixed boundary conditions. The restraint at the top of the inner wall was provided by a set of L-shaped steel profiles and mortar was used to fill the gap to the top row of bricks (see Figure 3c). The bottom section of the wall specimen lay on a mortar bed-joint resting on the specimen foundation, as in usual practice. A spring system was used to provide the axial force (see Figure 3d) on the CS wall and ensure that the increase in axial force at collapse (when the wall height is maximum), computed considering a rigid body failure mechanism, was less than 5% higher than the initial static force. The designed spring stiffness, experimentally tested, was 164.7 N/mm for those used to provide 0.3 MPa of axial stress and 53.5 N/mm for those providing 0.1 MPa stress. This solution guaranteed a double fixed condition with almost constant overburden axial stress in the inner CS wall during all the testing phases. This condition was not necessarily representative of a wall in a real building subjected to ground motions. In that case, the axial force was likely changing during the motion due to a general redistribution of axial



Table 1.3 Vertical position of the instruments installed on the specimens.

Instrument	SIN-03-00	CAV-01-02	CAV-03-02	CAV-01-04
	SIN-01-00			
	[mm]	[mm]	[mm]	[mm]
1/4 WP CS	612	612	695	693
1/2 WP CS	1340	1341	1503	1503
3/4 WP CS	1900	1900	2151	2151
1/4 WP CI	-	695	610	610
1/2 WP CI	-	1475	1355	1342
3/4 WP CI	-	2135	1955	1990
4/4 WP CI	-	-	2650	2650
½ Acc. CS	1260	1341	1341	1503
½ Acc. CI	-	1295	1355	1355

### 1.3.3. Dynamic input motion

Three acceleration time histories were employed in these dynamic tests. Gr-1 was supplied by the seismic hazard and risk assessment team involved in the project [12] as representative of an expected ground motion in the region of Groningen. The Gr-2 input was instead a first floor accelerogram obtained by means of the TREMURI program [19] using a model of a typical Dutch terraced house subjected to the aforementioned Gr-1 record along its flexible direction. A further input signal is represented by the 2 Hz Ricker Wave Acceleration input (RWA), which consists of a particular acceleration pulse (also known as Mexican hat wavelet). As a reference, Figures 5 and 6 show the 100% theoretical acceleration time-histories of the experimental inputs and their response spectra, respectively.

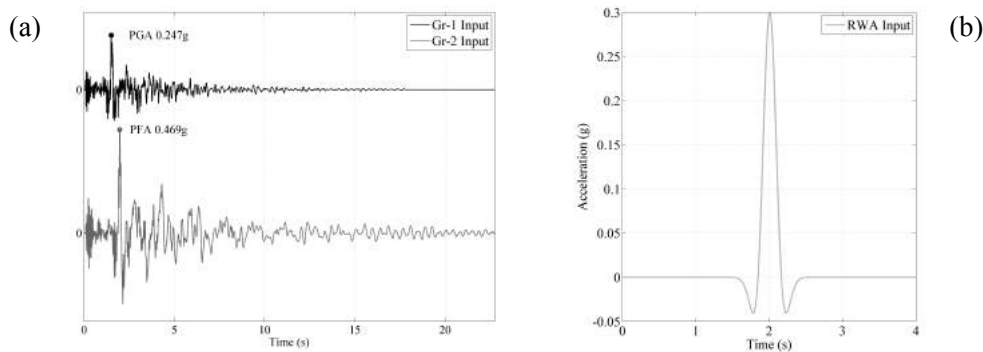
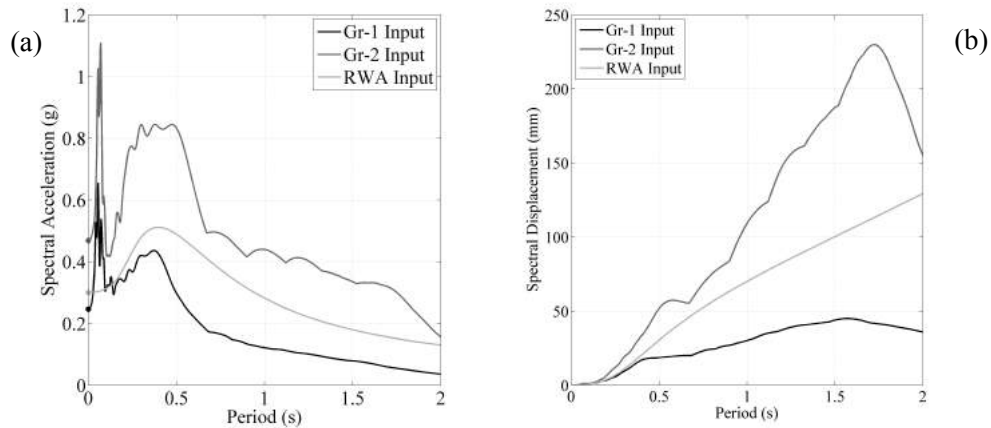


Figure 1.5 Gr-1, Gr-2 (a) and RWA (b) acceleration time histories.



**Figure 1.6 Comparison of acceleration (a) and displacement (b) response spectra (5% damping) for the adopted input signals.**

#### 1.3.4. Testing Programme

Initially, the specimens were subjected to low amplitude random excitations in order to identify their undamaged dynamic properties. The second testing phase consisted of an incremental dynamic testing procedure with the Gr-1 accelerograms, which could be considered a realistic excitation for a wall located at the ground floor of a building. Therefore, a series of Gr-1 acceleration table motions scaled to increasing amplitude were performed. A second incremental dynamic testing sequence was performed with the Gr-2 accelerograms, representing a possible dynamic excitation for a wall located at the building first floor, up until collapse of the specimen. A pulse excitation phase (adopting the RWA input) has been run between Gr-1 and Gr-2 in order to obtain samples of simplified wall response. These are ideal for the calibration of numerical models and studying the damping. Repetitions of tests with inverted directions (polarity) were performed in order to understand if, and how, the excitation direction affects the specimens' responses. The specimen/experiment listed as SIN\_01\_00 in Table 1.1 is the wall previously tested as SIN\_03\_00, where the test set-up was modified by substituting the springs in order to decrease the axial stress acting on the inner leaf from 0.3 to 0.1 MPa. Table 1.4 and Table 1.5 present the applied dynamic testing sequence, corresponding to the single-leaf and the cavity specimens respectively, and specifying the test number, the dynamic input typology, the peak acceleration, PGA, recorded on the specimen foundation during the test and the peak horizontal mid-height CS wall displacement response recorded by correspondent wire potentiometer. The overall chronological testing sequences are provided in Table 1.4 and Table 1.5, in order to better understand the state of degradation of the specimens at the beginning of each considered test. The tests best suited for the estimation of the energy dissipation (Section 1.4.6) are large amplitude RWA pulses (highlighted in bold characters). The shaded sections of the table identify different testing phases.

Table 1.4 Single-leaf specimen testing sequence.

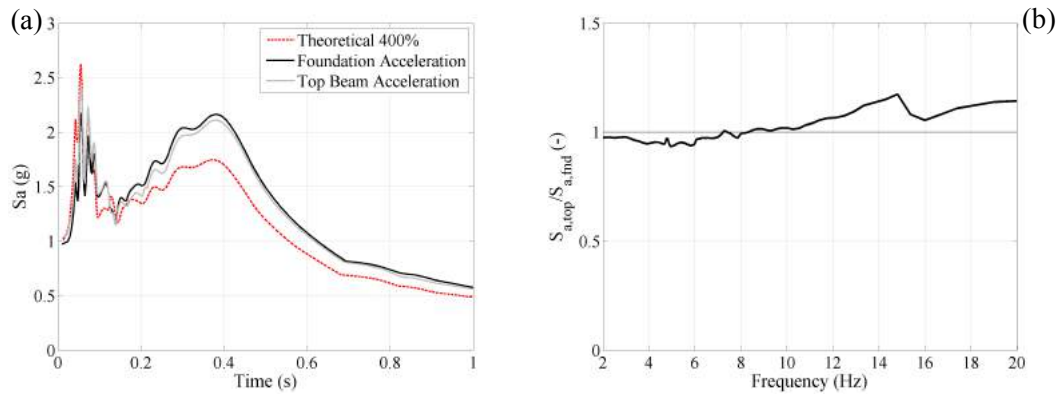
SIN-03-00 $\sigma_v = 0.3$ MPa				SIN-01-00 $\sigma_v = 0.1$ MPa			
Test #	Input	PGA [g]	Peak R. [mm]	Test #	Input	PGA [g]	Peak R. [mm]
0.1	WN	-	-	0.2	WN	-	-
1.1	Gr 1	-0.04	+0.06	3.1	Gr 1	-0.08	-0.35
1.2	Gr 1	-0.09	+0.11	3.2	Gr 1	-0.17	-0.73
1.3	Gr 1	-0.16	+0.40	3.3	Gr 1	-0.21	-0.92
1.4	Gr 1	-0.20	+0.57	3.4	Gr 1	-0.34	-1.28
1.5	Gr 1	-0.32	+0.92	3.5	Gr 1	-0.41	+1.94
1.6	Gr 1	-0.42	+1.22	3.6	Gr 1	-0.51	-7.42
1.7	Gr 1	-0.52	+1.40	3.7	Gr 1	-0.60	-14.42
1.8	Gr 1	-0.74	+1.70	3.8	Gr 1	-0.73	-16.60
1.9	Gr 1	-0.96	+4.93	4.1	RWA	+0.26	-0.38
2.1	RWA	+1.11	-1.97	4.2	RWA	+0.48	-1.88
<b>2.2</b>	<b>RWA</b>	<b>+1.63</b>	<b>-9.63</b>	<b>4.3</b>	<b>RWA</b>	<b>+0.72</b>	<b>-16.05</b>
2.3	RWA	+1.05	-2.68	<b>4.4</b>	<b>RWA</b>	<b>+0.96</b>	<b>-52.98</b>
<b>2.4</b>	<b>RWA</b>	<b>+1.88</b>	<b>-14.1</b>	5.1	Gr 2	-0.44	+2.87
				5.2	Gr 2	-0.64	-9.86
				5.3	Gr 2	-0.85	<b>-fail</b>

Table 1.5 Cavity wall specimen testing sequence.

CAV-01-02 $\sigma_v = 0.1$ MPa, 2 ties/m <sup>2</sup>				CAV-03-02 $\sigma_v = 0.3$ MPa, 2 ties/m <sup>2</sup>				CAV-01-04 $\sigma_v = 0.1$ MPa, 4 ties/m <sup>2</sup>			
Test #	Input	PGA [g]	Peak R. [mm]	Test #	Input	PGA [g]	Peak R. [mm]	Test #	Input	PGA [g]	Peak R. [mm]
0.1	WN	-	-	0.1	WN	-	-	0.1	WN	-	-
1.1	Gr 1	-0.04	0.00	1.1	Gr 1	-0.08	-0.18	1.1	Gr 1	-0.03	+0.05
1.2	Gr 1	-0.09	0.12	1.2	Gr 1	-0.12	-0.24	1.2	Gr 1	-0.09	-0.08
1.3	Gr 1	-0.12	0.19	1.3	Gr 1	-0.17	+0.15	1.4	Gr 1	-0.13	-0.17
1.4	Gr 1	-0.17	0.31	1.4	Gr 1	-0.21	+0.28	1.5	Gr 1	-0.17	-0.26
1.5	Gr 1	-0.21	0.36	1.5	Gr 1	+0.08	-0.04	1.6	Gr 1	-0.21	+0.36
1.6	Gr 1	+0.08	-0.15	1.6	Gr 1	+0.12	+0.12	2.1	RWA	-0.31	+0.33
1.7	Gr 1	+0.13	0.20	1.7	Gr 1	+0.16	-0.11	2.2	RWA	+0.34	-0.50
1.8	Gr 1	+0.17	-0.40	1.8	Gr 1	+0.20	-0.14	3.1	Gr 2	-0.30	+0.60
1.9	Gr 1	+0.23	-0.54	2.1	RWA	-0.29	+0.65	3.2	Gr 2	-0.44	+1.47
2.1	RWA	+0.22	-0.34	2.2	RWA	+0.29	-0.41	3.3	Gr 2	-0.63	-2.89
2.2	RWA	+0.32	-0.65	3.1	Gr 2	-0.30	+0.64	3.4	Gr 2	-0.73	-45.5
3.1	Gr 2	-0.33	-0.74	3.2	Gr 2	-0.44	+0.99	4.1	RWA	+0.30	-4.66
3.2	Gr 2	-0.50	2.45	3.3	Gr 2	-0.63	+1.70	4.2	RWA	-0.31	+2.25
3.3	Gr 2	-0.60	-10.6	3.4	Gr 2	-0.75	-2.88	0.2	WN	-	-
4.1	Gr 1	-0.61	-42.4	4.1	RWA	-0.50	+1.90	<b>4.5</b>	<b>RWA</b>	<b>-0.50</b>	<b>-28.8</b>
5.1	RWA	+0.32	-3.20	4.2	RWA	+0.52	-2.00	<b>4.6</b>	<b>RWA</b>	<b>+0.53</b>	<b>-45.3</b>
<b>5.2</b>	<b>RWA</b>	<b>+0.49</b>	<b>40.42</b>	5.1	Gr 2	-0.93	-6.12	5.1	Gr 2	-0.44	-32.9
6.1	Gr 2	-0.68	<b>-fail</b>	5.2	Gr 2	-1.11	<b>-fail</b>	5.2	Gr 2	-0.62	<b>-fail</b>
								5.3	Gr 2	+0.49	-
								5.4	Gr 2	+0.68	<b>+fail</b>

#### 1.4. Test results

The test set-up proved to be effective in allowing the specimens to be tested with the desired boundary conditions and inducing a pure OOP one-way bending action in the walls. Figure 8a shows the comparison between the top and bottom response spectra computed from the recorded shake table acceleration histories and the theoretical, or target, response spectra for a relevant Gr-1 test (e.g. SIN-03-00, test 1.9, input scaled to 400%). It is possible to observe some discrepancy between the target and the recorded acceleration spectrum due to the dynamic interaction between the test setup and the shaking table. The consequent distortion in the recorded response spectra is higher for tests with larger PGAs (as the one presented in figure 7a) and considerably smaller for test of lower intensity. A slightly undershoot of low period spectral accelerations is detectable while a more consistent overshoot (amplification) is seen for the higher periods. Figure 7b shows the top and bottom acceleration spectrum ratio considering just the frequency range relevant for the dynamic behaviour of the specimens. A slight amplification (not exceeding 15%) is detectable corresponding to the steel frame fundamental frequency of vibration ( $\approx 15\text{Hz}$ ). Notice that all the accelerations (nominal and recorded) during each testing phases are stored and available for processing.



**Figure 1.7 Spectral accelerations comparison (a) and spectral acceleration ratio (b) between specimen top and bottom locations for the specimen SIN-03-00 (test 1.9).**

##### 1.4.1. Dynamic identification

As already mentioned, all specimens were excited by means of a random signal (0.05g PGA), in order to detect the fundamental frequency of vibration of the undamaged wall. Analysing the mid-height acceleration response of both walls, significant amplifications corresponding to the natural frequency of vibration of the wall were detected. Table 1.6 lists the natural frequencies of vibration for each specimen obtained from the random test.

Table 1.6 Specimen dynamic identification.

Specimen	CS Wall		Clay Wall	
	Frequency [Hz]	Period [s]	Frequency [Hz]	Period [s]
SIN_03_00	18.75	0.053	-	-
SIN_01_00	14.27	0.070	-	-
CAV_01_02	17.23	0.058	20.08	0.049
CAV_03_02	25.00	0.040	20.68	0.048
CAV_01_04	19.24	0.052	19.13	0.052
CAV_01_04*	13.08	0.076	7.11	0.141

\*performed after test 4.2

#### 1.4.2. Deformed shapes

The deformed shapes have been obtained from the horizontal displacement recorded by the wire potentiometers at the time of maximum displacement of the CS wall at mid-height. As expected, deformed shapes change significantly according to the ground motion intensity level and specimen damage. Figure 8a shows the specimens' deformed shapes from the Gr1 tests (intensity 100% PGA 0.247g) where the peak acceleration direction is towards the clay wall side (positive direction).

The deformed shape of the single-leaf wall is approximately similar to that of a double fixed beam, with the response peaks located at  $\frac{1}{2}$  of the wall height for both the SIN-03-00 and SIN-01-00 configurations.

In cavity wall specimens, the CS wall deformed shapes were qualitatively similar to those recorded for the single-leaf walls. The clay wall, instead, due to the different stiffness and top boundary conditions, tended to displace differently exhibiting almost a cantilever deformed shape. Because of this, the relative horizontal displacement between the two walls is higher at the top, as shown by the CAV\_01\_02 and CAV\_03\_02 specimens. A progressive deterioration of the bond of the tie anchoring system, which resulted in the recording of a few millimetres of differential displacement between the two leaves, has been detected in these testing phases, even for low intensity levels of shaking. Such a phenomenon is less evident for the CAV\_01\_04 specimen where the density of ties is higher and consequently the relative displacement of the walls resulted to be lower.

Figure 8b shows the deformed shapes associated with all the specimens for different RWA input tests where the peak acceleration direction is towards the CS wall side (negative direction). As the acceleration input and the horizontal displacement increase, the deformed shapes change significantly. The specimens exhibited rocking behaviour with the formation of cracks at bottom, top and around mid-height sections. For cavity specimens, the differential displacement between the two leaves became progressively negligible with respect to the amplitude of the two walls mid-height displacement.

No top cracks in cavity specimens were detected in the clay wall, which was unrestrained at the top. The two quasi-rigid bodies above and below the mid-height crack sections rotated around the cracked sections, using them as pivot points and displacing simultaneously. It is possible to notice differences in the response of the panels: the CAV\_03\_02 specimen shows a considerably lower mid-height displacement when subjected to inputs with similar PGAs while the CAV\_01\_02 wall exhibited a peak mid-height response in the opposite direction of the acceleration pulse.



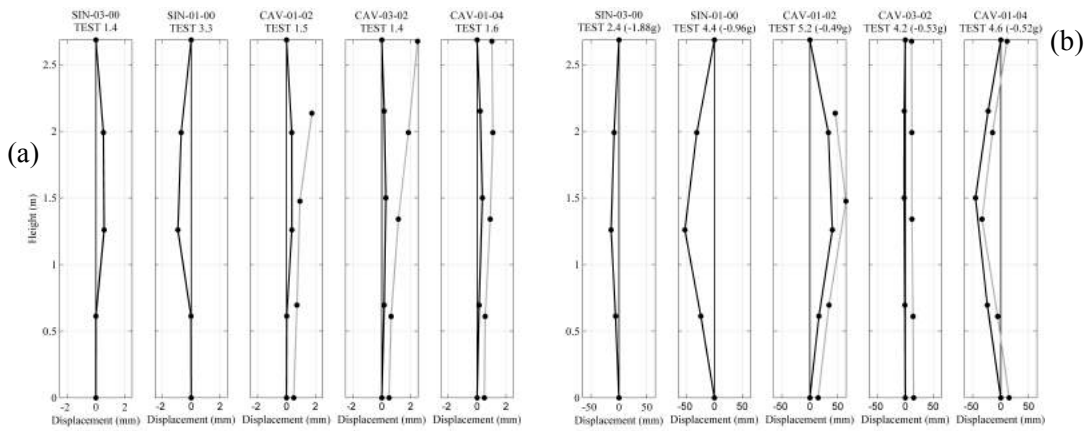


Figure 1.8 Deformed shapes for Gr1 (a) and RWA (b) input: CS wall black line, clay wall grey line.

### 1.4.3. Damage pattern and failure mechanisms

All the specimens exhibited rocking behaviour with the formation of horizontal cracks at the bottom, top and around mid-height sections of the walls. For cavity wall specimens, cracks at the wall top were detected only on the CS walls, with the tops of the clay walls being unrestrained. Figure 9 identifies the location of cracks for the single-leaf specimen and for cavity wall specimens in both the CS walls and clay walls (in terms of layer number). The tie grid is also shown to better understand the position of the cracks with respect to the anchoring system between the two walls.

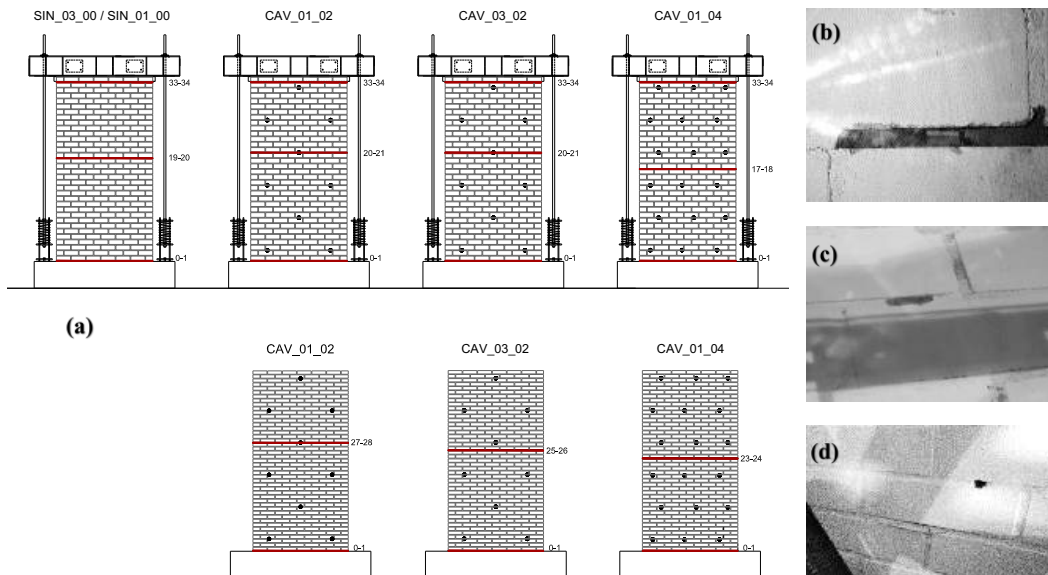


Figure 1.9 Specimens crack pattern (top CS wall, bottom clay wall) (a) and pictures of damage detected on the CS wall for the CAV-01-02 (b), CAV-03-02 (c) and CAV-01-04 (d).

The single-leaf specimen, which exhibited rocking only when subjected to 0.1 MPa of vertical overburden pressure (SIN-01-00), showed a mid-height crack at  $0.575h$  (between

the 19<sup>th</sup> and the 20<sup>th</sup> brick layer), where  $h$  is the nominal wall height, taken as the total panel height minus the height of one brick (due to the last brick layer being clamped by the steel L-shape profiles). The observed mechanism agrees well with the formulation proposed in literature for the estimation of the intermediate hinge height considering the wall tensile strength [20], which yielded a value  $0.557h$  according to the following equation:

$$\frac{h_1}{h} = 1 + \frac{\eta + t - \sqrt{(2 + t + 2\eta)(t + \eta)}}{2 + \eta} = 0.557 \quad (1)$$

where  $\eta = O/W$  is the ratio between vertical overburden force and the wall self-weight and  $t = f_w/(W/(t \cdot w))$  is the non-dimensional masonry tensile strength. The parameter  $t$  significantly influences the position of the mid-height hinge: the higher the tensile strength, the lower its position. Moreover, it is important to underline that Equation 1 has been proposed for the case when the vertical overburden force is applied at the wall mid-thickness; however, during the experimental test there is a migration of the resultant overburden force ( $O$ ) towards the thickness edge (hinge location) during the rocking behaviour (see Figure 10).

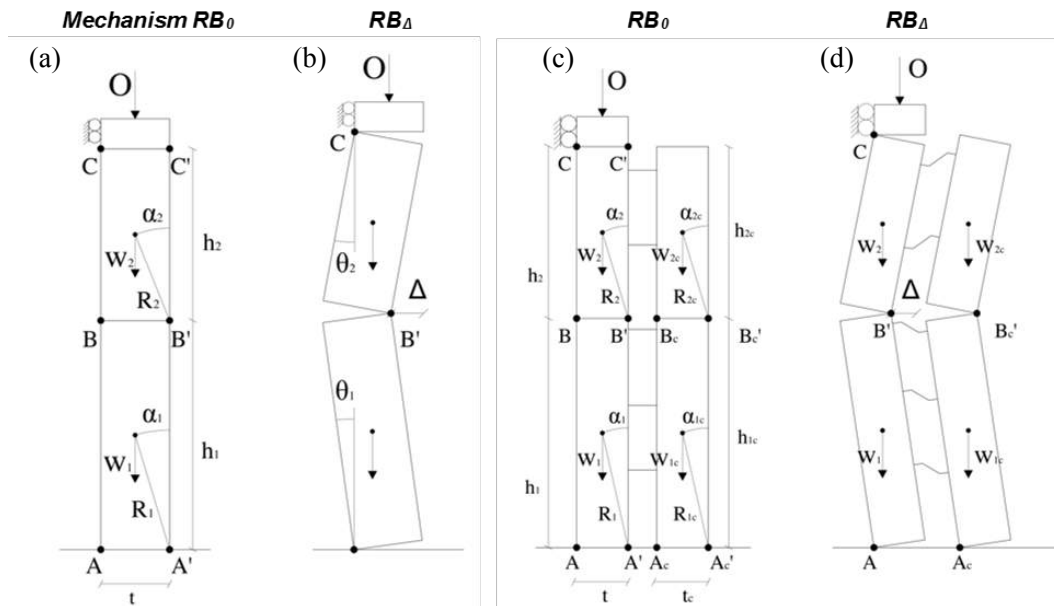


**Figure 1.10 Rigid body (RB) mechanisms: static and dynamic conditions for single-leaf (a-b) and cavity wall (c-d) specimens.**

For cavity wall specimens, instead, it can be observed that for the two specimens with a tie density of 2 ties/m<sup>2</sup> (CAV\_01\_02 and CAV\_03\_02) the horizontal mid-height cracks are at a height of approximately  $0.6h$ , which is the height of the tie connection between the two walls. The CAV\_01\_04 specimen/test (which had 4 ties/m<sup>2</sup>) showed instead mid-height cracks at exactly  $0.5h$ . Further cracks (not reported in the figure) developed only after the impact with the safety system and they cannot be considered part of the failure mechanism. Damage at the mortar bed-joints in the CS walls was detected at some of the locations corresponding to the position of the ties (see figure 9b, c, d). This was caused by

the relative positioning of the ties along the thickness of the leaf (the hook was always closer to the outer face of the CS leaf); the pull-out capacity in the positive direction (e.g. clay wall pulling the CS wall) was higher than in negative direction (e.g. clay wall pushing the CS wall) as found by [14].

The observed behaviour, as largely suggested in literature [8, 20, 21], can be described by the dynamic response of an assembly of rigid bodies. Figure 10, shows a rigid body schematic representation of the experimental test performed for the single-leaf wall and for the cavity specimens. The upper portion is represented by the last brick layer clamped by the L steel profiles and free to move vertically due to the mechanical hinge on the left arms extremity (see Figure 3c).

Looking at Figure 10, it may be observed that, with the incoming uplift of the wall, the overburden resultant axial force migrates towards the thickness edge of the CS wall (passing through the pivot point  $C$ ). The wall, indeed, displacing horizontally switches from an ideal RB mechanism with the axial force applied at the mid-thickness ( $RB_{\theta}$ ) to a RB mechanism where the force is applied at the thickness edge ( $RB_{\Delta}$ ). The horizontal weight multiplier that triggers those mechanisms and the associated instability displacements (when the wall resisting force drops to zero) is slightly different. Moreover, for a better understanding of the dynamic behaviour and the failure mechanisms involved, Figure 11 presents frames of the video at the moment of the specimens collapses. In particular, it is possible to appreciate the deformed shapes during the test and in the instants before the impact against the restraining system. All the cavity specimens collapsed under the Gr-2 earthquake towards the CS wall. It is believed that this fact, which is different from what observed in many real earthquakes (where often the outer leaf collapses outwards and the inner leaf remains standing) is probably the result of a combination of the following factors: a) the input acceleration, characterized by short duration and non-symmetric pulses (a “directional effect” in the input), and b) the mechanical and geometrical characteristics of the ties, whose anchor strength is lower in the push direction and which also may easily buckle in compression.

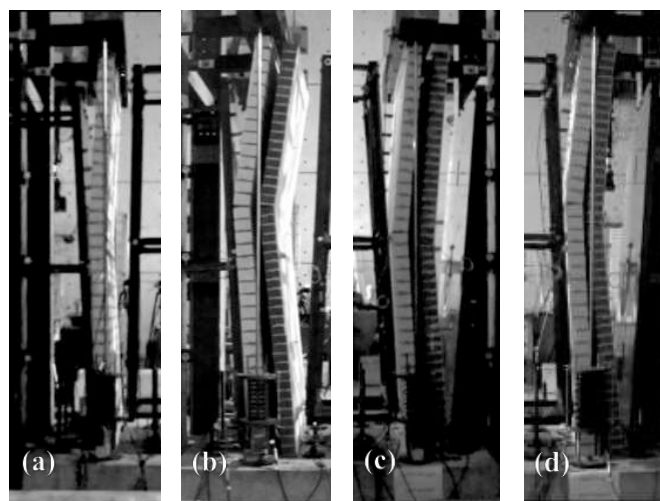


Figure 1.11 Snapshots of the specimen failures: SIN-01-00(a), CAV-01-02(b), CAV-01-04(c) and CAV-03-02(d).

Especially this latter factor b) leads the outer leaf to sway more easily towards the stiffer inner leaf, since the ties oppose a lower reaction when failing in compression, while it is more effectively restrained by the ties and the inner leaf when trying to sway away from it, in the outward direction. CAV-01-02 (Figure 11b) and CAV-01-04 (Figure 11c) specimens exhibited rocking behaviour in several tests before the failure whereas the CAV-03-02 (Figure 11d) exhibited a rocking behaviour only right before collapsing.

All the cavity specimens collapsed in horizontally-coupled one-way rocking behaviour and exhibited damage due to failure in compression of the anchoring of the steel ties into the mortar bed-joints of the CS walls. Although the ties had negligible flexural stiffness, their axial stiffness ensured a sufficient coupling of the horizontal displacement of the two leaves (i.e. limiting the differential displacement and maintaining the gap) up to near-collapse, even for the specimens with only 2 ties/m<sup>2</sup>, producing a one-way rocking failure mechanism in the cavity components. This is extremely important as it allows for the analysis of the OOP seismic behaviour of these cavity walls with simplified single-degree of freedom (SDOF) models, as proposed by several studies for solid walls [8, 20, 21]. This simplification may not necessarily be generalized to cavity walls with geometry and boundary conditions which are very different from those tested here. The present tests show that, for this specific cavity wall configuration (e.g. material strengths, geometry, ties positioning, un-degraded materials, input motions) the weak direction seems to be the inward one due to the failure in compression of the ties. This behaviour may not be necessarily representative of the behaviour of the entire building stock, if different ties or masonry leaves are present.

#### 1.4.4. Specimen F- $\Delta$ relationships

For the dynamic simulation of the OOP response of walls, the definition of a reliable capacity curve  $F$ - $\Delta$  (where  $F$  is the total horizontal force while  $\Delta$  defines the horizontal displacement of the mid-height hinge) is crucial. For single-leaf vertical spanning strip wall (VSSW), this relationship was successfully modelled by a trilinear curve by several researchers that provided mean parameters necessary to build such configuration [8, 22-24]. Ferreira *et al.* [25] proposed instead, a four-branch model. This section presents the experimental  $F$ - $\Delta$  curves for the single-leaf specimen and for the cavity specimens. Another experimental research project aimed at understanding the static  $F$ - $\Delta$  relationship of cavity walls with New Zealand detailing has been carried out by Walsh *et al.* [26]. Within the presented experimental campaign, TU Delft performed OOP static tests on components with typical Dutch detailing (as the one herein presented). Figure 12 shows the comparison between the experimental dynamic  $F$ - $\Delta$  curve and the RB bi-linear curves associated with static mechanisms  $RB_0$  and  $RB_\Delta$  (see Figure 10).

The experimental force has been obtained by multiplying the absolute acceleration of the centre of mass of the two bodies by the related masses while the displacement is the one relative to the mid-height hinge location. The two centre of mass accelerations were computed using the acceleration recorded by the mid-height accelerometer and assuming a triangular distribution of the relative acceleration along the wall height, with the maximum value at the mid-height hinge location (e.g. considering the two bodies as rigid). The RB bilinear static relationships have been built according to the two idealisations considering the corresponding instability displacements. Table 1.7 summarises the parameters necessary to build the bi-linear relationships (e.g. the static capacity curve) for the rigid body mechanisms shown in Figure 10.

Table 1.7 Rigid-Body force-displacement bi-linear parameters.

	<i>Mechanism RB<sub>0</sub></i>	<i>Mechanism RB<sub>Δ</sub></i>
$F_{RB}$	$F_{RB0} = \frac{2}{h_1}(W + O)t + \frac{1}{h - h_1}Ot$	$F_{RB\Delta} = \frac{2}{h_1}(W + O)t + \frac{2}{h - h_1}Ot$
$\Delta_{i,RB}$	$\Delta_{i,RB0} = \frac{\left[\frac{W + O}{h_1} + \frac{O}{2(h - h_1)}\right]}{\left[\frac{W + O}{h_1} + \frac{O}{(h - h_1)}\right]}t$	$\Delta_{i,RB\Delta} = t$

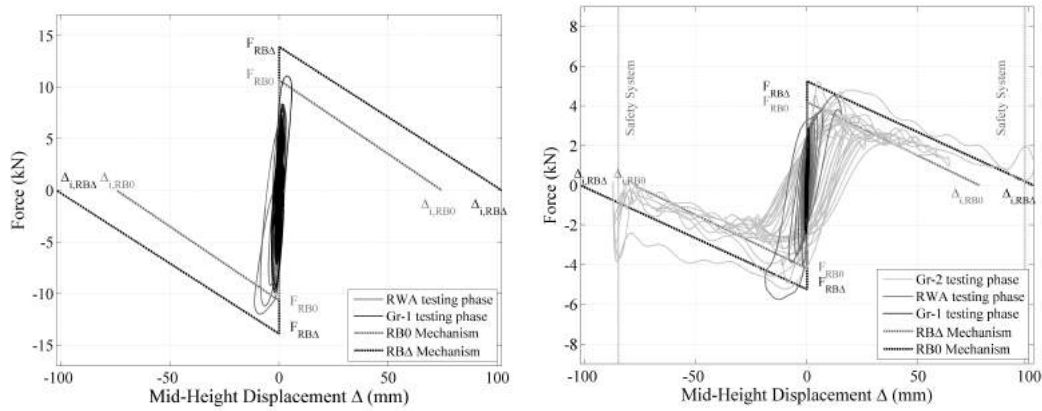


Figure 1.12 Single-leaf specimen  $F-\Delta$  relationships: SIN-03-00 (a) and SIN-01-00 (b).

Figure 13 shows the comparison between the experimental  $F-\Delta$  curve and the RB bi-linear curves for the two mechanisms shown in Figure 10 (right) for the cavity wall specimens. The RB force has been computed by the raw sum of the RB forces associated with the two independent mechanisms for the two walls (CS and Clay walls). The vertical grey lines (dotted) represent maximum horizontal displacements allowed by the safety system in different phases of the test. For the  $RB_{\Delta}$  mechanism the only maximum force is plotted. Regarding the experimental  $F-\Delta$  curve, the displacement at mid-height of the CS wall is shown. The energy dissipation, in good part associated with the area enclosed by the hysteresis loops, is significantly higher than the single-leaf specimen cases. It is also interesting to notice that the specimen force capacity is not far from the simple sum of the forces associated to the RB mechanisms of the two walls considered independently. The capacity shown by CAV-01-02 and CAV-01-04 is comparable even if the latter was able to resist more significant runs of excitation.

The energy dissipation, in good part associated with the area enclosed by the hysteresis loops, is significantly higher than the single-leaf specimen cases. It is also interesting to notice that the specimen force capacity is not far from the simple sum of the forces associated to the RB mechanisms of the two walls considered independently. The capacity shown by CAV-01-02 and CAV-01-04 is comparable even if the latter was able to resist more significant runs of excitation.

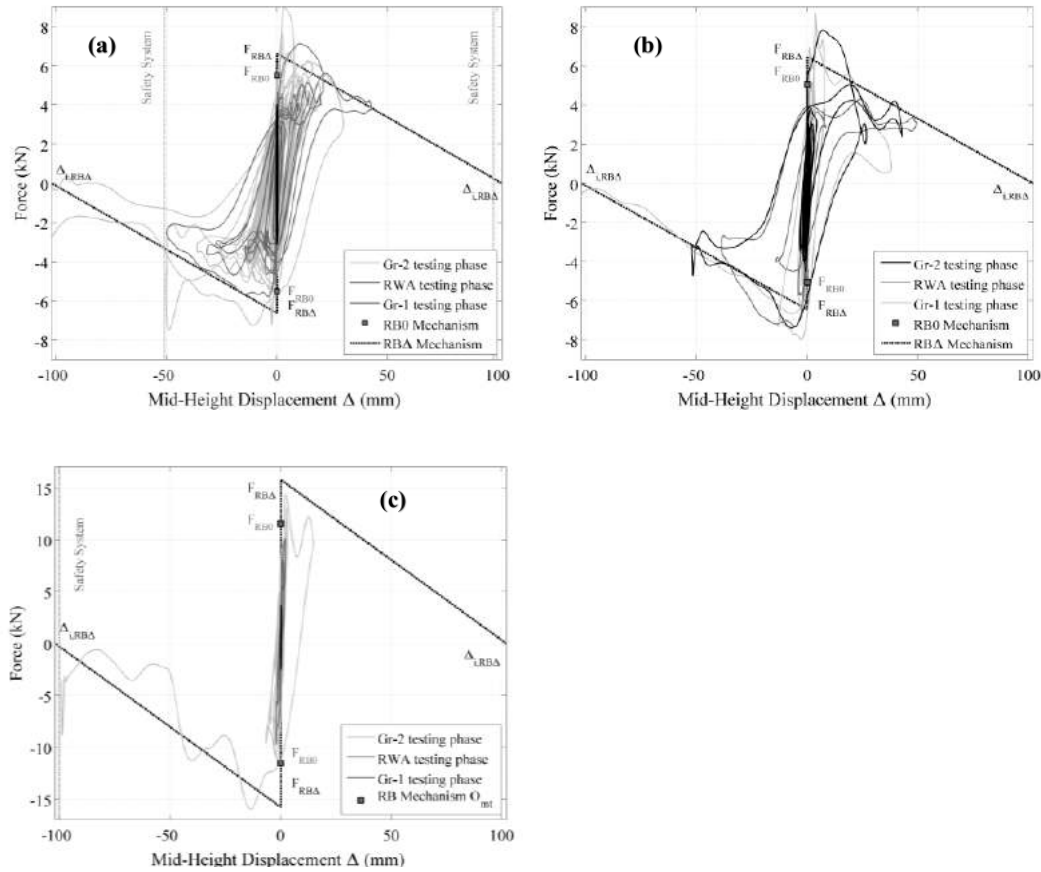
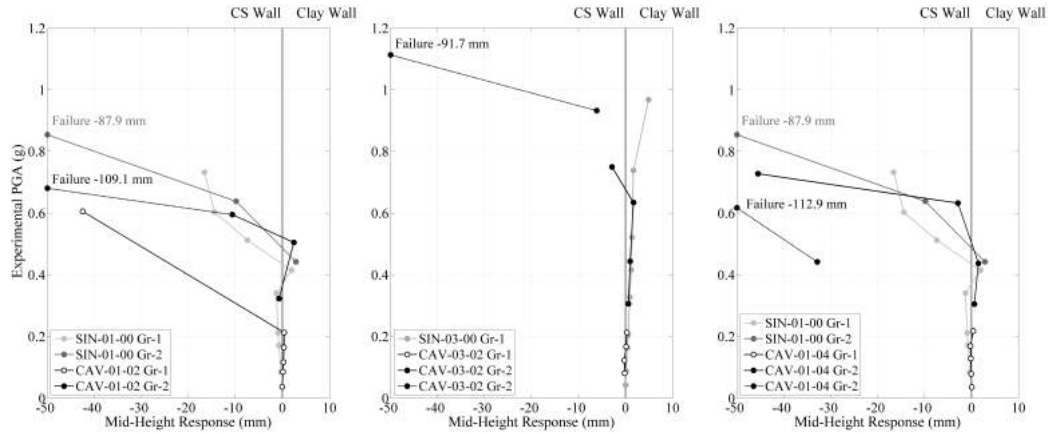


Figure 1.13 Cavity wall specimen F- $\Delta$  relationships: CAV-01-02 (a), CAV-01-04 (b) and CAV-03-02 (c).

#### 1.4.5. Specimen's acceleration capacity

This section presents the results of the experimental incremental tests (Gr-1 and Gr-2 inputs) in terms of mid-height horizontal displacement recorded by the wire potentiometer on the CS walls and PGAs (see Figure 14). The experimental work confirmed that the single-leaf wall capacity and the cavity wall capacity as well is strongly influenced by the overburden pressure acting. It can be observed also that in general the presence of an unloaded veneer clay wall reduce the specimens' capacity, resulting as an additional mass on the system with a very little contribution to the specimen's resistance. All the tested cavity wall specimens, in fact, exhibited lower capacities compared to the single-leaf specimen loaded at the same initial vertical force value (collapsed under Gr2-input with a PGA of 0.85g).

The CAV-03-02 specimen ( $\sigma_v=0.3$  MPa) collapsed when subjected to an acceleration time history with a PGA of 1.11g, 65% higher than the maximum applied to CAV-01-02 specimen ( $\sigma_v=0.1$  MPa).



**Figure 1.14 Experimental PGA vs peak horizontal mid-height displacement.**

The number of ties connecting the two walls does appear to influence the cavity wall response, with the CAV-01-04 (4 ties/m<sup>2</sup>) specimen exhibiting an almost 10% higher capacity than the CAV-01-02 specimen (2 ties/m<sup>2</sup>). This was associated with a general capacity to resist a larger number of excitations. The CAV-01-04 specimen resisted a maximum PGA of 0.73g; after this test the specimen was subjected to a further series of RWA inputs collapsing only 6 runs later under a lower peak acceleration (0.62g Gr-2 input). As already reported, it is interesting to note that all the specimens collapsed in the negative direction.

#### 1.4.6. Energy dissipation

Another crucial parameter for the simulation of the OOP dynamic behaviour of rocking systems and for the development of reliable SDOF systems is the energy dissipation involved in such a behaviour. The rocking behaviour herein described has been extensively investigated in the past. Housner [27], under the criteria of no sliding, no bouncing effect and energy dissipation concentrated at the instant of the impact, defined a SDOF equation of motion for the simulation of the dynamic response of rigid blocks. Sorrentino *et al.* [20], under similar criteria and assuming both supports moving simultaneously, derived a SDOF equation of motion for vertical spanning strip walls (VSSW) (as the one herein tested, *e.g.* SIN-03-00 and SIN-01-00) displacing as an assembly of two rigid bodies. DeJong and Dimitrakopoulos [21] and Restrepo [28] extended the solution to include equivalent SDOF systems governing the dynamic behaviour of complex multi-block systems responding in rocking. All of the aforementioned studies described the rocking phenomena as function of the equivalent rotation of the system and simulated the energy dissipation involved in the mechanism by means of the coefficient of restitution.

##### 1.4.6.1. The classical rocking theory

Housner [28] introduced a measure of the energy dissipation as the reduction of kinetic energy between the instants before and after the impact. Aslam *et al.* [29] defined the restitution coefficient as the direct ratio between angular velocities after and before the impact. Assuming an infinitesimal impact duration and hence instant velocity variation, in analogy with Housner's formulation for the single rigid block, it is possible to derive for a

VSSW system a theoretical coefficient of restitution as a ratio  $e_{an}$  between the angular velocities after ( $\dot{\theta}_{n+1}$ ) and before ( $\dot{\theta}_n$ ) the impact. This coefficient is derived assuming the conservation of angular momentum around the lower rotation hinge by equating the angular momentum after and before the impact. Equation 2 [20] provides an estimation of the velocity reduction for a VSSW knowing the geometric parameters of the wall.

$$e_{an} = \frac{\dot{\theta}_{n+1}}{\dot{\theta}_n} = \frac{m_1 R_1^2 + I_{G,1} - I_{G,2} \frac{\tan \alpha_2}{\tan \alpha_1} - 2m_1 R_1^2 \sin^2 \alpha_1 + m_2 R_1^2 \left[ 2 + \frac{\sin \alpha_1 \cos \alpha_1}{\tan \alpha_2} - \sin^2 \alpha_1 \left( 4 + \frac{\tan \alpha_2}{\tan \alpha_1} \right) \right]}{m_1 R_1^2 + I_{G,1} - I_{G,2} \frac{\tan \alpha_2}{\tan \alpha_1} + m_2 R_1^2 \left[ 2 + \sin \alpha_1 \cos \alpha_1 \left( \frac{1}{\tan \alpha_2} + \tan \alpha_2 \right) \right]} \quad (2)$$

where  $I_{G,1}$  and  $I_{G,2}$  are the polar moment of inertia around the two blocks centre of mass, while  $m_1$  and  $m_2$  are the two block masses and all the other parameters are defined according to Figure 10. The coefficient of restitution, depends on the  $\alpha_1$  parameter: the more squat the wall (higher  $\alpha_1$  or lower slenderness), the higher is the energy dissipation (lower  $e_{an}$ ) in analogy with the single block case. Moreover, Sorrentino et al. [20] showed also that  $e_{an}$  is much more sensitive to  $\alpha_1$  than to  $\alpha_2$  (Figure 10a) and that the migration of the mid-height hinge towards the mid-height of the wall increases the energy dissipation.

#### 1.4.6.2. Experimental computation of the coefficient of restitution

The theoretical values of the coefficients of restitution have been compared to those observed analysing the response of the specimens subjected to RWA impulses. The responses of the specimens are characterised by a significant damped free vibration phase, which provided precious information on the damping acting on the specimens. An experimental coefficient of restitution, according to the Aslam *et al.* [29] formulation and taking in account the assumption presented above, can be computed from angular velocity histories by manipulating and deriving the recorded mid-height displacement histories. The identification of the position of the pivot point and the subsequent kinematic transformation of the recorded displacement histories into rotation histories is extremely important in the analysis of the rocking mechanism. In reality, the two bodies do in fact have finite stiffness and the mortar bed-joint represents a flexible interface [30, 31]; this leads to an inwards shift of the hinge with respect to the perfect RB mechanism. The rotation and the hinge position are hence functions of the oscillation amplitude as well as the instability rotation. Considering the high slenderness ( $\lambda \approx 26$ ) of the tested specimens, the model assumed for the definition of the kinematic quantities involved is the RB one. The rotation history is obtained by dividing the horizontal displacement history recorded by the height of the wire potentiometer. Figure 15a and 15b plot the rotation and angular velocity time histories normalised with respect to the instability rotation (A) considering a mechanism with the vertical load applied on the wall thickness edge for the SIN-01-00 specimen (test 4.4) and the CAV-01-04 specimen (test 4.6). It is possible to appreciate, as largely known for rocking systems, the dependence of the frequency of the response on the oscillation amplitude. The CAV-03-02 specimen did not show significant free vibration oscillations in the RWA tests and therefore did not allow a straightforward computation of the energy dissipation.





computed as previously described, are assigned to the first of the two impacts.  $e_{exp,v}$  provided slightly lower and more scattered values compared to  $e_{exp,r}$ . The former can be influenced by the resolution of the monitoring devices for small levels of rotation, while the latter has been demonstrated to successfully simulate the energy losses in simplified SDOF model. For these reasons all the results have been proposed by means of  $e_{exp,r}$  [30]. The coefficients of restitution of the cavity wall specimens have been computed according to the CS inner wall crack patterns, geometry and rotation histories, taking into account the final goal of developing a reliable SDOF system that is able to simulate the OOP dynamic behaviour of cavity walls. The  $e_{exp,r}$  associated with cavity walls specimens (Figure 16b) are much lower, due to the energy dissipated by the tie system and due to interaction between the two walls which will not move perfectly in phase, causing a significant damping effect on the system. This phenomenon is much more evident in the CAV-01-02 specimen where the number of ties is limited to 2 ties/m<sup>2</sup> and consequently the number of impacts detected.

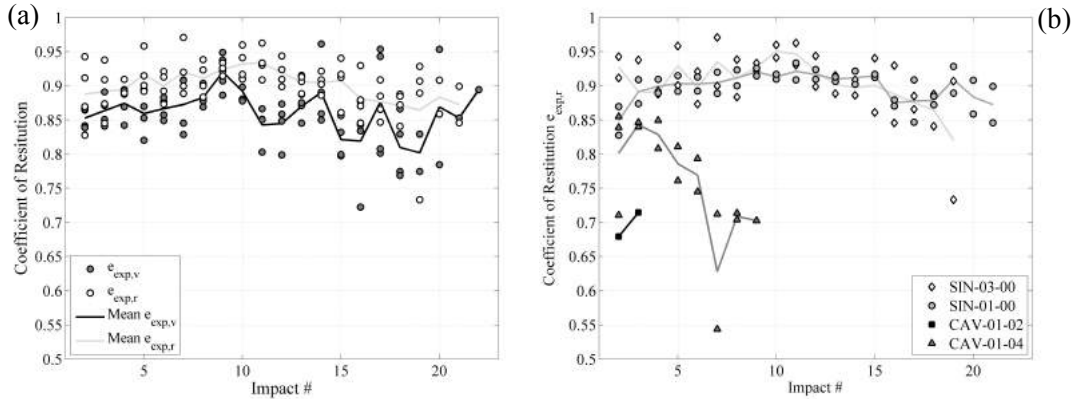


**Figure 1.16 Comparison between different coefficients of restitution for all the specimens (a) and comparison between coefficients of restitution  $e_{exp,r}$  for different specimens (b).**

Table 1.8 summarises the mean and standard deviation for coefficients of restitution computed for each run. No appreciable difference can be detected in the  $e$  values with the variation of the superimposed vertical load, while a slight reduction due to the specimen mortar bed joints damage at the hinge location can be detected. The ratio  $e_{exp,r}/e_{an}$  for the single-leaf specimen is equal to 0.91, very close to the 0.9 value proposed by Sorrentino [24]. As expected, it is also lower than 0.95 proposed by Sorrentino *et al.* [32] for cantilever walls responding in rocking. Derakhshan *et al.* [23] recently showed that simplified models assuming a coefficient of restitution between 0.78 and 0.83 successfully simulated the dynamic response of specimens [8, 9, 11] squatter than the ones tested in this work.

Table 1.8 Comparison of experimental and analytical coefficient of restitution.

Specimen	$e_{an}$	Test	Mean	St.Dev.	Mean	St.Dev.
			$e_{exp,r}$	$e_{exp,r}$	$e_{exp,v}$	$e_{exp,v}$
SIN_03_00	0.991	2.2	0.906	0.061	0.872	0.047
		2.4	0.902	0.038	0.852	0.070
SIN_01_00	0.991	4.3	0.906	0.027	0.878	0.039
		4.4	0.891	0.026	0.841	0.045
CAV_01_02	0.991	5.2	0.697	0.036	0.615	0.087
CAV_01_04	0.989	4.5	0.749	0.138	0.742	0.105
		4.6	0.785	0.084	0.713	0.203

#### 1.4.6.3. Experimental computation of the damping ratio

Some authors simulated this mechanism dynamics considering the horizontal displacement correspondent to the wall mid-height hinge as the unique kinematic quantity. In these cases, energy dissipation has been modelled as a velocity dependent acting force through a constant, variable (cycle to cycle) [33] or stiffness proportional damping ratio [34]. Doherty [8] provided an estimation of the equivalent viscous damping (EVD) ratio  $\xi$  associated with the cyclic energy loss through the decay of the oscillation amplitude in a series of free vibration tests. The damping ratio was hence determined according to equation 5:

$$\xi = \ln(\theta_{n+2}/\theta_n)/2\pi \quad (5)$$

observing a lower bound value equal to 6%. As shown in Figure 17a, the single-leaf specimen exhibits damping ratio values between 5 and 10%, whereas cavity specimens show values considerably higher than 10%. The change in the frequency response in the single-leaf specimen due to the different superimposed vertical load (from SIN-03-00 to SIN-01-00) is also detectable. In particular, the CAV-01-04 response appears linearly dependent on the frequency of the system, and hence on the oscillation amplitude. More tests will need to confirm this trend. Figure 17b plots the relationship between the coefficient of restitution (computed according to equation 4) and the damping ratio (computed through the logarithmic decay), for all the specimens tested. It confirms that the empirical relation between  $e$  and  $\xi$ , proposed by Makris and Konstantinidis [35] agrees well with the experimental data. Such empirical relation is presented by equation 6.

$$\xi = -0.68 \ln(e) \quad (6)$$

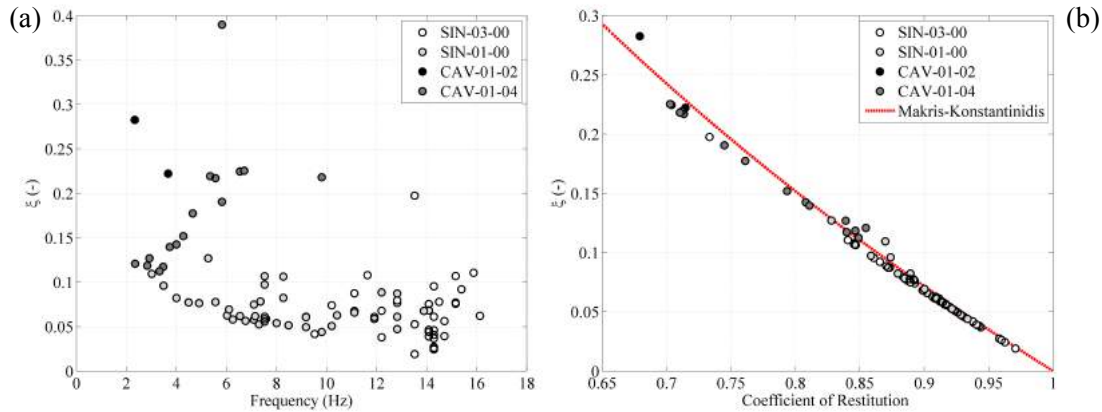


**Figure 1.17 Damping ratio vs Frequency values (a) and Coefficient of restitution vs damping ratio relationship (b).**

### 1.5. Conclusions

This paper presented the results of an OOP shaking table test campaign on cavity wall and single-leaf components. All the recorded signals (accelerations, displacements, videos) can be requested online (<http://www.eucentre.it/nam-project>). The presented work was part of an extensive experimental campaign aiming at assessing the seismic vulnerability of Dutch URM buildings. All the test specimens (single-leaf and cavity) collapsed in one-way vertical bending/rocking behaviour, exhibiting the classical top, bottom and mid-height hinges. Although the ties had negligible flexural stiffness in addition to poor mechanical characteristics of the CS wall mortar, the connections ensured a sufficiently horizontally-coupled response in the cavity components and guaranteed compatibility between the two leaves' horizontal displacements, even for the specimens containing only 2 ties/m<sup>2</sup>. This allows the analysis of the OOP seismic behaviour of cavity walls by simplified SDOF models, as previously proposed for single walls [8, 20, 21]. All the tested cavity wall specimens showed lower capacities when compared to the single-leaf specimen loaded with the same axial force. Damage due to failure of the bed joints caused by steel ties compression have been detected in all the cavity wall specimens. The experimental work confirmed that the specimen capacity is strongly influenced by the vertical stress acting on the walls, also for cavity walls.

The number of ties connecting the two walls does affect the cavity wall response. The CAV-01-04 (4 ties/m<sup>2</sup>) specimen has shown almost 10% higher capacity than the CAV-01-02 specimen (2 ties/m<sup>2</sup>) and the capability to resist a larger number of excitations. The CAV-01-04 specimen resisted, without collapse, a maximum peak acceleration of 0.73g, after this test the specimen was subjected to a further series of RWA inputs collapsing only 6 runs later under a lower peak acceleration (0.62g Gr-2 input).

The paper investigated also the force-displacement relationship and the dynamic energy dissipation involved in the mechanism. Regarding the F-  $\Delta$  relationship, it is interesting to underline that the cavity components showed capacities that can be modelled starting from the sum of RB mechanisms of the two walls considered independently. The energy dissipation has been estimated assuming two damping models: the impulsive dynamics with the coefficient of restitution and the classical dynamics theory with the damping

ratio. The former has been assessed around 0.90 for the single-leaf specimen with a ratio between theoretical and experimental value of 91%, close to the value of 90% obtained by Sorrentino [24]. Cavity components, due to the two walls dynamic interaction exhibited much lower values of the coefficient of restitution, i.e. 0.7 for CAV-01-02 and 0.77 for CAV-01-04, respectively. For what concerns the equivalent viscous damping ratio, values from 5 to 10% have been observed for the single-leaf specimen and much larger ones for cavity wall components (up to 30%).

## 1.6. Acknowledgments

This paper describes an activity that is part of the "Study of the vulnerability of masonry buildings in Groningen" project at the EUCENTRE, undertaken within the framework of the research program for hazard and risk of induced seismicity in Groningen sponsored by the Nederlandse Aardolie Maatschappij BV. The authors would like to thank all the parties involved in this project, namely EUCENTRE and University of Pavia (DICAR) laboratories that performed the tests, NAM, Arup and TU Delft. The authors are also grateful to H. Crowley and J. Bommer for defining the seismic input for the out-of-plane shaking table tests, which used the Groningen field hazard and disaggregation results provided by S. Bourne. The useful advices of professors R. Pinho, L. Sorrentino and M.C. Griffith are gratefully acknowledged. Thanks go also to M.J. Fox, I.E. Senaldi, A. Rossi and M. Mandirola for the practical support.

## 1.7. References

- [1] Giuffrè A. A mechanical model for statics and dynamics of historical masonry buildings. Protection of the Architectural Heritage Against Earthquakes. Springer-Verlag: Wien, 1996; 71-152.
- [2] Dizhur D, Ingham J, Moon L, Griffith M, Schultz A, Senaldi I, Magenes G, Dickie J, Lissel S, Centeno J, Ventura C, Leite J, Lourenco P. Performance of masonry buildings and churches in the 22 February 2011 Christchurch earthquake. Bull. New Zealand Society for Earthquake Engineering 2011; 44(4):279-296.
- [3] Ingham J, Griffith M. Performance of unreinforced masonry buildings during the 2010 Darfield (Christchurch, NZ) earthquake. Australian Journal of Structural Engineering 2011; 11(3): 207-224.
- [4] Giaretton, M, Dizhur D, Da Porto, F, Ingham J. Construction details and observed earthquake performance of unreinforced clay brick masonry cavity-walls. Structures 2016; 6, 159-169.
- [5] Griffith MC. Performance of Unreinforced Masonry Buildings during the Newcastle Earthquake, Australia. University of Adelaide, Report No. R86; 1991.
- [6] ABK. Methodology for Mitigation of seismic hazards in existing unreinforced masonry buildings: The methodology. A joint venture of Agbabian Associates, SB Barnes and Associates, and Kariotis and Associates (ABK), Topical Report 08, c/o Agbabian Associates, El Segundo, California; 1984.
- [7] Baggio C, Masiani, R. Dynamic Behaviour of historical masonry. In: Proc. 9<sup>th</sup> Int. brick/block masonry conf. Berlin, Germany; 1991.
- [8] Doherty KT. An investigation of the weak links in the seismic load path of unreinforced masonry buildings, PhD Thesis, University of Adelaide, Australia; 2000.
- [9] Simsir CC, Aschheim MA, Abrams DP. Out-of-plane dynamic response of unreinforced masonry bearing walls attached to flexible diaphragms. In: Proc. 13th World Conf. on Earthquake Engineering, Vancouver, BC, Canada; 2004.
- [10] Meisl C, Elwood KJ, Ventura CE. Shake table tests on the out-of-plane response of unreinforced masonry walls. Canadian Journal of Civil Engineering 2007; 34(11): 1381-1392.

- [11] Penner O, Elwood KJ. Out-of-Plane dynamic stability of unreinforced masonry walls in one-way bending: shake table testing. *Earthquake Spectra*, in-press, 2016;
- [12] NAM (2015) Hazard and Risk Assessment for Induced Seismicity Groningen. Study 1 Hazard Assessment. (Update 1st May 2015).
- [13] Tomassetti U, Graziotti F, Penna A, Magenes G. Out-of-plane shaking table test on URM cavity walls, In: Proc. 16<sup>th</sup> Int. brick/block masonry conference, Padua, Italy; 2016.
- [14] Messali F, Esposito R, Maragna M. Pull-out Strength of Wall Ties. Report, TU Delft, NL; 2016.
- [15] Graziotti F, Rossi A, Mandirola M, Penna A, Magenes G. Experimental characterization of calcium-silicate brick masonry for seismic assessment. In: Proc. 16<sup>th</sup> International brick/block masonry conference, Padua, Italy; 2016.
- [16] EN 1052-1. Methods of test for masonry – Part 1: Determination of compressive strength. CEN/TC. European Standard: 1998.
- [17] EN 1052-5. Methods of test for masonry - Part 5: Determination of bond strength by the bond wrench method. CEN/TC. European Standard; 1998.
- [18] EN 1015-11. Methods of test for mortar for masonry - Part 11: Determination of flexural and compressive strength of hardened mortar. CEN/TC. European Standard; 1999.
- [19] Lagomarsino S, Penna A, Galasco A, Cattari S. TREMURI program: An equivalent frame model for the nonlinear seismic analysis of masonry buildings, *Engineering Structures* 2013; 56: 1787-1799.
- [20] Sorrentino L, Masiani R, Griffith MC. The vertical spanning strip wall as a coupled rocking rigid body assembly, *Structural Engineering and Mechanics* 2008; 29: 433-453.
- [21] DeJong MJ, Dimitrakopoulos EG. Dynamically equivalent rocking structures, *Earthquake Engineering & Structural Dynamics* 2014; 43(10): 1543-1563.
- [22] Derakhshan H, Dizhur DY, Griffith MC, Ingham, JM. Seismic Assessment of out-of-plane loaded unreinforced masonry walls in multi-storey buildings, *Bull. New Zealand Society for Earthquake Eng.* 2014; 47(2): 119-138.
- [23] Derakhshan H, Griffith MC, Ingham, JM. Seismic Out-of-plane seismic response of vertically spanning URM walls connected to flexible diaphragms. *Earthquake Engineering & Structural Dynamics* 2015: 45(4), 563-580. 2015
- [24] Sorrentino L. Dinamica di muri sollecitati fuori del piano come sistemi di corpi rigidi. PhD thesis, Sapienza University of Rome, Italy; 2003 (in Italian).
- [25] Ferreira TM, Costa AA, Vicente R, Varum H. A simplified four-branch model for the analytical study of the out-of-plane performance of regular stone URM walls, *Engineering Structures* 2015; 83:140-153
- [26] Walsh K, Dizhur D, Shafaei J, Derakhshan H, Ingham JM. In situ out-of-Plane testing of unreinforced masonry cavity walls in as-built and improved conditions. *Structures*, 2015; 3, 187-189.
- [27] Housner GW. The behavior of inverted pendulum structures during earthquakes. *Bull Seismological Society of America* 1963; 53(2): 403-417.
- [28] Restrepo Vélez LF. Seismic risk of unreinforced masonry buildings. PhD thesis, ROSE School, University of Pavia, Italy; 2004.
- [29] Aslam M, Godden W, Scalise D. Rocking and overturning response of rigid bodies to earthquake motions. Report University of California, Berkeley, LBL-7539 UC-11; 1978.
- [30] Costa AA, Arêde A, Penna A, Costa A. Free rocking response of a regular stone masonry wall with equivalent block approach: experimental and analytical evaluation. *Earthquake Engineering & Structural Dynamics* 2013; 42(15), 2297-2319.
- [31] Psycharis I, Jennings P. Rocking of slender rigid bodies allowed to uplift. *Earthquake Engineering & Structural Dynamics* 1983; 11(1), 57-76.
- [32] Sorrentino L, Shawa OA, Decanini LD. The relevance of energy damping in unreinforced masonry rocking mechanisms. Experimental and analytic investigations. *Bulletin of Earthquake Engineering* 2011; 9(5):1617-1642.
- [33] Lam NTK, Griffith M, Wilson J, Doherty K. Time-history analysis of URM walls in out-of-plane flexure. *Engineering Structures* 2003; 25(6):743-754.

- 
- [34] Tomassetti U, Graziotti F, Penna A, Magenes G. A Single-Degree of Freedom Model for the Simulation of the Out-of-Plane Response of Unreinforced Masonry Walls, In: Proc. 16<sup>th</sup> Italian Conf. on Earthquake Engineering, L'Aquila, Italy; 2015.
- [35] Makris N, Konstantinidis D. The rocking spectrum and the limitations of practical design methodologies. *Earthquake Engineering & Structural Dynamics* 2003; 32(2):265–89.





## 2. Shaking table test on a full-scale URM cavity wall building

Graziotti F., Tomassetti U., Kallioras S., Penna A., Magenes G. Shaking table test on full scale URM cavity wall building, *Bulletin of Earthquake Engineering*, 2017 15, 12.

**Abstract.** A shaking table test on a two-storey full scale unreinforced masonry (URM) building was performed at the EUCENTRE laboratory within a comprehensive research programme on the seismic vulnerability of the existing Dutch URM structures. The building specimen was meant to represent the end-unit of a terraced house, built with cavity walls and without any particular seismic design or detailing. Cavity walls are usually composed of an inner loadbearing leaf and an outer leaf having aesthetic and weather-protection functions. In the tested specimen, the loadbearing masonry was composed of calcium silicate bricks, sustaining two reinforced concrete floors. A pitched timber roof was supported by two gable walls. The veneer was made of clay bricks connected to the inner masonry by means of metallic ties, as seen in common construction practice. An incremental dynamic test was carried out up to the near-collapse limit state of the specimen. The input motions were selected to be consistent with the characteristics of induced seismicity ground motions. The article describes the characteristics of the building and presents the results obtained during the material characterization and the shaking table tests, illustrating the response of the structure, the damage mechanism and its evolution during the experimental phases. All the processed data are freely available upon request (see <http://www.eucentre.it/nam-project>).

### 2.1. Introduction

The results presented in this manuscript are part of a wider research project aimed at assessing the vulnerability of buildings typical of the Groningen region (located in Northeast Netherlands). This area, historically not prone to tectonic ground motions, during the last two decades has been subjected to seismic events induced by reservoir depletion due to gas extraction. The most severe event was an earthquake of local magnitude 3.6 that occurred on August 16<sup>th</sup>, 2012, near Huizinge, above the central part of the Groningen gas field [1]. Buildings not specifically designed for seismic actions are thus now exposed to this type of low intensity shaking. Unreinforced masonry (URM) buildings represent the large majority of the local existing building stock (almost 90%). Currently, very limited data are available on the seismic response of construction typologies similar to those of the Dutch practice. An experimental campaign, starting in 2015, aimed at investigating the performance of structural components, assemblies and systems typical of building typologies present in the Groningen area. The testing campaign included in situ mechanical characterization tests [2] and laboratory tests comprising: characterisation tests performed on bricks, mortar and small masonry

assemblies; in-plane cyclic shear-compression [3] and dynamic out-of-plane tests on full-scale masonry piers [4]. Two full-scale shaking table tests have been conducted in 2015 and 2016 on two different URM building typologies on the testing facilities of the EUCENTRE laboratory. The first one is described in this manuscript, while information on the second one are available in Graziotti *et al.* [5], [6].

The shaking table test presented in this article was designed to address several open questions related to the seismic behaviour of terraced houses that constitute the majority of the Dutch URM building stock, mainly with residential purposes. They are usually two-storey buildings with openings on only two of their sides, consisting of several structurally independent side-by-side units (4 to 6). The greatest part of this architectural typology is built with cavity walls, a construction system that became widespread after World War II.

A cavity wall building is a type of construction where an air gap is left between the two leaves of bricks. Sometimes insulating material is inserted in the cavity. The external leaf of a cavity wall is often a brick veneer wall without any load bearing function, while the internal leaf is the loadbearing one, carrying the vertical loads transmitted by the floors and the roof. It is common for the inner leaf to be constructed with different materials than the outer leaf. In several European countries, an example of this solution is to have the inner wall made of calcium silicate brick/blocks, while the outer wall uses clay bricks. Wythes on either side of a cavity wall are typically connected by regularly spaced metal cavity ties, which can vary in material, shape and spacing. Because of their relatively light weight, good thermal insulation properties and effective protection against driving rain, cavity walls are widely used in Central and Northern Europe countries, especially for residential construction. Information on the seismic behaviour of cavity walls is quite limited, and mostly related to earthquakes occurring in Australia (Newcastle, 1989) and New Zealand (Christchurch sequence, 2010-2011) [7]. Furthermore, a shaking table test on a cavity-wall building specimen with loadbearing concrete blocks was performed by Degée *et al.* [8].

The shaking table test presented in this manuscript aims at studying the seismic response of this type of building. In particular, relevant results of the experimental study are: drift limits for different performance levels, damage evolution for increasing shaking levels; storey accelerations amplified along the building height, and displacement/drift profiles for increasing shaking intensity. In particular, specific attention was paid to the dynamic performance of the roof structure and on the possible activation of gable out-of-plane mechanisms. With the aim of reproducing the seismic behaviour of an existing URM terraced house, an incremental dynamic test was carried out up to the near collapse conditions of the specimen. This work presents the geometric and mechanical characteristics of the specimen (Section 2.2), the input motions applied to the shaking table, the testing protocol and the instrumentation (Section 2.3). Section 2.4 discusses the performance of the building under ground motion excitation, the test results in terms of damage evolution, hysteretic responses, performance of the roof structure and the identification of the local and global limit states (Section 2.4).

## 2.2. Specimen Characteristics

The building specimen was intended to represent the end-unit of a URM cavity-wall terraced house of the late 70s. This residential typology is characterised by wide openings on the front and back sides. The transverse walls, that separate units, are double-wythe

cavity walls without any openings. Internal transverse walls are composed of a couple of loadbearing walls, carrying most of the vertical loads coming from floors and roof and, therefore, they are capable of resisting significant in-plane lateral forces. Houses built with this common configuration are expected to be characterised by two very different seismic behaviours in the two principal directions. These structures are generally more flexible and vulnerable in the longitudinal direction. For this reason, a unidirectional shaking table test was carried out by applying base excitations along this direction. Figure 2.1 shows the front view of a classic terraced house and its plan view.

Adjacent units are generally structurally detached, and the discontinuous slabs rest only on the loadbearing walls of the individual units. Each unit is therefore completely self-supported by transverse walls and structurally independent from the other units. The only common walls are the outer veneer walls. For this reason, it was possible to test on the shaking table a representative sub-volume (one end-unit) of an entire terraced house (as shown in the coloured part of Figure 2.1a). The first floor is generally made of a reinforced concrete (RC) slab, while the second floor is either a RC or timber diaphragm. The presence of a timber roof usually dominates over other typical roofing solutions for this building typology.

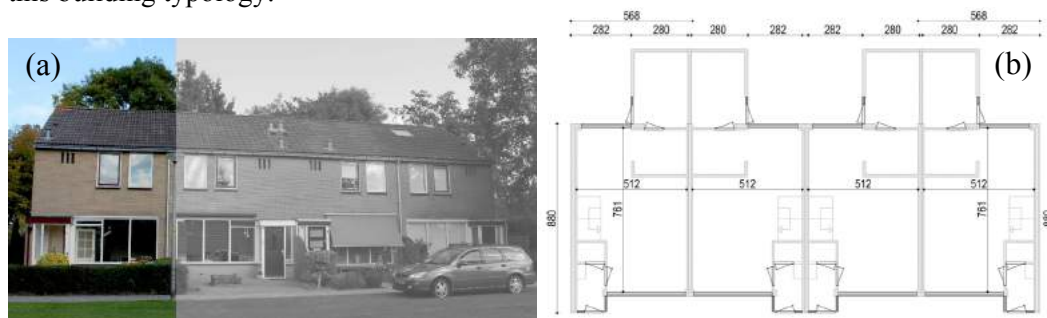


**Figure 2.1** A typical terraced house in Loppersum, Groningen, NL: (a) illustration of the front façade; (b) plan view.

### 2.2.1. Geometry of the specimen

The test-house was a full-scale two-storey building, with a timber roof and RC slabs. The specimen was built directly on the shaking table of the EUCENTRE laboratory (Figure 2.2a). It was 5.82 m long, 5.46 m wide (slightly reduced compared to the typical width found in the building stock, due to the shaking table dimensions) and 7.76 m high with a total mass  $M$  of 56.4 t. The walls, supported by a steel-concrete composite foundation, consisted of two unreinforced masonry leaves. The inner loadbearing leaf was made of calcium silicate (CS) bricks whereas the external leaf was a clay brick veneer without any loadbearing function. The two pre-cast RC floor slabs (with a mass of 10.3 t and 11 t for the first and second floor, respectively) were supported only by the two transverse (North and South) inner CS walls. The inner CS masonry was continuous along the entire perimeter of the house, while the outer clay brick leaf was not present in the South façade, simply because the specimen was meant to represent the end-unit of a system of row houses. Pictures of the specimen after the end of the construction are shown in Figure 2.2, while Figure 2.3 depicts the ground and first floor plan views of the specimen.



Figure 2.2 Views of the full-scale specimen: (a) North-West (from top); (b) South-West; (c) North-West (from bottom).

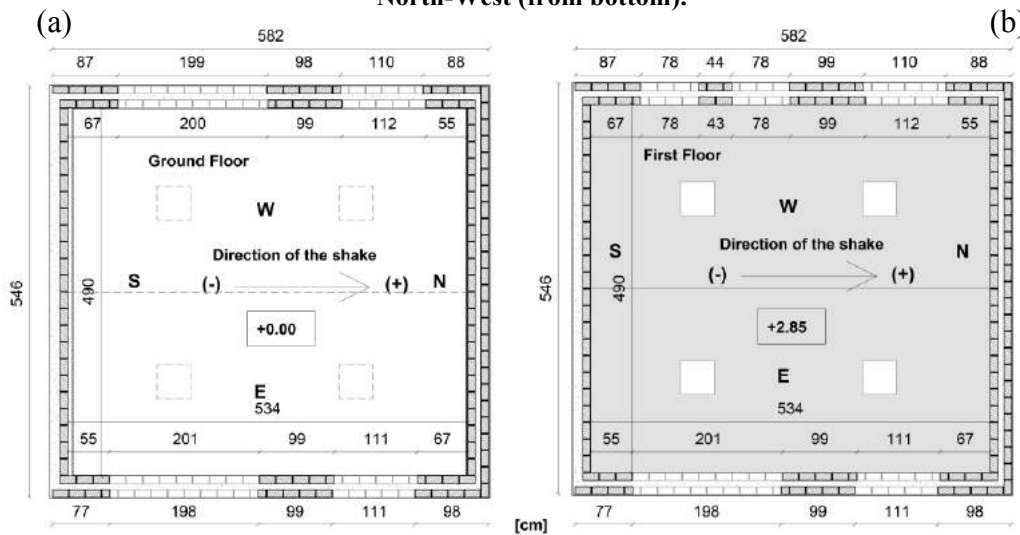
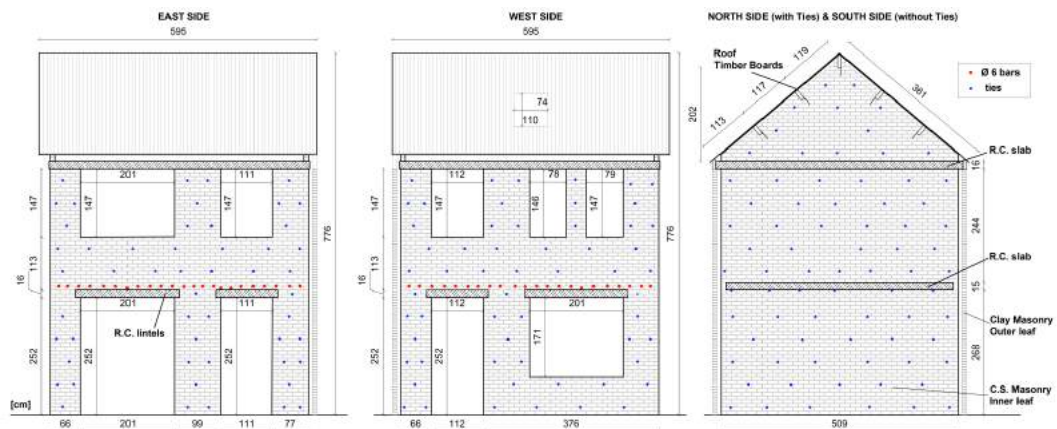


Figure 2.3 (a) Plan view of the ground floor, and (b) the first floor of the specimen. Arrows indicate the assumed positive direction of the shaking table motion. Units of cm.

An air gap of 80 mm was left between the two leaves, as usually seen in common practice. L-shaped steel ties with a diameter of 3.1 mm and a length of 200 mm were inserted in the 10-mm-thick mortar bed-joints during the laying of the bricks, ensuring the connection between the two masonry leaves (the location of the steel ties is showed by blue dots in Figure 2.4). The L hook side was embedded in the inner CS walls for a length of 70 mm, while the “zig-zag” extremity was embedded in the clay masonry for a length of 50 mm (Figure 2.5a and Figure 2.5d). Two gable walls in the transverse façades (North and South) supported a 43° pitched timber roof. In the ground storey, pre-cast reinforced concrete lintels were placed above the openings on both inner and outer walls. The dimensions of the lintels were 160×100 mm for CS walls and 110×100 mm for clay walls. Lintels were 1.33 m and 2.22 m long for shorter and wider openings, respectively.



**Figure 2.4 Elevation views of the specimen's inner CS leaf. Units of cm.**

A rigid steel-frame was installed in the interior of the test-house. This structure served mainly as a safety system, providing support for the two slabs in case of partial or global collapse of the specimen, as well as a rigid reference system for a direct measure of the floors, walls and roof displacements (Figure 2.5f). The frame was not in contact with the building, since its columns passed through 450-mm-square holes in the two slabs, large enough to accommodate significant lateral displacements of the specimen (Figure 2.3c).

### 2.2.2. Building construction details

It is well known among the engineering community that construction details can significantly affect the seismic response of a structure, especially a URM building. Observation of damage caused by major earthquakes, as well as laboratory tests ([9], [10]) have shown that the role of the connections between horizontal and vertical structural elements is of primary importance for ensuring a good structural performance. The construction details of the specimen were representative of the Dutch common practice of the '60s and '70s. Figure 2.5 presents pictures captured during the construction phase of the specimen. The connection between the first-floor slab and the inner CS longitudinal leaves (East and West walls) was ensured by means of 6-mm-diameter threaded bars, the position of which is indicated by red dots in Figure 2.4. Details of this connection are also shown in Figure 2.5c and Figure 2.5d. This solution was meant to represent a common technique associated with a cast-in-situ RC slab where the bars were embedded in the masonry before casting the slab. Since the construction in the laboratory environment required the slabs to be precast, the connectors were pre-inserted in the concrete and then anchored to the masonry in a second phase. As recurrent in the building stock, an air gap (hole sleeve in Figure 2.6c) was left in order to guarantee differential thermal expansion of the components. There was no direct connection between the outer clay veneer wall and the first-floor slab.





**Figure 2.5 Construction details of the specimen: (a) positioning of cavity steel ties; (b) building phase of inner CS leaf; (c) laying of the second-floor slab; (d) geometry of steel tie; (e) construction of CS leaves at second floor level; (f) safety steel frame.**

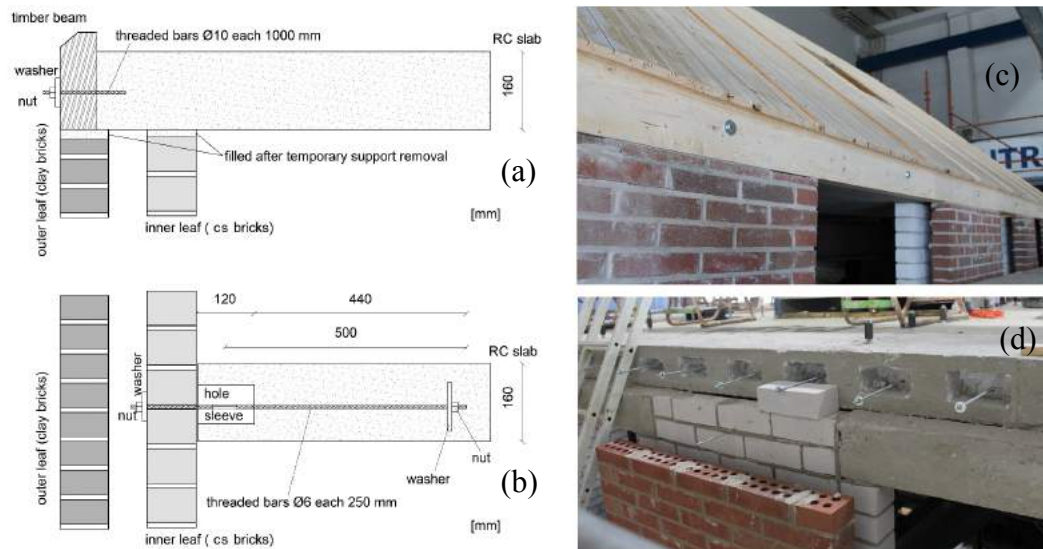


**Figure 2.6 Details of the connections between the precast RC slabs and the longitudinal CS walls: (a, b) second floor, and (c, d) first floor level**

The second-floor slab was not directly supported by the longitudinal walls (East and West); the gap between the slab and the inner CS longitudinal walls was filled with mortar after the removal of the temporary supports and the attainment of the deflection of the slab. Similarly, the timber wall plates were not in contact with the longitudinal clay walls (East and West), but they were attached to the edge of the second floor slab by means of 100-cm-spaced 10-mm-diameter threaded bars, while the resulting gap between the beams and the top of the veneer was afterwards filled with mortar (Figure 2.6a and Figure 2.6b). Such details were adopted in order to reproduce a loading configuration common in the building stock. This solution resulted in almost no vertical load being transmitted to the longitudinal walls under static conditions.

The timber roof was a simple structure consisting of one ridge beam, two wall plates on top of the longitudinal outer leaves and two girders per side between the ridge beam and the wall plates, at approximately every 1.2 m. Tongue and groove planks, with a width equal to 182 mm and a thickness of 18 mm, were nailed on top by means of two 60×2 mm nails at each intersection (Figure 2.7a). The timber beams of the roof were supported by the transverse inner CS leaves (North and South gables), whereas this connection was further reinforced by the presence of L-shaped steel anchors, as shown in Figure 2.7c. The roof was completed by the installation of clay tiles and the total mass of the finished roof was 2.8 t. The in-plane stiffness of the timber diaphragm was essentially provided by the nailed connections between beams and planks, as well as by the effectiveness of the tongue and groove joints.

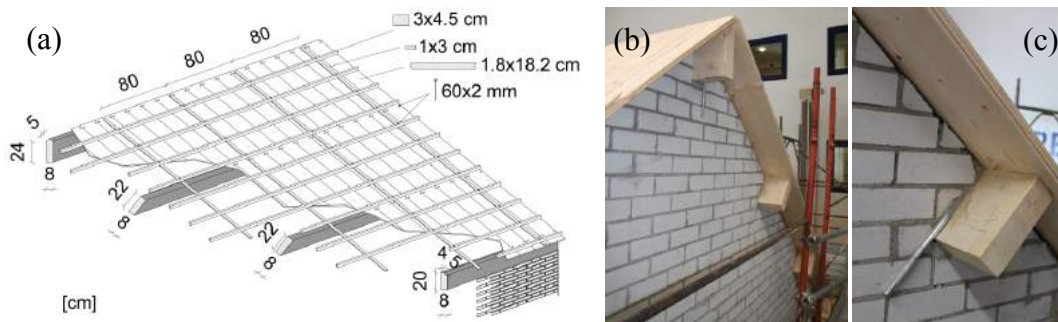


**Figure 2.7 Details of the roof structure: (a) geometry of the timber diaphragm; (b) connection between the timber beams and the South gable; (c) steel anchors**

### 2.2.3. Mechanical properties of materials

Part of the experimental campaign that was carried out at the laboratory of the University of Pavia, allowed the mechanical properties of the building materials employed for the construction of the specimen to be determined. It comprised strength tests on units and mortar samples, as well as tests on small masonry assemblages, such as compression tests, bond wrench tests and shear tests on triplets. CS and clay units were tested in compression according to EN 772-1 [11]. The dimensions of the CS units were 212×102×71 mm. The clay bricks were perforated with ten vertical holes, they had a void ratio of 17% and dimensions of 211×100×50 mm. The flexural and compressive strength of the mortar were determined according to the prescriptions of EN 1015-11 [12]. Six masonry wallettes made of CS and clay bricks were tested in compression in the direction perpendicular to the horizontal bed-joints, according to EN 1052-1 [13]. These tests allowed the determination of the compressive strength of masonry ( $f_m$ ), as well as the secant elastic modulus of masonry at 33% of the compressive strength ( $E_m$ ). Bond wrench tests on twenty CS and twenty clay masonry wallettes were performed in order to determine the bond strength of masonry, according to EN 1052-5 [14]. Specimens of both types of masonry were also subjected to the shear test for the determination of the initial shear strength ( $f_{v0}$ ) and the friction coefficient ( $\mu$ ), according to the guidelines given by EN 1052-3 [15].

A parallel testing campaign was conducted at the Delft University of Technology (TU Delft) on specimens built using the same materials [16]. In particular, tests that allowed the determination of the tensile load capacity of the steel ties connecting the two masonry

leaves were performed by Messali *et al.* [17]. They found that the pull-in and pull-out strengths of the “zigzag” tie extremity (Figure 2.5d) embedded in clay masonry specimens, considering an overburden pressure of 0.3 MPa, was higher than the strengths associated with the hook extremity embedded in CS specimens and subjected to the same imposed pressure. The average pull-out and push-in strengths recorded for CS specimens were approximately 1.46 kN and 1.09 kN, respectively. Moreover, the tensile ultimate capacity of the steel anchors was approximately 4.3 kN. The concrete used to cast the two slabs had an average compressive strength of 29.5 MPa. The masses of the test unit are summarized in Table 2.1, while Table 2.2 lists the masonry mechanical properties resulting from material characterization tests.

**Table 2.1 Summary of structural masses, units of t**

		<i>First storey</i>	<i>Second storey</i>	<i>Gables</i>	<i>Total</i>
<i>Masonry structure</i>	<i>Inner leaf (CS)</i>	8.5	8.7	2.4	19.6
	<i>Veneer (Clay)</i>	5.6	5.9	1.2	12.7
<i>RC slabs</i>		10.3	11.0	-	21.3
<i>Roof (tiles and timber trusses)</i>		-	-	-	2.8
<i>Entire building</i>		<b>56.4</b>			

**Table 2.2 Masonry mechanical properties**

<i>Material property</i>	<i>Sym bol</i>	<i>U.M.</i>	<i>Calcium Silicate</i>		<i>Clay</i>	
			<i>Average</i>	<i>C.o.V.</i>	<i>Average</i>	<i>C.o.V.</i>
<i>Density of bricks</i>	$\rho_b$	kg/m <sup>3</sup>	1900	0.02	1650	0.02
<i>Density of masonry</i>	$\rho$	kg/m <sup>3</sup>	1835	0.01	1905	0.03
<i>Compressive strength of bricks</i>	$f_b$	MPa	17.18	0.14	32.45	0.13
<i>Compressive strength of mortar</i>	$f_c$	MPa	5.71	0.25	6.24	0.09
<i>Flexural strength of mortar</i>	$f_t$	MPa	1.78	0.23	1.48	0.19
<i>Masonry compressive strength</i>	$f_m$	MPa	5.49	0.10	12.72	0.15
<i>Masonry Young's modulus in compression</i>	$E_m$	MPa	1736	0.26	4742	0.17
<i>Flexural bond strength of masonry</i>	$f_w$	MPa	0.056	0.47	0.152	0.65
<i>Masonry (bed joint) initial shear strength</i>	$f_{v0}$	MPa	0.03	-	0.11	-
<i>Masonry (bed joint) shear friction coefficient</i>	$\mu$	-	0.50	-	0.68	-

## 2.3. Testing protocol and instrumentation

### 2.3.1. Input signals

The specimen was subjected to a sequence of incremental dynamic tests. A series of table motions of increasing intensity were applied with the objective of assessing the ultimate capacity and failure modes of the building. Since the shaking table is uniaxial, the seismic input was applied parallel to the longitudinal direction (North-South) of the tested building, exciting out-of-plane the loadbearing transverse walls (North and South façades). The selected input motions aimed at being representative of expected ground motion in the region of Groningen. A detailed study on the seismic hazard characteristics identified two main scenarios with return periods of 50 and 500 years (see Appendix B2



of Graziotti *et al.* [18]). Two records EQ1 and EQ2 with 5-75% significant duration of 0.375 s and 1.72 s and a PGA of 0.095g and 0.159g, respectively, were finally selected to be representative of the two scenarios. Their smooth response spectra were considered ideal for a higher control of both the shaking table and the response of the structure. Figure 2.8 shows the theoretical acceleration time-histories of the experimental inputs and their acceleration response spectra.

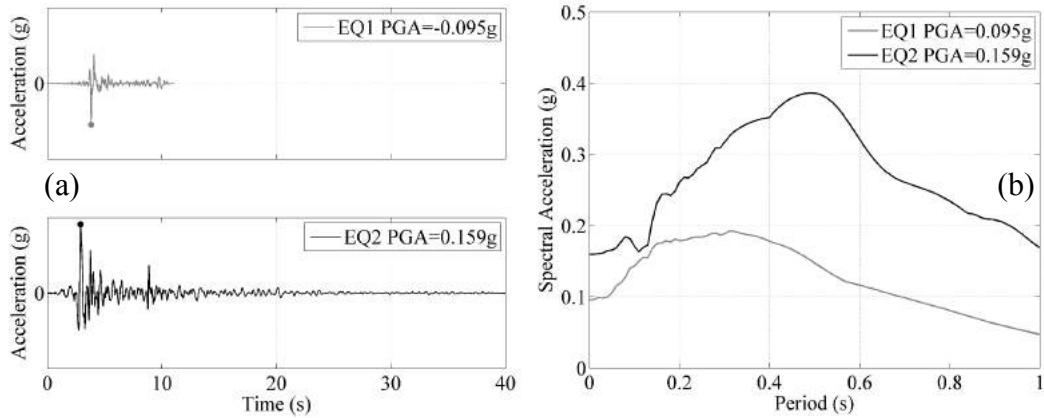


**Figure 2.8 EQ1 and EQ2 input signals: (a) acceleration time histories, and (b) acceleration response spectra**

### 2.3.2. Testing protocol

The sequence of incremental dynamic tests was performed by gradually increasing the intensity of the two ground motions with EQ1 being applied first, followed by EQ2. Table 2.3 presents the applied testing sequence specifying the input typology, the intensity and the comparison between nominal and recorded PGAs and 5% elastic spectral accelerations,  $Sa(T_{1,1})$  at the fundamental period  $T_{1,1} = 0.17$  s of the undamaged structure (calculated by means of a dynamic identification test, see further details in section 2.4.4). Further intensity measures (IMs) listed in Table 2.3 are the peak ground velocity PGV, the 5%-damping elastic spectral displacement obtained from the recorded base acceleration, and the modified Housner intensity ( $mHI$ ). The  $mHI$  has shown very good correlations with the nonlinear displacement demand induced in short period URM structures [19]. It is defined as the integral of the pseudo-velocity elastic response spectrum between a structural period of 0.1 s and 0.5 s (which correspond to the range of periods of interest of the tested specimen):

$$mHI(5\%) = \int_{0.1}^{0.5} PSV(5\%, T) dT \quad (1)$$

The shaded sections in Table 2.3 refer to the tests with increasing intensity. It is worth noting that such tests have been often preceded by tests of the same typology, but with reduced intensity for the purpose of shake table calibration (*e.g.* tests #6, #11, #12, #13 and #18). The intensity level of these calibration tests (labelled with a C in the test name, *e.g.* EQ1-50%C) has been chosen in order to prevent further damage or deterioration in the specimen. In general, a good agreement between nominal and recorded quantities have been observed, with a slight overshoot of the recorded spectral acceleration

corresponding to the initial fundamental period  $T_{1,1}$ . Each test with increasing intensity was alternated by random noise tests (RNDM), which, by means of a dynamic identification procedure, allowed the changes in the dynamic properties of the structure to be detected as the damage level increased. In particular, the following sections report the evolution of the fundamental period denoted as  $T_{1,i}$  (where  $i$  is the test identification number as reported in Table 2.3). The incremental testing sequence has been stopped after the attainment of a near collapse condition in order to prevent a global collapse of the specimen that could have caused damage to the laboratory facilities.

**Table 2.3 Summary of the testing sequence**

<i>Test #</i>	<i>Test Input</i>	<i>Test Name</i>	<i>Nominal PGA [g]</i>	<i>Recorded PGA [g]</i>	<i>Calculated PGV [m/s]</i>	<i>Nominal Sa(T<sub>i</sub>) [g]</i>	<i>Calculated Sa(T<sub>i</sub>) [g]</i>	<i>Calculated Sd(T<sub>i</sub>) [mm]</i>	<i>Calculated mHI [mm]</i>
1	RNDM	RNDM-01	0.050	-	-	-	-	-	-
2	EQ1	EQ1-25%	0.024	0.024	0.015	0.049	0.055	0.4	8.3
3	RNDM	RNDM-03	0.050	-	-	-	-	-	-
4	EQ1	EQ1-50%	0.049	0.050	0.031	0.097	0.126	0.9	18.2
5	RNDM	RNDM-05	0.050	-	-	-	-	-	-
6	EQ1	EQ1-50%C	0.048	0.050	0.031	0.089	0.108	0.8	17.3
7	EQ1	EQ1-100%	0.096	0.099	0.056	0.179	0.229	1.6	34.9
8	RNDM	RNDM-08	0.050	-	-	-	-	-	-
9	EQ1	EQ1-150%	0.144	0.137	0.077	0.268	0.369	2.6	47.7
10	RNDM	RNDM-10	0.050	-	-	-	-	-	-
11	EQ2	EQ2-30%C	0.053	0.064	0.049	0.081	0.096	0.7	23.4
12	EQ2	EQ2-30%C	0.053	0.059	0.045	0.081	0.087	0.6	22.2
13	EQ2	EQ2-30%C	0.053	0.056	0.043	0.081	0.083	0.6	21.5
14	EQ2	EQ2-50%	0.079	0.087	0.067	0.122	0.125	0.9	31.8
15	RNDM	RNDM-15	0.050	-	-	-	-	-	-
16	EQ2	EQ2-100%	0.159	0.170	0.123	0.245	0.286	2.1	62.1
17	RNDM	RNDM-17	0.050	-	-	-	-	-	-
18	EQ2	EQ2-50%C	0.079	0.114	0.088	0.122	0.183	1.3	41.3
19	EQ2	EQ2-125%	0.199	0.194	0.133	0.306	0.324	2.3	69.0
20	RNDM	RNDM-20	0.050	-	-	-	-	-	-
21	EQ2	EQ2-150%	0.239	0.243	0.164	0.367	0.404	2.9	84.4
22	RNDM	RNDM-22	0.050	-	-	-	-	-	-
23	EQ2	EQ2-200%	0.319	0.307	0.218	0.489	0.654	4.7	111.6
24	RNDM	RNDM-24	0.050	-	-	-	-	-	-

### 2.3.3. Instrumentation

In order to detect and monitor the structural response under different levels of input motion, several instruments were installed on the building. The location and typology of the instrumentation was determined based on the identification of the critical zones and on the physical quantity to be recorded. The instrumentation consisted of 33 accelerometers and 30 displacement transducers. Figure 2.9a shows the locations of the three types of employed accelerometers (uni-, bi- and tri-axial). The accelerometers were installed on both inner and outer leaves, as well as on the two floors and the ridge beam of the roof. Figure 2.9b shows, instead, the displacement transducers installed on the

specimen: 10 wire and 20 linear variable displacement transducers (LVDTs). The displacements measured between the specimen and the rigid frame were considered equivalent to the relative displacements with respect to the shaking table surface. In particular, wire potentiometers were installed in order to record the out-of-plane response of the North and South façades at the mid-height of the first and second storeys and the gable. The LVDTs were, instead, utilized to monitor directly the longitudinal and transverse displacement of the first and second slabs. The displacements of some points of the external façades and internal walls were monitored by a 3D optical acquisition system (see Appendix B). These data allow to compute the differential displacement between inner and outer leaves.

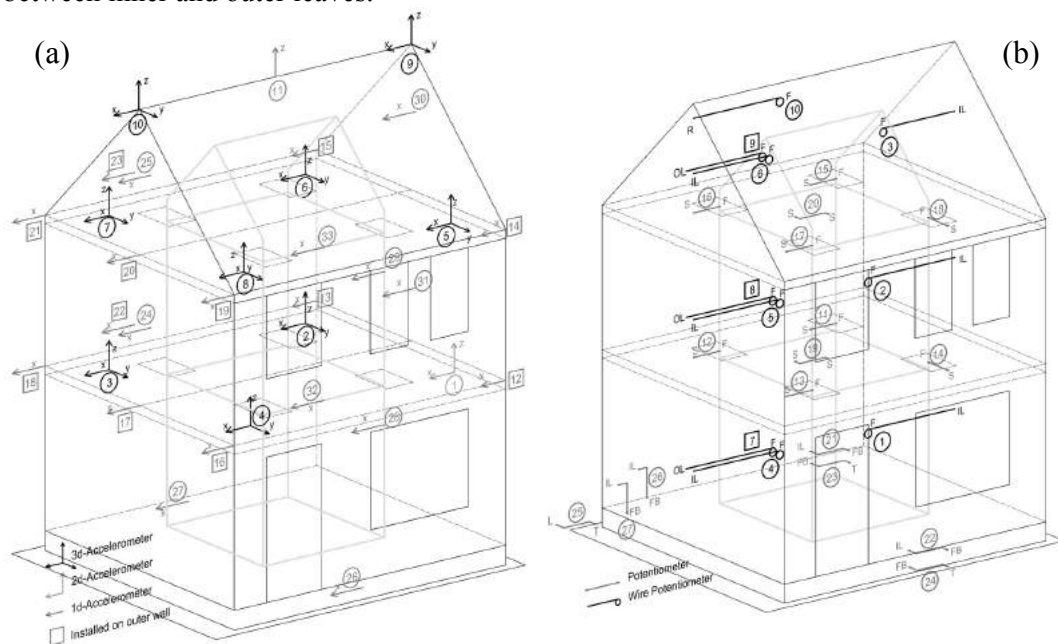


**Figure 2.9 Locations of the instrumentation: (a) accelerometers, and (b) displacement transducers (letters indicate the component at which the transducers is attached to: S = slab, F = frame, IL = inner leaf, OL = outer leaf, FB = foundation beam, T = shaking table, R = roof ridge beam and L = laboratory floor)**

## 2.4. Test results

The following sections report the main results of the shaking table tests. In particular, some issues related to the global seismic response of the tested building are discussed, in terms of the observed crack patterns, the deformed shapes and the hysteretic behaviour. To summarise briefly: the building sustained shaking of  $PGA = 0.14g$  (EQ1 150%) with no visible damage and was in a near-collapse state after testing at  $PGA = 0.31g$  (EQ2 200%), when the test sequence was stopped. Videos of the applied testing sequence are available online [20].

### 2.4.1. Shaking table performance

The comparison between the theoretical response spectra and those obtained from the accelerations recorded on the specimen's foundation, shows a general good match. A very slight overshooting of low period spectral ordinates was noticed in all the tests. A 15% undershooting of spectral acceleration in the high period range was observed only in the test EQ2-200%. In the same test a considerable amplification peak occurred at a period of  $T=0.18$  s. The sudden change of the specimen dynamic characteristics (the fundamental period was doubled), due to its heavy damage and its interaction with the table, did not allow a perfect match of the target spectrum. The comparison of the acceleration response spectra for the tests of EQ2-100% (PGA = 0.17g) and EQ2-200% (PGA=0.307g) is shown in Figure 2.10.

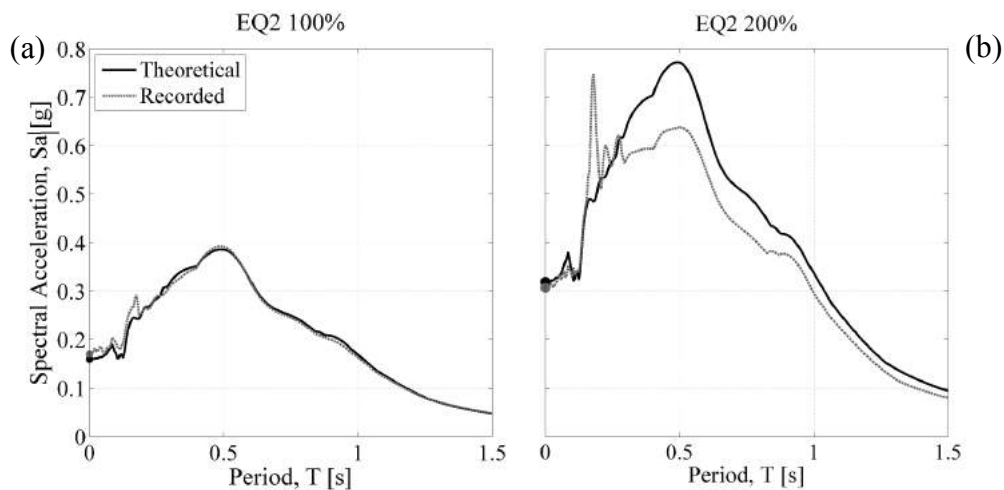


**Figure 2.10 Comparison of the acceleration response spectrum of the recorded base acceleration against the target one for testing under (a) EQ2-100% (PGA = 0.17g), and (b) EQ2-200% (PGA = 0.307g)**

### 2.4.2. Damage evolution

At the end of each stage of the shaking table testing sequence, detailed surveys were carried out for the report of every possible evidence of damage having affected the structure (Figure 2.11 and Figure 2.12). During the testing under the first scenario seismic excitations (EQ1 scaled from 25% PGA = 0.024g to 150% PGA = 0.137g), the building did not experience any noticeable damage. The specimen suffered only slight damage that became visible just after testing under EQ2-100% test (PGA = 0.17g). The formation of a few cracks was observed at the base of the first storey inner-leaf corner piers, associated mainly with their flexural behaviour. The observed damage did not change significantly after testing at EQ2-125% (PGA = 0.194g).

The first significant cracks observed in the CS masonry of the second storey were recorded after the test EQ2-150% (PGA = 0.243g). They were mainly horizontal cracks observed just below the interface between masonry piers and the second-floor level slab, as mapped in Figure 2.11. A horizontal crack developed along the base of the squat pier of the second storey, on the West side, indicative of the pier's bending-rocking response. This crack was further extended with a stair-stepped diagonal pattern to the centre of the

adjacent spandrel. Until this intensity level no damage in the two transverse walls was detected.



**Figure 2.11 Crack pattern evolution of the inner CS walls**

The building experienced a substantial level of damage (compared to that observed under lower intensity shaking) after the test EQ2-200% (PGA = 0.307g). At this shaking level a global response of the structure was triggered, as evidenced by the formation of new cracks or the elongation of pre-existing ones, identified on every one of the piers, as shown in Figure 2.11. A detailed survey of the building was conducted and revealed extensive damage in the spandrels of the calcium silicate masonry. In particular, the formation of wide diagonal cracks (starting from the corners of the openings), with sliding of the mortar joints and de-cohesion of blocks were observed (Figure 2.13e). In

addition, the horizontal cracks located at the top of the second storey piers were extended, reaching a maximum residual sliding of 15 mm.

As far as the damage reported in the transversal walls is concerned, the formation of 45° stair-stepped diagonal cracks (no greater than 1.2 mm) was clearly observed. This could be associated with the activation of an out-of-plane two-way bending mechanism. Focusing on the gables, horizontal cracks along their base were apparent (one or two layers above the second-floor level), indicative of an out-of-plane overturning mechanism activated at the gable level. Other cracks were also identified at the locations where the timber beams of the roof were supported on the gable walls. Cracks around these beams were due to interaction of the beams with the supporting masonry gable walls Figure 2.11 and Figure 2.13a).

Regarding the damage noticed in the veneer walls, perceptible cracks developed only during the last test, EQ2-200% (PGA = 0.307g). In particular, the long spandrel of the eastern façade developed a flexural mechanism with vertical cracks at both ends, originating from the concrete lintels (Figure 2.12 and Figure 2.13h), whereas the shorter spandrel presented failure in shear, forming the characteristic X-shape crack pattern (Figure 2.12 and Figure 2.13g). On the western side, large stair-stepped shear cracks were observed, such as those crossing the entire short spandrel with an angle of 45°. To a great extent, most of the deformations were absorbed by sliding of the concrete lintels with respect to the masonry supports, as well as sliding at the interface of the roof wall plates and the second storey masonry piers (Figure 2.13i). In the northern veneer, the only cracks observed were located at the second-floor level. As they extended along the entire length, they were associated with the tendency of the gable wall to develop an out-of-plane overturning mechanism (Figure 2.12).

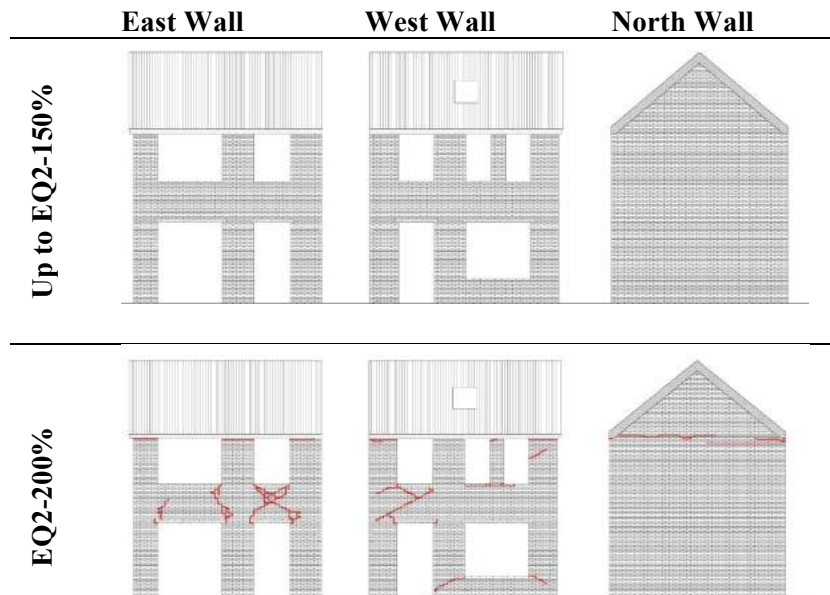
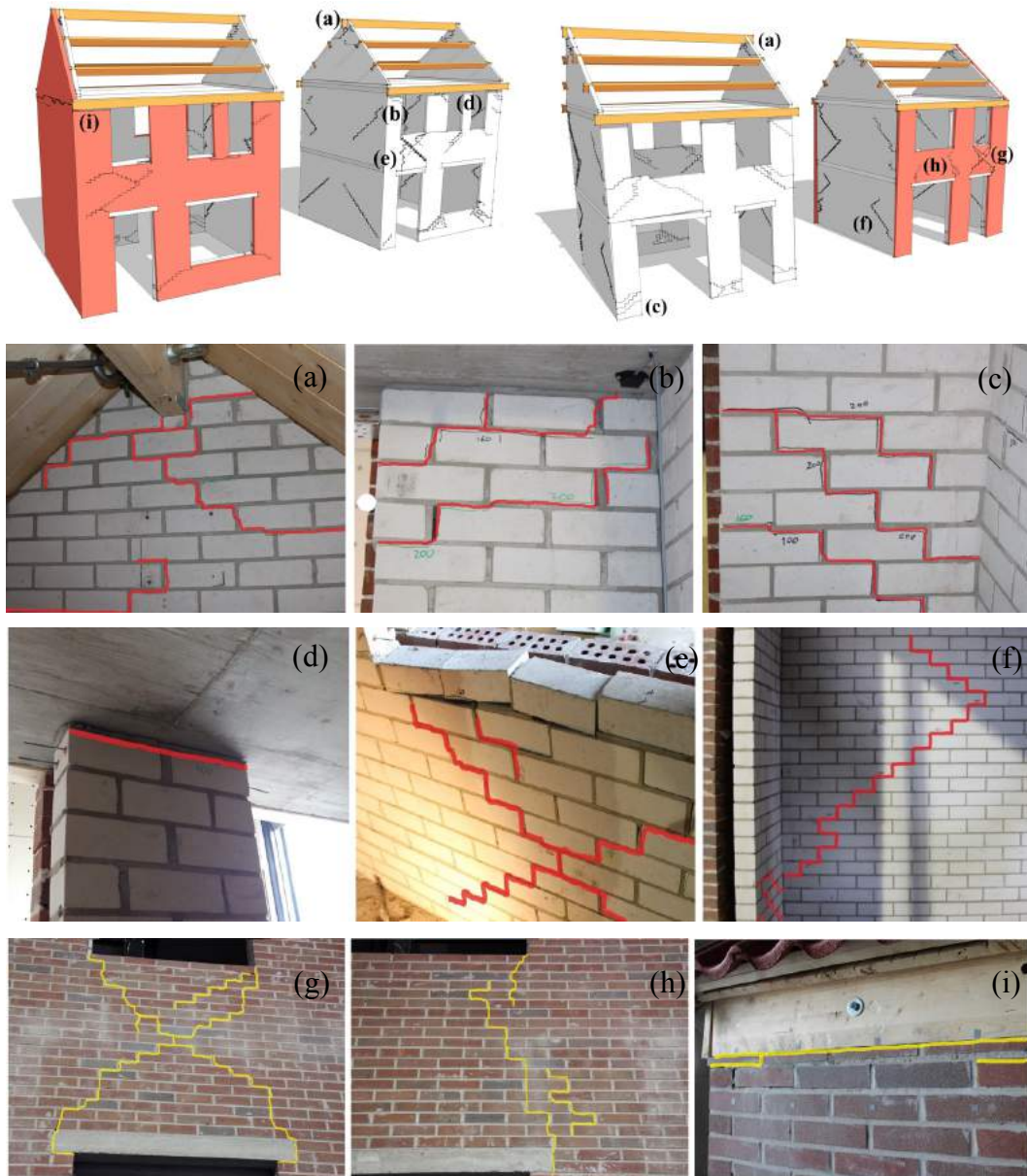


Figure 2.12 Crack pattern evolution of the outer clay walls





**Figure 2.13** 3D view of the observed crack pattern at the instant of attainment of the peak second floor displacement: (a) pounding of the ridge beam on the North CS gable; (b) flexural cracks on the top of the second storey; (c) flexural cracks on the bottom of a first storey pier; (d) sliding at the interface of the second storey pier and the slab; (e) de-cohesion of masonry blocks and diagonal shear cracks through the joints; (f) stair-stepped cracks in the transverse walls; (g) shear failure of the veneer's short spandrel with the formation of X-shaped crack pattern, (h) flexural cracks in the veneer's long spandrel; (i) sliding at the interface of the veneer and the timber wall plate

Figure 2.14 reports the evolution of the maximum residual crack width measured after the end of every test. The same quantity is also plotted versus the peak and residual correspondent inter-storey drift ratio ( $\theta$  and  $\theta_{res}$ , respectively). A higher residual crack width was measured in the ground storey (i.e. 1st storey). This was due to two main

factors: the higher drift demand (see Figure 2.20) at lower levels and the concentration of the 2nd storey deformation in the interface between the CS wall and the top floor slab. Regarding the first floor, where the slab displacement was completely accommodated by the deformations of the piers, a good correlation between  $\theta$  and crack width was observed. The relation between the crack width and the  $\theta_{res}$  was found to be almost linear for both storeys.

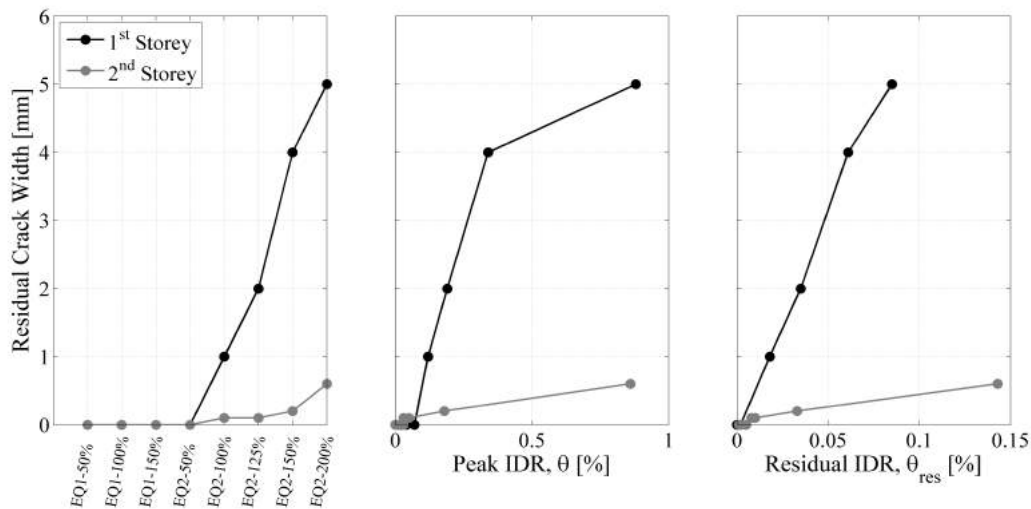


**Figure 2.14** Evolution of the maximum residual width of the observed cracks as a function of the: (a) testing sequence, (b) peak IDR, and (c) residual IDR

#### 2.4.3. Deformed shapes

Deformed shapes in elevation have been generated by plotting the horizontal displacements recorded by the traditional potentiometers mounted on the floors and the wire potentiometers located at the level of the storeys' mid-height and ridge of the roof. Figure 2.15 represents the out-of-plane deflected shape of a longitudinal cross section of the specimen at the instant of peak second floor displacement for EQ2-100% and EQ2-200%, respectively.

The deformed shapes changed significantly according to the ground motion intensity level and the state of deterioration of the specimen. In both cases the higher drifts were observed at the roof level. This sub-structure was significantly more flexible. The initial response (similar from EQ1-25% to EQ2-150%, herein represented by the Figure 2.15a) was instead characterised by a higher drift demand in the first storey with the second floor remaining almost rigid and experiencing a very low drift demand. During the last test (EQ2-200%), the specimen exhibited similar inter-storey drifts in both storeys, resulting in an almost linear trend (similar to the one corresponding to the first mode of vibration), associated with rocking response of the slender piers over the height of the building, as illustrated in Figure 2.15b.

Furthermore, during the EQ2-200% test, after the failure of the interface between the top of the clay wall and the timber wall plates (Figure 2.13i), a clear relative displacement was observed between the CS wall and the clay veneer, showing that the presence of cavity ties was not sufficient to ensure their collaboration. Most of the ties were



permanently bent at the end of the tests. The inner loadbearing CS structure displaced significantly, while the southern portion of the East and West veneer walls was not involved in such an oscillation. A video of the test shows clearly this phenomenon [21].

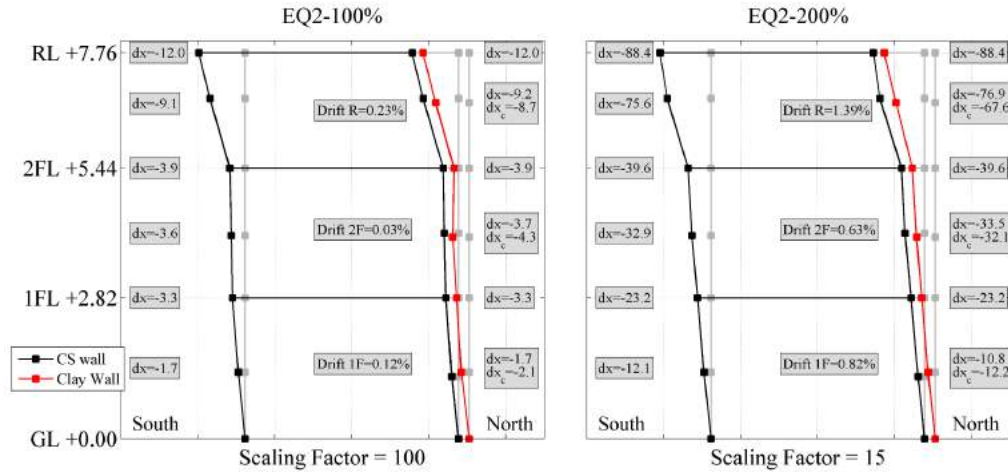


Figure 2.15 Deflected shapes of the specimen during the tests (a) EQ2-100% (PGA = 0.17g) and (b) EQ2-200% (PGA = 0.307g). Displacement units of mm

#### 2.4.4. Hysteretic responses

The evolution of the specimen’s hysteretic response is shown in Figure 2.16, in terms of base shear,  $V$ , versus global drift of the first two storeys,  $\tilde{\theta}$ , through all the tests. The global drift is defined as the relative displacement of the second floor slab divided by its distance from the base, given by:

$$\tilde{\theta} = \frac{\Delta_2}{h_1+h_2} = \frac{\Delta_2}{5440 \text{ [mm]}} \quad (2)$$

The time histories of the base shear have been computed as the sum of the products of each acceleration recording times the tributary mass of the corresponding accelerometer. Masses are assumed to be lumped at the accelerometer locations. The mass of the masonry body from the foundation level to the mid-height of the ground storey (at 1.38 m from the base) was assigned to the ground floor (and hence multiplied by the base acceleration time history).

The base shear coefficient  $BSC$  is defined as:

$$BSC = \frac{V}{M \cdot g} \quad (3)$$

where  $Mg$  is the total weight of the specimen.

In each plot of Figure 2.16, the hysteretic response of preceding tests is reported in grey. The white dots represent the positive and negative peak force responses with the corresponding displacements. The proportion between the two axes of all the plots is the same. In this way the progressive specimen stiffness degradation and the consequent fundamental period elongation are appreciable.

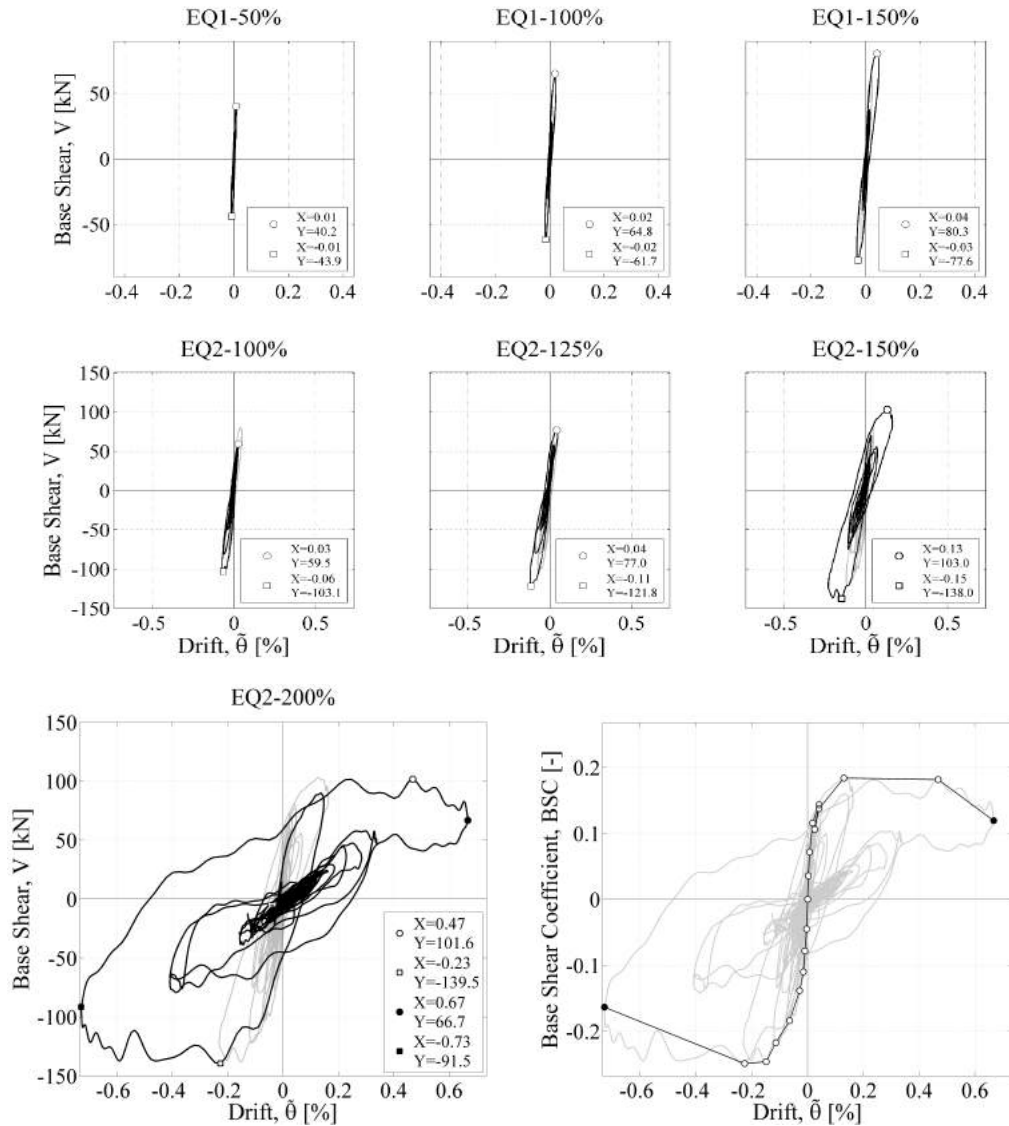


**Figure 2.16 Evolution of the global hysteretic response in terms of base shear versus global drift ratio (Left); Backbone curve in terms of base shear coefficient (Right)**

The EQ2 input induced a more pronounced asymmetry in the specimen response with respect to the EQ1 earthquake. The displacement demand in the negative direction (towards South), indeed, was rather higher than the one in the positive direction. The first significant nonlinearity in the hysteretic response is observed during testing under EQ2-150% (PGA = 0.243g), associated with the occurrence of spread flexural cracks in the inner CS walls. During the test at EQ2-200% (PGA of 0.307g), a large nonlinear behaviour was observed associated with extended damage to the specimen, highlighted by the dramatic enlargement of the hysteresis loops, and the consequent significant increase of the specimen's fundamental period of vibration.

An ultimate global drift ratio  $\hat{\theta} = 0.7\%$  was reached, while a shear deformation of the roof diaphragm  $\gamma_R = 1.5\%$  was observed for the significantly more flexible roof structure. The

maximum base shear  $V_{max}$  attained was approximately 139 kN, corresponding to a base shear coefficient  $BSC_{max} = 0.25$ . The dynamic force-displacement backbone curve can be obtained by connecting the peak points of the experimental curves. In other words, it is defined as the plot of the maximum resisted base shear,  $V_{max}$ , and the corresponding global drift,  $\bar{\theta}$ , for each stage of testing. The last point of both the positive and negative branch was obtained as the pair of the maximum drift attained and the corresponding base shear. A force “plateau” in the specimen capacity was reached in both directions. The attainment of the higher base shear occurred for sway towards the negative direction (towards the single-leaf side, South). In particular, the base shear attained for southward motion ( $V_{max}^- = 139.5$  kN) was 37% higher than the force reported for motion towards the double-leaf side of the structure ( $V_{max}^+ = 101.6$  kN). The asymmetry in the envelope response curve could be attributed to the northward “spike” of the applied accelerogram EQ2 and to the asymmetry of the structure.

#### 2.4.5. Response of the roof structure

The gable-roof system response was of particular interest for further investigation. The behaviour of the roof was acknowledged as one of the main factors that has driven the response of the substructure during the evolution of the dynamic tests, while the testing procedure ended because of the very large deflections of the gables. The detailed response of the roof in the course of the shaking table testing is illustrated in Figure 2.17, in terms of acceleration versus relative displacement curves. The first quantity regards the acceleration,  $a_R$ , recorded by the accelerometers located at the ridge beam level, whereas the second refers to the relative displacement of the ridge,  $\delta_R$ , with respect to the second floor level. The slope of the dashed line is representative of the effective stiffness,  $K_R$ , the gable-roof system, while its ever-decreasing trend indicates that the roof diaphragm undergoes a significant stiffness degradation. Trends for the progressive stiffness degradation, defined as the ratio between the current degraded stiffness,  $K_{Ri}$ , and the initial stiffness,  $K_{R1}$ , can be derived and plotted as a function of the maximum in-plane shear deformation,  $\gamma_{Rmax}$  that the roof diaphragm undergoes during each test, as shown in Figure 2.18. The relative roof displacement,  $\delta_R$ , of Figure 2.17 and Figure 2.18 is calculated from the relative ridge displacement (with respect to the second floor) by removing the residual displacements. Similarly, for generating the plots of Figure 2.18, the roof shear deformations,  $\tilde{\gamma}_R$ , was computed after subtracting the residual shear deformations,  $\gamma_{R,res}$ , since they resulted in curves biased towards the right, and should not be confused with the roof shear deformations,  $\gamma_R$ , reported in Figure 2.20. The roof shear deformation is computed as the relative ridge displacement divided by the inclined length of the roof pitch,  $L_R = 3.61$  m.

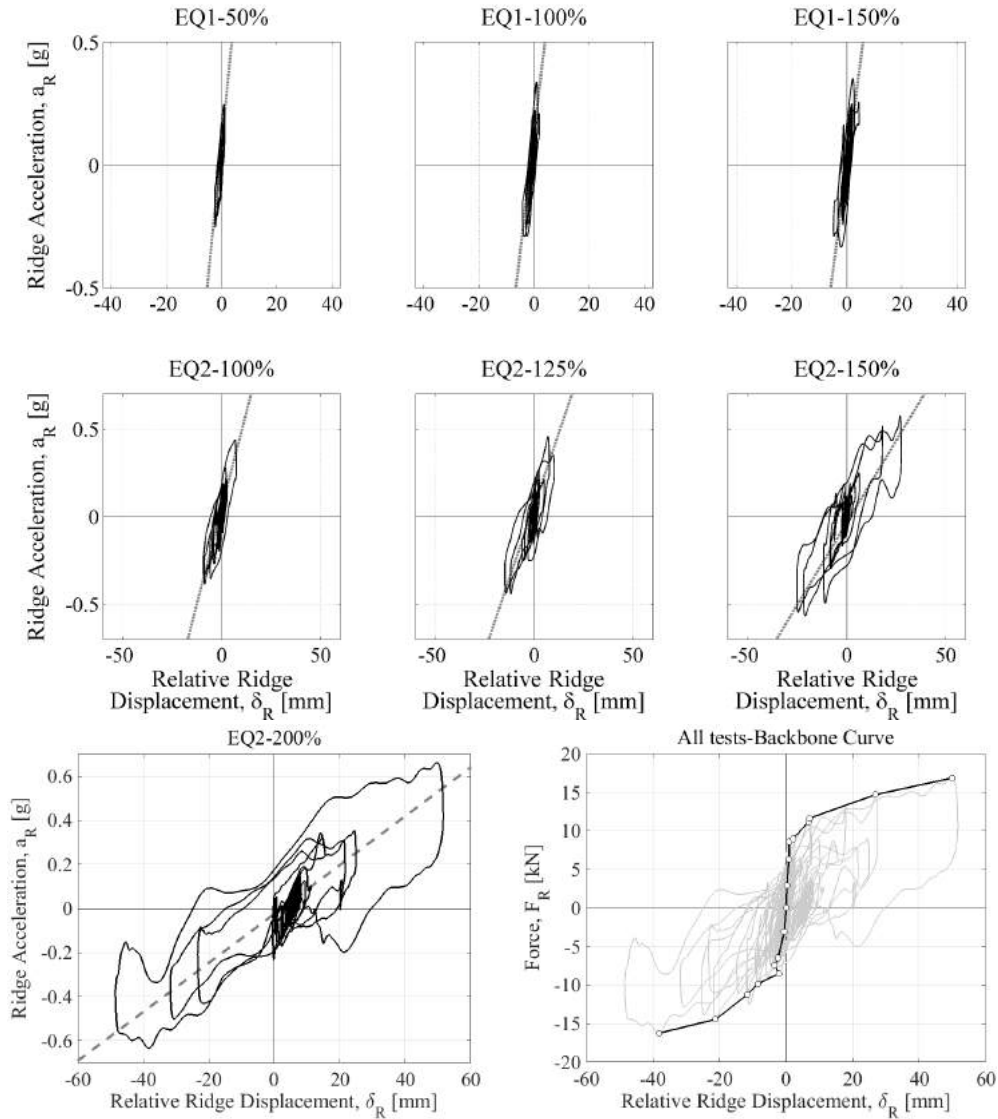


**Figure 2.17 Evolution of the roof hysteretic response in terms of acceleration versus relative displacement at the ridge beam level (Left); Backbone curve (Right)**

The inertia force of the entire roof system,  $F_R$ , system could be estimated by attributing a representative portion of the total mass of the gable-roof system to the ridge beam level. The lumped mass assumed at the top of the roof was equal to one third of the self-weight of the gable-walls plus half of the weight of the roof, estimated around 2.6 t. Figure 2.17 reports the force-displacement response of the roof structure, as well as the resulting backbone curve of the system, defined by the peak points of the experimental curves (plot of the maximum attained force,  $F_R$ , against the corresponding relative ridge displacement,  $\delta_R$ , occurring at the same instant, for each stage of testing).

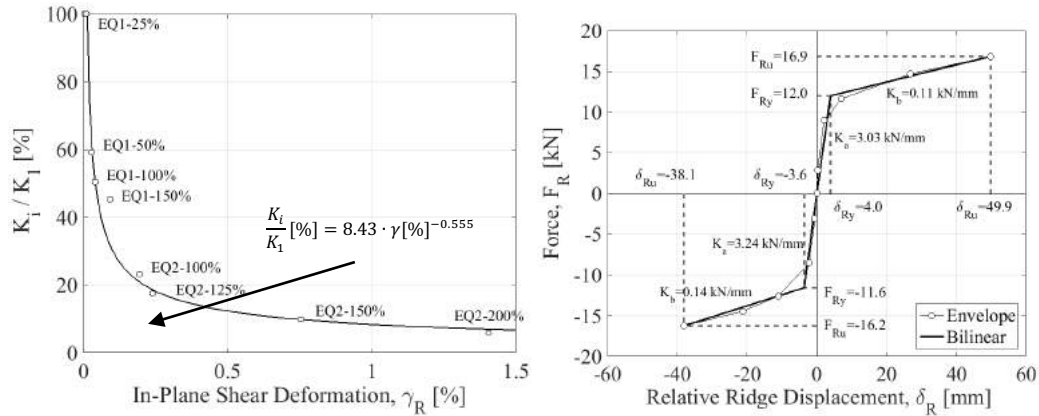


**Figure 2.18 (a) Roof stiffness degradation as a function of the maximum attained in-plane shear deformation; (b) Envelope of the force-displacement responses of the roof**

The envelope of the force-displacement responses displays no indication of strength degradation, which confirms diaphragm flexibility and the absence of observable structural failures in the roof. The plots on Figure 2.18 show that the roof exhibited an almost linear elastic behaviour up to a displacement of approximately 4 mm, with a stiffness,  $K_a$ , equal to approximately 3.2 kN/mm. Beyond this value the roof entered into a nonlinear phase characterized by a higher dissipation of energy and a reduced stiffness of  $K_b \approx 0.12$  kN/mm. The wide hysteresis loops demonstrate that the diaphragm is capable of dissipating considerable amounts of energy when subjected to lateral loading.

In order to determine performance parameters of the roof that could be further exploited to investigate its seismic response, it was necessary to appropriately characterize the force-displacement data using a consistent and rational methodology. In the absence of a universally accepted method, the performance of the system could be captured using a bilinear idealization of the backbone response curve. As reported by Peralta *et al.* [22] and Wilson *et al.* [23], the response can be approximated by a bilinear representation by applying the principle of hysteretic energy conservation, imposing at the same time the following constraints: the curve should pass through zero load and displacement; the ultimate displacement,  $\delta_u$ , could be taken as the maximum experimental displacement of the secondary linear branch; and the secondary stiffness should be computed as the global gradient of the approximate linear portion of the experimental envelope curve (here, observed for displacement amplitudes above 10 mm). Figure 2.18 illustrates the key performance parameters for the roof of the tested house, consisting in the initial stiffness,  $K_a$ , the secondary stiffness,  $K_b$ , the effective yield displacement,  $\delta_{Ry}$ , and the corresponding yield load,  $F_{Ry}$ , for both positive and negative displacements.

Because of the composite nature of the roof structure it was difficult to fully single out the experimental response of the timber diaphragm. The experimental data acquired from the tests could only be used to infer conclusions for the roof system response when examined as an ensemble, composed of the gable walls and the timber diaphragm (constructed by boards fastened perpendicular to timber joists).

#### 2.4.6. Identification of the specimen damage limit states

In this section, the identification of global quantitative thresholds that adequately describe the overall structural damage state of the building, is attempted. The roof sub-structure damage evolution is treated in a separate section 2.4.2 and not included in this one. The seismic performance of existing buildings is usually evaluated through four damage limit states as proposed, for example, by Calvi [24]: *DL1*: no damage, *DL2*: minor structural damage and moderate non-structural damage (still usable building), *DL3*: significant structural damage and extensive non-structural damage, *DL4*: severe damage leading to demolition. Due to the high non-linearity characterising URM buildings leading to difficulties in distinguish between *DL1* and *DL2*, Calvi [24] suggested to condense them into a unified damage state. Recently, Lagomarsino and Cattari [25] proposed a multiscale approach for the definition of the damage thresholds related to each of the four performance levels; at a global scale, the damage levels are identified on the pushover curve according to the fraction of resistant base shear attained, at a sub-system scale such thresholds are defined in terms of inter-storey drift; at the structural element scale, the seismic performance is evaluated according to the percentage of piers and spandrels exceeding a pre-defined deformation limit condition.

This section compares such damage limits with the actual damage observed through the testing stages of the present experimental test. Difficulties arise in the definition of clear damage states mainly due to two factors: the progressive accumulation of damage and the limited number of tests. Figure 2.19 shows the global response of the building in terms of global drift  $\tilde{\theta}$  (Eq. 2) and base shear coefficient BSC (Eq. 3). The global drift  $\tilde{\theta}$  (as the displacement of the second floor) is not the best engineering demand parameter, EDP, but it could be useful to give a general idea of the specimen performance in terms of deformation achieved. The white dots represent the points of maximum resisted base shear,  $V_{max}$ , and the corresponding global drift,  $\tilde{\theta}$ , for each stage of testing (notice that this point is lower than the maximum global drift achieved in the correspondent test,  $\tilde{\theta}_{max}$ ); the successive corner points of the black solid line are local peaks achieved in the last test EQ2-200%, while the black dot represents  $\tilde{\theta}_{max}$  recorded during the test EQ2-200%. The different limit states, defining the thresholds between damage states, are defined as follows. Figure 2.19 plots them associated with views of the West side inner CS wall crack patterns.

*DL1* is defined as the maximum achieved level of displacement with no visible damage. The inspection after the execution of test EQ1-150% (PGA = 0.137g) did not report any cracks. The structure could be considered as fully operational. The maximum recorded global drift was  $\tilde{\theta}_{max} = 0.047\%$ , while the maximum inter-storey drift, recorded at first floor level, was  $\theta_1 = 0.07\%$ .

*DL2* is defined as the maximum achieved level of displacement with minor/slight structural damage. The observed damage could be easily repaired (maximum crack residual not higher than 1 mm, [26]) for a possible immediate occupancy. In particular, this damage limit was achieved during the test EQ2-100% (PGA = 0.17 g), when the cracks appeared at the bottom of the S-W pier of the first storey ( $\tilde{\theta}_{max} = 0.073\%$ ,  $\theta_1 = 0.12\%$ ). The determination of *DL2* on a global scale is very sensitive to engineering judgment. In this particular case, it was associated with EQ2-100% test because during the following run (*i.e.* EQ2-125%) the residual crack width reached 2 mm, even though this damage was still limited to the S-W corner of the building.

*DL3* is defined as the maximum achieved level of displacement with moderate structural damage (but still repairable). This state was associated with damage observed in all the piers contributing to the longitudinal resistance of the specimen after test EQ2-150% (PGA = 0.243g). *A posteriori*, it was interesting to notice that this run was the first one to demand the full exploitation of the specimen lateral strength. *DL3* could be considered as a life safety limit state. The maximum residual width of the crack was 4 mm. The behaviour was characterized by a peak global drift  $\tilde{\theta} = 0.23\%$ , and a first storey drift  $\theta_1 = 0.34\%$ . Beyond this limit, the house could not be repaired economically.

*DL4* is defined as the maximum displacement reached by the specimen before the decision to stop the test due to a near collapse condition. The definition of a clear near collapse limit state is, hence, not trivial as for the case of the other limit states. The limit could be considered as a collapse-prevention threshold. Moreover, due to the significant reduction of stiffness, small variations in the input intensities could lead to significantly different peak displacements. The observed heavy structural damage (in piers and spandrels of inner and outer leaves) suggests that repairing a house that has reached this limit state may not be convenient. During the last test EQ2-200% (PGA = 0.307g), a peak global drift  $\tilde{\theta}_{max} = 0.729\%$  and first storey drift  $\theta_1 = 0.88\%$  were achieved. After this test, the maximum residual crack width was 5 mm.

Table 2.4 compares the experimental and analytical damage limits as proposed by Calvi [24] and by Lagomarsino and Cattari [25]. In particular, a comparison in terms of sub-system scale variable (*i.e.* interstorey drift  $\theta_1$ ) and global scale variable (*i.e.*  $V/V_{max}$  ratio) is proposed for each damage state.

**Table 2.4 Comparison of the experimental and theoretical damage limits proposed by Calvi [24] and Lagomarsino & Cattari [25]**

	<i>Scale</i>	<i>Variable</i>	<i>DL1</i>	<i>DL2</i>	<i>DL3</i>	<i>DL4</i>
Calvi [24]		$\theta_i$	0.1%		0.3%	0.5%
Lagomarsino & Cattari [25]	Sub-system	$\theta_i$	0.05- 0.1%	0.15- 0.3%	0.35- 0.5%	0.55- 0.7%
Experimental		$\theta_1$	0.07%	0.12%	0.34%	0.88%
Lagomarsino & Cattari [25]		$V/V_{max}$	$\geq 0.5$	0.95- 1.0	0.8- 0.9	0.6- 0.7
Experimental	Global	$V/V_{max}$	0.57	0.76	1.0	0.66
		$\tilde{\theta}$	0.047%	0.073%	0.23%	0.73%

In general, there is a very good agreement between the damage thresholds defined based on the experimental observations and those proposed in the considered analytical approaches. Only the collapse-prevention limit, *DL4*, is underestimated by both criteria. This may be due to the fact that the analytical approaches take into account a possible shear failure, *e.g.* Calvi [24] refers to Magenes and Calvi [27], while the response of the building under examination is dominated by flexural/rocking behaviour, typically associated with a higher displacement capacity (*e.g.* [3]). As the experimental limit states are associated with a dynamic building response governed by bending/rocking mechanisms the softening which can be observed in the force-displacement envelope

(Figure 2.19) is much less pronounced than the one assumed in the analytical approach by Lagomarsino and Cattari [25].

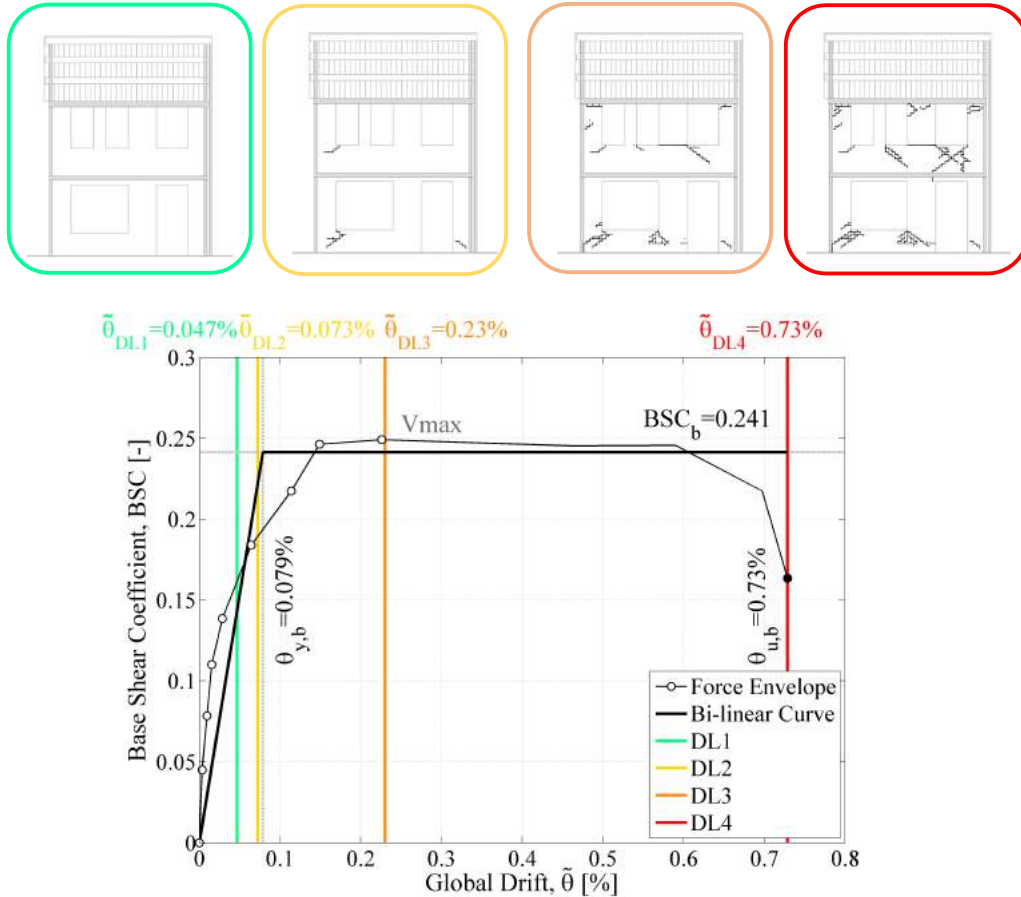


**Figure 2.19 Definition of damage limits on the experimental backbone curve, illustration of the corresponding damage extent on the West side inner wall**

The backbone curve has been further idealised by means of a bilinear approximation based on the equal energy criterion as prescribed by NTC08 [28]. The ultimate strength in terms of base shear coefficient was  $BSC_b = 0.241$  and the ultimate global drift  $\tilde{\theta}_{u,b} = 0.73\%$ , this deformation coincides with the peak global drift  $\tilde{\theta}_{max}$  achieved in the last test EQ2-200%. The bi-linearization procedure proposed by NTC08 [28] has been developed in order to simply characterize the capacity curve of a building. In this case, the bi-linear idealisation has not been truncated in correspondence to a drop  $V/V_{max} = 0.8$  (as prescribed by NTC08 in case of pushover analysis) but it was extended to the actual maximum displacement achieved (without collapse) during the shaking table test. The “yielding” point corresponds to global drift of  $\tilde{\theta}_{y,b} = 0.079\%$ . It is worth noticing that the quantitative definition of *DL2* almost coincides with the end of the linear elastic range of the bilinear curve whereas *DL3* almost corresponds to the maximum lateral force.



#### 2.4.7. Derivation of engineering demand parameters according to the specimen performance

EDPs, such as peak inter-storey drift ratio (IDR), residual inter-storey drift ratio (RIDR) or peak floor acceleration (PFA) are important synthetic measures of the seismic behaviour of a building under a given earthquake. The selection of proper EDPs is a crucial point in order to characterize the performance of a structure. The analysis of data derived from shaking table tests, as those herein presented, is a good chance to directly correlate the physical observed damage with EDPs. Figure 2.20 shows a series of parameters related to the building performance. It is worth remarking that the specimen performance has been influenced by the progressive accumulation of damage during the entire testing sequence, since the test was incremental. This should be taken into account when a correlation between EDPs and intensity measures (IM) is formulated.

Figure 2.20 reports the building performance in terms of peak displacements ( $\Delta_I$ ,  $\Delta_2$  and  $\Delta_R$ ), IDR ( $\theta_I$ ,  $\theta_2$  and roof diaphragm shear deformation  $\gamma_R$ ) usually strictly connected to the in-plane damage occurring in structural elements like piers and spandrels, and RIDR very often associated with a general damage and damage accumulation. The response in terms of PFA/PGA is also shown. This EDP could be correlated with the OOP performance of masonry (or more in general secondary) components or the damage occurring to acceleration sensitive non-structural components.

The evolution of the building fundamental period of vibration during all test phases is also shown. The fundamental period evolution is calculated by means of dynamic modal identifications performed before each strong motion by means of low amplitude RDNM excitations (see Table 2.3). The peaks in the power spectral density can generally be assumed to represent either peaks in the excitation spectrum or normal modes of the structure (Pick Picking method). The normal modes were determined from the identification of the peaks in the power spectral density, the analysis of the phase angles and the computation of the ordinary coherence function. The Peak Picking method used in this study was the one extended by Brincker *et al.* [29],[30] that introduced the so-called Frequency Domain Decomposition method. The basis of the method is the Singular Value Decomposition of the response spectral density matrix into a matrix of singular values and an orthogonal complex matrix containing the mode shape vectors of each spectral peak. Once the frequencies of vibration were defined, the mode shape components were computed from the amplitude of the cross-spectra normalized to the maximum component, with the direction of motion derived from the phase angles from the cross spectra between channels. The first mode of vibration of the undamaged building has been identified at a fundamental period  $T_{1,1} = 0.17$  s, for the inner walls system only. The first period of the external veneer walls is assumed to be presumably close to the same value. Figure 2.15, representing the deformed shapes under earthquake-type excitation, also well depicts the calculated deformed shape of a first mode type of behaviour, with the longitudinal walls responding in-plane and the gable walls overturning out-of-plane, parallel to the direction of the shaking table motion. More details regarding the modal identification outcomes are available on [18].

The IDR associated with the first floor,  $\theta_1$ , was systematically higher than the one of the second floor,  $\theta_2$ , up to the test EQ2-200% (PGA = 0.307 g). Attaining the *DL4* condition, they reached a similar maximum value of approximately 0.88%. The first damage limit state (*DL2*), where damage has been observed in the first storey piers, is associated with a

first-floor drift of  $\theta_1 = 0.12\%$ , while the severe damage limit state (*DL3*) with the exploitation of the specimen full capacity is associated with inter-storey drift ratios  $\theta_1 = 0.34\%$  and  $\theta_2 = 0.18\%$  for the first and second storey, respectively. From the same plot, looking at the evolution of  $\gamma_R$ , it is also noticeable that the roof substructure seems to experience non-linearity starting from early stages of the test (see also Figure 2.18a). Residual inter-storey drifts (RIDR) have been noticed after the end of the testing phase EQ2-100%, with the attainment of *DL2*.

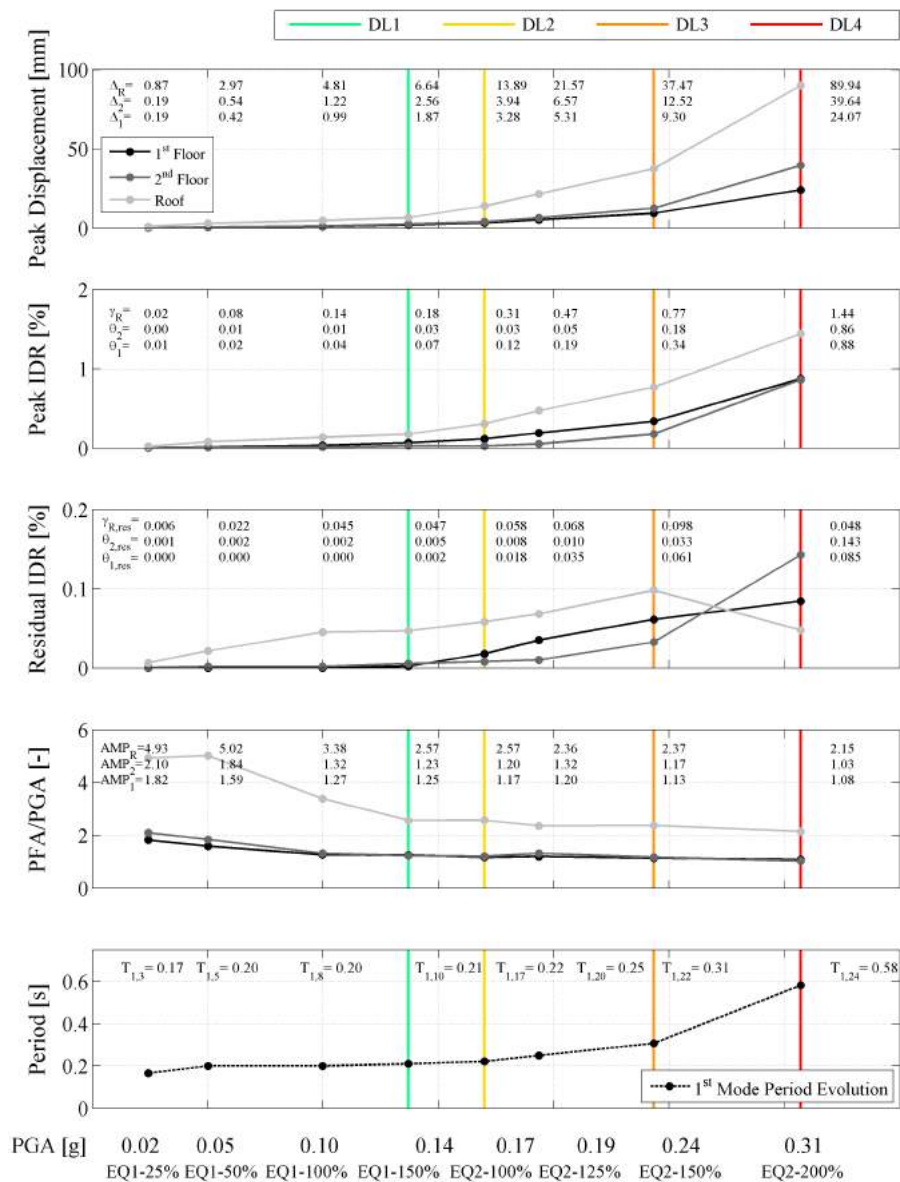


Figure 2.20 Summary of the performance of the building specimen

The plot of the floor acceleration amplification,  $AMP_i$ , shows a progressive decrease, starting from values around 1.5 in the first tests to values close to 1 in the last tests. In accordance to the very limited  $\theta_2$  an almost negligible amplification has been recorded

between the first and the second floor. In the EQ2-200% test the observed two-way out-of-plane cracks in all the North and South walls developed after the specimen has been subjected to floor acceleration  $PFA > 0.3g$ . This EDP could be considered as a first crack damage state for the OOP walls (further research are ongoing on this topic). The roof structure amplified the ground acceleration by a factor of 5 in the first runs down to a factor of 2 in the last test.

The results of the present experimental tests allow also the EDPs and the observed damage to be related with a seismic intensity measure (*i.e.* the PGA) for the input motions selected according to the hazard study. This could represent a reference for a sanity check of structural analyses on similar buildings.

## 2.5. Conclusions

The presented work was part of an extensive experimental campaign aimed at assessing the seismic vulnerability of Dutch URM buildings. It presents results of a unidirectional shaking table test performed on a full-scale specimen representative of a Dutch two-storey URM building with cavity walls and timber roof. The building specimen was intended to represent the end-unit of a terraced house of the late '70s, without any specific seismic detailing. The loadbearing walls were built with a 10-cm-thick calcium silicate URM, while three out of the four façades were completed by a clay veneer connected to the calcium silicate walls by means of steel ties. The materials were characterized by mechanical characteristics compatible with the ones found in the building stock. The specimen was subjected to incremental input motions representative of two different induced seismicity scenarios characterized by smooth response spectra and a short significant duration. The processing of the recorded signals, both in terms of accelerations and displacements sustained by the tested structure, allowed the evaluation of the seismic resistance and displacement demand at each stage of testing. All the recorded signals (accelerations, displacements, videos) can be requested online (<http://www.eucentre.it/nam-project>).

The loadbearing structure exhibited a box-type global response thanks to the presence of the rigid concrete slabs, which engaged the longitudinal walls and prevented the occurrence of local out-of-plane failure mechanisms in the transverse walls of the 1<sup>st</sup> and 2<sup>nd</sup> stories, no torsional effect was recorded. As a consequence, the full in-plane capacity of the longitudinal walls was exploited. Four damage states were identified and compared with some of the theoretical proposals available in literature, with good agreement. In summary, the building withstood the input motion with a PGA of 0.17g with little damage (maximum first inter-storey drift  $\theta_1 = 0.12\%$ ) and was in the near-collapse state at a PGA of 0.31g ( $\theta_1 = 0.88\%$ ). No significant shear damage occurred in the masonry piers, which were in general slender, and their response was mainly governed by rocking, whereas sliding occurred at the top of masonry walls parallel to the table motion. A substantial compatibility of displacements was observed between the inner and outer walls up to the near collapse state. During the last run (PGA = 0.31g), the two substructures moved almost independently and, as the stiffness contribution of the external clay masonry was reduced, the displacement demand of the internal structure increased. The fundamental period of the structure after the tests was almost 3.5 larger than the initial undamaged one. Furthermore, some diagonal stepped cracks were observed in the transversal load bearing walls due to the out-of-plane excitation.

The structure was characterized by a very flexible roof. A study of its dynamic behaviour is proposed in the manuscript. The timber diaphragm was subjected to a maximum shear deformation of almost 1.5%. Values for the amplifications of accelerations are also given herein.

Despite the high flexibility and the consequent vulnerability of roof system, the shaking table tests were able to fully exploit all the strength of the loadbearing structure. The maximum base shear coefficient was almost 0.25. The hysteretic plots, the large amount of experimental data derived from the dynamic tests (available upon request), the series of tests on smaller structural assemblies and the characterization tests on materials constitute a useful basis for the development and calibration of numerical models that can reproduce the response of structures with different configurations. These calibrated models, thanks to the identification of different damage limit states herein presented, will be a reference for the vulnerability studies of the Groningen building stock.

## 2.6. Acknowledgements

This paper describes an activity that is part of the project entitled “Study of the vulnerability of masonry buildings in Groningen” at EUCENTRE, undertaken within the framework of the research program for hazard and risk of induced seismicity in Groningen sponsored by the Nederlandse Aardolie Maatschappij BV. The authors would like to thank all the parties involved in this project: DICAr Lab of University of Pavia and EUCENTRE Lab that performed the test, together with NAM, Arup and TU Delft. The useful advices of R. Pinho, are gratefully acknowledged. Thanks, go also to H. Crowley, A. Rossi, M. Mandirola, E. Cenja, F. Dacarro, S. Peloso, F. Cuppari and E. Mellia for their support in the different phases of the experimental campaign.

## 2.7. References

- [1] S. J. Bourne, S. J. Oates, J. J. Bommer, B. Dost, J. Van Elk, and D. Doornhof, “A Monte Carlo method for probabilistic hazard assessment of induced seismicity due to conventional natural gas production,” *Bull. Seismol. Soc. Am.*, vol. 105, no. 3, pp. 1721–1738, 2015.
- [2] M. Tondelli, F. Graziotti, A. Rossi, and G. Magenes, “Characterization of masonry materials in the Groningen area by means of in-situ and laboratory testing,” *Tech. Report, Eucentre, Pavia, Italy.*, 2015.
- [3] F. Graziotti, A. Rossi, M. Mandirola, A. Penna, and G. Magenes, “Experimental characterisation of calcium-silicate brick masonry for seismic assessment,” in *Proceedings of the 16th International Brick and Block Masonry Conference*, 2016, pp. 1619–1627.
- [4] F. Graziotti, U. Tomassetti, A. Penna, and G. Magenes, “Out-of-plane shaking table tests on URM single leaf and cavity walls,” *Eng. Struct.*, vol. 125, 2016.
- [5] F. Graziotti *et al.*, “Shaking table tests on a full-scale clay-brick masonry house representative of the Groningen building stock and related characterization tests,” 2016.
- [6] F. Graziotti *et al.*, “Shaking Table Test on a Full-Scale Unreinforced Clay Masonry Building with Flexible Diaphragms, Proc. of 13th Canadian Masonry Symposium, Halifax, Canada. 2017.”
- [7] J. Ingham and M. Griffith, “Performance of unreinforced masonry buildings during the 2010 Darfield (Christchurch, NZ) earthquake,” *Aust. J. Struct. Eng.*, vol. 11, no. 3, pp. 207–224, 2011.
- [8] H. Degée, V. Denoel, P. Candeias, A. Campos-Costa, and E. Coelho, “Experimental investigation on non-engineered masonry houses in low to moderate seismicity areas,” *14th World Conf. Earthq. Eng.*, 2008.
- [9] M. Tomažević, P. Weiss, and T. Velechovsky, “The influence of rigidity of floors on the seismic

- behaviour of old stone-masonry buildings,” *Eur. Earthq. Eng.*, no. 3, pp. 28–41, 1991.
- [10] G. Magenes, A. Penna, I. E. Senaldi, M. Rota, and A. Galasco, “Shaking table test of a strengthened full-scale stone masonry building with flexible diaphragms,” *Int. J. Archit. Herit.*, vol. 8, no. 3, pp. 349–375, 2014.
- [11] EN 772-1, “Methods of test for masonry units – Part 1: Determination of compressive strength. European Standards, CEN/TC, Brussels, Belgium;” 2011.
- [12] EN 1015-11, “Methods of test for mortar for masonry – Part 11: Determination of flexural and compressive strength of hardened mortar. Brussels, Belgium: European Standards, CEN/TC;” 1999.
- [13] EN 1052-1, “Methods of test for masonry – Part 1: Determination of compressive strength. Brussels, Belgium: European Standards, CEN/TC;” 1998.
- [14] EN 1052-5, “Methods of test for masonry – Part 5: Determination of bond strength by the bond wrench method. Brussels, Belgium: European Standards, CEN/TC;” 2005.
- [15] EN 1052-3, “Methods of test for masonry – Part 3: Determination of initial shear strength. Brussels, Belgium: European Standards, CEN/TC;” 2002.
- [16] R. Esposito, F. Messali, R. Crielaard, and J. Rots, “Tests for the characterization of replicated masonry, physical testing and modelling - Masonry structures, Private Technical Report, TU Delft, NL. 2015.”
- [17] F. Messali, R. Esposito, and M. Maragna, “Pull-out strength of wall ties, Technical Report, TU Delft, NL,,” 2016.
- [18] F. Graziotti *et al.*, “Experimental campaign on cavity-wall systems representative of the Groningen building stock, Technical Report EUC318/2015U, Eucentre, Pavia, I.”
- [19] F. Graziotti, A. Penna, and G. Magenes, “A nonlinear SDOF model for the simplified evaluation of the displacement demand of low-rise URM buildings,” *Bull. Earthq. Eng.*, vol. 14, no. 6, pp. 1589–1612, 2016.
- [20] Eucentre, “Videos of full-scale shaking table test on a URM cavity-wall building model,” 2015. [Online]. Available: <https://www.youtube.com/watch?v=h8sZCRUCons&list=PLRDmVfXhFvQm8pxSTPpzHN1AQH0G7sMGk.%0A>.
- [21] Eucentre, “Videos of full-scale shaking table test on a URM cavity-wall building model,” 2015. [Online]. Available: <https://www.youtube.com/watch?v=1xw2GqIQfTw.%0A>.
- [22] D. F. Peralta, J. M. Bracci, and M. B. D. Hueste, “Seismic behavior of wood diaphragms in pre-1950s unreinforced masonry buildings,” *J. Struct. Eng.*, vol. 130, no. 12, pp. 2040–2050, 2004.
- [23] A. Wilson, P. J. H. Quenneville, and J. M. Ingham, “In-Plane Orthotropic Behavior of Timber Floor Diaphragms in Unreinforced Masonry Buildings,” *J. Struct. Eng.*, vol. 140, no. 1, p. 4013038, 2014.
- [24] G. M. Calvi, “A displacement-based approach for vulnerability evaluation of classes of buildings,” *J. Earthq. Eng.*, vol. 3, no. 3, pp. 411–438, 1999.
- [25] S. Lagomarsino and S. Cattari, “PERPETUATE guidelines for seismic performance-based assessment of cultural heritage masonry structures,” *Bull. Earthq. Eng.*, vol. 13, no. 1, pp. 13–47, 2015.
- [26] C. Baggio *et al.*, “Field Manual for post-earthquake damage and safety assessment and short term countermeasures ( AeDES ),” 2007.
- [27] G. Magenes and G. M. Calvi, “In-plane seismic response of brick masonry walls,” *Earthq. Eng. Struct. Dyn.*, vol. 26, no. 11, pp. 1091–1112, 1997.
- [28] Ministry of Infrastructures and Transport (MIT), *Norme tecniche per le costruzioni, DM 14/01/2008*. 2008.
- [29] R. Brincker, L. Zhang, and P. Andersen, “Modal identification from ambient responses using frequency domain decomposition,” in *Proceedings of the 18th International Modal Analysis Conference (IMAC)*, 2000, pp. 625–630.
- [30] R. Brincker, C. Ventura, and P. Andersen, “Damping Estimation by Frequency Domain Decomposition,” in *IMAC. 19th International Modal Analysis Conference*, 2001, pp. 698–703.



### 3. Two-way bending out-of-plane collapse of a full-scale URM building tested on a shake table

Tomassetti U., Correia A.A., Candeias P. X., Graziotti F., Costa A. C. Two-way bending out-of-plane collapse of a full-scale URM building tested on a shake table. *Bulletin of Earthquake Engineering* (accepted), 2018.

**Abstract.** This paper describes a shake table test on a one-storey full-scale unreinforced masonry (URM) structure, which complements an earlier testing of a two-storey structure with similar characteristics. The building specimen was meant to represent the upper floors of the end-unit of a terraced house, built with cavity walls and without any particular seismic design or detailing. In these specimens, the masonry walls were composed of two leaves: a load-bearing inner one made of calcium silicate (CS) bricks sustaining a reinforced concrete (RC) floor and an external leaf made of clay-bricks connected to the inner leaf by means of metallic ties. A pitched timber roof was supported by two triangular gable walls. Floor acceleration response histories of the previously tested two-storey specimen were used as input motions. An incremental dynamic test, with vertical and horizontal inputs, was carried out up to the explicit collapse of some bearing elements of the structure. In particular, a two-way bending out-of-plane (OOP) collapse of a loadbearing wall was observed and described.

#### 3.1. Introduction

The experimental test presented in this paper aims at investigating the vulnerability of unreinforced masonry (URM) cavity-wall terraced houses of the late 1970s. This residential typology, built with the construction technique of cavity walls, is typical of the Groningen region located in Northeast of the Netherlands, where almost 90% of the local building consists of URM buildings.

This area, historically not prone to tectonic ground motions, during the recent years has been subjected to seismic events induced by reservoir depletion due to natural gas extraction. Buildings not specifically designed for seismic actions are thus now exposed to this type of low intensity shaking (highest recorded local magnitude equal to 3.6 [1]).

Within this context, experimental and numerical activities were focused on estimating the overall seismic risk. This includes the evaluation of initial damage thresholds, which in many cases govern the economic losses in moderate and low seismicity areas, and the “Local Personal Risk” of buildings, defined as the annual probability of fatality for a hypothetical person continuously present inside or near a building [2][3]. This requires a

robust estimate of the probability of occurrence of the different damage states and collapse of structural and non-structural elements.

An experimental campaign, started in 2015, aimed at investigating the performance of structural components, assemblies and systems of typical building typologies present in the Groningen area. The testing campaign included *in situ* mechanical characterisation tests [4][5] and laboratory tests comprising: characterisation tests performed on bricks, mortar and small masonry assemblies, in-plane cyclic shear-compression [6], dynamic out-of-plane (OOP) one-way bending [7] and two-way bending [8] tests on full-scale URM specimens. Six full-scale shake table tests have been conducted on the testing facilities of the EUCENTRE and LNEC laboratories in 2015 [9], 2016 [10], 2017 (on a roof substructure only, [11]) and 2018 [12] on two different URM building typologies: terraced houses and detached houses. In the framework of the same project, static tests on similar structures and components were also performed by TU Delft laboratory (*e.g.* [13][14][15]). The reasons of such experimental effort lie on the very little knowledge of the seismic behaviour of Dutch URM buildings. Experimental dynamic tests on cavity wall buildings not specifically designed for earthquake loading are, in fact, limited to the work carried out by [16]. All the data collected and elaborated from the laboratory tests constituted a reliable reference for the calibration of numerical models simulating the static and dynamic behaviour of structures or part of them (*e.g.* [17][18][19][20]).

Having not reached collapse in the first shake table tests on a full-scale two-storey end-unit terraced house (EUC-BUILD-1 presented in [9]), the main goal of the herein presented shake table test performed at LNEC on a similar structure was to assess the collapse failure mechanism. For this reason, a structure representing a sub-volume of EUC-BUILD-1 (second-floor and roof) was tested with the aim of establishing if the collapse might be controlled by a global mechanism (*e.g.* soft-storey mechanism) or by a local one such as overturning of the roof assembly or OOP failure of a wall. The study of the collapse mechanism allows an estimation of the amount of collapsed debris and provides information to compute the probability of injury or death [2].

This paper describes geometrical and mechanical characteristics of the building specimen (LNEC-BUILD-1) as well as construction details (Section 3.2); the shake table input motions, the testing protocol and the instrumentation layout are discussed in Section 3.3. Section 3.4 examines the performance of the building under the input excitation, the test results in terms of damage evolution, hysteretic responses, performance of the roof structure and identification of global limit states. Finally, a detailed description of the observed failure mechanism triggered by a local OOP collapse of the transverse wall is presented.

## 3.2. Specimen Characteristics

### 3.2.1. Geometry of the specimen and construction details

The building prototype was a full-scale one-storey structure, with a timber roof and a RC slab, representing a sub-volume (second-floor and roof) of the EUC-BUILD-1 specimen (tested in 2015 at EUCENTRE by Graziotti *et al.* [9]). The building prototype was 5.82 m long, 5.46 m wide and 4.93 m high with a total mass of 31.7 t. Figure 3.1 shows the plan view and pictures of the specimen during transportation and positioning on the shake table. Figure 3.2 shows inner and outer elevations. The walls, supported by a steel foundation, consisted of two URM leaves. The inner load-bearing leaf was made of



calcium silicate (CS) bricks whereas the external leaf was a clay brick veneer without any load-bearing function. An air gap of 80 mm was left between the two leaves, as usually seen in common practice. L-shaped steel ties (2 per m<sup>2</sup>) with a diameter of 3.1 mm and a length of 200 mm were inserted in the 10 mm-thick mortar bed-joints during the laying of the bricks, ensuring the connection between the two masonry leaves (location shown in Figure 2a). In particular, the “L-hook” side was embedded in the inner CS walls for a length of 70 mm, while the “zig-zag” extremity was embedded in the clay masonry for a length of 50 mm (see Figure 3.3a).

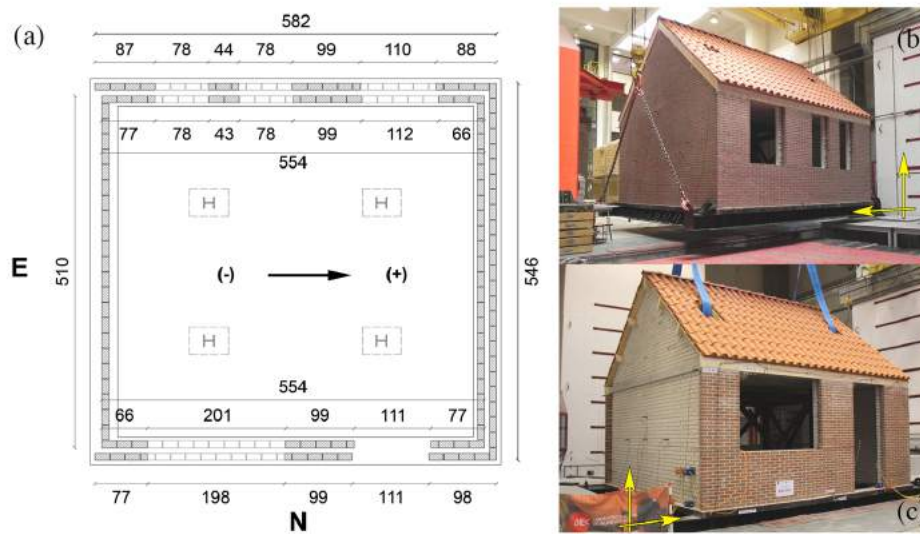


Figure 3.1 Geometry and views of the specimen: (a) plan view; transportation from South-West (b) and positioning on the shake table from North-East (c). Arrows indicate the positive sign convention in the shaking directions.

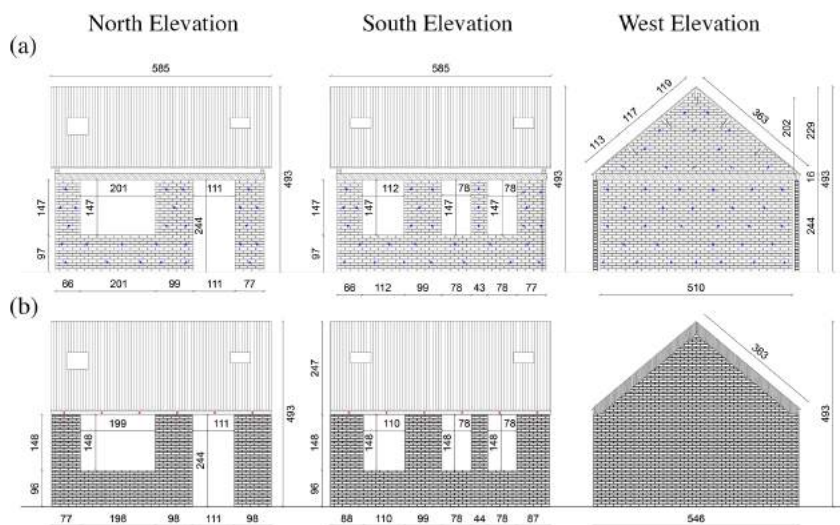


Figure 3.2 Elevation views: inner CS leaves showing location of ties (a), outer clay leaves (b). The RC first floor slab covered the span between the two transverse (East and West) inner CS walls. The inner CS masonry was continuous along the entire perimeter of the house,

while the outer clay brick leaf was not present in the East façade, simply because the specimen was meant to represent the end-unit of a system of terraced houses. The only geometrical difference with respect to the upper portion of EUC-BUILD-1 was represented by the door in the North elevation, which allowed an easy access to the inside of the building.

Two gable walls in the transverse façades (East and West) supported a 43° pitched timber roof. A rigid steel frame placed inside the specimen was used as reference system for direct measurement of the floor, walls and roof displacements. A 20 cm gap in both directions ensured no interference between the slab of the building prototype and the rigid frame. The arrows in Figure 3.1 indicate the positive sign convention in the horizontal and vertical shaking directions.

The construction details of the specimen, which can significantly affect the seismic response of any structure [21][22], are representative of the Dutch common building practice during the 1960s and 1970s. In particular, the slab was not directly supported by the longitudinal walls; the gap between the slab and the inner CS longitudinal walls being filled with mortar after removal of the temporary supports. Figure 3.3 presents pictures of the construction phase of the specimen. The detail of the connection between the slab and the two longitudinal walls is shown in Figure 3.3f and in Figure 3.4a,b,c. This solution resulted in almost no vertical load being transmitted to the longitudinal walls under static conditions.



**Figure 3.3 Construction details of the specimen: (a) geometry and positioning of cavity steel tie; (b) building phase of inner CS leaf; (c) construction of the ground floor; (d) inner and outer leaves before the laying of the RC slab; (e) laying of the first-floor slab; (f) connection of slab to longitudinal walls and timber plate.**

Similarly, the timber plates, beams flanking the RC slab in the North and South sides, were not in contact with the longitudinal clay walls. The resulting gap between timber plates and top of the veneer walls was also filled with mortar afterwards. Moreover, these timber beams were attached to the edge of the first-floor slab by means of threaded bars, with 10 mm of diameter and spaced of 100 cm, cast to the RC slab. Such details were adopted in order to reproduce a load-bearing configuration common in the Dutch building stock.

The timber roof is a simple structure consisting of one ridge beam, two timber plates on top of the longitudinal outer leaves of the walls and two girders per side between the ridge beam and the timber plates, at an approximate distance of 1.13 m (see Figure 3.4d,e). Tongue and groove planks, not covering the entire inclined length, with a width equal to 182 mm and a thickness of 18 mm, were nailed on top by means of two 60×2 mm nails at each intersection (Figure 3.4f). The timber beams of the roof are supported by the transverse inner CS leaves (West and East gables), whereas this connection was further reinforced by the presence of L-shaped steel anchors, as shown in Figure 3.4f. The roof diaphragm is characterised by four openings (three with dimensions of 54x45 cm, one of 54x72 cm) allowing, by means of a cable system, to sustain the RC slab in case of need and preventing a global collapse of the specimen on the shake table. The opening in the North-East corner is larger, granting access to the interior of the roof, in the first floor. The in-plane stiffness of the timber diaphragm was essentially provided by the nailed connections between beams and planks, as well as by the effectiveness of the tongue and groove joints. The roof was completed with the installation of clay tiles. In order to study the performance of non-structural components inside the building, a layer of plaster was applied on the ground floor, as well as, common furniture.

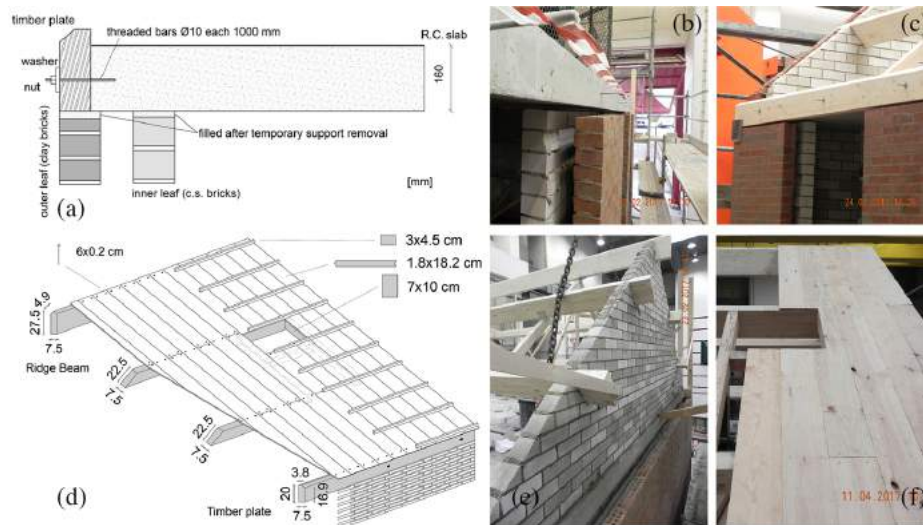


**Figure 3.4** Detail of the connection between the two longitudinal walls, the RC slab and the timber plate (a), pictures of the same detail during the specimen construction (b,c), 3d detail of the roof structure (d), and pictures taken during the construction of the roof (e,f).

### 3.2.2. Mechanical properties of materials

This experimental campaign included also tests for the characterisation of the mechanical properties of the materials employed in the construction of the specimen. It comprised strength tests on mortar samples, as well as tests on small masonry assemblages, such as compression tests on wallettes and bond-wrench tests and shear tests on triplets. The dimensions of the CS units were 212×102×71 mm. The clay bricks were perforated with ten vertical holes, a void ratio of 17% and dimensions of 211×100×50 mm. The flexural ( $f_t$ ) and compressive ( $f_c$ ) strength of the mortar were determined according to [23].

Compressive ( $f_b$ ) and tensile ( $f_{bt}$ ) strength of bricks, following [24], were also determined. Six masonry wallettes made of CS and six made of clay bricks were tested in compression in the direction perpendicular to the horizontal bed-joints, according to [25]. These tests allowed the determination of the compressive strength of masonry ( $f_m$ ), as well as its secant elastic modulus at 33% of the compressive strength ( $E_m$ ). Bond-wrench tests on CS and clay masonry triplets were performed in order to determine the bond strength of masonry, according to [26]. Specimens of both types of masonry were also subjected to shear tests for the determination of the cohesive component of shear strength ( $f_{v0}$ ) and their friction coefficients ( $\mu$ ), according to the guidelines given by [27]. Masses of the different elements characterising the specimen are summarised in Table 3.1 while Table 3.2 lists the masonry mechanical properties resulting from material characterisation tests.

**Table 3.1 Summary of structural masses, units of t**

		<i>Inner leaf (Gable)</i>	<i>Veneer (Gable)</i>	<i>Total</i>
<b>Masonry structure</b>	<i>North facade</i>	1.47	1.62	<b>3.09</b>
	<i>South facade</i>	1.79	1.94	<b>3.73</b>
	<i>West facade</i>	3.39 (1.16)	3.82(1.18)	<b>7.21</b>
	<i>East facade</i>	3.39 (1.16)	-	<b>3.39</b>
<b>RC Slab</b>				<b>11.40</b>
<b>Roof</b>	<i>Wooden planks</i>		0.442	
	<i>Profiles for tiles positioning</i>		0.096	
	<i>Wood profiles around holes</i>		0.029	<b>2.83</b>
	<i>Beams</i>		0.295	
	<i>Tiles</i>		1.970	
<b>Entire Building</b>				<b>31.7</b>

**Table 3.2 Masonry mechanical properties**

<b>Material property</b>	<b>Symbol</b>	<b>U.M.</b>	<b>Calcium Silicate</b>		<b>Clay</b>	
			<b>Average</b>	<b>C.o.V.</b>	<b>Average</b>	<b>C.o.V.</b>
<i>Density of bricks</i>	$\rho_b$	$kg/m^3$	1887	0.02	1593	0.02
<i>Density of masonry</i>	$\rho$	$kg/m^3$	1800	0.01	1839	0.01
<i>Compressive strength of bricks</i>	$f_b$	<i>MPa</i>	18.72	0.12	63.23	0.10
<i>Compressive strength of mortar</i>	$f_c$	<i>MPa</i>	6.20	0.06	8.34	0.11
<i>Flexural strength of mortar</i>	$f_t$	<i>MPa</i>	2.87	0.03	3.03	0.03
<i>Masonry compressive strength</i>	$f_m$	<i>MPa</i>	9.80	0.10	19.19	0.05
<i>Masonry's Young modulus</i>	$E_m$	<i>MPa</i>	7955	0.18	12798	0.13
<i>Brick's Young modulus</i>	$E_{bt}$	<i>MPa</i>	8990	0.36	7211	0.53
<i>Flexural bond strength of masonry</i>	$f_w$	<i>MPa</i>	0.36	0.20	0.19	0.47
<i>Masonry (bed-joint) initial shear strength</i>	$f_{v0}$	<i>MPa</i>	0.45	-	0.41	-
<i>Masonry (bed-joint) shear friction coefficient</i>	$\mu$	-	0.48	-	0.75	-

Tests performed at Delft University of Technology (TU Delft) allowed the determination of the tensile strength of the steel ties connecting the two masonry leaves [28]. The push-in and pull-out strengths of the “zig-zag” tie extremity (see Figure 3.3a) embedded in

clay masonry specimens, considering an overburden pressure of 0.3 MPa, was higher than the strengths associated with the hook extremity embedded in CS specimens and subjected to the same imposed compression. The average pull-out/push-in strengths associated with this tie typology in CS and Clay URM specimens are approximately 1.25/1.13 kN and 1.94/1.78 kN respectively, while the ultimate tensile capacity of the ties is approximately 4.3 kN [29].

### 3.3. Testing protocol and instrumentation

#### 3.3.1. Input signals

The specimen was subjected to two different types of base motion: *i*) dynamic identification tests using a sequence of impulsive responses of both the shake table and the specimen by applying a displacement square wave, with 1 mm peak-to-peak amplitude at 0.1 Hz and *ii*) two-component earthquake records: horizontal (or longitudinal) and vertical.

Since the specimen constituted a reduced version of EUC-BUILD-1 (*i.e.* only the second floor and the roof), the recorded first-floor accelerations have been adopted as horizontal component input at the base of the new building. The testing protocol applied to EUC-BUILD-1 consisted in incremental dynamic tests (only horizontal component) with two records: EQ1 and EQ2 representative of the dynamic characteristics of induced seismicity ground motions [9]. These two ground motion inputs (see Figure 3.5a) correspond to the two main scenarios, with smaller and larger return periods respectively, identified after a detailed study on the seismic hazard characteristics of the region. For practicality and to allow a better control of the shake table performance, only the recorded first-floor accelerograms produced by EQ1-100%, EQ1-150%, EQ2-100%, EQ2-150% and EQ2-200% (named as FEQ1-100%, FEQ1-150%, FEQ2-100%, FEQ2-150% and FEQ2-200%) were adopted as horizontal input components. These five floor accelerograms have been considered well representative of the progressive damage evolution occurring in the EUC-BUILD-1 specimen (see the response spectra changes in Figure 3.5b and associated damage states) allowing for a realistic comparison between the two tests.

As mentioned above, the specimen prototype has been subjected to combined horizontal and vertical motions; the selected vertical components were directly the EQ1 and EQ2 vertical ground motions scaled linearly at the considered level of intensity (see response spectra in Figure 3.5c), assuming, hence, the ground floor of EUC-BUILD-1 as rigid in the vertical direction.

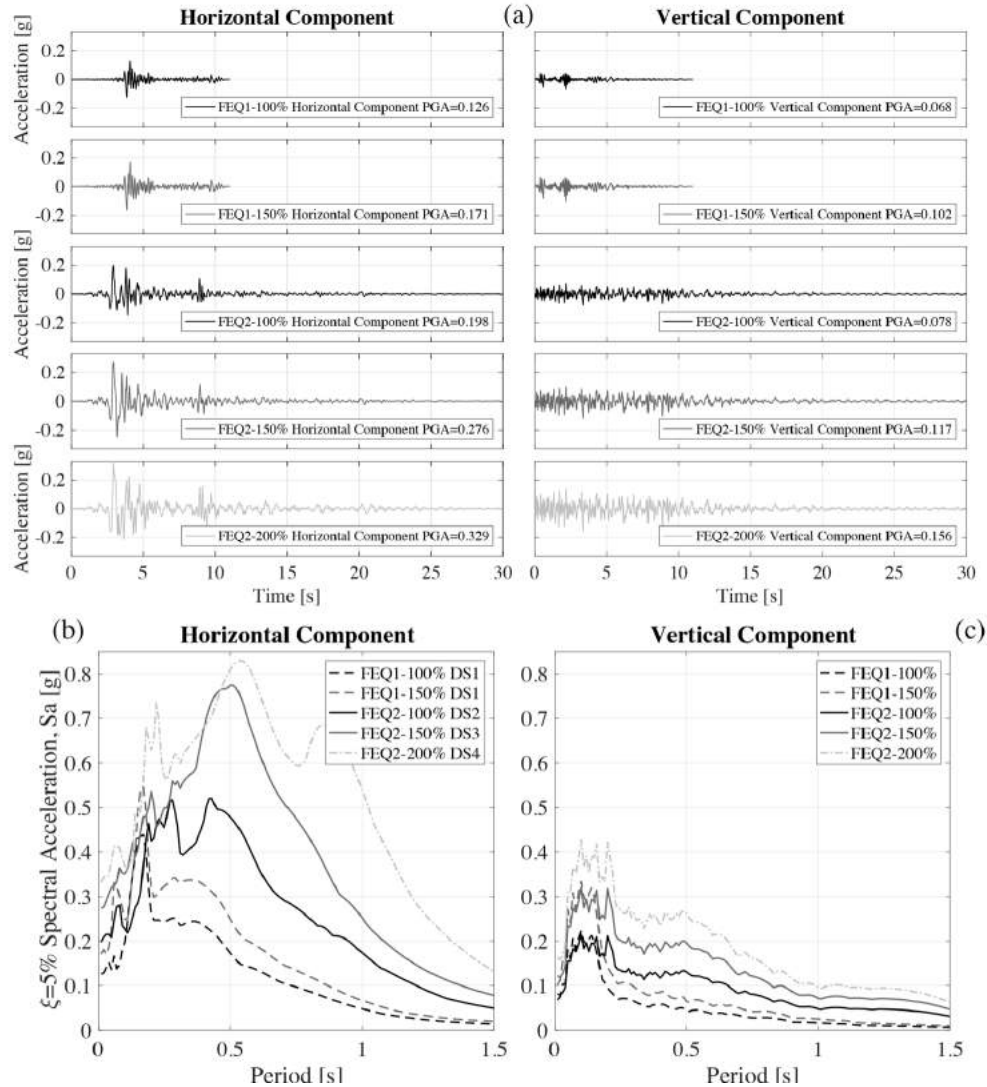


Figure 3.5 Theoretical horizontal (a) and vertical (b) 5% damped acceleration response spectra of the experimental inputs.

### 3.3.2. Testing protocol

The sequence of incremental tests followed strictly the one performed at EUCENTRE [9], increasing gradually the intensity of the ground motions and applying first FEQ1, followed by FEQ2. Table 3.3 presents the applied testing sequence specifying the input typology and the scaling factor characterising both motion components, the nominal and actual horizontal and vertical peak table accelerations ( $H-PTA$  and  $V-PTA$ ) and the horizontal 5% damped spectral acceleration at the initial fundamental period  $T_{1,1}$  equal to 0.22 s. Calibration tests at reduced intensity are named with a final “-C”.

The incremental testing sequence stopped at test FEQ2-300% with the partial collapse of the building prototype. After each test (indicated in bold in Table 3.3) of increasing  $PTA$  the building prototype was subjected to impulsive excitations by applying a displacement



square wave, in order to allow for structural identification, assessing the progressive effect of damage on the structural dynamic properties.

Other intensity measures were evaluated to characterise the input shake table motions for possible correlations with the specimen's performance. Table 3.4 lists both directions' peak table displacements (*PTDs*) and peak table velocities (*PTVs*), as well as the conventionally defined cumulative absolute velocity (*CAV*), the Arias intensity (*IA*, [30]), and the average 5% damped pseudo-spectral acceleration between 0.1 and 0.5 periods (*AvgSa*, calculated according to [31]) for all the applied earthquake motions. The modified Housner intensity (*mHI*, [32]), defined as the integral of the pseudo-velocity spectrum at 5% viscous damping between 0.1 s and 0.5 s (period range of interest for the tested building specimen) and the significant durations (*SD,5-75*), defined as the time interval between the development of 5% and 75% of *IA* are also shown in Table 3.4.

**Table 3.3 Applied testing sequence.**

Test#	Test Name	H-Component:			V-SF [%]	Nom. H-PTA [g]	Nom. V-PTA [g]	Nom. Sa <sub>(TI)</sub> [g]	H-PTA [g]	V-PTA [g]	Sa <sub>(TI)</sub> [g]
		1 <sup>st</sup> Floor Acc. produced by:	H-SF [%]	Vertical Component							
2	FEQ1-50%	EQ1-100%	50	EQ1-v	50	0.063	0.034	0.123	0.056	0.036	0.124
4	FEQ1-100%	EQ1-100%	100	EQ1-100%-v	100	0.126	0.068	0.247	0.119	0.075	0.259
6	FEQ1-150%	EQ1-150%	100	EQ1-100%-v	150	0.171	0.102	0.303	0.146	0.122	0.327
8	FEQ2-50%-C	EQ2-100%	50	EQ2-100%-v	50	0.099	0.039	0.231	0.137	0.054	0.292
10	FEQ2-50%	EQ2-100%	50	EQ2-100%-v	50	0.099	0.039	0.231	0.095	0.071	0.251
11	FEQ2-100%	EQ2-100%	100	EQ2-100%-v	100	0.198	0.078	0.462	0.218	0.100	0.603
13	FEQ2-150%	EQ2-150%	100	EQ2-100%-v	150	0.276	0.117	0.455	0.380	0.214	0.626
15	FEQ2-60%-C	EQ2-200%	30	EQ2-100%-v	60	0.099	0.047	0.221	0.129	0.045	0.224
16	FEQ2-120%-C	EQ2-200%	60	EQ2-100%-v	120	0.198	0.094	0.441	0.295	0.128	0.539
17	FEQ2-200%	EQ2-200%	100	EQ2-100%-v	200	0.330	0.156	0.735	0.393	0.184	0.644
19	FEQ2-300%	EQ2-200%	150	EQ2-100%-v	300	0.495	0.234	1.103	0.630	0.343	1.020

**Table 3.4 Further intensity measures characterising the testing sequence.**

Test#-Test Name	H-PTD [mm]	V-PTD [mm]	H-PTV [mm/s]	V-PTV [mm/s]	AvgSa [g]	mHI [mm]	IA [mm/s]	CAV [mm/s]	SD,5-75 [s]
2-FEQ1-50%	2.9	1.1	33.0	8.50	0.116	21.4	10.9	424.8	0.60
4-FEQ1-100%	5.5	2.2	66.3	26.6	0.232	42.2	46.3	859.4	0.59
6-FEQ1-150%	7.9	3.4	86.3	28.9	0.297	56.9	83.5	1218.5	0.81
8-FEQ2-50%-C	10.7	3.8	73.5	22.9	0.228	46.1	70.4	1608.6	1.74
10-FEQ2-50%	9.3	4.1	78.6	29.9	0.205	41.7	66.4	1834.6	3.3
11-FEQ2-100%	20.7	7.8	141.4	45.3	0.428	85.9	272	3308.5	2.09
13-FEQ2-150%	26.8	11.3	200.6	55.8	0.613	120.6	587.3	4307.2	1.57
15-FEQ2-60%-C	12.2	4.5	88.7	24.3	0.191	39.1	73.8	1881.4	2.21
16-FEQ2-120%-C	26.7	10.0	190.2	40.0	0.445	87.3	382.6	4147.5	2.46
17-FEQ2-200%	40.1	14.2	272.7	66.5	0.610	121.5	782	6185.3	2.67
19-FEQ2-300%	60.9	21.3	419.6	85.3	0.942	185.1	1948.8	9777.4	3.76

### 3.3.3. Instrumentation

In order to detect and monitor the structural response under different levels of input motion, several kinematic measuring instruments were installed on the building. The location and typology of the instruments were selected considering the physical quantities to be recorded focusing particular attention to the critical zones identified in the previously tested EUC-BUILD-1. The instrumentation consisted of 40 accelerometers and 24 displacement transducers. Figure 3.6a shows the ID number and the locations of the accelerometers installed on both inner and outer leaves, as well as on the floor and on the ridge beam of the roof.

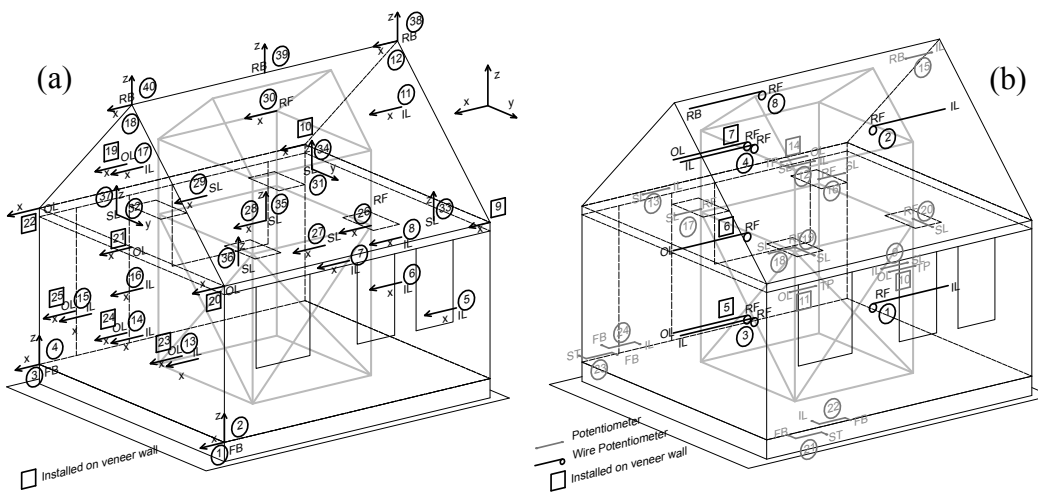


**Figure 3.6 Locations of the instrumentation: accelerometers (a) and displacement transducers (b) (letters indicate the component at which the transducer is attached to: SL = slab, RF = reference frame, IL = inner leaf, OL = outer leaf, FB = foundation beam, ST = shake table, TP = timber plate and RB = roof ridge beam).**

The displacements measured between the specimen and the rigid reference frame were considered equivalent to the relative displacements with respect to the shake table surface. In particular, wire potentiometers were installed in order to record the out-of-plane response of the East and West façades at mid-height of the ground floor and of the gable (see Figure 3.6). Transducers were used to monitor directly the longitudinal and transverse displacements of the slab with respect to the reference steel frame. Further transducers were also installed to monitor the eventual slippage between the base of the walls and the steel foundation beam, between the RC slab and the top of the first-floor CS longitudinal walls and the differential displacement between the RC slab and the outer leaf observed during the last stages in [9].

## 3.4. Test results

### 3.4.1. Shake table performance

The target shake table motions for this specimen were very demanding, since the shake table should reproduce the floor motions of EUC-BUILD-1. Such floor motions recorded on a specimen from a previously performed dynamic experiment are typically affected



not only by the dynamics of the specimen and its damage evolution but also by the dynamic characteristics of the shake table system. In this case, the application of the input avoiding significant distortions was particularly challenging since the floor motions were being applied on a different shake table with more degrees of freedom (than what was used for EUC-BUILD-1).

Nevertheless, the comparison between the theoretical response spectra and those obtained from the accelerations recorded on the specimen's foundation showed generally a good match, with the exception of a slight overshooting of low-period horizontal spectral ordinates in all FEQ2 tests [33]. The only FEQ2-150% test (shown in Figure 3.7a), in particular, presented a considerable overshooting around periods of 0.20 s (70%) and 0.10 s (200%), respectively for the horizontal and vertical directions. For this reason, a tuning procedure for the shake table was followed before proceeding to level FEQ2-200%, by performing two tuning iterations at smaller levels of excitation (FEQ2-60%-C and FEQ2-120%-C). On the other hand, the sudden change of the specimen dynamic characteristics during test FEQ2-300%, due to its heavy damage and its interaction with the table, did not allow a perfect match of the target spectrum (see Figure 3.7b). Additionally, overshooting at low-period spectral accelerations was observed in both horizontal (30%) and vertical (50%) directions, associated with undershooting at long periods (below 10%). The overshooting at the addressed fundamental period horizontal spectral acceleration was limited to less than 15%.

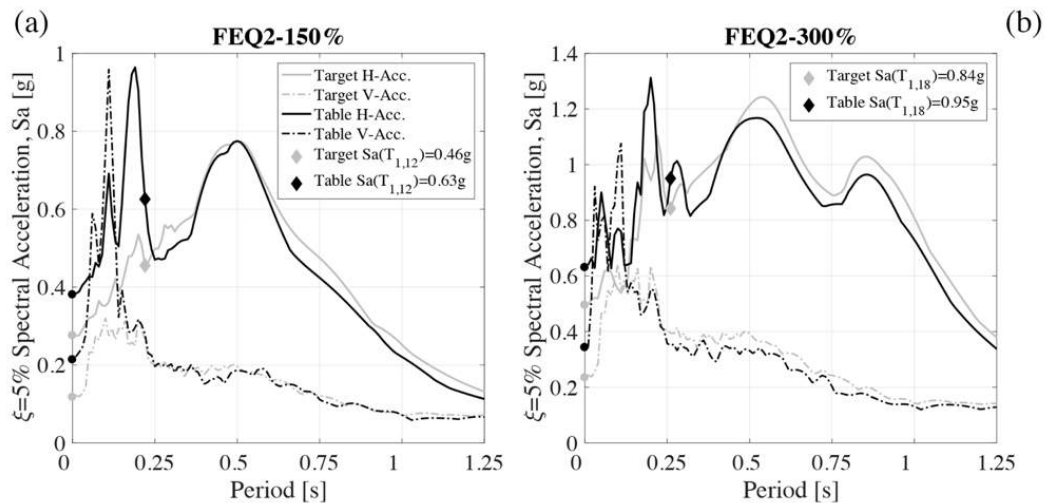


**Figure 3.7 Comparison of horizontal and vertical acceleration response spectrum of the recorded base acceleration against the target one for testing under (a) FEQ2-150% (H-PTA = 0.38g), and (b) FEQ2-300% (H-PTA = 0.63g).**

### 3.4.2. Damage evolution and identification of damage states

This section examines the evolution of structural and non-structural damage identifying, consistently with the approach adopted by [9][10], global quantitative thresholds which allow the overall structural damage state experienced by the building to be characterised. The presence of the plaster permitted the identification of an initial further damage state related to cracking of the building finishes. Therefore, six damage states (DS) were considered: DS0, completely undamaged; DS1, no structural damage; DS2, minor

structural damage; DS3, moderate structural damage; DS4, extensive structural damage; and DS5, very heavy structural damage, total or local collapse [34][35][9][10]. The analysis of the structural performance allowed for the identification of damage limits ( $DL_i$ ), consisting in quantitative boundaries in terms of inter-storey drift between damage states  $DS_i$  and  $DS_{i+1}$ .

As observed in EUC-BUILD-1, the roof responded as an independent substructure allowing the individual definition of local damage states for the structure and roof substructure, whereas, the global damage state of the building can be considered as the more critical between the two. Considering the low redundancy of the structural system and the progression of damage being observed mainly in the masonry elements supporting the slab, the global damage states were defined according to the in-plane and out-of-plane performance of such masonry piers.

Figure 3.8 and Figure 3.9 illustrate the evolution of the crack pattern on the CS walls (from the inside) and on the outer clay walls (from the outside) throughout the entire testing sequence. Figure 3.10 shows pictures of the surveyed damage.

The building prototype suffered slight damage during the transportation to the shake table, due to a minor deflection of the steel foundation and despite the vertical pre-compression applied to the walls for this operation. Airline cracks have been surveyed associated with the elongation of the fundamental period of vibration. In particular, the most significant crack developed at the base of the CS central pier of the North façade (P2, as identified in Figure 3.8), starting from the bottom edge of the window. Other minor cracks have been observed on the plaster layer of the southern CS façade (spandrel between P6 and P7 and at the base of P5). Finally, some horizontal cracks, with the associated loss of the cohesion bond between the upper mortar bed-joint and the RC slab, appeared at the top of some of the CS piers, particularly visible in the walls with the plaster layer (see Figure 3.10a). The same horizontal cracks have been noticed on top of the outer clay longitudinal walls. The failure of the mortar bed-joint interface between the top of the clay piers and the timber plate caused the premature loss of the stiffening contribution effect of the clay walls in the longitudinal sway direction. The cavity ties were indeed not sufficient to ensure their collaboration to the longitudinal direction of motion causing a partial isolation of the North and South clay façades. This level of distress was classified as  $DS_2$ . Clear relative displacements were measured between the timber plate and the top of the clay longitudinal walls (potentiometers #10, 11 and 14) starting from initial stages of testing. Figure 3.10 shows pictures of the surveyed damage, while Figure 3.8 and Figure 3.9 illustrate the evolution of the crack pattern on the CS walls (from the inside) and on the outer clay walls (from the outside) throughout the entire testing sequence. At the end of each stage of the shake table testing sequence, detailed surveys were carried out for reporting every possible evidence of damage having affected the structure. Although the slight structural damage suffered by the building prototype during the transportation phase (classified as  $DS_2$ ),  $DS_0$  and  $DS_1$  have been identified analysing the damage observed after the firsts stages of testing.

The first damage (crack width of 0.2 mm) associated with a shake table motion appeared on the plaster layer of the spandrel between piers 5 and 6 in the South CS wall, during test FEQ1-100% ( $H-PTA=0.119$  g, see Figure 3.10b). Therefore,  $DL_0$ , defined as the maximum achieved level of displacement with no visible seismic damage (structural or non-structural), was identified with the peak floor drift equal to 0.04% achieved during FEQ1-50% ( $H-PTA=0.056$ g) which did not cause any damage.

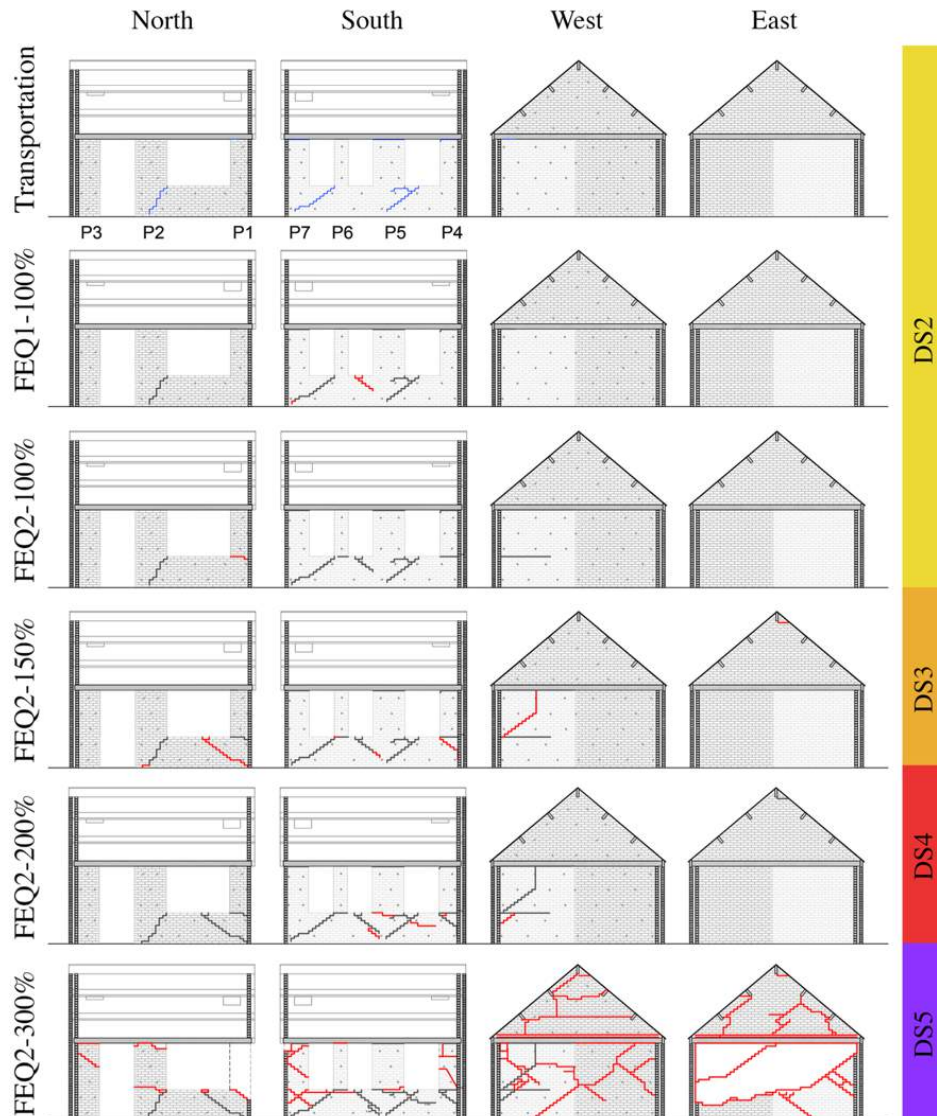


**Figure 3.8 Damage evolution: views of the inner CS walls from the inside; in light grey the walls covered with a plaster layer. Cracks observed after transportation are shown in blue, cracks reported at the end of the considered test in red while cracks formed in previous tests in black.**

During test FEQ1-150% ( $H-PTA=0.146$  g), two horizontal cracks with a negligible width developed at the base of the CS piers 4 and 6 of the South wall, associated with the activation of a flexural/rocking behaviour. The crack at the base of pier 4 continued horizontally, for a length of approximately 1 m, in the transverse CS wall of the West side, probably due to a sort of flange effect. DL1, defined as the maximum achieved level of displacement with no visible structural damage was identified at the end of this stage with a peak floor drift experienced by the specimen equal to 0.11%; the northern wall (without plaster) did not show any further damage, reason why the surveyed damage was

considered limited only to the specimen finishing. This damage pattern did not change during tests FEQ2-50%-C and FEQ2-50% ( $H-PTA= 0.137$  and  $0.095$  g).

Another crack, due to a flexural/rocking behaviour, was surveyed at the base of pier 1 of the North wall at the end of test FEQ2-100% ( $H-PTA= 0.218$  g, see Figure 3.10c). This level of distress, attained at a floor drift equal to  $0.13\%$ , was associated with DL2 (*i.e.* maximum achieved level of displacement with minor/slight structural damage).

The FEQ2-150% test ( $H-PTA= 0.380$  g) caused the development of new cracks and the elongation and widening of the pre-existing ones; a 1 mm stepped diagonal crack appeared on the spandrel between piers 1 and 2 of the North CS wall; a small crack at the top corner of the clay pier 3 and a slight detachment of the wood planks caused by the uplift of the East gable were observed (see Figure 3.10d). The attained peak floor drift of  $0.30\%$  was considered as DL3, the maximum achieved level of displacement with moderate structural damage (but still repairable).

DL4, defined as the maximum achieved level of displacement with extensive structural damage (*i.e.* not repairable), was reached during test FEQ2-200% ( $H-PTA = 0.393$ g) with a recorded peak floor drift displacement of  $0.59\%$ . A further widening of the existing crack pattern was noticed at the end of the test with the accumulation of residual displacements on the pre-existing cracks (see Figure 3.10e); new horizontal cracks with negligible width were observed in the plaster of pier 5 and spandrel between piers 4 and 5 of the South CS wall. A slight detachment of the timber plate was noticed in the South-West corner (Figure 3.10f). Despite a clear rocking behaviour of the gable walls, evident from the displacement histories recorded by the installed displacement transducers, no visible cracks were detected on them.

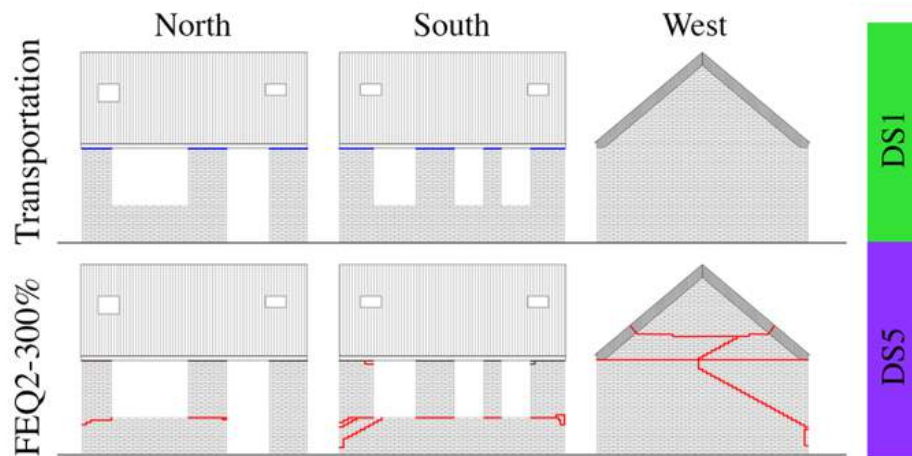


**Figure 3.9 Damage evolution: views of the outer veneer walls from the outside. Cracks observed after transportation are shown in blue, cracks reported at the end of the considered test in red.**



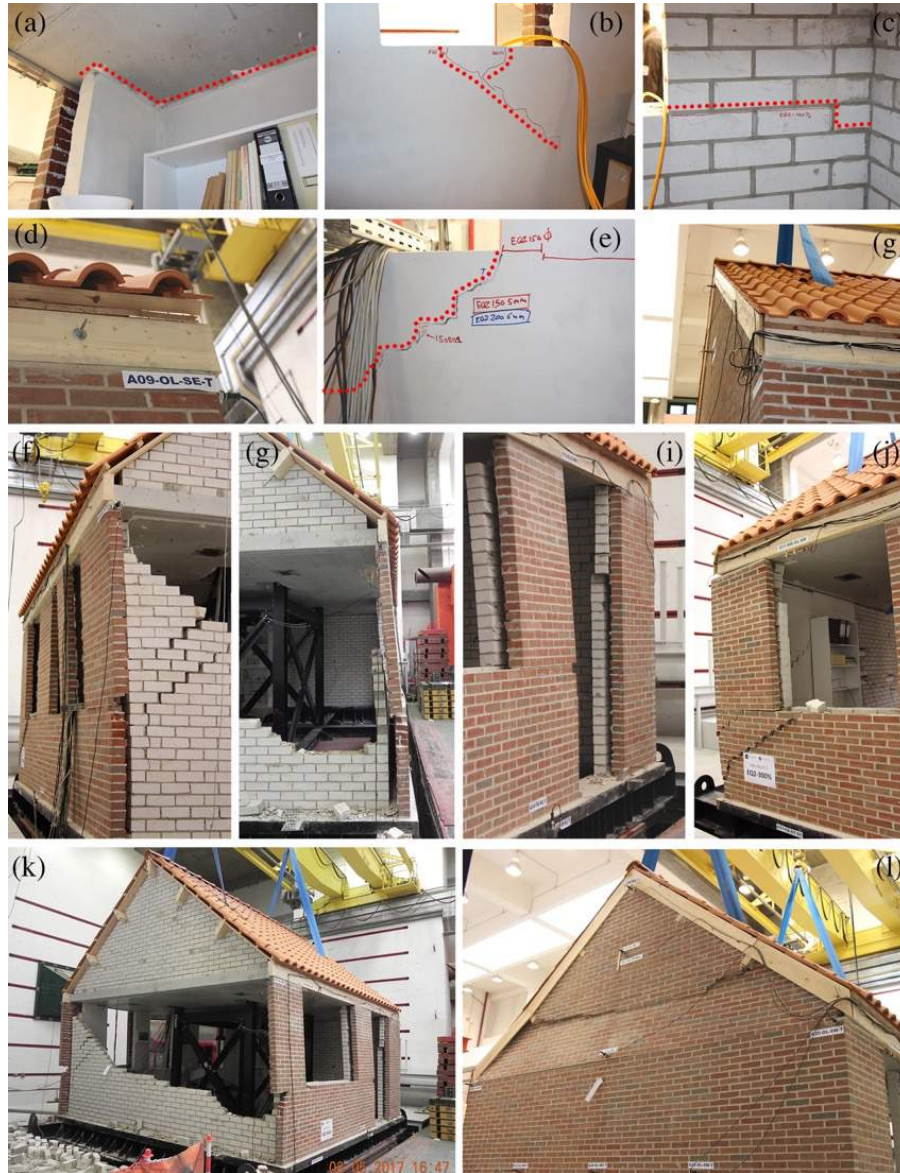


**Figure 3.10** Pictures of the observed damage: (a) top horizontal crack at the SW corner (transportation phases), (b) first crack on the plaster layer (FEQ2-100%), (c) first flexural crack on the N CS wall, (d) detachment of the timber planks of the SE corner (FEQ2-150%), (e) elongation of pre-existing crack width in the spandrel between piers 6 and 7 (FEQ2-200%), (f) slight detachment of the timber profile in the SW corner (FEQ2-200%); pictures of the specimen at the end of the FEQ2-300% test: (g) SE, (h) NE, (i) NW and (j) SW corners. General views of the damaged building prototype (k,l).

The (partial) collapse of the specimen prototype and consequently DL5 was attained at a peak floor drift of 4.43% during test FEQ2-300% ( $H-PTA = 0.630$  g) exhibiting a rather fragile behaviour of the panel failing OOP. The pronounced rocking mechanism developed by the slender longitudinal piers and the vertical input motion on the prototype led to an uplift of the RC slab, causing a loss of restraint at the top of the East CS

transverse wall, which failed out-of-plane. The collapse of the East wall was accompanied by very severe damage (*e.g.* P7) and collapses (*i.e.* P1) in the longitudinal piers, comprising expulsion of materials and large residual displacements in both longitudinal and transverse directions (out of plumb higher than 50mm, see Figure 3.10h,i). As a result, the RC slab was precariously in equilibrium on the SE and NE corners outer clay walls not intended to be loadbearing. Severe damage occurred in the West CS transverse wall due to the interaction between the displacement drift imposed by the floor and the out-of-plane actions induced by the wall's inertial forces and the outer veneer wall (*e.g.* pushing and pulling the wall by means of the steel ties). Cracks have been observed on both East and West CS gable walls, in particular close to the L-shaped steel anchors. The surveyed damage demonstrates the achievement of a near-collapse DS. Regarding the performance of the outer veneer wall, no significant damage (other than that occurring during transportation) was observed up to test FEQ-300%. Consequently, its level of damage passed from a DS1 after transportation to a DS5 after test FEQ-300%. Large relative displacements between the two leaves were measured (similarly in [9]), even at earlier stages of testing. During the testing stage where the specimen reached a partial collapse, horizontal cracks were surveyed at the base of all longitudinal piers, a clear sign of rocking/sliding behaviour. The crack pattern surveyed on the West wall shows both the rocking mechanism of the system gable walls and roof and the triggering of a global pull-out/push-in of the veneer wall which is not directly connected to the slab. The experience gained after analysing the seismic response of two full-scale terraced houses allowed for the definition of proper threshold limits in terms of floor drift for the identification of damage states. One of the drawbacks of dynamic tests is the impossibility of continuative visual monitoring of the damage, therefore damage states can only be defined between a finite number of tests [36]. Table 3.5 compares experimental (EUC-BUILD-1 and LNEC-BUILD-1) and analytical damage limits as proposed by [35][37]. Proposed values are thresholds for a classification of the possible damage state experienced by this building typology according to the exhibited floor drift. They represent an approximation to the nearest 0.05% of the higher between experimentally observed values. For example, the proposed DL4 is an approximated upper bound of experimental ones since LNEC-BUILD-1 might remain in DS4 also for larger values of floor drift as in EUC-BUILD-1. In general, there is a very good agreement between the damage thresholds defined based on the experimental observations and those proposed in literature. Only the collapse-prevention limit, DL4, is underestimated by both criteria. This may be due to the fact that the analytical approaches take into account a possible shear failure, (*e.g.* [35] refers to [38]), while the response of both buildings is dominated by flexural/rocking behaviour, typically associated with a higher displacement capacity [6].

**Table 3.5 Comparison of experimental and theoretical damage limits proposed by [35][37] in terms of floor drift values.**

	<i>DL0</i>	<i>DL1</i>	<i>DL2</i>	<i>DL3</i>	<i>DL4</i>
Calvi [35]	-	0.1%		0.3%	0.5%
Lagomarsino & Cattari [37]	-	0.05-0.1%	0.15-0.3%	0.35-0.5%	0.55-0.7%
EUC-BUILD-1 [9]	-	0.07%	0.12%	0.34%	0.88%
LNEC-BUILD-1	0.04%	0.11%	0.13%	0.30%	0.59%
<b>Proposed Terraced House</b>	<b>0.05%</b>	<b>0.10%</b>	<b>0.15%</b>	<b>0.35%</b>	<b>0.90%</b>

### 3.4.3. Analysis of the dynamic behaviour of the structure

The response of this structure is strongly affected by the dynamic behaviour of the masonry flange systems composed by the load-bearing transverse wall and interlocked return piers. These systems are represented by the CS transverse wall connecting pier 1 to pier 7 in the East side of the building and by the CS and clay walls connecting to piers 3 and 4 and coupled by ties. The ties system, despite its inefficiency of coupling the leaves when subjected to in-plane excitation [29], ensured compatibility of horizontal displacements in the OOP direction. In other words, as expected by design, they were able to transmit mainly axial forces.

The presence of several transducers monitoring slippage between the top of longitudinal walls (both CS and clay) and the RC slab (timber plate in case of clay walls) allowed for the determination of the displacement histories of several longitudinal walls including those connected to transverse walls; a significant sliding phenomenon of the RC slab on top of the piers was thus able to be observed. Figure 3.11a compares the floor horizontal displacement history of FEQ2-150% and FEQ2-200% tests with those of the eastern CS flange (computed by means of potentiometer #12) and of the western clay flange (computed with potentiometer #11 in Figure 3.6). As the simplified scheme in Figure 3.11c shows, both flanges tend to displace only in the outward direction exhibiting zero displacement in the building inward direction. This asymmetric response is due to the characteristic of a flange system, presenting considerably higher stiffness in the inward direction due to the higher overturning resisting moment governed by the weight of the transverse wall and the additional stiffness of the in-plane return walls. In the outward direction, the out-of-plane deformation of the transverse wall leads to the uplift of the adjacent piers. The dynamics of the flange system was associated with sliding of the RC slab (see Figure 3.11c), particularly visible during FEQ2-200% when a clear differential residual displacement of the floor and the eastern flange was observed (Figure 3.11b).

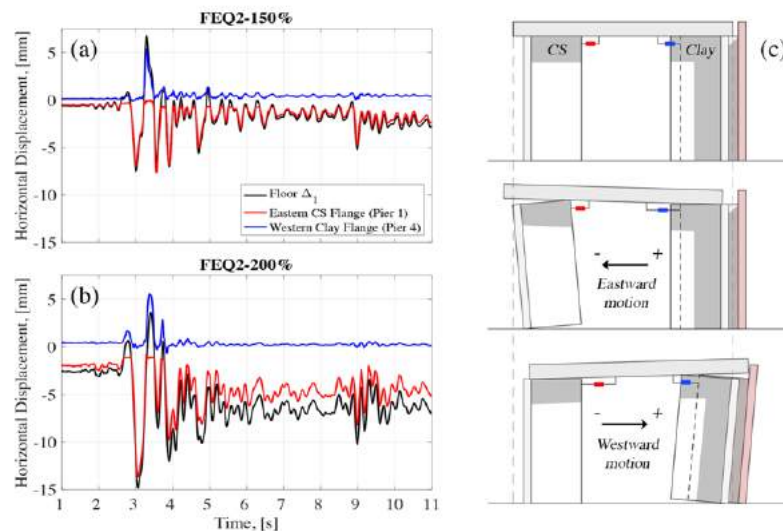


**Figure 3.11** Horizontal displacement histories of the two flange systems for: FEQ2-150% (a) and FEQ2-200% (b); schematic representation in section of the flange system motion (c); for simplicity, the presence of further longitudinal in-plane piers is neglected.

### 3.4.4. Performance of building furniture

This experimental test presented also the chance to investigate the performance of building finishes (*e.g.* the plaster layer) and non-structural building components such as common furniture. Figure 3.12a illustrates the different equipment installed in the building prototype: bookshelf anchored to the wall, bookshelf not anchored to the wall (total weight of approximately 40 kg each), ground lamp, table with flowerpot and table lamp, table with notebook, painting on the out-of-plane wall, paintings on the in-plane walls, and ceiling light. The building furniture did not show any damage until test FEQ2-200% (H-PGA= 0.39 g and V-PGA= 0.18 g); whereas it experienced significant damage during test FEQ2-300% (H-PGA= 0.63 g and V-PGA= 0.34 g) with the overturning of the bookshelf not anchored to the wall (see Figure 3.12b-c).



Figure 3.12 Pictures of the building furniture: (a) before testing, (b, c) after FEQ2-300% test.

### 3.4.5. Hysteretic Response

The evolution of the specimen's hysteretic response is shown in Figure 3.13, in terms of base shear,  $V$ , versus first-floor drift,  $\theta_1$ , which takes into account the residual displacements. The base shear history has been computed as the sum of the products of each acceleration recording times the tributary mass of the corresponding accelerometer. Masses are assumed to be lumped at the accelerometer locations. In particular, the mass of the masonry components from the foundation level to the mid-height of the ground floor (at 1.22 m from the base) was assigned to the ground floor (and hence multiplied by the base acceleration history).

The base shear coefficient,  $BSC$ , is defined as:

$$BSC = \frac{V}{M \cdot g} \quad (1)$$

where  $M \cdot g$  is the total weight of the specimen.

In each plot of the hysteretic response, the preceding tests are reported in grey. The white markers represent the positive and negative peak force responses with the corresponding displacements while black markers indicate peak displacements with the associated base shear values. Similarly to EUC-BUILD-1, no appreciable stiffness degradation is detectable up to FEQ2-150%. In test FEQ2-300%, the displacement and base shear



histories have been truncated at the instant of the peak floor horizontal displacement ( $\theta_1 = -4.43\%$ ) corresponding to the complete development of the OOP mechanism and the loss of equilibrium of the East wall. The dynamic force-displacement backbone curve (Figure 3.13h) can be obtained by connecting the peak points of the experimental curves. In other words, it is defined as the plot of the maximum resisted base shear,  $V_{max}$  or  $V_{min}$ , and the corresponding first-floor drift depurated from residual displacements,  $\theta_{1,nr}$ , for each stage of testing (*i.e.* the floor displacement starts from zero at each test stage). The last points of both the positive and negative branches were obtained as local peaks and maximum drift attained and the corresponding base shear.

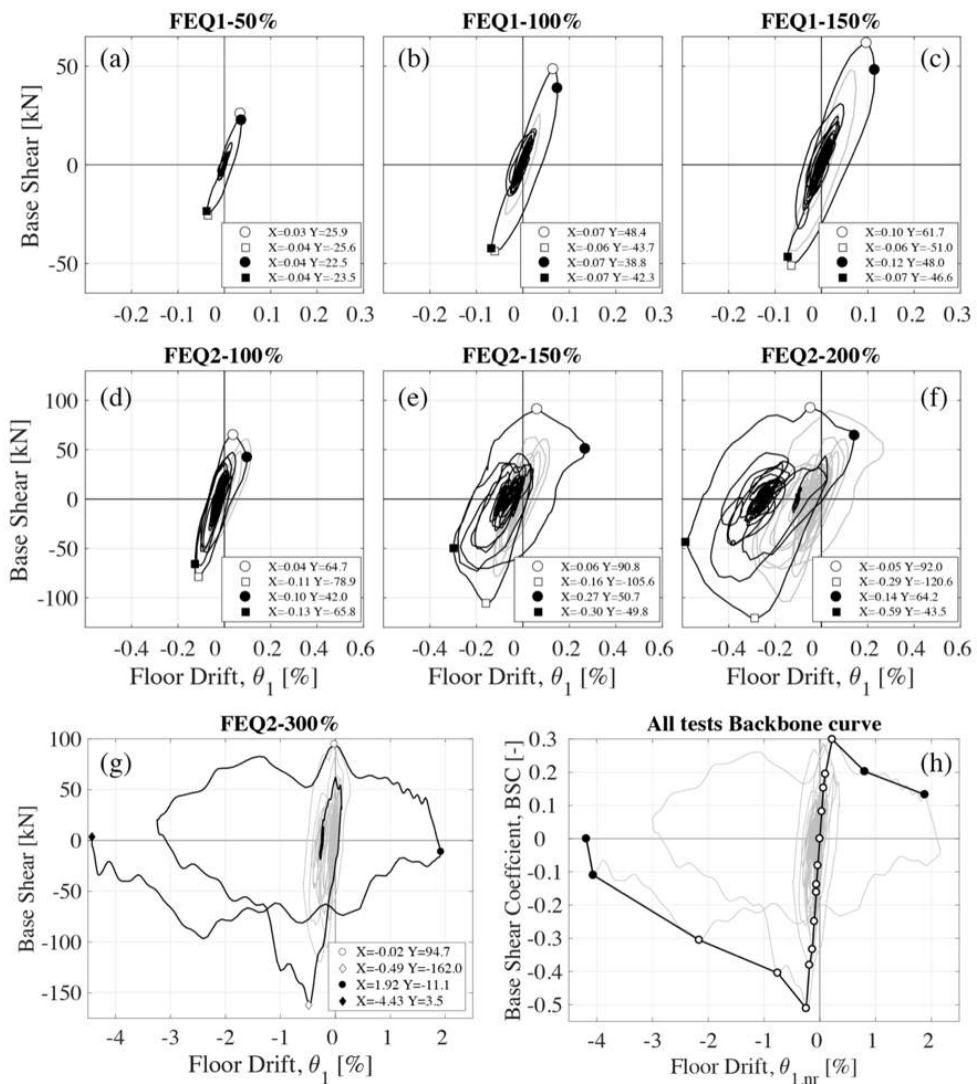


**Figure 3.13 Evolution of the global hysteretic response in terms of base shear versus first-floor drift ratio: from FEQ1-50% to FEQ2-200% adopting the same proportion between the two axes in all the plots (a-f), FEQ2-300% (g); Backbone curve in terms of base shear coefficient (h).**

The larger base shear value occurred for sway towards the negative direction (towards the single-leaf side, South). In particular, the base shear attained for southward motion ( $V_{min} = -162.0$  kN), corresponding to a  $BSC_{max}$  equal to 0.51, was 42% higher than the force reported for motion towards the double-leaf side of the structure ( $V_{max} = 94.7$  kN,  $BSC = 0.30$ ). The asymmetry in the envelope response curve can be attributed to the westward “spike” of the applied input and to the asymmetry of the structure.

### 3.4.6. Response of the roof structure

The large deflections observed in the roof of EUC-BUILD-1, were one of the reasons that drove the decision to stop that test. Graziotti *et al.* [9] recognized that this roof typology represents a highly flexible substructure composed of masonry gables and timber diaphragm in which the L-shaped connectors ensure compatibility of displacement between the different elements. Therefore, the lateral resistance is provided by the typical non-linear rocking behaviour of the masonry gables together with the highly dissipative timber diaphragm force-displacement behaviour [39].

The hysteretic response of the roof throughout the different test stages is illustrated in Figure 3.14, in terms of roof base shear,  $V_R$ , versus roof diaphragm drift,  $\gamma_R$ . The roof base shear was computed as the sum of the products of each acceleration recording multiplied by the tributary mass of the corresponding accelerometer, considering the total mass of the roof (6.5 t). This inertial force represents the total shear force transferred by the roof to the floor differing from the roof force in [9],  $F_R$ . This latter force represented an estimate of the non-linear roof-to-floor recentring force computed by multiplying a lumped mass of 2.6 t by the ridge beam acceleration. The roof diaphragm drift is instead the diaphragm shear deformation computed as the relative ridge displacement, with respect to the RC slab, divided by the inclined length of the roof pitch,  $L_R = 3.61$  m.

The force-displacement responses display no indication of strength degradation and the wide hysteretic loops confirm that the roof diaphragm is capable of dissipating a considerable amount of energy. The peak roof base shear,  $V_{r,min} = -31.7$  kN, was attained during test FEQ2-300% for eastward motion, 24% higher than the maximum value attained for sway towards the West ( $V_{r,max} = 25.3$  kN); the peak diaphragm drift attained in the East and West directions were  $\gamma_{r,min} 1.92\%$  and  $\gamma_{r,max} 1.48\%$  corresponding to roof relative displacements of  $\delta_{r,min} = 69.3$  mm and  $\delta_{r,max} = 53.3$  mm, respectively.

The dynamic force-displacement backbone curve (shown by Figure 3.14) can be obtained by connecting the peak points associated with the first main cycle of the experimental curves. The diaphragm shear deformation is here calculated from the relative ridge displacement (with respect to the floor) by removing the residual displacements. Figure 3.14 shows also hysteretic behaviour and backbone curve EUC-BUILD-1 roof. Solid dots represent local peaks and maximum drift attained by the roof system.

Although the two systems had the same geometry, their overall responses differ in terms of dissipated energy and backbone curve; the equivalent viscous damping values (EVD) of the peak diaphragm drift cycle, according to Jacobsen approach [40], are 34% and 55% for EUC-BUILD-1 and LNEC-BUILD-1, respectively. This difference could be attributed to the different workmanship of the builders, the mechanical properties and typology of the timber sheeting as well as their positioning and connection with the beam system. In the EUC-BUILD-1 roof the timber planks were continuous along the entire inclined length whereas in the LNEC roof they covered 1/3 and 2/3 (alternated, see Figure 3.4d) of the total length, resulting in a higher number of nailed connections. Moreover, in LNEC-

BUILD-1 the horizontal wood profiles allowing for the positioning of the tiles were directly nailed on the planks providing some constraint to the diaphragm shear deformation whereas in the EUC-BUILD-1 they were nailed on a second level of vertical profiles.

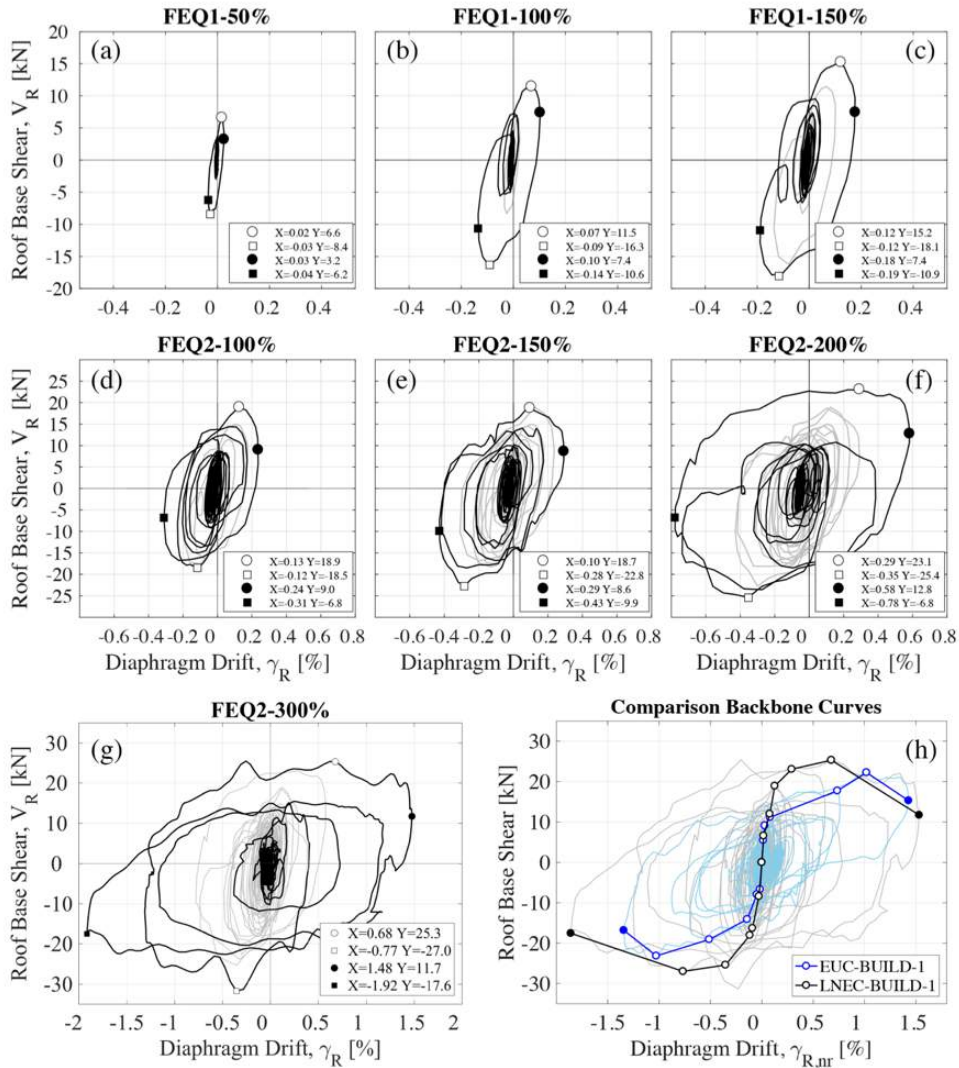


**Figure 3.14 Evolution of the roof hysteretic response in terms of roof base shear versus diaphragm drift ratio: from FEQ1-50% to FEQ2-200% adopting the same proportion between the two axes in all plots (top), FEQ2-300% (bottom left); Backbone curve (bottom right); Comparison between hysteresis and backbone curves of EUC-BUILD-1 and LNEC-BUILD-1.**

The lower strength of the EUC-BUILD-1 roof was also related to the different boundary condition at the base of the clay gable wall; in the EUC\_BUILD-1 roof its contribution to the lateral resistance might be compromised by the fact that it stood on a more flexible two-storey clay wall, connected to the load-bearing structure only by means of the ties

system. This seems further confirmed by the fact that the strength envelopes of the two roofs converge towards one another at a higher level of displacements when the P-delta effect significantly reduces the gables recentring force. The initial stiffness of both roof structures was, instead, close to 10.6 kN/mm in both directions.

#### 3.4.7. Two way bending out-of-plane collapse

The partial collapse of the structure was induced by the pronounced in-plane rocking behaviour of the slender longitudinal walls which caused a significant uplift of the rigid slab leading to the loss of restraint and axial load transfer to the connection with the top of the East CS transverse wall (see Figure 3.15a). The lack of top restraint, coupled with high input accelerations and the reduced-to-zero overburden pressure, dramatically increased the transverse wall vulnerability. This allowed for the development of a two-way bending out-of-plane mechanism of the undamaged East CS wall (see Figure 3.15b,c). Figure 3.15a illustrates a frame of the video taken during the specimen partial collapse showing the East wall deflecting in two-way-bending supported only at the base and at the two vertical edges. At this particular instant, slab and roof substructure are entirely supported by the longitudinal piers (unloaded in static conditions). This axial load transferring from the transverse wall to the longitudinal piers increases their lateral strength capacity; however, this may not be an actual benefit in terms of global behaviour due to the higher OOP vulnerability of the transverse wall. In other words, without a load redistribution, the building would have a higher capacity in terms of displacement associated with a lower capacity in terms of shear strength. On the other hand, the redistribution of the vertical load is increasing the maximum lateral strength of the structure decreasing the ultimate achievable displacement due to the premature OOP collapse.

When the vertical uplift at the two corner supports on the two longitudinal sides (North and South) is higher than the slab deflection at the mid-span point, the transverse walls can be considered completely detached from the RC slab, *i.e.* with the top horizontal edge free of any restraint. An estimate of the maximum deflection of the slab along East edge, assuming the diaphragm supported by the two “rocking” longitudinal piers (*i.e.* P1 and P7) and along the West edge is 4.7 mm. This value is close to the one assuming the slab deflecting as a simple beam spanning in the transverse direction between the two piers (5.0 mm).

Unfortunately, the slab vertical displacements and the relative displacements between the slab and the top of the transverse walls were not directly monitored. For the collapse test, these quantities were derived by means of two different techniques: the double integration of vertical acceleration records and analysis of the video adopting a dedicated software [41]. The good match between the vertical relative displacements computed in these two ways gave a relatively good degree of confidence to the accuracy of the aforementioned vertical displacement time histories.

Figure 3.16a illustrates the vertical displacement of the slab together with the floor and the flange systems horizontal displacement time histories relative to the foundation. The OOP-excited East-wall mid-height displacement (MHD) time history until its overturning is plotted as well. Similar to what was observed in previous tests (Figure 3.11a-b), for negative displacement the East-flange displays together with the slab with a sliding phenomenon limited to 6 mm. The complete positive displacement history was not recorded due to the saturation of the potentiometer #12; this indicates a large sliding

between slab and East-flange in this direction. The specular phenomenon was observed in the West-flange subjected to negative displacement.

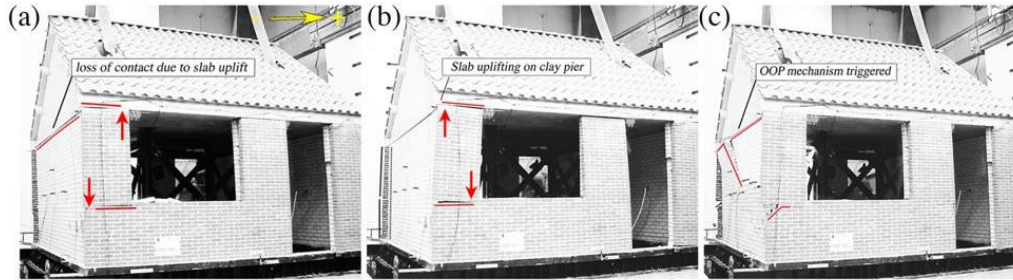


**Figure 3.15** Frames of the E-wall collapse during FEQ2-300% test: first negative response peak (a), positive response peak (b), triggering of the failure mechanism (c).

The peak slab vertical displacements of the NE corner are also shown in Figure 3.16a. Given the flange motion mechanism (previously described and not uplifting the floor), the uplift of approximately 25 mm observed for positive displacement of the structure (towards West) indicates that the floor vertical displacement was entirely due to rocking of the external clay piers (Figure 3.15b). Consequently, the wall was not restrained on top also for positive displacement leading to a possible development of a two-way bending mechanism also in the inward direction. In the transition phase (*i.e.* displacements close to zero), the East-wall may have been subjected to some slab-to-wall dynamic impacts (horizontal and/or vertical) which may have further damaged the panel and compromised its stability.

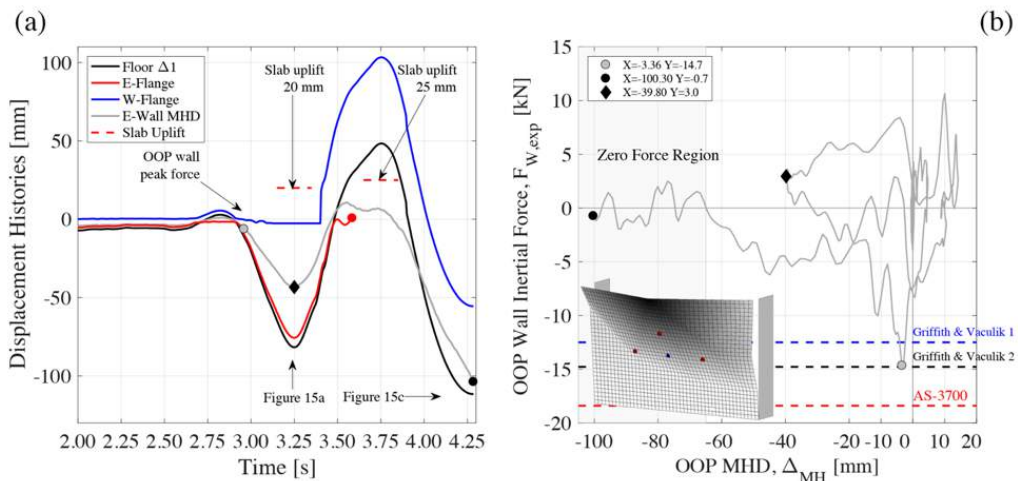


**Figure 3.16** Horizontal displacement histories of eastern and western flanges, floor and mid-height East wall (a); inertial force of the East wall during FEQ2-300% (b). 3d view of the observed failure mechanism and position of accelerometers (the blue dot was also monitored with a wire potentiometers)

The identification of the instant at which the OOP mechanism is triggered is not an easy task, nevertheless the four accelerometers installed on the specimen allowed for the determination of the wall's inertial force time history; this force can be determined as the

sum of the products of the acceleration recorded on the wall times their tributary mass (location of accelerometers shown by the wall scheme in Figure 3.16b). The wall's inertial force is plotted against the OOP East-wall MHD in Figure 3.16b. The peak wall force is 14.7 kN, associated with a MHD of 3.36 mm (relative to the table), while the maximum inertia force is not necessarily associated with the activation of the complete OOP mechanism [8].

As a first approximation, given the non-symmetrical flange deflection, the OOP MHD of the transversal wall may represent a pure OOP displacement only in the positive direction. In the negative direction, all the flange is participating in the motion, not allowing a direct measure of the net OOP transversal wall deflection. The maximum inertial force sustained by the wall is in very good agreement with the two-way bending strength calculated using the virtual work method codified by AS 3700 [42] and implementing the moment capacity equations proposed by Griffith and Vaculik [43] for a wall un-restrained on top (see Table 3.6). Two calculations were performed applying Griffith and Vaculik's equations using the torsional strength as proposed by Willis [44] ( $GV1$ ,  $\tau_{tor} = 1.6 \cdot f_w + 0.9 \cdot \sigma_v = 0.73 \text{ MPa}$ ) and the one directly correlated with direct shear tests ( $GV2$ ,  $\tau_{tor} = 1.86/0.81 \cdot f_{v0} + 1.2 \cdot \sigma_v = 1.23 \text{ MPa}$ ). In the latter case, the torsional strength of the specimen was estimated considering a linear proportion between the experimental direct shear strength obtained from mechanical characterisation and the results of torsional tests and direct shear tests reported in [8] for the same CS masonry typology.

Sharma *et al.* [45], conducting shake table tests on U-shaped full-scale URM CS specimens with top support kept free (similar configuration of the collapsed wall), observed very similar strengths for two identical specimens: the first one subjected to combined vertical and horizontal input, the second one only to horizontal excitation. For this reason, the assessment procedures were applied neglecting the vertical acceleration contribution assuming a static acting axial load configuration.

**Table 3.6 Analytical prediction of out-of-plane two-way bending peak strength according to Griffith and Vaculik [46] and AS 3700 [42] for different boundary conditions. Comparison in terms of wall shear coefficient (WSC) and wall's inertial force (F).  $GV1$  and  $GV2$  adopt Griffith and Vaculik's equations using the torsional strength as proposed by Willis and those correlated with direct shear tests.  $AS$  stands for the code AS 3700.**

<i>OOP wall boundary conditions</i>	$\sigma_v$ [MPa]	$WSC_{GV1}$ [-]	$F_{GV1}$ [kN]	$WSC_{GV2}$ [-]	$F_{GV2}$ [kN]	$WSC_{AS}$ [-]	$F_{AS}$ [kN]	$WSC_{exp}$ [-]	$F_{exp}$ [kN]
<i>4 edges restrained (static condition)</i>	0.16	0.94	21.5	1.12	25.5	1.14	26.1	0.64	14.7
<i>3 edges restrained (dynamic condition)</i>	0	0.54	12.5	0.65	15.0	0.81	18.4		



After the first cracking, the wall decreased its lateral capacity showing almost zero lateral resistance (evident beyond 60 mm of MHD displacement). This fragile behaviour has also been observed in shake table tests carried out by Graziotti *et al.* [8] on CS and clay URM walls subjected to two way bending seismic excitation.

The observed failure mechanism highlights the importance of considering eventual variations of the structural elements' boundary conditions (*i.e.* acting axial load and restraints) in assessing their seismic performance, especially for OOP mechanism. This concept was already pointed out by [47][48]. The latter investigated the interaction of in-

plane and one-way-bending out-of-plane walls, as well as the influence of boundary conditions. Both experimental and numerical works showed that the largest deformations occur when the vertical bearing at the top of the wall is not vertically fixed, since the arching effect is lost due to the lack of axial load. In a building with characteristics similar to the tested one (*i.e.* rigid diaphragm supported by slender walls, light roof), the importance of considering actual boundary conditions is crucial. Their definition based on an un-deformed static analysis may lead to un-conservative predictions (as shown in Table 3.6). In this specific case the overestimation in terms of wall inertial force is approximately 50% and 80% for the methodology proposed by Griffith and Vaculik and AS3700, respectively.

This experimental work suggests that the assessment of the OOP performance of the transverse wall may be conducted by considering a free top horizontal edge and zero acting axial load beyond a certain value of in-plane global or local drift of the slender walls. These drift values are strictly connected to the piers' uplift and consequently to the unit-width slab vertical deflection as shown in Table 3.7. The deformation check on the floor drift or, alternatively, the one on the element drift could be considered as a threshold for the OOP assessment of the transverse wall. If the proposed value is exceeded, the vertical overburden stress on the top of the face-loaded-excited wall is likely to be null. This is generally associated with the loss of wall top restraint.

**Table 3.7 Floor and element drift limits for the assessment of the OOP performance of transverse walls.**

<i>Check on the floor drift <math>\theta_i</math></i>	<i>Alternative check on the element drift <math>\theta_{i,el}</math></i>	<i>Assessment of the OOP panel</i>	<i>OOP panel boundary conditions</i>
$\theta_i < \frac{h_p}{l_p \cdot h_i} \cdot r_{hv} \frac{5}{384} \frac{q_f \cdot l_f^4}{E_f \cdot I_f}$	$\theta_{i,el} < \frac{r_{hv}}{l_p} \frac{5}{384} \frac{q_f \cdot l_f^4}{E_f \cdot I_f}$	4 edges restrained $\sigma_v$ in static condition	
$\theta_i > \frac{h_p}{l_p \cdot h_i} \cdot r_{hv} \frac{5}{384} \frac{q_f \cdot l_f^4}{E_f \cdot I_f}$	$\theta_{i,el} < \frac{r_{hv}}{l_p} \frac{5}{384} \frac{q_f \cdot l_f^4}{E_f \cdot I_f}$	3 edges restrained $\sigma_v = 0$	

where  $h_p$  and  $l_p$  are effective height and length of the in-plane piers,  $h_i$  is the storey height,  $r_{hv}$  is a ratio between rigid uplift of the piers (*e.g.* the pier in-plane drift multiplied by the pier length) and the experimentally observed one. The outcomes of in-plane cyclic tests on CS specimens subjected to similar axial overburden pressure suggested a value of 1.4 [6]. All the remaining parameters ( $E_f$ , concrete elastic modulus,  $I_f$ , unit-width moment of inertia,  $q_f$ , load per unit length and width and  $l_f$  span length) are related to the calculation of the floor peak deflection computed as in the case of a simple beam spanning in the transverse direction. Note that in cavity wall buildings hollow core slabs are also widely used, in this case larger deflections are expected. Moreover, the vertical component of acceleration might affect the mid-span deflection and consequently the loss of overburden stress in the wall. Further studies may be conducted to investigate this specific phenomenon.

In this specific case, assuming a ratio  $h_p/l_p$  as average between the ratio observed in P1 and P7 (equal to 2.36 with  $h_1/l_1=1.62/0.66=2.45$  and  $h_7/l_7=1.72/0.76=2.26$  according to

the crack pattern) and a mid-slab deflection of 4.7 mm, the threshold floor drift value is equal to 0.63% ( $f \cdot r_{hv} \cdot h_p / l_p / h_i = 4.7 \cdot 1.4 \cdot 2.36 / 2440$ ) corresponding to an in-plane element local drift of 0.91% ( $f \cdot r_{hv} \cdot h_p / l_p / h_p = 4.7 \cdot 1.4 \cdot 2.36 / 1675$ ). This latter threshold value may occur before the attainment of the maximum deformation capacity of the in-plane elements computed according to the flexural in-plane local drift capacity of 1.20% (C.4.2.2 of [49] considering a fixed-fixed configuration for P1 and P7) and 1.25% (equation G.37 of [50], assuming fully-loadbearing P1 and P7 piers) prescribed by codes.

### 3.4.8. Building's performance in terms of common EDP parameters

The analysis of data derived from shake table tests allowed for the direct correlation of the physically observed damage with common EDPs such as inter-storey drift ratio (IDR), residual inter-storey drift ratio (RIDR) or peak horizontal and vertical floor and roof accelerations. Figure 3.17 illustrates the evolution of the building's performance in terms of these EDPs. It is worth remarking that the specimen's performance was influenced by initial and progressive accumulation of damage during the entire testing sequence, since the test was incremental. This should be taken into account when a correlation between EDPs and intensity measures (IMs) is formulated. Figure 3.17 reports the building performance in terms of: peak displacements ( $\Delta_I$  and  $\Delta_R$ ); IDR ( $\theta_I$  and roof diaphragm shear deformation  $\gamma_R$ ), usually strongly correlated to the in-plane damage occurring in structural elements like piers and spandrels; and RIDR, very often associated with a general damage and damage accumulation. The response in terms of horizontal ( $H-PFA/H-PTA$  or  $H-PRA/H-PTA$ ) and vertical ( $V-PFA/V-PTA$  or  $V-PRA/V-PTA$ ) floor and roof acceleration amplifications is also shown. These EDPs can be related with the OOP performance of masonry (or, more in general, secondary) components or the damage occurring to acceleration sensitive non-structural components.

The evolution of floor and roof peak horizontal displacements with increasing PTA shows an almost straight line up to test FEQ2-150%. The floor level exhibited a higher flexibility at an early stage of testing when compared to the second floor of EUC-BUILD-1 (probably due to the damage occurred during the specimen transportation and to the door opening). The displacement and IDR associated with the floor,  $\theta_I$ , were systematically lower than those associated to the ridge beam level up to the test FEQ2-200%. In the final test, FEQ2-300%, the failure mechanism involving the East wall led to an increase of the floor IDR up to values beyond 4%. The floor RIDR at the end of the same test was beyond 2%. Regarding the damage on the plaster, it was observed at a first-floor drift of  $\theta_I = 0.07\%$ , whereas the first structural damage induced by the shake table motion occurred at  $\theta_I = 0.13\%$ ; severe damage was observed for values of  $\theta_I$  beyond 0.30%.

The plot of the floor horizontal acceleration amplification,  $H-AMP_I$ , shows a slight decrease, starting from values around 2 in the first tests to values close to 1 in the last tests. Given the observed two-way out-of-plane failure mechanism in the East wall during the FEQ2-300% test, this EDP could be considered as a collapse acceleration for the transverse walls responding on OOP (with only 3 restrained edges). The roof structure ( $H-AMP_R$ ) amplified the ground acceleration by a factor of 3.5 in the first runs; this amplification factor went down to 1.2 in the last test.

The plots of floor and roof vertical acceleration amplifications corresponding to E, W and centre locations did not show any appreciable decrease of amplification. The vertical acceleration amplification ( $V-AMP_{IC}$ ) at the centre of the RC floor was rather high during



the entire testing sequence, with values always beyond 3.3. The amplification at the centre of the ridge beam was instead limited to values around 2. The sudden increase in the accelerations recorded on the E side during the ultimate FEQ2-300% test is due to the impacts between floor and transverse wall described in section 3.4.7.

The evolution of the building's modes and periods of vibration was also analysed for all test phases. In comparison to an ambient vibration dynamic identification performed before moving the specimen onto the shake table, there was an apparent elongation of the periods or reduction in the modal frequencies (from  $T_{1,0} = 0.232$  s to  $T_{1,1} = 0.243$  s). However, this should not be attributed only to the damage in transportation but may be due to other reasons. The first one is that the impulsive response used in the first dynamic identification test (#1 with reference to Table 3.3) on the shake table was much larger than the one for ambient vibrations. In fact, the impulsive motion was reduced in subsequent dynamic identifications in order not to damage the model unnecessarily. The second reason was already mentioned and corresponds to a different dynamic of the specimen on the laboratory floor or on a flexible dynamic system as the shake table. The second dynamic identification test (#3), performed after test FEQ1-50%, and all of the following, used an impulsive motion with half the amplitude of the previous one (i.e. 0.5 mm). For a smaller amplitude, it was verified that one finds relatively lower values of the fundamental periods since the secant stiffness of the specimen is slightly larger (from  $T_{1,1}=0.243$  s to  $T_{1,3}=0.224$  s). Despite the small damage caused by transportation, a general overview of the values obtained for the fundamental mode of vibrations shows that such damage is not reflected in its overall dynamic characteristics.

Figure 3.18 presents the vibration modes, modal frequencies (identified via singular value decomposition) and equivalent modal damping (*EMD*) values for the first 5 modes of vibration associated with the dynamic identification test #3 (after FEQ1-50%). The first vibration mode presents a configuration where the model and the shake table move in phase in the longitudinal direction, while the second mode shows an opposite phase motion between the top of the building specimen, going to one side, and the shake table and base of the model, moving to the opposite side. The third mode is a longitudinal mode also involving some motion of the shake table. The fourth mode is essentially a longitudinal mode with a configuration where the outer walls move in opposite phase with respect to the inner walls. Finally, the fifth mode is again a longitudinal mode, but now involving some vertical motion at mid-span of the ridge beam.

Between the 3<sup>rd</sup> and 6<sup>th</sup> dynamic identification tests (#5, 7, 12) there was no major evolution in the specimen's dynamic properties. After test FEQ2-150%, during the 7<sup>th</sup> dynamic identification test (#14), the fundamental mode reduced to a frequency around 4.2 Hz ( $T_{1,14}=0.24$  s), after keeping a constant frequency around 4.5 Hz in all previous dynamic identifications. Moreover, the modal damping of the first two modes increased significantly, implying a larger energy dissipation in the existing cracks even for very small deformations. It was also apparent from the mode shapes that the inner walls were now moving independently from the outer walls. After motion FEQ2-200%, another important reduction in all initial frequencies was detected: the fundamental frequency reduced to around 3.8 Hz ( $T_{1,18}=0.26$  s), corresponding to a stiffness reduction of about 30% with respect to the initial stiffness.

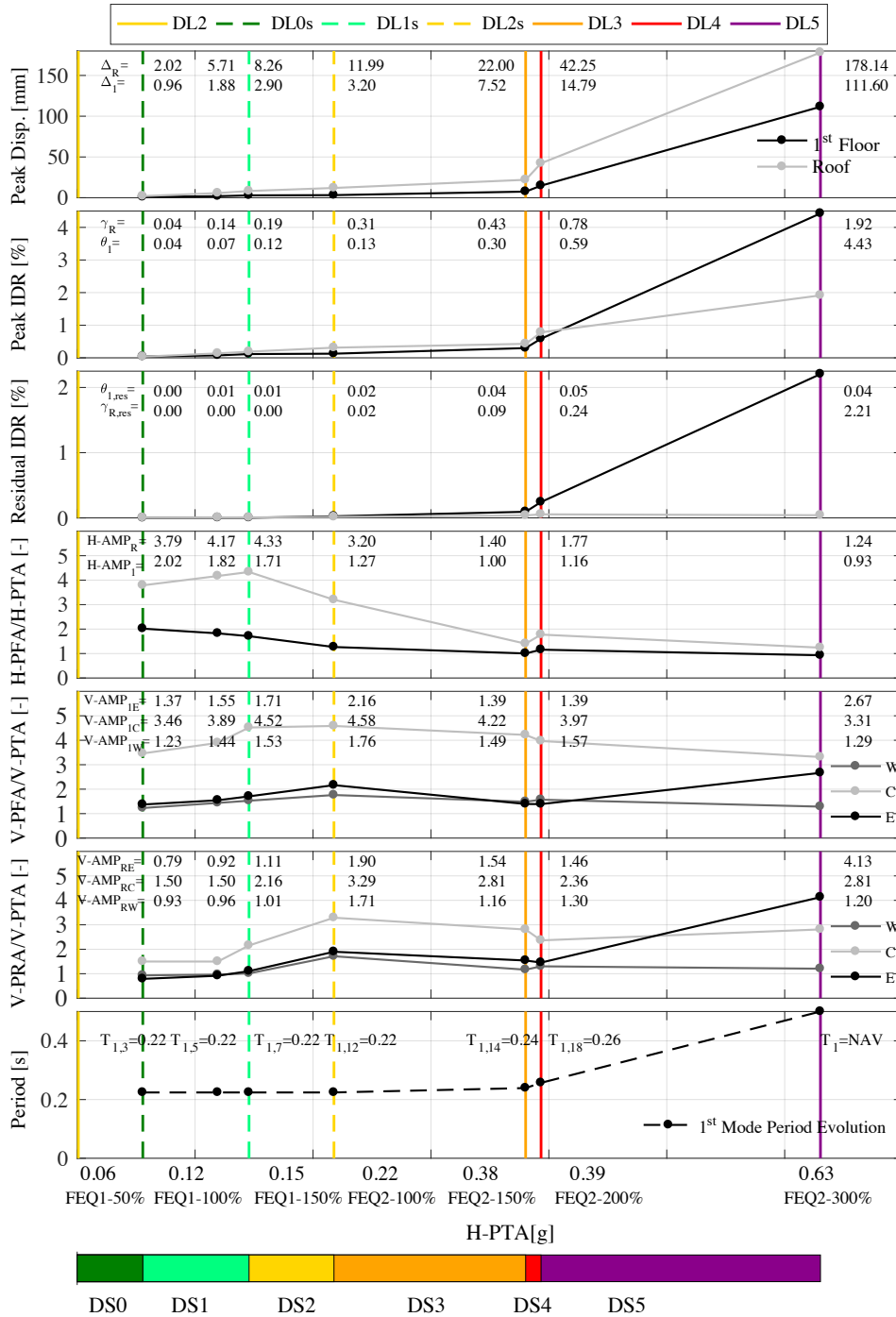


Figure 3.17 Summary of the performance of the building specimen.

The evolution of the fundamental period of vibration of the specimen is also summarised in Figure 3.17. These results show that the dynamic characteristics of the specimen, in terms of its first mode of vibration, were basically unchanged throughout most of the test. A clear degradation of the specimen's dynamic properties only took place during the

application of FEQ2-150%, FEQ2-200% and FEQ2-300%. Besides the degradation of the dynamic properties, the mode shapes also show some significant changes. For instance, the second mode of vibration, whose frequency decreased from 5.83 Hz to 4.64 Hz, clearly presents a sliding motion of the slab with respect to the walls during the last dynamic identification test which is revealing of the damage state attained by the structure [33].

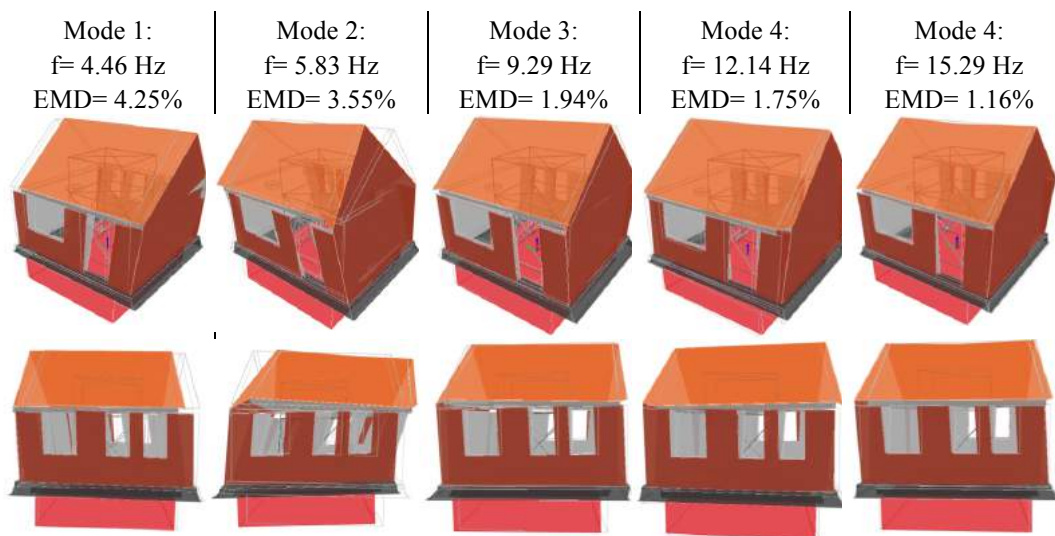


Figure 3.18 Vibration modes and frequencies from the 2<sup>nd</sup> dynamic identification test.

### 3.5. Conclusions

The presented work was part of an extensive experimental campaign aimed at assessing the seismic vulnerability of Dutch URM buildings, exposed in recent years to small magnitude induced seismicity. It presents results of a two-component (horizontal and vertical) shake table test performed on a one-storey full-scale specimen representative of a Dutch URM building with cavity walls and timber roof. The specimen reproduced a sub-structure (*i.e.* the second floor and roof) of another building prototype tested in 2015 by Graziotti *et al.* [9]. While the latter specimen was tested up to a near-collapse condition, the specimen herein described was designed in order to investigate the collapse mechanism of the building prototype. The specimen was subjected to incremental input motions adopting as horizontal component the first-floor accelerograms recorded during the tests performed on the two-storey building tests and following the same testing protocol in order to allow for a realistic comparison between the two experiments.

The structure exhibited a box-type global response up to test FEQ2-200% (horizontal peak table acceleration,  $H-PTA = 0.39$  g) with a first damage surveyed on the plaster layer and a first structural damage observed during test FEQ1-100% ( $H-PTA = 0.12$  g) and test FEQ2-100% ( $H-PTA = 0.22$  g), respectively. The observed damage pattern on the longitudinal walls was typical of flexural-rocking behaviour.

Despite the large flexibility and the consequent vulnerability of the roof system, the partial collapse of the specimen, during test FEQ2-300% ( $H-PTA = 0.63$  g), was driven by the out-of-plane failure of the East wall. The pronounced rocking mechanism developed

by the slender longitudinal piers combined with the vertical input motion led to an uplift of the RC slab causing a loss of restraint at the top of the East transverse wall, making it much more vulnerable to out-of-plane actions. The RC slab, after the failure of the East load-bearing wall, rested, at the end of the test, on the outer veneer wall with a significant residual displacement (beyond 50 mm).

The observed failure mechanism is extremely interesting since it may highlight the importance of considering eventual variations of the structural elements' boundary conditions (*e.g.* acting axial load) in assessing their seismic performance. A first attempt of analytical formulation is proposed to take into account the interaction between the boundary condition of the out-of-plane panel (collapsed in the test) and the uplift of the slab due to flange effect caused by the return walls.

The furniture did not show any damage until test FEQ2-200% ( $H-PTA= 0.39$  g and  $V-PTA= 0.18$  g); whereas it experienced significant damage during test FEQ2-300% ( $H-PTA= 0.63$  g and  $V-PTA= 0.34$  g) with the overturning of the bookshelf not anchored to the wall. All the processed data of the test are freely available upon request at [www.eucentre.it/nam-project](http://www.eucentre.it/nam-project).

### 3.6. Acknowledgements

This paper describes an activity that is part of the project entitled “Study of the vulnerability of masonry buildings in Groningen” at EUCENTRE, undertaken within the framework of the research program for hazard and risk of induced seismicity in Groningen sponsored by the Nederlandse Aardolie Maatschappij BV. The authors would like to thank all the parties involved in this project: LNEC Lab and EUCENTRE Lab, together with NAM, Arup and TU Delft. The useful advice of R. Pinho, are gratefully acknowledged. Special thanks, go also to J. Uilenreef, G. Magenes, A. Penna, H. Crowley, A. I. Marques, M. Mandirola, S. Sharma for their support in the different phases of the experimental campaign.

### 3.7. References

- [1] S. J. Bourne, S. J. Oates, J. J. Bommer, B. Dost, J. Van Elk, and D. Doornhof, “A Monte Carlo method for probabilistic hazard assessment of induced seismicity due to conventional natural gas production,” *Bull. Seismol. Soc. Am.*, vol. 105, no. 3, pp. 1721–1738, 2015.
- [2] H. Crowley, B. Polidoro, R. Pinho, and J. van Elk, “Framework for Developing Fragility and Consequence Models for Local Personal Risk,” *Earthq. Spectra*, vol. 33, no. 4, pp. 1325–1345, 2017.
- [3] H. Crowley, R. Pinho, J. van Elk, and J. Uilenreef, “Probabilistic damage assessment of buildings due to induced seismicity,” *Bull. Earthq. Eng.*, Sep. 2018.
- [4] M. Tondelli, F. Graziotti, A. Rossi, and G. Magenes, “Characterization of masonry materials in the Groningen area by means of in-situ and laboratory testing,” *Tech. Report, Eucentre, Pavia, Italy.*, 2015.
- [5] B. Z. Blanco, M. Tondelli, S. Jafari, F. Graziotti, J. Rots, and M. Palmieri, “A Masonry Catalogue for the Groningen Region,” in *16th European Conference on Earthquake Engineering*, 2018.
- [6] F. Graziotti, A. Rossi, M. Mandirola, A. Penna, and G. Magenes, “Experimental characterisation of calcium-silicate brick masonry for seismic assessment,” in *Proceedings of the 16th International Brick and Block Masonry Conference*, 2016, pp. 1619–1627.
- [7] F. Graziotti, U. Tomassetti, A. Penna, and G. Magenes, “Out-of-plane shaking table tests on URM single leaf and cavity walls,” *Eng. Struct.*, vol. 125, 2016.

- 
- [8] F. Graziotti, U. Tomassetti, S. Sharma, L. Grottoli, and G. Magenes, “Experimental response of URM single leaf and cavity walls in out-of-plane two-way bending generated by seismic excitation,” *Constr. Build. Mater.*, vol. (in press), 2018.
- [9] F. Graziotti, U. Tomassetti, S. Kallioras, A. Penna, and G. Magenes, “Shaking table test on a full scale URM cavity wall building,” *Bull. Earthq. Eng.*, vol. 15, no. 12, 2017.
- [10] S. Kallioras *et al.*, “Experimental seismic performance of a full-scale unreinforced clay-masonry building with flexible timber diaphragms,” *Eng. Struct.*, vol. 161, no. November 2017, pp. 231–249, Apr. 2018.
- [11] A. A. Correia, U. Tomassetti, A. Campos Costa, A. Penna, G. Magenes, and F. Graziotti, “Collapse shake-table test on a URM-timber roof structure,” in *16th European Conference on Earthquake Engineering*, 2018, pp. 1–12.
- [12] S. Kallioras, A. A. Correia, A. I. Marques, P. X. Candeias, and F. Graziotti, “LNEC-BUILD-3: Experimental investigation of the seismic response of a Dutch URM detached house with chimneys,” *Tech. Report, EUCENTRE, Pavia, Italy*, 2018.
- [13] F. Messali, G. Ravenshorst, R. Esposito, and J. G. Rots, “Large-scale testing program for the seismic characterization of Dutch masonry walls,” *16th World Conf. Earthq.*, no. June, p. Paper N° 4753, 2017.
- [14] J. G. Rots, F. Messali, R. Esposito, V. Mariani, and S. Jafari, *Multi-scale approach towards groningen masonry and induced seismicity*, vol. 747 KEM. 2017.
- [15] S. Jafari, J. G. Rots, R. Esposito, and F. Messali, “Characterizing the Material Properties of Dutch Unreinforced Masonry,” in *Procedia Engineering*, 2017, vol. 193, pp. 250–257.
- [16] H. Degée, V. Denoel, P. Candeias, A. Campos-Costa, and E. Coelho, “Experimental investigation on non-engineered masonry houses in low to moderate seismicity areas,” *14th World Conf. Earthq. Eng. Beijing, China*, 2008.
- [17] S. Kallioras, “Numerical Simulation of Shaking Table Tests on a URM Cavity-Wall Building,” *J. Int. Mason. Soc.*, vol. 30, no. 2, p. 39, 2017.
- [18] C. Avenas, C. Fusco, A. Mooneghi, Y. Huang, M. Palmieri, and R. Sturt, “LS-DYNA Numerical Simulation of Full Scale Masonry Cavity Wall Terraced House Tested Dynamically,” in *16th Europ. Conf. on Earthq. Eng., 16ECEE*, 2018.
- [19] U. Tomassetti, F. Graziotti, A. Penna, and G. Magenes, “Modelling one-way out-of-plane response of single-leaf and cavity walls,” *Eng. Struct.*, vol. 167, pp. 241–255, Jul. 2018.
- [20] D. Malomo, R. Pinho, and A. Penna, “Using the applied element method for modelling calcium silicate brick masonry subjected to in-plane cyclic loading,” *Earthq. Eng. Struct. Dyn.*, vol. 47, no. 7, pp. 1610–1630, 2018.
- [21] M. Tomažević, P. Weiss, and T. Velechovsky, “The influence of rigidity of floors on the seismic behaviour of old stone-masonry buildings,” *Eur. Earthq. Eng.*, no. 3, pp. 28–41, 1991.
- [22] G. Magenes, A. Penna, I. E. Senaldi, M. Rota, and A. Galasco, “Shaking table test of a strengthened full-scale stone masonry building with flexible diaphragms,” *Int. J. Archit. Herit.*, vol. 8, no. 3, pp. 349–375, 2014.
- [23] EN 1015-11, “Methods of test for mortar for masonry – Part 11: Determination of flexural and compressive strength of hardened mortar. Brussels, Belgium: European Standards, CEN/TC;” 1999.
- [24] EN 772-1, “Methods of test for masonry units – Part 1: Determination of compressive strength. European Standards, CEN/TC, Brussels, Belgium;” 2011.
- [25] EN 1052-1, “Methods of test for masonry – Part 1: Determination of compressive strength. Brussels, Belgium: European Standards, CEN/TC;” 1998.
- [26] EN 1052-5, “Methods of test for masonry – Part 5: Determination of bond strength by the bond wrench method. Brussels, Belgium: European Standards, CEN/TC;” 2005.
- [27] EN 1052-3, “Methods of test for masonry – Part 3: Determination of initial shear strength. Brussels, Belgium: European Standards, CEN/TC;” 2002.
- [28] F. Messali, R. Esposito, and M. Maragna, “Pull-out strength of wall ties, Technical Report, TU Delft, NL;” 2016.

- [29] G. Skroumpelou, F. Messali, R. Esposito, and J. G. Rots, "Mechanical characterization of wall tie connection in cavity walls," in *10th Australian Masonry Conference*, 2018.
- [30] A. Arias, "A measure of earthquake intensity," in *Seismic Design for Nuclear Power Plants*, 1970, pp. 438–483.
- [31] M. Bianchini, P. P. Diotallevi, and J. W. Baker, "Prediction of inelastic structural response using an average of spectral accelerations," *10th Int. Conf. Struct. Saf. Reliab.*, pp. 2164–2171, 2009.
- [32] G. W. Housner, "Intensity of Ground Motion During Strong Earthquakes.," *Calif. Inst. Technol.*, 1952.
- [33] U. Tomassetti, A. A. Correia, F. Graziotti, A. I. Marques, M. Mandirola, and P. X. Candeias, "Collapse shaking table test on a URM cavity wall structure representative of a Dutch terraced house," *Tech. Report, EUCENTRE, Pavia, Italy*, 2017.
- [34] G. Grünthal, *European Macroseismic Scale 1998*, vol. 15. 1998.
- [35] G. M. Calvi, "A displacement-based approach for vulnerability evaluation of classes of buildings," *J. Earthq. Eng.*, vol. 3, no. 3, pp. 411–438, 1999.
- [36] F. Graziotti, A. Penna, and G. Magenes, "A comprehensive in situ and laboratory testing programme supporting seismic risk analysis of URM buildings subjected to induced earthquakes," *Bull. Earthq. Eng.*, Sep. 2018.
- [37] S. Lagomarsino and S. Cattari, "PERPETUATE guidelines for seismic performance-based assessment of cultural heritage masonry structures," *Bull. Earthq. Eng.*, vol. 13, no. 1, pp. 13–47, 2015.
- [38] G. Magenes and G. M. Calvi, "In-plane seismic response of brick masonry walls," *Earthq. Eng. Struct. Dyn.*, vol. 26, no. 11, pp. 1091–1112, 1997.
- [39] A. Wilson, P. J. H. Quenneville, and J. M. Ingham, "In-Plane Orthotropic Behavior of Timber Floor Diaphragms in Unreinforced Masonry Buildings," *J. Struct. Eng.*, vol. 140, no. 1, p. 4013038, 2014.
- [40] L. Jacobsen, "Steady Forced Vibrations as Influenced by Damping," *Transactions of the American Society of Mechanical Engineers*, vol. 1, no. 1. pp. 169–181, 1930.
- [41] Kinovea Software, "Kinovea," 2011. [Online]. Available: <http://www.kinovea.org/>.
- [42] AS 3700-2001, *Masonry Structures, Australian Standard, Sydney, Australia*. 2001.
- [43] M. C. Griffith, J. Vaculik, N. T. K. Lam, J. Wilson, and E. Lumantarna, "Cyclic testing of unreinforced masonry walls in two-way bending," *Earthq. Eng. Struct. Dyn.*, vol. 36, no. 6, pp. 801–821, 2007.
- [44] C. . Willis, "Design of unreinforced masonry walls for out-of-plane loading," PhD Thesis, University of Adelaide, 2004.
- [45] S. Sharma, U. Tomassetti, L. Grottoli, and F. Graziotti, "Out-of-Plane Two-Way Bending Shaking Table Tests on Single Leaf and Cavity Walls," *Tech. Rep. EUC137/2018U. EUCENTRE, Pavia, Italy*, 2018.
- [46] M. C. Griffith and J. Vaculik, "Out-of-plane flexural strength of unreinforced clay brick masonry walls," *Mason. Soc. J.*, vol. 25, no. 1, pp. 53–68, 2007.
- [47] K. Beyer, M. Tondelli, S. Petry, and S. Peloso, "Dynamic testing of a four-storey building with reinforced concrete and unreinforced masonry walls: prediction, test results and data set," *Bull. Earthq. Eng.*, vol. 13, no. 10, pp. 3015–3064, 2015.
- [48] M. Tondelli, K. Beyer, and M. Dejong, "Influence of boundary conditions on the out-of-plane response of brick masonry walls in buildings with RC slabs," *Earthq. Eng. Struct. Dyn.*, vol. 45, no. 8, pp. 1337–1356, 2016.
- [49] CEN, *Eurocode 8 – Design of structures for earthquake resistance – Part 3: Assessment and retrofitting of buildings. EN 1998-3:2005*. Brussels, 2005.
- [50] Nederlands Normalisatie Instituut (NEN), *NEN NPR 9998:2017 Assessment of structural safety of buildings in case of erection, reconstruction and disapproval –Basic rules for seismic actions: induced earthquakes*. 2017.

## 4. Modelling one-way out-of-plane response of single leaf and cavity walls

Tomassetti U., Graziotti F., Penna A., Magenes G. Modelling one-way out-of-plane response of single leaf and cavity walls, *Engineering Structures*, 2018 167, 241-255.

**Abstract.** Existing unreinforced masonry (URM) buildings have often exhibited both damage and collapse in the out-of-plane (OOP) direction due to the activation of a local mechanism when subjected to earthquake excitations. The assessment of the out-of-plane response of masonry structures has been largely studied in the literature, typically assuming walls responding as rigid blocks or assemblies of rigid bodies. This paper presents a single-degree-of-freedom (SDOF) numerical model for the analysis of the dynamic OOP behaviour of URM walls or portion of walls. It takes into account both the linear and the non-linear rocking response phase of URM walls. The numerical model has been developed to capture the experimental dynamic response of both single leaf and cavity wall specimens subjected to a pure one-way bending action with both top and bottom end supports of the wall moving simultaneously. A detailed investigation into the force-displacement relationships characterising both wall typologies has been carried out in order to provide reliable parameters for the simulation of their dynamic behaviour. Particular emphasis is placed on the energy dissipation involved in such mechanisms. Different equivalent viscous damping models have been adopted and compared in order to identify the most appropriate one to capture the dependency of the damping phenomenon on the oscillation amplitude and subsequently the system frequency.

### 4.1. Introduction

The high seismic vulnerability of unreinforced masonry (URM) structures has been highlighted in many studies in literature [1-5]. The out-of-plane (OOP) behaviour of URM structures subjected to ground motion excitations has been extensively investigated by referring to the rocking dynamics of semi-rigid wall segments, characterised by consistent rotations impacting each other. Such simplification, confirmed by several experimental campaigns [6], could be considered acceptable under specific hypothesis and in case the masonry quality is good enough to ensure the formation of such mechanism. The understanding of this complex dynamic behaviour is essential in assessing the seismic performance of existing structures, for which an accurate prediction of displacement capacity and demand is essential in both safety verifications and risk analyses.

Housner [7] published a pioneer study deriving a single degree of freedom (SDOF) equation of motion for dynamic response of slender rigid blocks (inverted pendulum

structures) that could easily represent the nonlinear one-way OOP response of a parapet wall (PW). Several studies [8-9], assuming that both end supports of the wall move simultaneously, derived SDOF equation of motion for the one-way vertical spanning strip walls (VSSW) displacing as an assembly of two rigid bodies. Dejong and Dimitrakopoulos [10] as well as Restrepo [11] extended the solution to include equivalent SDOF systems governing the dynamic behaviour of complex multi-block systems responding in rocking.

Makris and Konstantinidis [12] highlighted that the typical linear oscillator (regular pendulum) often adopted to analyse the OOP behaviour of masonry sub-structures, and the rocking block represent two fundamentally different dynamical systems. Rocking structures, indeed, do not have a fundamental period of vibration, the responding frequency is, hence, oscillation-amplitude dependent [7,9]. Further differences between these two systems are also represented by restoring mechanisms, stiffness and characteristics of the damping phenomena. Therefore, equivalent stiffness methods based on the adoption of classical response spectra [13] cannot sufficiently predict the response of rocking structures. Makris and Konstantinidis [12] proposed the derivation of rocking spectra as a more adequate approach for characterising the earthquake input. For these reasons, the solution proposed by several researchers to the challenging problem of assessing the OOP performance of URM structures has been to directly integrate the rocking equation of motion to reproduce their dynamic responses.

Recognising that the URM wall segments do not have infinite stiffness, researchers proposed bi-linear [14], tri-linear [8] and four-branch [15] non-linear elastic curves to model their force-displacement (F-u) relationship.

The energy dissipation in elastic non-linear systems (i.e. rocking structures) is of major importance to successfully simulate their dynamic behaviour, capturing the dependence of the damping phenomenon with the system frequency. Building off the classical hypothesis of the impulse dynamics, some studies simulated the energy dissipation involved in such mechanisms by means of the coefficient of restitution assuming that the overall reduction of energy was concentrated at the instant of the impact [7,9]. In other works, the damping force has been modelled as a velocity dependent force through a constant [13] and variable (with cycle-to-cycle iterations) damping ratio [16]. The effectiveness of damping models acting on the system secant stiffness with a constant or linear damping ratio-frequency ( $\xi$ - $\omega$ ) relationship was also investigated [14,17].

Based on the experimental observations outlined in [18, 19], some researchers have also developed MDOF models [18,20-23] to analyse VSSW systems taking into account the top diaphragm flexibility and its interaction with the wall response.

The development of a reliable and computationally efficient SDOF model for the analysis of the OOP behaviour of masonry walls capable of capturing cracking and collapse oscillation amplitudes is ideal for large-scale risk analyses. This paper therefore proposes a numerical model for the OOP analysis of PW and VSSW systems, emphasizing the role of the energy dissipation adopting both of the aforementioned solutions. Section 4.2 and 4.3 review the static force-displacement (F-u) relationship, the dynamic behaviour and the energy dissipation of single leaf and cavity URM walls subjected to OOP one-way bending action, respectively. A detailed presentation of the proposed model in terms of equation of motion, damping characteristics is reported in Section 4.4. The experimental response of single leaf and cavity URM specimens subjected to shaking table tests performed by Graziotti et al. [23] has been adopted to calibrate the numerical model and



provide the best tri-linear and damping parameters to model their dynamic behaviour (section 4.5). Further considerations on the damping model adopted are also discussed in section 4.5.

## 4.2. One-way bending out-of-plane response of single leaf walls

The OOP one-way bending response of a masonry wall can be characterised by defining the OOP static force-displacement relationship, the equation of motion describing the dynamic rocking behaviour and the energy dissipation involved in this phenomenon. These critical points will be discussed in the following sections.

### 4.2.1. Static Force-Displacement Relationship

The  $F-u$  relationship of a wall responding in one-way bending can be directly studied from experimental tests. Figure 4.1a shows the results of a static air-bag test on a vertical-spanning two-leaf masonry panel [23] in terms of applied lateral force and mid-height horizontal displacement (MHD). Before undergoing non-linear rocking behaviour, URM structures are initially characterised by a linear response controlled by the masonry flexural stiffness. The rocking response phase, hence, can develop only after the formation of the classical pivot interfaces due to cracking occurring at different locations and the attainment of the cracking force ( $F_{cr}$ ).

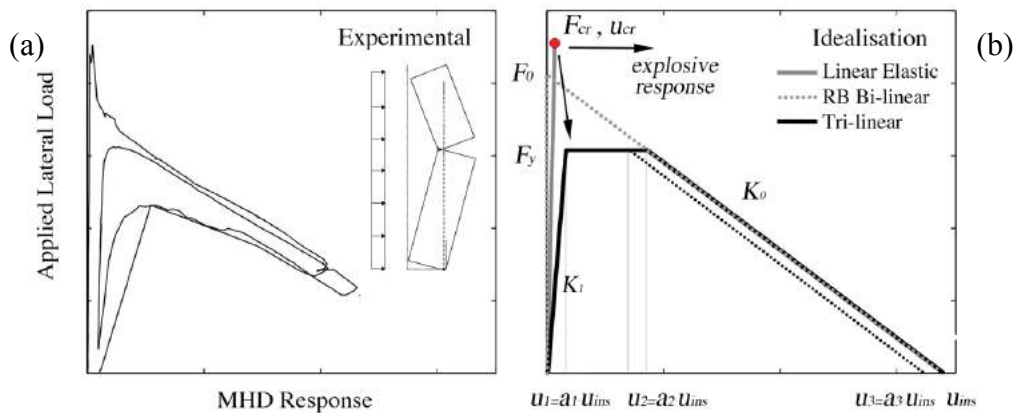


**Figure 4.1** Air-bag test on two leaf masonry panel performed by Derakhshan *et al.* [24] (Test T1-A) (a), idealisation of the response assumed: linear curve for the initial elastic phase (pre-cracking), tri-linear curve adopted for the rocking phase built on the rigid body idealisation defined by  $F_0$  and  $u_{ins}$  with a negative stiffness  $K_0$  (b).

Figure 4.1b shows, instead, the commonly assumed idealisation to model the experimental response that considers a linear elastic relationship until the attainment of the typical OOP one-way bending cracking pattern ( $F_{cr}$ ) followed by an equivalent tri-linear curve simulating the rocking response phase. The definition of reliable reference parameters to determine both curves is crucial to model the OOP response of these types of URM systems. Section 4.2.1.1 and 4.2.1.2 report a discussion on both pre-activation and post-activation mechanism phases, respectively in terms of forces and associated displacements.

#### 4.2.1.1. Modelling the pre-activation mechanism phase

Modelling the un-cracked response by the first linear curve is extremely important. Experimental evidences [8, 24] have shown that the lateral force associated with the wall's flexural strength can be higher than the resistance calculated neglecting the contribution of the tensile flexural strength at the interface, especially for slender and slightly loaded walls.

A proper consideration of the wall un-cracked response, both in terms of initial stiffness and lateral resistance provided by the tensile strength at the interfaces, may prevent an overestimation of the OOP displacement demand in slender and less slender walls. Taking into account the pre-cracking phase could also allow to simulate the OOP explosive response exhibited by slender walls during the last earthquakes. Moreover, in a performance-based earthquake engineering framework, where the response of the structure is characterised through different limit states, it could help define a cracking limit state to assess the wall performance in addition to the collapse that is mainly controlled by the rocking behaviour that follows the initial cracking of the wall.

In VSSW systems, the limit condition for the initial elastic phase in terms of force and associated displacement is strictly dependent on the top and bottom restraints conditions; double fixed and double pinned can be considered the two limit configurations (see Figure 4.2).

The inertial forces and the displacement associated with the developing of the rocking mechanism, for these two limit configurations are consistently different in terms of wall initial stiffness and cracking acceleration.

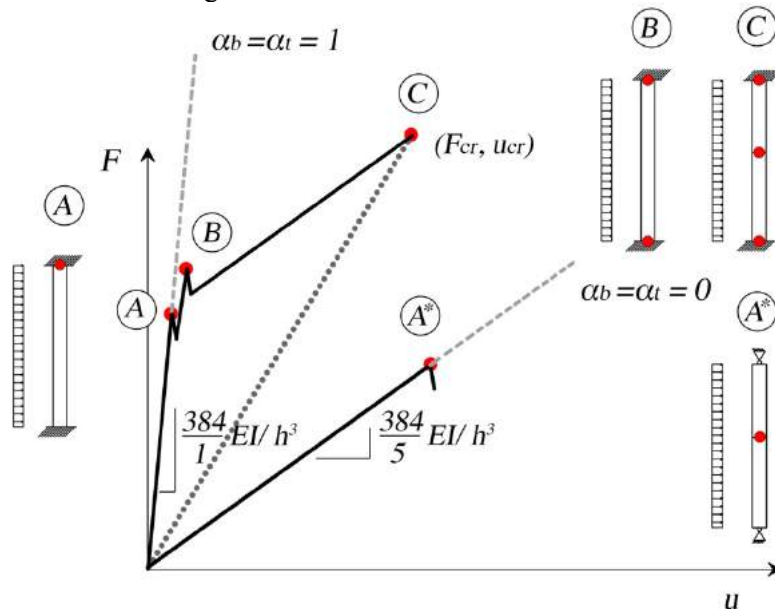


**Figure 4.2 VSSW pre-cracking phase considering the two limit boundary condition cases: fixed-fixed and pinned-pinned. The dotted line represents the secant stiffness at cracking point considered by the proposed model.**

In order to analyse the behaviour of walls with different top and bottom boundary conditions,  $\alpha_t$  and  $\alpha_b$  factors varying from 0 to 1 define the degree of moment restraint associated with the related top and bottom extremities.  $\alpha_t=1$  or  $\alpha_b=1$  indicate that the full

cracking moment can be developed at the top or bottom ends. In fixed-fixed cases ( $\alpha_t = \alpha_b = 1$ ), the rocking mechanism develops after cracking at the wall top (point A), usually the weakest section due to the lower axial load, followed by cracking at the bottom (point B) and finally at the wall mid-height (point C). In the pinned-pinned case ( $\alpha_t = \alpha_b = 0$ ), the rocking response starts simply with cracking at the wall mid-height. In real masonry walls,  $\alpha_b$  is often higher than  $\alpha_t$  and close to values equal to 1 because of the more effective restraint conditions at the base.

By simply adopting the equilibrium method according with plastic analysis principles and assuming a uniformly distributed lateral face load (considering uniform thickness and density along the wall height), it is possible to compute the inertial forces necessary to trigger a rocking mechanism causing the formation of 3 hinges at the wall bottom, top and mid-height. The  $\alpha_t$  and  $\alpha_b$  factors, weighting the top and bottom cracking moments  $M_t$  and  $M_b$ , allow to compute the cracking lateral force associated with any possible boundary condition (e.g. when the top restraint condition is different from the bottom one). This cracking lateral load ( $F_{cr}$ ), in the case of a fixed-fixed configuration, is achieved with three different levels of stiffness corresponding to the formation of the three hinges (see Figure 4.2). A local loss of strength associated to the formation of each hinge is also shown. Equations 1 (neglecting the eccentricity of the imposed vertical load,  $O$ ) can be used to compute  $F_{cr}$ .

$$F_{cr} = \frac{\zeta + \sqrt{\zeta^2 - \frac{W^2}{4 \cdot t^2} - \frac{(\alpha_b \cdot M_b - \alpha_t \cdot M_t)}{t^3} - \frac{(\alpha_b \cdot M_b - \alpha_t \cdot M_t)^2}{t^4}}}{\frac{3}{2} \cdot \frac{h}{t^2}}$$

$$\zeta = f_w + \frac{1}{t} \left( \frac{W}{2} + O + \frac{3 \cdot (\alpha_b \cdot M_b + \alpha_t \cdot M_t)}{t} \right) \quad (1)$$

$$M_b = \left( f_w + \frac{W + O}{t} \right) \frac{t^2}{6}; \quad M_t = \left( f_w + \frac{O}{t} \right) \frac{t^2}{6}$$

where  $W$  represents the weight of the wall,  $t$  is the wall thickness and  $f_w$  the masonry flexural strength. Equation 1 relies on the definition of the distribution of the maximum tensile stress  $\sigma_t(x)$  along the panel height ( $h$ ), based on wall boundary and loading conditions. Equating the derivative of  $\sigma_t(x)$  to zero ( $\sigma_t'(x) = 0$ ) yields to equation 2. It identifies the location along the panel height ( $h_1$ ) where the maximum tensile stress equals the masonry flexural strength ( $f_w$ ).

$$\frac{h_1}{h} = \frac{1}{2} + \frac{1}{h \cdot F_{cr}} \left[ \frac{W \cdot t}{6} + (\alpha_b \cdot M_b - \alpha_t \cdot M_t) \right] \quad (2)$$

It is worth noticing that the ratio  $h_1/h$  is indirectly sensitive to  $f_w$  via the term  $F_{cr}$  and to the applied overburden load ( $O$ ). The higher these terms are, the closer the hinge is to the mid-height of the wall. Note also that  $h_1/h$  depends also on the difference between top and bottom moments, where the larger the difference the further the crack is to the wall mid-height. Experimental values from static and dynamic tests suggest 0.5-0.7 to be a practical range for the ratio  $h_1/h$  [23-25].

The model proposed in this paper considers only the secant stiffness at the point of the complete development of the mechanism (see dashed line through point C in Figure 4.2). The cracking displacement ( $u_{cr}$ ) is defined as follow:

$$u_{cr} = \frac{\beta F_{cr} \cdot h^3}{384 E \cdot I} \quad (3)$$

where  $E$  is the Young's modulus and  $I$  the section moment of inertia. The  $\beta$  parameter may vary between 5, from solid mechanics in pinned-pinned configuration ( $\alpha_i = \alpha_b = 0$ ) and 2, empirically well representative of a fixed-fixed condition ( $\alpha_i = \alpha_b = 1$ ).

#### 4.2.1.2. Modelling the OOP mechanism phase

Having defined the pre-activation mechanism behaviour of the walls and derived the pertaining expressions, the next phase of response is characterised by the activation of the rocking behaviour of the walls that is described here. Assuming infinite compressive strength and slender walls, Figure 3 shows a VSSW deformed shape responding in pure rocking behaviour characterised by the formation of the classical pivot interfaces at the wall top, bottom and mid-height. The resulting top and bottom rigid bodies rotate around such pivot points ( $A'-B-C'$  in Figure 4.3) impacting each other every time the system passes through mid-height horizontal rest-condition displacement.  $\alpha_2$  and  $\alpha_1$  are geometric angles defining the slenderness of the two bodies;  $W_2$  and  $W_1$  represent the weight of the top and bottom bodies applied at the bodies centre of mass,  $O$  is the overburden vertical force applied with eccentricity  $e$ .  $\theta_2$  and  $\theta_1$  are the top and bottom body rotations equal to  $u/h_2$  and  $u/h_1$  respectively.

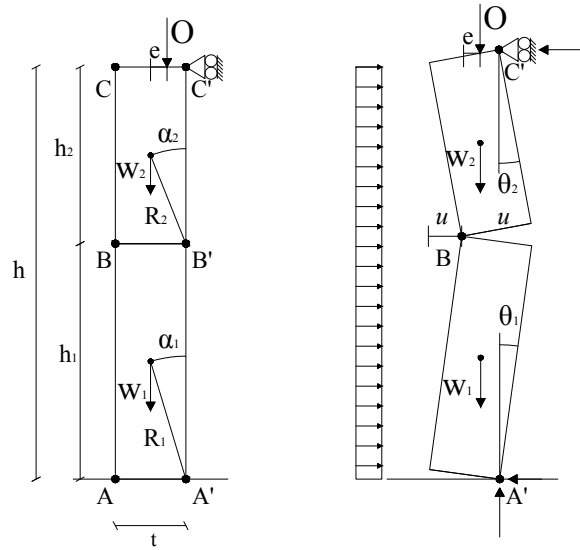


Figure 4.3 VSSW responding in rocking behaviour: geometry at rest and deformed shape.

The tri-linear  $F$ - $u$  curve illustrated in Figure 4.1b is constructed from the rigid bi-linear curve defined by  $F_0$  and  $u_{ins}$ . This bi-linear idealisation relies on the assumption of wall responding as an assembly of two rigid bodies with an infinite initial stiffness and strength, representing an upper bound of the real OOP static resistance of a VSSW. Equations 4 and 5 define  $F_0$  and  $u_{ins}$  respectively:

$$F_0 = \frac{2}{h_1} (W + O) \cdot t + \frac{O}{h - h_1} (t + 2e) \quad (4)$$

$$u_{ins} = \frac{2/h_1 (W + O)t + O \cdot (t + 2 \cdot e)/(h - h_1)}{2/h_1 (W + O) + 2O/(h - h_1)} \quad (5)$$

$K_0$  ( $=F_0/u_{ins}$ ) represents the negative stiffness of the system. The experimental  $F-u$  relationship of a VSSW could be more realistically represented by a tri-linear curve built on the rigid body bi-linear idealisation. Figure 4.1 illustrates both the rigid-bilinear curve and the tri-linear relationships implemented in the model. The key parameters of the tri-linear relationship are  $u_1$  ( $=a_1 u_{ins}$ ) controlling the wall's initial cracked stiffness, and  $F_y$  ( $=b_1 F_0$ ) identifying a force plateau. The tri-linear idealisations proposed in literature beyond  $u_2$  (second corner displacement of the tri-linear curve), generally located along the bi-linear curve ( $u_2 = u_{ins} - F_y/K_0 = a_2 u_{ins}$ ), in some cases, drop to zero matching the bi-linear idealisation ( $u_3 = u_{ins}$ ); in some other cases, taking into account the masonry compressive strength and the physical dimension of the hinges [26], the third branch presents a backward translation (with negative stiffness equal to  $K_0$ ) of the last tri-linear branch ( $u_3 = a_3 u_{ins}$ ). This latter case, leads to a reduction of the  $u_2$  value ( $u_2 = u_3 - F_y/K_0$ ).

The values for  $a_1$ ,  $a_3$  and  $b_1$  are strongly affected by aspects such as wall thickness, acting vertical overburden force and masonry mechanical properties [26]. Doherty [8] identified three stages of degradation: new, moderate and severe damage corresponding to  $b_1$  values of 0.72, 0.60 and 0.50 and  $a_1$  values of 0.06, 0.13 and 0.20 respectively. Other researchers later suggested  $a_1$  values of 0.04 [24] and 0.05 [27] based on both experimental results of air-bag quasi-static tests and successful numerical modelling of the dynamic behaviour of VSSW systems. Derakhshan *et al.* [24] showed that  $a_2$  value of 0.25 represents an upper bound level for this parameter. Their experimental work also suggested that the average ratio between the maximum lateral force resistance and the  $F_0$  rigid force for two-leaf and three-leaf walls was around 0.81 with  $b_1$  values around 0.75 ( $1 - a_2$ ) [28]. A refined work on the characterisation of the  $F-u$  relationship can be found in [26]. Other analytical models for the determination of the  $F-u$  relationship of VSSW systems have been proposed by Priestley [29] or Godio & Beyer [30]; the  $F-u$  relationship and the related parameters (comparable with those proposed in literature) necessary to simulate OOP experimental responses are discussed in section 4.4 and 4.5, respectively.

#### 4.2.2. Dynamic behaviour

The equation of motion of rocking systems can be derived directly from Lagrange's equation of motion [10-11]. Under the hypothesis of no sliding, no bouncing effect, slender blocks (that allows the linearization of the equation) and assuming both supports moving simultaneously, as proposed by Derakhshan *et al.* [28], the generic undamped SDOF equation of motion of a VSSW system can be written as follows:

$$m_{eff} \cdot \ddot{u}(t) + f_{bi}(u, t) = -\lambda \cdot m_{eff} \cdot \ddot{u}_g(t) \quad (6)$$

where  $u$  represents the horizontal displacement associated with the wall mid-hinge location (shown in Figure 4.3),  $m_{eff}$  is the effective mass of the system affected by the rotational moment of inertia of the two blocks (equation 7),  $f_{bi}(u, t)$  is the bi-linear rigid restoring force relationship (equation 8) assuming a uniformly distributed lateral face load (considering uniform thickness and density along the wall height,  $F_0$  and  $u_{ins}$  in Figure 1);  $\lambda$  (equation 9) is the parameter that allows to mobilise the entire mass ( $m_1 + m_2$ ) in the excitation term (right side of the equation) with the ground acceleration ( $\ddot{u}_g(t)$ ). Equation 7, 8 and 9 define the listed parameters:

$$m_{eff} = \frac{2}{3}(m_1 + m_2) \quad (7)$$

$$f_{bi}(u, t) = \frac{2}{h_1} \cdot W \cdot (t - u(t)) + \frac{h}{h_1 \cdot h_2} \cdot O \cdot (t + 2e - u(t)) + \frac{2}{h_1} \cdot O \cdot (t - 2e) \quad (8)$$

$$\lambda = \frac{3}{2} \quad (9)$$

The resulting equation of motion is equivalent to those proposed by Sorrentino *et al.* [9], DeJong & Dimitrakopoulos [10]. The aforementioned studies described the rocking phenomena as function of the rotation of the lower body. Sorrentino *et al.* [9] have shown that the system frequency parameter considering  $h_1/h$  ratios different from 0.5 may slightly affect  $m_{eff}$  and  $\lambda$ .

#### 4.2.3. Energy dissipation

The overall damping force acting in URM panels or assemblies responding in OOP rocking is given primarily by the energy dissipated through the impact of the wall during rocking in addition to a small contribution from the hysteretic energy dissipation, which both need to be considered in the model. A common approach, relying on the classical hypothesis of the impulse dynamics, is simulating the energy dissipation involved in such mechanisms through a coefficient of restitution [7, 9, 22]. Another option is adopting an equivalent viscous damping approach defining a velocity-dependent damping force through a constant, variable (with cycle-to-cycle iterations) and stiffness proportional damping ratio. The iterative procedure introduced by Doherty [8] and Lam *et al.* [16] consisted in evaluating the damping associated with each half-response cycle according to a calibration of Rayleigh damping against dynamic experimental  $\xi - \omega$  data. The calibration study proposed in this work assumes only non-iterative damping force models presented in the following section. Tomassetti *et al.* [17] proposed an equivalence between a coefficient of restitution model and velocity dependent damping forces by equating the energy losses provided by these different sources of damping.

##### 4.2.3.1. Equivalent viscous damping

A classical damping model with a constant damping coefficient (CDC), assuming a constant damping ratio ( $\xi$ ) acting on the system initial stiffness ( $\omega_1$ ), has been adopted in literature to simulate the dynamic response of rocking systems [10]. Moreover, two other damping systems have also been investigated and compared in order to capture the dependence of the damping phenomenon on the oscillation amplitude and on the current frequency of vibration of the system. Both damping models act on the instantaneous secant frequency  $\omega(t)$  [14] defined by the instantaneous secant stiffness  $K_{sec}(t)$  of the system and presented in equation 10:

$$\omega(t) = \sqrt{\frac{K_{sec}(t)}{m_{eff}}} \quad (10)$$

The first one of the two associates a constant damping ratio through all the system frequencies, whereas the second one assumes a stiffness proportional term ( $\xi - \omega$  linear relationship) identified by the damping ratio ( $\xi_{in}$ ) corresponding to the frequency of the

first branch of the tri-linear relationship ( $\omega_1$  or  $F_I$ ). The damping coefficient of the three damping models: CDC, constant damping ratio (CDR) and stiffness proportional damping ratio (SDR), are defined by equations 11, 12, 13 respectively:

$$C_{CDC} = 2 \cdot m_{eff} \cdot \omega_1 \cdot \xi \quad (11)$$

$$C_{CDR}(t) := 2 \cdot m_{eff} \cdot \omega(t) \cdot \xi \quad (12)$$

$$C_{SDR}(t) := 2 \cdot m_{eff} \cdot \omega(t) \cdot \xi(\omega(t)) \quad (13)$$

Figure 4.4 compares the three damping models in terms of the relationship between damping ratio and frequency ( $\xi$ -  $\omega$ ) and the one between damping forces (product of the damping coefficients and system velocity) and non-dimensional mid-height displacement (MHD) in matched rocking free vibration decays of a VSSW. The wall geometry is the same of the one tested in [23], assuming the same tri-linear parameters ( $a_I=0.04$ ,  $b_I=0.85$  and  $u_3= u_{ins}$ ) for all the three configurations and releasing the systems from an initial normalised displacement equal to 0.9. Independently from the actual or secant frequency the CDC damps the system proportionally to the initial angular frequency. CDR and SDR damping models associate to the current secant frequency a damping ratio according to a constant or a linear law (defined by the  $\xi$  value assigned to  $\omega_1$ ). Both CDR and SDR models, acting on the secant frequency, tend to concentrate the energy dissipation around the zero-oscillations amplitude, which correspond to the impact region, acting in a similar fashion of a coefficient of restitution [17]. The area within the loops in Figure 4.4b representing the dissipated energy is the same for each damping model.

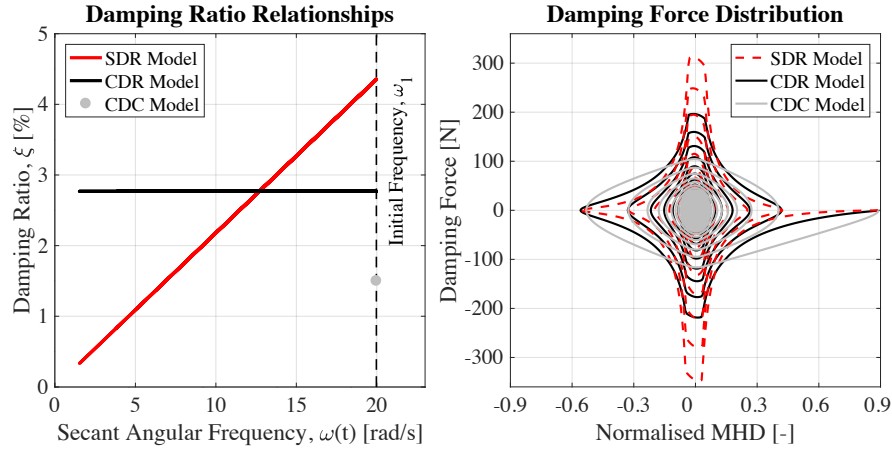


**Figure 4.4 (a) comparison between  $\xi$ -  $\omega$  relationships of the three models. Independently from the actual or secant frequency of the system the CDC damp the system proportionally the initial angular frequency. CDR and SDR damping models associate to the current secant frequency a damping ratio according to a constant or a linear (defined by the  $\xi$  value assigned to  $\omega_1$ ) law; (b) distribution of the damping force through the normalised oscillation amplitude of the three damping models: CDC, CDR, SDR.**

### 4.3. One-way out-of-plane response of cavity walls

Cavity wall buildings are particularly vulnerable to out-of-plane actions due to the walls being both slender and lightly loaded, which prevents the development of their full in-plane strength capacity. Cavity construction is a form of wall construction where a cavity is left between the two leaves of bricks. The external leaf of a cavity wall is often a brick veneer wall without any load bearing function, whereas the internal leaf is a load-bearing wall, carrying the vertical loads transmitted by the floors and roof. Leaves on either side of a cavity wall are typically connected by regularly spaced metal cavity ties, which can vary in material, shape and spacing.

The dynamic behaviour and failure mechanism of cavity wall systems (CAVS) is strongly affected by the boundary conditions of the two walls in addition to the amount and the topology of connection between the two leaves. The experimental campaign performed by Graziotti *et al.* [23] has shown that despite the adopted L-shaped ties having negligible flexural stiffness, their axial stiffness and bond ensured a sufficient coupling of the horizontal displacement of the two leaves (*i.e.* limiting the differential displacement and maintaining the gap) up to near-collapse, even for the specimens with only 2 ties/m<sup>2</sup>. This displacement compatibility (ensured also by the slenderness of the leaves) is important since it permits the analysis of the OOP seismic behaviour of CAVS as an equivalent single leaf panel echoing to the methodology presented earlier. Nevertheless, this simplification may not necessarily be applicable to all types of cavity walls with different geometry and boundary conditions (*e.g.* when the failure mechanism is dominated by the pull-out of the outer leaf). The following sections will discuss the methodology adopted to simulate their dynamic response.

#### 4.3.1. Static Force-Displacement Relationship

When sufficient coupling of displacements is ensured, the specimen cracking force can be obtained as the sum of the two independent leaves cracking forces (inner wall *iw* and outer wall *ow*); the cracking displacement ( $u_{cr}$ ) is instead set to the lesser of the ones associated with the two walls. Similarly, the rocking tri-linear  $F-u$  relationship of CAVS has been built on the rigid force obtained as sum of the forces associated with the rigid body mechanisms of the two leaves considered independently. The instability displacement has been considered equal to the one of the inner load-bearing leaf only. Table 1 summarises the key parameters necessary to model both pre-cracking and post-cracking phases. A further contribution to the lateral resistance is given by the ties coupling system and is denoted with the term  $F_c$ .

**Table 4.1 Modelling pre-activation and post-activation mechanism  $F-u$  relationship of CAVS.**

Pre-cracking behaviour		Post-cracking behaviour	
$F_{cr}$	$u_{cr}$	$F_0$	$u_{ins}$
$F_{cr,iw} + F_{cr,ow} + F_c$	$u_{cr,iw}$	$F_{0,iw} + F_{0,ow} + F_c$	$u_{ins,iw}$

The tri-linear curve can be constructed using the analogy of what has been suggested for single leaf panels in Section 4.2.1.2. Observations from experiments [23] and modelling work suggested the identification of three possible stages of response of CAVS, shown by Figure 4.5. During the first stage, when the specimen is undamaged or only slightly



damaged, the specimen's lateral resistance relies not only on the resisting force provided by the two leaves independently but also on the contribution given by the coupling system. It produces shears and moments on the two leaves edges to provide an overall stabilising effect against the rocking overturning rotation, (see Figure 4.5a). The global stabilising effect of the ties system, considering the free body diagram of the inner leaf and assuming an un-deformed configuration, can be approximated by means of the following equation:

$$F_c = 2 \cdot V_t \cdot t \cdot \frac{h}{h_1 \cdot h_2} + 2 \cdot M_t \cdot \frac{h}{h_1 \cdot h_2} \quad (14)$$

where  $M_t$  and  $V_t$  are the sum of the  $n$  tie plastic moments and the corresponding shears (upon developing a flexural mechanism) at the inner wall edge interface, respectively ( $M_t = \sum_1^n M_i$ ;  $V_t = \sum_1^n V_i$ ). This coupling force needs to be summed up with the rigid forces associated with the two leaves identifying the CAVS  $F_0$ .

The second stage of the response is characterised by the complete formation of the rocking mechanism in both leaves. Due to the bond degradation at the tie-mortar interface, the coupling force contribution ( $F_c$ ) drops to zero and the ties system, working as a strut, can only guarantee compatibility of horizontal displacements between the two leaves. The lateral resistance is ensured only by the sum of the two leaves resistance considered independently.

The third stage is characterised by a further degradation of the specimen and a decrease of the lateral resistance due to damage occurring at the pivot mortar bed-joints, which can be accounted for through a reduction of the global  $b_1$  and  $a_3$  values. Figure 4.5 shows also qualitatively the evolution of the tri-linear configurations through the different stages of degradation of the CAVS.

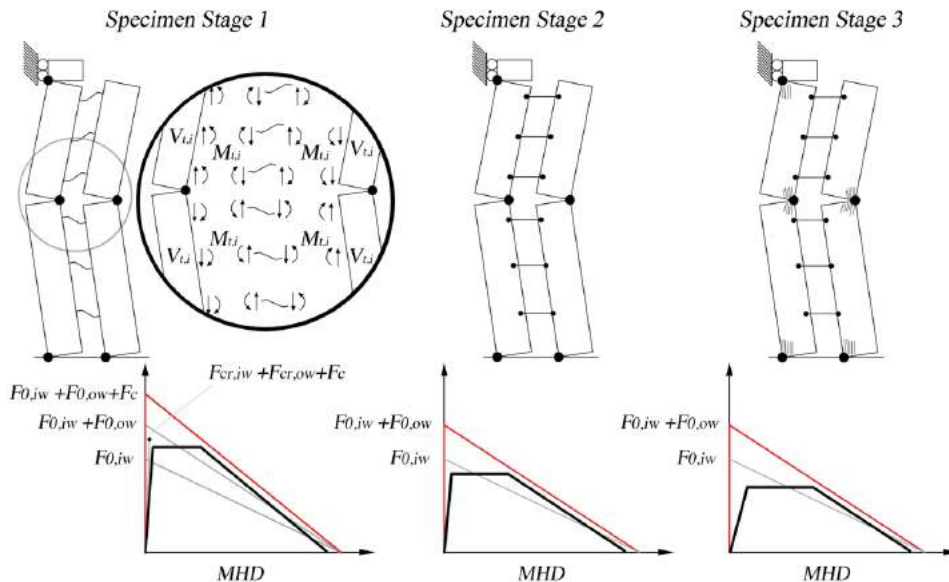


**Figure 4.5 Schematic representation of the OOP response of cavity walls and associated F-u relationship.**

Figure 4.6 shows as the experimental  $F-u$  curve of a cavity wall specimen exceeds the force associated with the sum of the two rigid body mechanism forces of the two walls considered independently (black dashed line). Forces associated with triggering of

rocking mechanisms considering superimposed load eccentricity equal to 0 ( $F_0$ ) and half of the wall thickness ( $F_0^*$ ) are also shown.

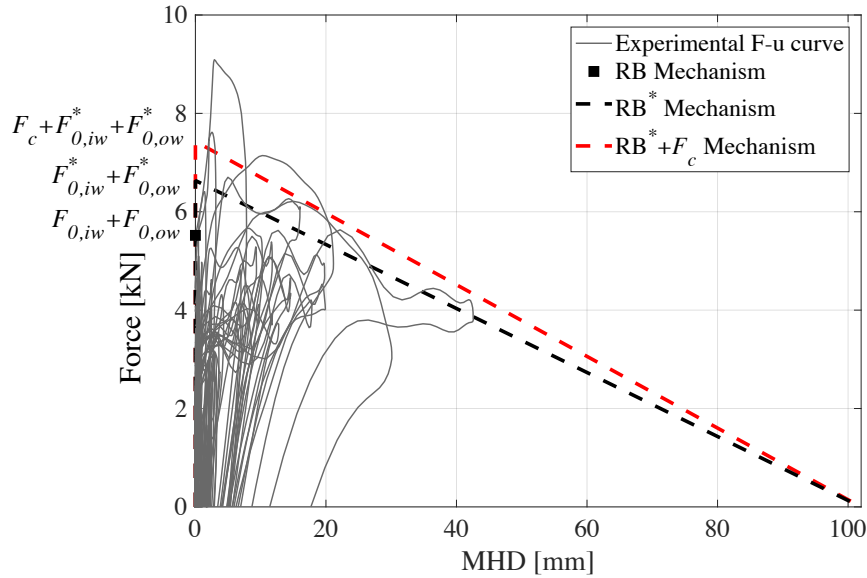


**Figure 4.6 Experimental F-u relationship of a cavity wall specimen (CAV-01-04), adapted from [23].**

In particular, during the dynamic response the cavity wall CAV-01-04 capacity reached values beyond 9 kN. The bi-linear curve taking into account the coupling force contribution computed according to equation 14, is also shown (red dashed line).

#### 4.3.2. Dynamic Behaviour and Energy Dissipation

The dynamic behaviour of CAVS efficaciously coupled could be described by equation 7, resulting as a coupled rocking behaviour of the two leaves. The system effective mass is simply 2/3 of the sum of the two wall masses (see equation 6) taking into account the rotational inertia of the two bodies. The energy dissipation characterising cavity wall specimens is much higher than that associated with the single leaf specimens. Graziotti *et al.* [23] reported equivalent viscous damping (EVD) values between 15 and 20% with peaks up to 30% from experimental testing. In addition to impacts and the small amount of hysteretic energy, two further damping contributions need to be modelled: the energy dissipated due to damage and yielding of the anchor system and the damping effect provided by the two leaves moving slightly out of phase at low oscillation amplitudes. The progressive degradation of the tie bond, started from earlier stages of testing, generated few millimetres gaps that allowed a slight differential displacement between the two leaves. This damping contribution was rather higher in cavity specimens where the connection between the two leaves was limited to 2 of ties/ m<sup>2</sup>.

#### 4.4. The proposed numerical model

The proposed numerical model has been validated against experimental tests. Results and comparisons are reported in the following sub-sections.

#### 4.4.1. The reference experimental campaign

The tests performed by Graziotti *et al.* [23] represent the reference experimental campaign to which the calibration of the proposed numerical model is conducted. The laboratory work consisted in series of shaking table tests on URM single leaf and cavity walls (with Dutch detailing) subjected to a pure OOP one-way bending action. The single leaf specimen and the inner leaf of cavity wall specimens were made of calcium silicate (CS) bricks, while clay bricks were used for the outer leaf of cavity specimens. The masonry leaves were approximately 2750 mm high,  $h$ , 1450 mm wide,  $w$ , and 102 mm thick and connected, in cavity wall specimens, means of 200 mm long L-shape steel ties with a diameter of 3.1 mm. The number of ties was chosen according to code prescriptions and common masonry practices (2 and 4 ties/m<sup>2</sup>). The dynamic inputs (Gr-1 and Gr-2) were chosen to be representative of the expected hazard [32] in the region of Groningen, which has seen an increase in seismic activity during the last two decades due to induced seismicity. Another input signal was represented by a 2 Hz Ricker Wave Acceleration input (RWA), which consisted of a particular acceleration pulse that triggered a clear damped free vibration phase in the specimens, providing valuable information on the damping forces acting within the specimens. The average compressive strength, flexural tensile strength and Young modulus of the CS walls were 6.20 MPa ( $f_m$ ), 0.238 MPa ( $f_w$ ) and 3256 MPa ( $E$ ), respectively. Regarding the clay walls, the corresponding average mechanical parameters were: 11.32 MPa ( $f_m$ ), 0.158 MPa ( $f_w$ ) and 5760 MPa ( $E$ ).

#### 4.4.2. The Assumed F-u Relationship

The tri-linear model shown in Figure 7(a) was adopted to model a series of dynamic responses of different amplitudes on vertical spanning walls, capturing the variation of the associated rigid force with the migration of the top resultant overburden force ( $O$ ) towards the thickness edge at high levels of MHD (see Figure 7(b)). This led to an increase of the bi-linear rigid force  $F_0$  from a static or low level of MHD (when the eccentricity is approximately equal to zero) to a high level of MHD (when the eccentricity approach half of the wall thickness). Therefore, the proposed  $F$ - $u$  relationship is defined at low level of displacement by a bi-linear curve with a superimposed load eccentricity equal to zero ( $e=0$ ) and approaching the collapse by a bi-linear curve with maximum eccentricity (equal to half of the wall thickness,  $e=t/2$ ); the resulting relationship is still tri-linear but with an “hardening” second branch. Therefore, to compute the various points along the proposed tri-linear curve, the following is proposed:  $a_1$  (fraction of  $u_{ins}$  associated with zero eccentricity mechanism) is an empirical value that has been calibrated on the experimental response;  $b_1$  is the same for both rigid mechanisms considered ( $F_{0(e=0)}$  and  $F_{0(e=t/2)}$ ) while  $u_3$  is computed subtracting some eventual reduction or degradation along the wall edge  $p$  (it takes into account the mortar pointing expulsion ranging between 50% and 100% of the thickness of the bed-joint) and half of the actual physical dimensions of the hinge controlled by the masonry compression strength ( $f_m$ ) from the instability displacement ( $u_{ins}$ , associated with half thickness eccentricity mechanism) as follow:

$$u_3 = a_3 \cdot u_{ins}^* = u_{ins}^* - p - \frac{1}{2} \cdot \frac{W \left(1 - \frac{h_1}{h}\right) + O}{0.85 \cdot f_m} \quad (15)$$

$u_3$  resulted slightly higher than the values observed in static air-bag test [24] on a specimen with similar characteristics of those dynamically tested.  $u_2$  is simply moved backward keeping the negative stiffness  $K_0$  as constant:

$$u_2 = a_2 \cdot u_{ins}^* = (a_3 - b_1) \cdot u_{ins}^* \quad (16)$$

The  $F-u$  relationship was kept constant during the analysis since the increase of applied vertical load approaching the collapse of the wall was less than 5% thanks to a spring system designed specifically for this.

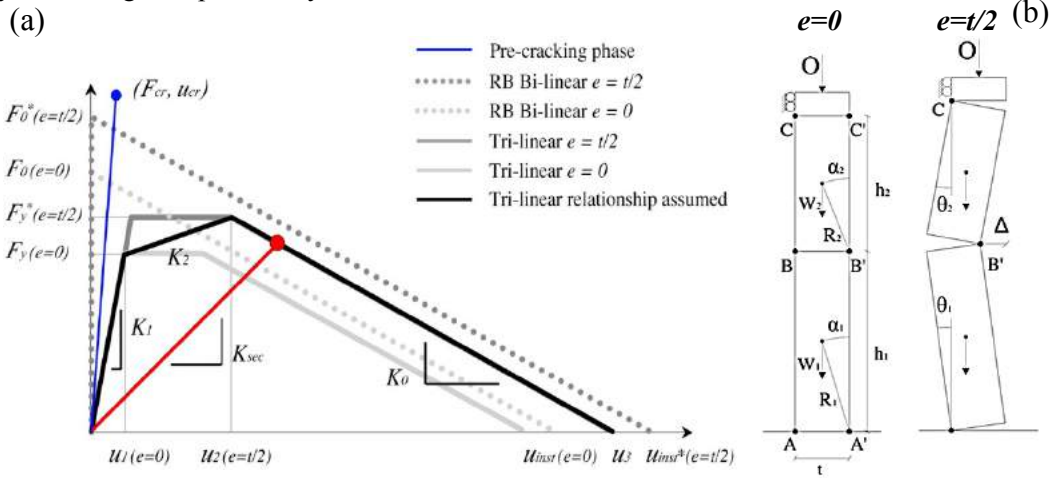


**Figure 4.7 (a) proposed tri-linear relationship built on a bi-linear curve with zero eccentricity ( $e=0$ ) at low level of displacement and on a bi-linear curve with maximum eccentricity ( $e=t/2$ ) approaching the OOP collapse of the wall; the instantaneous secant stiffness of the system is also shown in red; (b) migration of the top resultant overburden force (adapted from [23]).**

#### 4.4.3. The numerical model

The numerical model adopts the Newmark ‘linear acceleration method’ [31] integration scheme implemented in the non-iterative formulation version. As earlier introduced two distinct phases have been considered: pre and post activation mechanism. The former is violated at the attainment of the cracking force  $F_{cr}$  with the model that initially assumes the pre-mechanism stiffness given by  $F_{cr}$  and  $u_{cr}$  and then switching to the rocking  $F-u$  relationship represented by the tri-linear configuration. The SDOF dynamic equation during the pre-activation mechanism phase is defined by equation 17.

$$m_{eff} \cdot \ddot{u}(t) + C_{lin} \cdot \dot{u}(t) + f_{lin}(u, t) = -\lambda \cdot m_{eff} \cdot \ddot{u}_g(t) \quad (17)$$

The effective mass considered (equation 7) in this pre-cracking phase assumes a linear deflected shape typical of a rocking response, experimental evidences have shown as initially the deformed shape is slightly different [23]. This is one of the approximations and current limitations of the model. The damping coefficient ( $C_{lin}$ ), independently from the damping system adopted, being the  $F-u$  displacement simply linear elastic, is constant during the analysis steps.

Once the cracking condition is violated, the numerical solves the SDOF equation introduced in equation 6 substituting the rigid bi-linear system restoring force  $f_{bi}(u(t))$

(equation 8) with the elastic non-linear tri-linear curve  $f_{tri}(u(t))$  discussed in section 4.2.1.2. The implemented damped SDOF equation of motion in the three damping configurations investigated follows:

$$m_{eff} \cdot \ddot{u}(t) + C_i \cdot \dot{u}(t) + f_{tri}(u(t)) = -\lambda \cdot m_{eff} \cdot \ddot{u}_g(t) \quad (18)$$

where  $C_i$  depends on the damping model selected among  $C_{CDC}$ ,  $C_{CDR}(t)$  and  $C_{SDR}(t)$ . In particular for the SDR case, the elastic damping ratio is equal to the damping ratio associated with the first branch frequency ( $\xi_m$ ). For simplicity, the value of the damping ratio associated with the pre-mechanism activation phase is assumed equal to the damping ratio considered during the rocking phase.

#### 4.4.4. The calibration approach

The work was focused in finding the best parameters that resulted in an efficient simulation of the experimental response through series of tests of different response amplitude, where the mechanical properties of the specimens could be considered as constant. Therefore, the experimental response has been analysed and calibrated by considering different testing phases according to the input sequences and the state of degradation of the specimens. Table 2 presents such testing phases for all the specimens specifying the considered tests [23], input typology and the state of degradation of the specimen.

**Table 4.2 Testing phases analysed with constant modelling parameters for each specimen.**

Specimen	$\sigma_v$ [MPa]	#ties [#/m <sup>2</sup> ]	Test Phase	Test # (ref. [18])	Input	Stage of the specimen
SIN-03-00	0.3	-	1	from 1.1 to 1.9	Gr-1	New, uncracked
			2	from 2.1 to 2.4	RWA	Cracked
			3	from 3.1 to 3.7	Gr-1	Cracked
SIN-01-00	0.1	-	4	from 4.1 to 4.4	RWA	Cracked
			5	from 5.1 to 5.3	Gr-2	Degraded, Cracked
CAV-01-02	0.1	2	1	from 1.1 to 3.3	Gr-1, Gr-2	New, uncracked (Stage 1)
			2	from 4.1 to 6.1	Gr-1, RWA, Gr-2	Cracked (Stage 2)
CAV-03-02	0.3	2	1	from 1.1 to 5.1	Gr-1, RWA, Gr-2	New, uncracked (Stage 1)
			2	5.2	Gr-2	Cracked (Stage 2)
CAV-01-04	0.1	4	1	from 1.1 to 3.4	Gr-1, Gr-2	New, uncracked (Stage 1)
			2	from 4.1 to 4.5	RWA	Cracked (Stage 2)
			3	from 4.6 to 5.2	RWA, Gr-2	Degraded, Cracked (Stage 3)

The average parameters of the trilinear model fitted to represent the lateral response of the two single leaf configurations are listed in Table 3. The assumed tri-linear relationships have been compared with the results of an air-bag test performed by Messali *et al.* [33] on a specimen with similar characteristics in the framework of the same research project. The selection of these parameters was made according to the definition of reasonable error indicators accounting for both frequency match of experimental and numerical histories and their response peaks.

**Table 4.3 Tri-linear parameters assumed for the dynamic calibration of experimental tests** ( $\wedge$  depends on  $a_3, b_1$ ).

Specimen	$\sigma_v$ [MPa]	$\sigma_v/f_m$ [-]	$a_1= u_1/u_{ins}$ [-]	$a_2= u_2/u_{ins}^*$ [-]	$a_3= u_3/u_{ins}^*$ [-]	$b_1$ [-]
SIN-03-00	0.3	0.048	0.04	0.14 $\wedge$	0.92	0.775
SIN-01-00	0.1	0.016	0.03	0.06 $\wedge$	0.96	0.90

The  $a_3$  parameter has been computed assuming a  $p$  value equal to half of the bed-joint thickness (5 mm),  $a_2$  depends, instead, on the other parameters ( $b_1, a_3$ ). It is worth noticing the influence of the applied overburden force on the tri-linear curve, decreasing  $O$  lead to an increase of the  $b_1$  parameter and a reduction of  $a_1$  to give a stiffer configuration, which agrees with previous observations by Derakhshan *et al.* [26]. Figure 4.8 plots the two trilinear configurations proposed compared with the air-bag experimental results of a specimen subjected to an overburden pressure equal to 0.25 MPa. The two tri-linear configurations therefore represent a sort of upper (SIN-01-00) and lower (SIN-03-00) bound of a tri-linear curve fitted on the experimental envelope curve of the wall tested by Messali *et al.* [33] with overburden pressure equal to 0.25 MPa. The match in terms of envelope capacity curve is rather good even if the hysteretic energy dissipation observed during air-bag testing seems rather high compared to the one dynamically obtained [23].

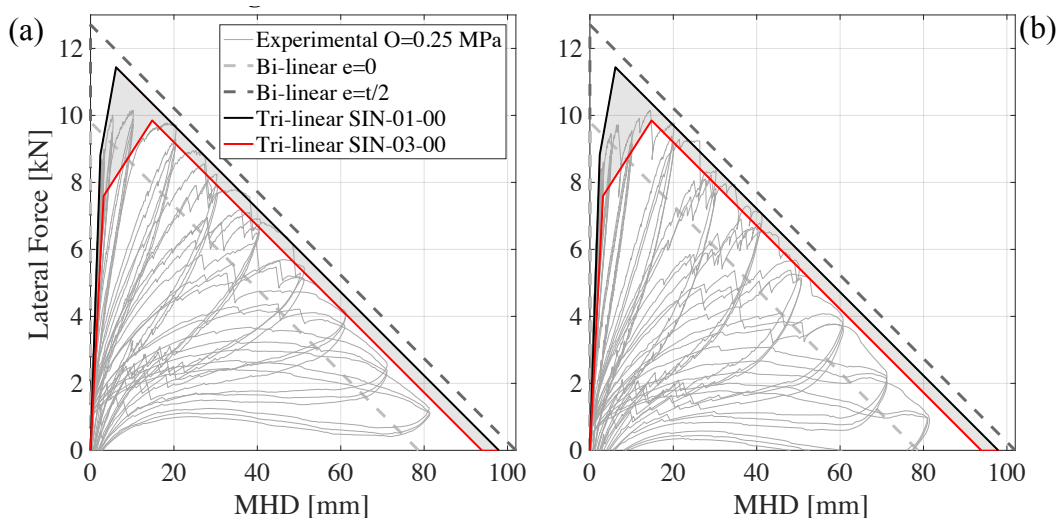


**Figure 4.8 Comparison between proposed tri-linear envelope curves and results of air-bag test performed by Messali *et al.* [33]: negative (a) and positive (b) directions.**

Moreover, the experimental airbag test provided information about the specimen cracking resistance; the response peak of the first cycle where a reduction of the initial stiffness has been recorded is associated with a lateral force of 7964 N and a displacement of 2.22 mm in the positive direction and 7652 N and 2.15 mm in the negative direction (following cycles). Considering the geometry, the mechanical properties and the boundary conditions ( $\alpha_b = \alpha_t = 1; \beta = 2$ ) specified in [33], the predicted cracking coordinates ( $F_{cr}, u_{cr}$ ) using the proposed equations (1,2) are 7884 N and 1.81 mm that agrees well with the experimental observations.

## 4.5. Comparison with experimental results

### 4.5.1. Simulation of the dynamic response of single leaf specimens

The reference single leaf specimen was tested in two configurations SIN-03-00 and SIN-01-00, with an imposed overburden pressure of 0.3 and 0.1 MPa, respectively. The simulation of the pre-cracking phase regards only the initial testing phases of the SIN-03-00 configuration. The specimen boundary conditions were double fixed at both wall extremities, with the top restraint ensured by L steel profiles that prevented any rotation of the top brick layer. The resulting effective height considered in the numerical simulation is 2.68 m that corresponds to the specimen full height minus the height of the last clamped brick layer. The  $\alpha_b$  and  $\alpha_t$  factors were therefore both taken equal to 1 and  $\beta$  equal to 2. All the mechanical parameters assumed to compute the cracking force were the nominal mean values. Table 4 lists the parameters that best simulated the experimental response of the different tests grouped according to Table 2. The selection of these parameters is in agreement to the procedure discussed in section 4.4.4. The damping model assumed for the analysis herein presented is the SDR one, the reasons of this choice will be discussed in section 4.5.4. Consequently, the damping value specified in Table 2 represents the damping ratio ( $\xi_{in}$ ) corresponding to the frequency of the first branch of the tri-linear relationship ( $\omega_1$ ).

**Table 4.4 SDOF parameters adopted to simulate the experimental response in the different testing phases for the single leaf specimens.**

<i>Spec.</i>	<i>T.</i>	$F_{cr}$	$u_{cr}$	$F_0$	$F_0^*$	$u_{ins}$	$u_{ins}^*$	$a_1$	$a_2$	$a_3$	$b_1$	$\xi_{in}$
	<i>P.</i>	[kN]	[mm]	[kN]	[kN]	[mm]	[mm]	[-]	[-]	[-]	[-]	[%]
SIN-03-00	1	8.36	1.97	10.69	14.63	75.4	102	0.04	0.15	0.92	0.775	6.5
	2	-	-	10.69	14.63	75.4	102	0.04	0.15	0.92	0.775	5.5
	3	-	-	4.19	5.51	77.6	102	0.03	0.11	0.96	0.85	6.0
SIN-01-00	4	-	-	4.19	5.51	77.6	102	0.03	0.06	0.96	0.90	7.0
	5	-	-	4.19	5.51	77.6	102	0.03	0.21	0.96	0.75	6.0

Figure 4.9 shows the comparison between the Gr-1 incremental dynamic testing (IDT) sequences (SIN-03-00 T.P. 1, SIN-01-00 T.P. 3) and the numerical response (NR). The results are presented in terms of the intensity measure, taken here as peak ground acceleration (PGA) and peak mid-height hinge displacement (MHD).

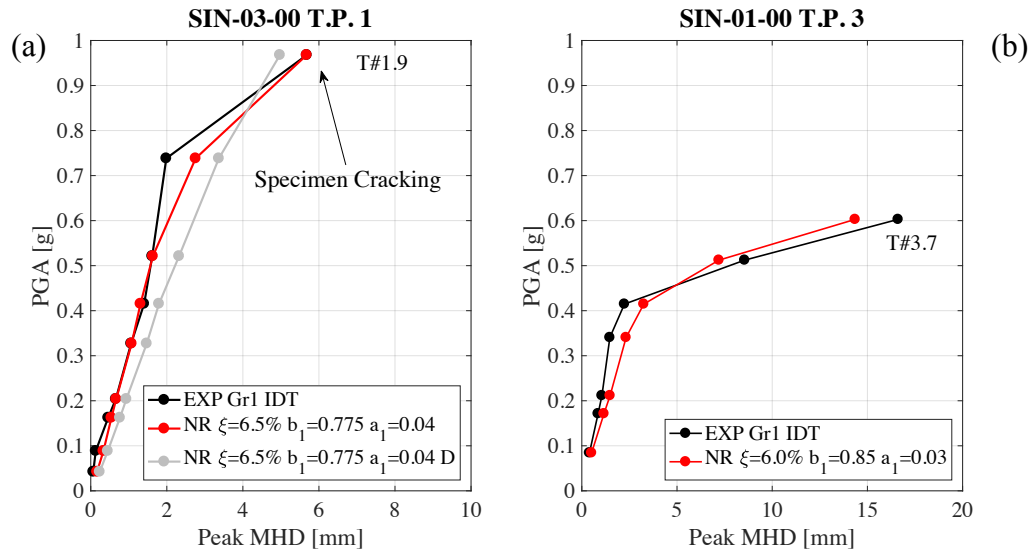


**Figure 4.9 Comparison between experimental (black line) and numerical (red line) MHD for the Gr-1 IDT sequences: SIN-03-00 (a), SIN-01-00 (b). The gray line (with a final “D” in legend) (a) indicates the numerical response of a wall in pre-cracked condition.**

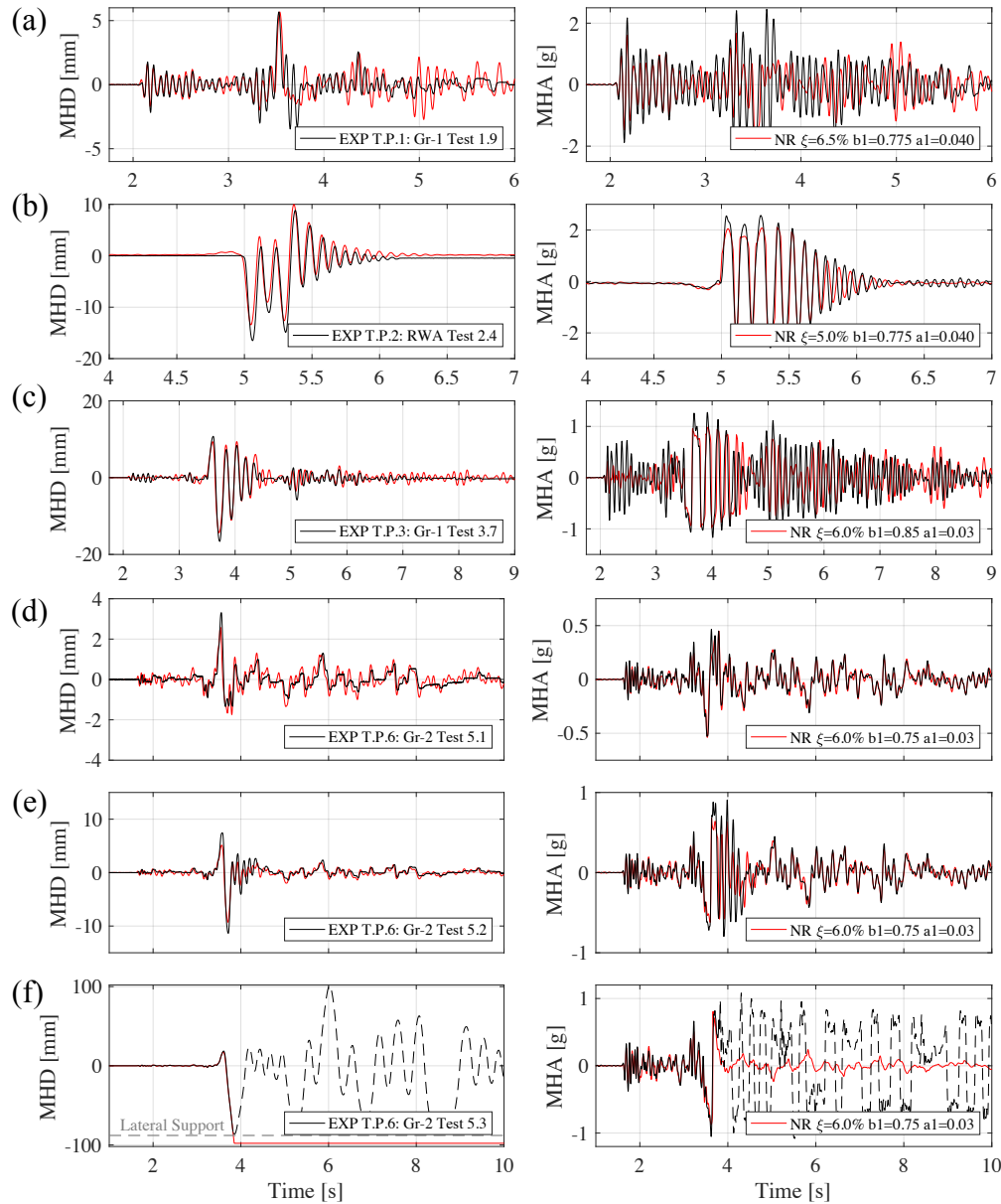
In general, the match between experimental and numerical MHD response peaks is quite good, with Figure 4.9a showing the initial elastic stiffness to be very well captured by the numerical model. This could be appreciated also by looking to Figure 4.10a in the response phase before the peak displacement. After the attainment of cracking the model initial stiffness is reduced to the first branch of the tri-linear  $F-u$  relationship, while the actual wall conserved a part of the initial stiffness (especially for oscillation amplitudes that may not induce the tension in the section). This may explain the difference in the time history responses after the MHD peak in Figure 10(a). The specimen cracking actually occurred at the test 1.9 while the numerical model (assuming average mechanical parameters) predicts cracking in the test 1.8. Figure 4.9a shows also a numerical response assuming same SDOF parameters but neglecting the wall pre-cracking phase leading to a significant overestimation of the response at low intensity levels.

Figure 4.9a allows observing a phenomenon that seems paradoxical: for the highest input run (PGA=0.96g) the displacement demand of an already cracked model is lower than the demand on a model representing a specimen that was undamaged at the beginning of that run. This behaviour is particularly evident when the cracking strength  $F_{cr}$  is mostly governed by the flexural strength of masonry (e.g. high  $f_w$ , low overburden stress  $O$ ); in these cases,  $F_{cr}$  could be much higher than  $F_0$ . The higher displacement demand related to the initially un-cracked model could be related to the transition between the two points of dynamic equilibrium after and before cracking associated with different stiffness and strength.

Figure 4.10 shows the comparison between experimental and numerical of MHD and mid-height hinge acceleration (MHA) histories for some tests associated with different testing phases. From this, it is seen that the numerical model can predict the experimental response in terms of both MHDs and MHAs quite well. The parameters assumed are the ones listed in Table 4 and shown in legend of Figure 4.10. The  $a_1$  parameter controls the low amplitude response while the collapse is affected mainly by the force plateau ( $b_1$  parameter). It is also worth noticing that the damping ratio values assumed in the



numerical simulations (between 5.5 and 7%) are consistent with the one calculated by [23] assuming a logarithmic decay, which were reported to be between 5% and 10%. Moreover, a reduction of the force plateau has been necessary in the testing phase 6 in order to simulate the specimen strength and stiffness degradation due to repeated tests and to capture the collapse that occurred in test 5.3.



**Figure 4.10. Comparison between experimental and numerical MHD and MHA histories for the following tests: SIN-03-00 Test 1.9 (a), SIN-03-00 Test 2.3 (b), SIN-01-00 Test 3.7 (c), SIN-01-00 Test 5.1 (d) SIN-01-00 Test 5.2 (e) SIN-01-00 Test 5.3 (f).**

#### 4.5.2. Simulation of the dynamic response of cavity wall specimens

Experimental evidence has shown that the cavity wall typology tested by Graziotti et al. [23] is characterised by compatibility of horizontal displacement between the two masonry leaves until the OOP collapse of the wall, even for the specimens built with only 2 ties/m<sup>2</sup>. This allowed for simulation of their response with the numerical model presented here. For consistency, the tri-linear parameters assumed for the single leaf specimen have been adopted to characterise the cavity  $F-u$  relationship loaded at the same value of vertical pressure. The only difference is in the parameter  $a_3$ , where for the cavity wall specimens the mortar pointing degradation  $p$  has been set equal to zero, consequently  $a_3$  is slightly larger. This choice simplifies the  $F-u$  curve considering the uncertainty of a precise instability displacement for a CAVS. The cracking force is simply the sum of the cracking forces associated with the two leaves plus the coupling force contribution, while the cracking displacement is the one associated with the inner CS leaf. The assumed  $\beta$  parameter is equal to 2. The coupling force contribution assumed to successfully simulate the responses of the two degrees of connection considered in this study (2 and 4 ties/m<sup>2</sup>) were 0.7 and 1.4 kN. These values resulted slightly higher than the ones computed by adopting equation 15 giving 0.4 and 0.8 kN, respectively. Consider also that the effective increase of the wall resistance is given by a percentage ( $b_1$ ) of the input coupling force,  $F_c$ . The ties plastic moments and the corresponding shears ( $M_i$  and  $V_i$ ) used for the calculation are 3 Nm and 100 N, respectively. The tie tensile strength was 430 MPa. Further research for the understanding of the role of the tie system in the cavity wall lateral resistance is needed.

Table 5 presents the parameters that resulted in a satisfactory modelling of the experimental response through the different testing phases. The damping ratio values adopted are again consistent with those found by Graziotti *et al* [23]. (between 15 and 20%). Moreover, consistently with experimental observations, damping ratio values in the specimens with 2 ties/m<sup>2</sup> are higher due to a slight out-of-phase displacement phenomenon between the two masonry leaves (especially for low amplitude motions). In general, a reduction of the damping with increasing number tests on the same specimens, which is associated with the degradation of the ties bond and the reduction of their contribution to the response, has been both experimentally and numerically observed. This trend is particularly evident in the response of the CAV-01-04 specimen.

**Table 4.5 SDOF parameters adopted to simulate the experimental response in the different testing phases for the cavity wall specimens.**

<i>Spec.</i>	<i>T.P.</i>	$F_{cr}$ [kN]	$\beta$ [-]	$u_{cr}$ [mm]	$F_0$ [kN]	$F_0^*$ [kN]	$F_c$ [kN]	$u_{ins}$ [mm]	$u_{ins}$ [mm]	$a_1$ [-]	$a_2^*$ [-]	$a_3$ [-]	$b_1$ [-]	$\xi_{in}$ [%]
CAV-01-02	1	9.04	2	1.3	5.81	7.13	0.7	77.6	102	0.03	0.08	0.98	0.90	19
	2	-	-	-	5.11	6.43	-	77.6	102	0.03	0.19	0.98	0.80	16
CAV-03-02	1	11.89	2	2.0	12.23	16.48	0.7	75.4	102	0.04	0.18	0.96	0.775	15
	2	-	-	-	11.54	15.78	-	75.4	102	0.04	0.21	0.96	0.75	15
CAV-01-04	1	10.18	2	1.3	6.89	8.00	1.4	77.6	102	0.03	0.08	0.98	0.90	18
	2	-	-	-	5.49	6.60	-	77.6	102	0.03	0.19	0.98	0.80	15
	3	-	-	-	5.49	6.60	-	77.6	102	0.03	0.25	0.98	0.725	11

Figure 4.11 shows the comparison between the experimental response and the results of the numerical model in terms of PGA and peak MHD (CS inner wall) for the testing

phase 1 and 2 of the CAV-01-02 specimen. The response of the numerical model agrees well with what was observed experimentally, and the transition between elastic and rocking phase is excellently captured. The second phase of the response, characterised by oscillation amplitude beyond 15 mm, is characterised by a drop of the tri-linear plateau to 0.80 and a reduction of the damping to 16%. The comparison between experimental and numerical values of MHD and MHA shows that as the accelerations recorded at the wall mid-height are characterised by several acceleration spikes before the significant pulses of the input. Those spikes were partially induced by a “pounding” phenomenon of the outer leaf against the stiffer inner leaf allowed by the progressive degradation of the tie bond system. In this phase of the response the cavity wall is basically a two DOF system, the numerical model cannot capture this behaviour, but it can successfully simulate the response at high level of MHD.

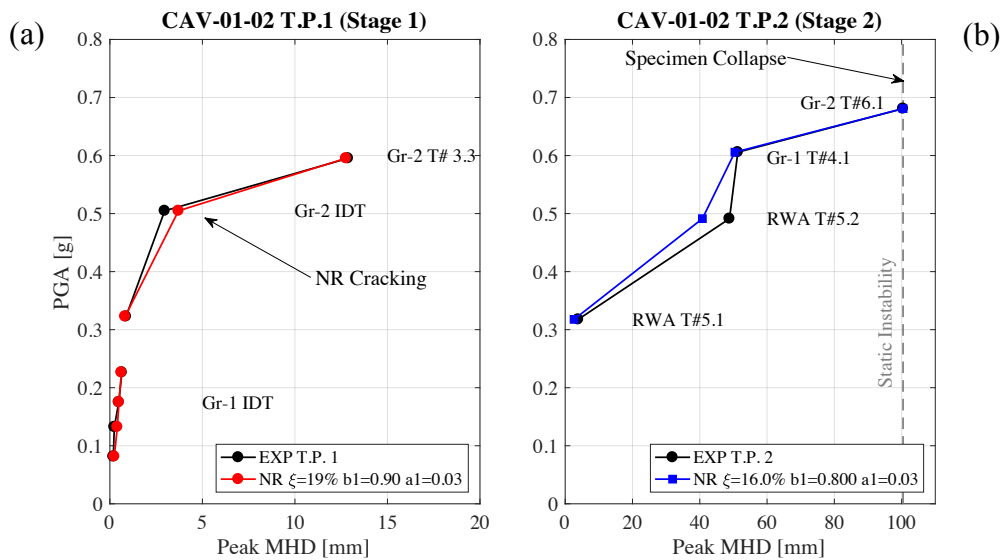


Figure 4.11. Comparison between experimental and numerical MHD: testing phases 1 (a) and 2(b) of the CAV-01-02 specimen.

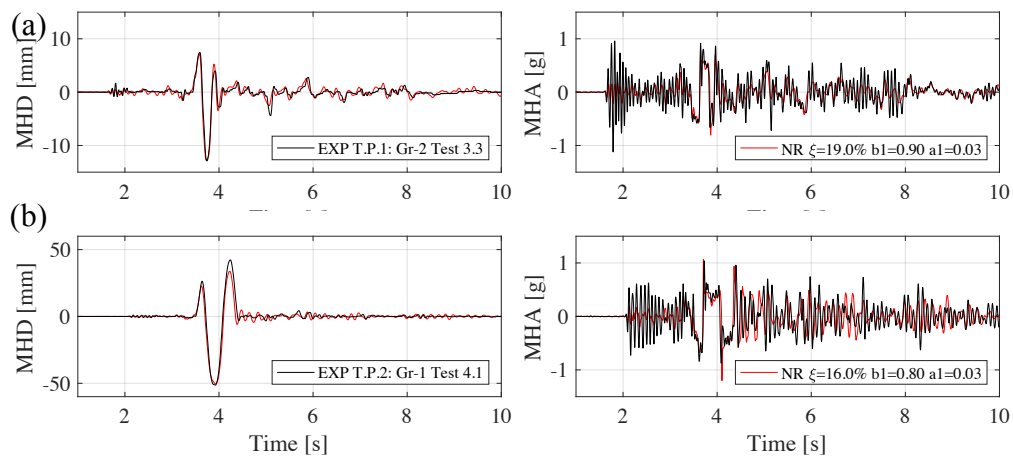
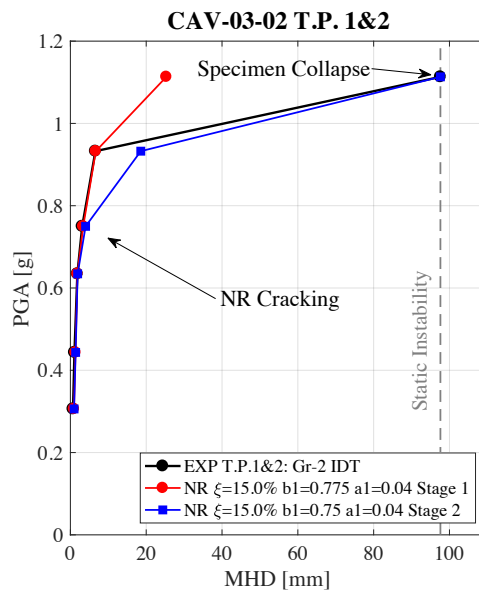
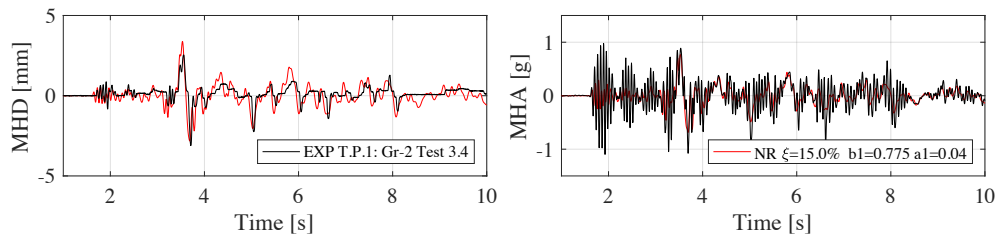


Figure 4.12. Comparison between experimental and numerical MHD and MHA histories for the tests: CAV-01-02 Test 3.3 (a), CAV-01-02 Test 4.1 (b).

Figure 4.13 shows the comparison between the experimental response and the results of the numerical model in terms of PGA and peak MHD (CS inner wall) for the testing phase 1 and 2 of the CAV-03-02 specimen. The numerical model, considering the specimen undamaged, can successfully simulate the experimental response until the test #5.1 (red line). The specimen stage 2 is simply the last test (#5.2) when the specimen attained collapse. It has been captured by neglecting the coupling force  $F_c$  and reducing the  $b_l$  value to 0.80. The response to the entire testing sequence assuming this configuration is also shown (blue line). Figure 4.14 shows the comparison between experimental and numerical MHD and MHA histories for the test #3.4. Again, an acceptable match between MHD and MHA time histories has been achieved, despite the incapacity of the numerical model to capture the acceleration spikes given by the pounding phenomenon between the two walls.



**Figure 4.13. Comparison between experimental-numerical MHD: testing phases 1 and 2 of the CAV-03-02.**



**Figure 4.14. Comparison experimental-numerical MHD and MHA histories for the Test 3.4 (CAV-03-02).**

The last specimen considered for the calibration is the CAV-01-04. The higher number of ties (4 ties /m<sup>2</sup>) ensured the capability to sustain a larger number of high intensity tests. The proposed parameters for testing phase 1 have shown to successfully simulate the

experimental response up to an oscillation amplitude beyond 50 mm (see Figure 4.15a); also the transition between pre-cracking and post-cracking is very well captured. The tests belonging to testing phases 2 and 3 have been simulated by progressively decreasing force plateau, acting damping and neglecting the contribution of the coupling force (see Figure 4.15b). Figure 4.16 shows the very good match between experimental and numerical of MHD and MHA histories for the test #3.4.

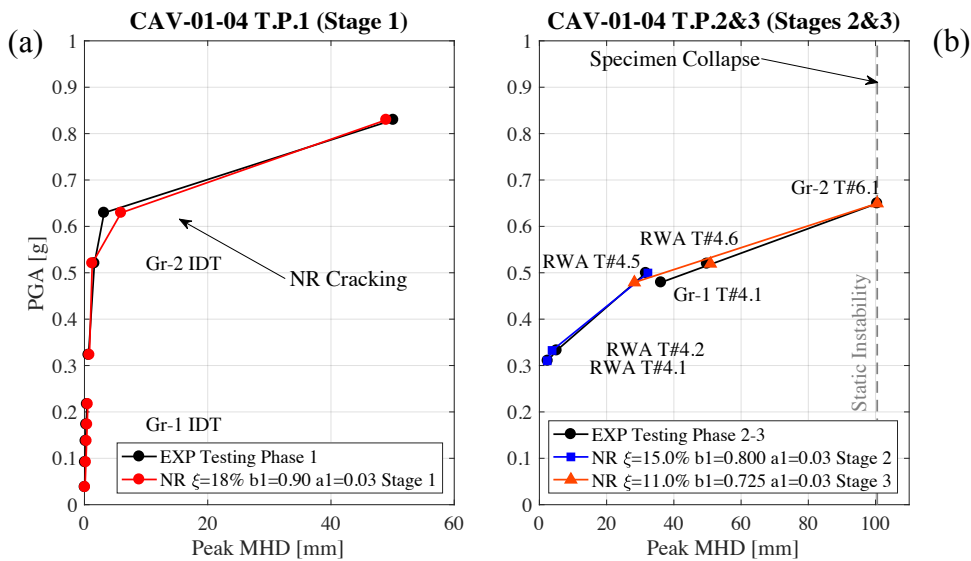


Figure 4.15. Comparison experimental-numerical MHD: testing phases 1(a), 2 and 3(b) of the CAV-01-04.

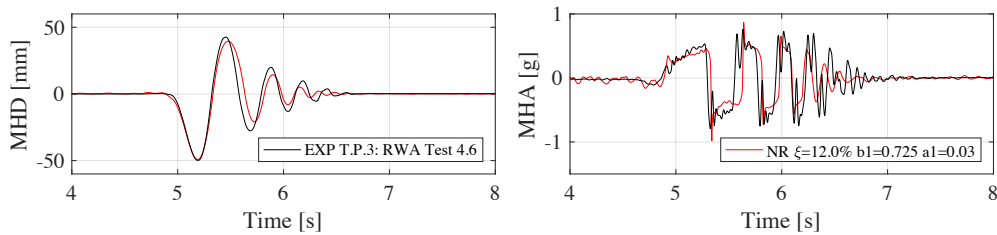
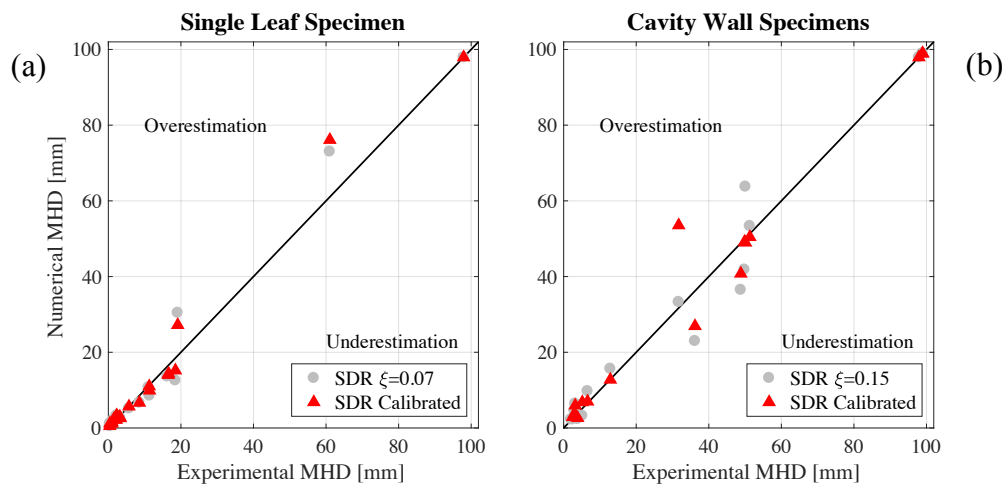


Figure 4.16. Comparison experimental-numerical MHD and MHA histories for the Test 4.6 (CAV-01-04).

### 4.5.3. Summary of the results

One of the main goals of the present study is to provide reliable indications to model the OOP behaviour of single leaf and cavity walls specimens. If the  $F-u$  relationships of the two vertical load conditions (*e.g.* different eccentricity of the imposed vertical load) can be sufficiently characterised by the parameters proposed in Table 3 and adopted for the simulations of each testing sequence, a further effort is required for the definition of an average damping value. The damping ratio values presented in Table 4 and 5 have been calibrated for the different testing phases. The results of these tests have been compared with analysis performed with the same tri-linear relationships (considering also the specimen degradation) but keeping the damping ratio as constant value for all of the tests. Figure 4.17 plots the experimental-numerical peak MHDs for single leaf and cavity walls

specimens comparing the performance of the parameters listed in Table 4 and 5 (red triangles) with the one provided by a single damping value (gray dots). MHD values of about 100mm correspond to the static instability of the panel. In the experimental study the displacement was limited to this value by a safety restraining system. When the peak MHD obtained numerically exceeded this threshold it was automatically set equal to it. This allowed to evaluate if the numerical model with the selected damping was able to capture the collapse of the specimen. The suggested damping values are 7% for the single leaf specimen and 15% for cavity walls specimens. These damping ratio values have been selected because they minimise, for each the tests, the sum of the squared difference percentages between numerical and experimental MHD peak responses.



**Figure 4.17. Comparison between numerical MHD peak response predictions: damping ratio varying for each testing sequence (red triangles) vs average damping ratio value (gray circles).**

Further considerations are needed regarding the simulation of the OOP behaviour of cavity wall specimens, in particular regarding the  $F-u$  curve. A distinction needs to be made according to the degree of connection between the two walls: the collapse of both walls with only 2 ties/m<sup>2</sup> (CAV-01-02 and CAV-03-02) have been captured by assuming a lateral resistance composed simply by the sum of the rigid body assumption force associated with the two wythes considered independently, neglecting the coupling force  $F_c$  lost in earlier testing stages at low levels of MHD. The overstrength associated with the contribution of force coming from the ties has been lost at earlier stages of testing at very low intensities of shaking and MHDs. For the specimen with 4 ties/m<sup>2</sup> (CAV-01-04), instead, a high amplitude response (beyond 50 mm of MHD) has been successfully simulated considering this contribution of the coupling force. Consequently, when interested in the collapse limit state only, the authors suggest to model cavity walls with weak connections (2 ties/m<sup>2</sup>) by simply summing the two leaves' rigid forces and cavity walls with stronger connection (4 ties/m<sup>2</sup>) by considering the coupling force contribution. This suggestion is further justified if the specimens are exposed to natural ground motions that are characterised by higher number of cycles leading to a quick deterioration of the tie bond and the drop of coupling contribution force mentioned earlier are considered.

#### 4.5.4. Selection of the most appropriate damping model

The satisfactory simulations presented herein have been obtained by assuming an SDR damping model. The performance of the three damping models presented in section 4.2.3 have been compared in order to evaluate their accuracy in predicting the experimental response and justify the proposed model. For each damping model, only the best  $\xi$  value ( $\xi_{in}$  for the SDR model) has been selected (according to section 4.4.4) and compared; the  $F-u$  tri-linear curves characterising the specimen status through the different testing stages were the same for the three sets of analyses.

Figure 4.18 shows the comparison of peak MHDs for the three damping models for both the single leaf and cavity wall specimens. In general, both systems acting on the system secant stiffness SDR and CDR models have shown to better capture the rocking phenomenon. The CDC model tended to overestimate low oscillations amplitudes, underestimating high oscillations close to collapse.

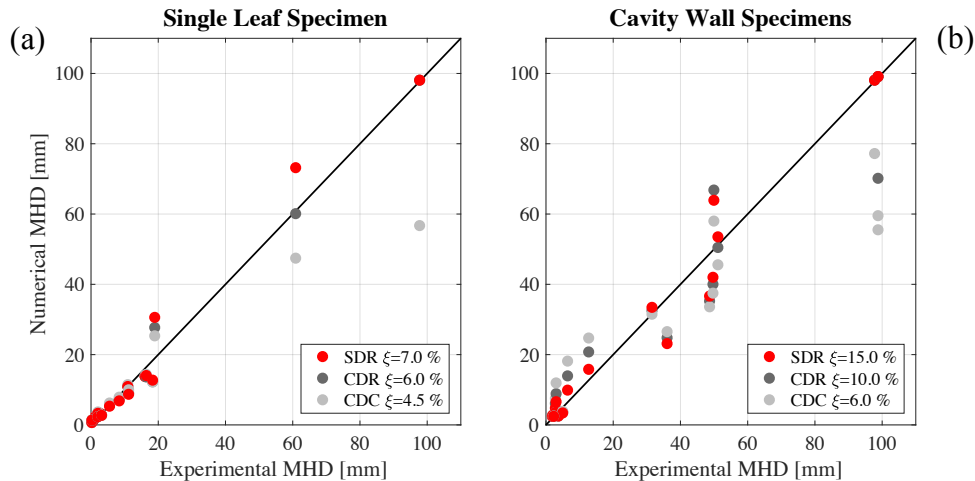


**Figure 4.18. Comparison between numerical MHD peak response predictions performed by different damping models.**

Table 4.6 compares the performance of the three damping models indicating the related sum of the squared difference percentages between numerical and experimental MHD peak responses.

Regarding the single leaf specimen, the best performance is obtained by adopting a CDR model, whereas the SDR model tends to slightly overestimate high oscillations (between second and third branch of the tri-linear curve). A frequency-damping ratio function with the classical Rayleigh formulation (as experimentally observed by [8]) may entirely capture the damping phenomenon. However, further research and experimental tests with rocking response of single leaf walls in the third tri-linear branch region are needed to confirm this trend. For what concerns cavity wall specimens, the best performance is given by the SDR model. These outcomes agree well with the frequency-damping relationships experimentally measured by Graziotti *et al.* [23] for both wall typologies. They observed a constant frequency-damping relationship for the single leaf wall and a linear (stiffness proportional) trend for cavity specimens. In general, the SDR model guaranteed the lowest error on peak MHDs considering both wall typologies.

**Table 4.6 Comparison between summation of squared difference percentages between experimental and numerical MHD response peaks performed by different damping models for all the tests.**

<i>Single leaf Specimen</i>		<i>Cavity Wall Specimens</i>	
$\xi$	$\sum_{p=1}^{n^{\circ} \text{ of test}} \frac{(MHD_{p,NR} - MHD_{p,EXP})^2}{MHD_{p,EXP}}$	$\xi$	$\sum_{p=1}^{n^{\circ} \text{ of test}} \frac{(MHD_{p,NR} - MHD_{p,EXP})^2}{MHD_{p,EXP}}$
SDR 7.0%	15.9	SDR 15%	20.8
CDR 6.0%	10.9	CDR 10%	49.8
CDC 4.5%	23.4	CDC 6%	113.0

#### 4.6. Conclusions

This paper proposes a numerical SDOF model for the OOP analysis of masonry walls. The model was implemented to successfully simulate the OOP one-way bending dynamic response of single leaf and cavity wall URM specimens with Dutch detailing [23].

The calibration work provides useful information on the force displacement relationship and the damping properties of these wall typologies in both pre-and-post activation mechanism phases. A simplified formulation is proposed in section 4.2.1.1 to estimate cracking force and initial stiffness of the wall typologies. Modelling such elastic phase is extremely important if interested in assessing not only for assessing collapse controlled by rocking but also the cracking limit state.

Two tri-linear configurations (Table 3) corresponding to vertical overburden pressure equal to 0.3 and 0.1 MPa have been proposed to successfully model the rocking behaviour of 102-mm-thick CS single leaf walls. Stiffness and strength degradation of the specimens has been modelled by reducing the tri-linear plateau as previously suggested by Doherty [8].

The tri-linear rocking relationships of cavity systems (assuming the same parameters found for the two single leaf configurations) has been built on rigid bi-linear curves obtained by simply summing the forces associated with the RB mechanism of the two leaves considered independently. A further contribution to the lateral resistance has been outlined to originate from the tie coupling system forces. Three stages of degradation of the cavity specimen have thus been identified. A methodology for modelling the dynamic behaviour of cavity walls accounting for the contribution of the ties is presented in this work. It explicitly allows considering the degree of connection between the two leaves.

The efficiency of different damping models in simulating the experimental responses was also tested. As a result, the work highlighted that a classical EVD damping model (constant damping coefficient) cannot capture the dependence of the damping phenomenon on the oscillation amplitude underestimating large oscillation peaks. Damping models acting on the system's current secant stiffness was shown to better simulate the experimental dynamic response. In general, a stiffness-proportional damping model (SDR), assuming  $\zeta_{in}$  values equal to 7% and 15% for single leaf and cavity wall specimens respectively, has been shown to have the best performance for the simulation of response peaks of both wall typologies (Table 4.6). Adopting a constant damping ratio (CDR) also showed rather good performance in simulating the experimental responses.



#### 4.7. Acknowledgments

This paper is partially financed by the research project “*Seismic assessment of natural stone masonry buildings in Basel - A research and training project*”, jointly carried by the École Polytechnique Fédérale de Lausanne and the University of Pavia, funded by the Swiss Federal Office for the Environment and the Canton Basel-City. The useful advices of Dr. G. O’Reilly, Dr. G. Guerrini and S. Sharma are gratefully acknowledged.

#### 4.8. References

- [1] Giuffrè A. A mechanical model for statics and dynamics of historical masonry buildings. Protection of the Architectural Heritage Against Earthquakes. Springer-Verlag: Wien, 1996; 71-152.
- [2] Dizhur D, Ingham J, Moon L, Griffith M, Schultz A, Senaldi I, Magenes G, Dickie J, Lissel S, Centeno J, Ventura C, Leite J, Lourenco P. Performance of masonry buildings and churches in the 22 February 2011 Christchurch earthquake. Bull. New Zealand Society for Earthquake Engineering 2011; 44(4):279-296.
- [3] Ingham J, Griffith M. Performance of unreinforced masonry buildings during the 2010 Darfield (Christchurch, NZ) earthquake. Australian Journal of Structural Engineering 2011; 11(3): 207-224.
- [4] Sorrentino L, Liberatore L, Liberatore D, Masiani R. The behavior of vernacular buildings in the 2012 Emilia earthquakes. Bulletin of Earthquake Engineering, 2014, 12:2367-2382.
- [5] Penna A, Morandi P, Rota M, Manzini CF, Da Porto F, Magenes G. Performance of masonry buildings during the Emilia 2012 earthquake. Bulletin of Earthquake Engineering, 2014, 12(5):2255-2273.
- [6] Costa AA, Arède A, Penna A, Costa A. Free rocking response of a regular stone masonry wall with equivalent block approach: experimental and analytical evaluation. Earthquake Engineering & Structural Dynamics 2013; 42(15), 2297–2319.
- [7] Housner GW. The behavior of inverted pendulum structures during earthquakes. Bull Seismological Society of America 1963; 53(2): 403–417.
- [8] Doherty KT. An investigation of the weak links in the seismic load path of unreinforced masonry buildings, PhD Thesis, University of Adelaide, Australia; 2000.
- [9] Sorrentino L, Masiani R, Griffith MC. The vertical spanning strip wall as a coupled rocking rigid body assembly, Structural Engineering and Mechanics 2008; 29: 433–453.
- [10] DeJong MJ, Dimitrakopoulos EG. Dynamically equivalent rocking structures, Earthquake Engineering & Structural Dynamics 2014; 43(10): 1543–1563.
- [11] Restrepo Vélez LF. Seismic risk of unreinforced masonry buildings. PhD thesis, ROSE School, University of Pavia, Italy; 2004.
- [12] Makris N, Konstantinidis D. The rocking spectrum and the limitations of practical design methodologies. Earthquake Engineering & Structural Dynamics 2003; 32(2):265–89.
- [13] Griffith M C, Magenes G, Melis G, Picchi L, Evaluation of out-of-plane stability of unreinforced masonry walls subjected to seismic excitation. Journal of Earthquake Engineering, 2003, 7,141-169.
- [14] Lagomarsino L, Seismic assessment of rocking masonry structures, Bulletin of Earthquake Engineering, 2014, 13:97-128.
- [15] Ferreira TM, Costa AA, Vicente R, Varum H. A simplified four-branch model for the analytical study of the out-of-plane performance of regular stone URM walls, Engineering Structures 2015; 83:140–153
- [16] Lam NTK, Griffith M, Wilson J, Doherty K. Time-history analysis of URM walls in out-of-plane flexure. Engineering Structures 2003; 25(6):743–754.
- [17] Tomassetti U, Graziotti F, Penna A, Magenes G. Energy dissipation involved in the out-of-plane response of unreinforced masonry walls, In: Proc. 6th Compdyn, Rhodes, Greece, 2017. DOI: 10.7712/120117.5622.18454
- [18] Simsir CC, Aschheim MA, Abrams DP. Out-of-plane dynamic response of unreinforced masonry bearing walls attached to flexible diaphragms. In: Proc. 13th World Conf. on Earthquake Engineering, Vancouver, BC, Canada; 2004.

- [19] Penner O, Elwood KJ. Out-of-Plane dynamic stability of unreinforced masonry walls in one-way bending: shake table testing. *Earthquake Spectra*, in-press, 2016; doi: <http://dx.doi.org/10.1193/011415EQS009M>.
- [20] Costa AA, Penna A, Arede A, Costa A. Simulation of masonry out-of-plane failure modes by multi-body dynamics. *Earthquake Engineering & Structural Dynamics*, 2015, 44(14).
- [21] D'Ayala D, Shi Y. Modeling masonry historic buildings by multi-body dynamics. *International Journal of Architectural Heritage*, 2011, 5(4-5), 483-512.
- [22] Derakhshan H, Griffith MC, Ingham, JM. Seismic Out-of-plane seismic response of vertically spanning URM walls connected to flexible diaphragms. *Earthquake Engineering & Structural Dynamics* 2015: 45(4), 563-580.
- [23] Graziotti F, Tomassetti U, Penna A, Magenes G. Out-of-plane shaking table tests on URM single leaf and cavity walls, *Engineering Structures*, 2016 125, 455-470. DOI: 10.1016/j.engstruct.2016.07.011
- [24] Derakhshan H, Griffith MC, Ingham JM, Airbag testing of multi-leaf unreinforced masonry walls subjected to one-way bending. *Engineering Structures*, 2013, 57, 512-522.
- [25] ABK. Methodology for Mitigation of seismic hazards in existing unreinforced masonry buildings: The methodology. A joint venture of Agbabian Associates, SB Barnes and Associates, and Kariotis and Associates (ABK), Topical Report 08, c/o Agbabian Associates, El Segundo, California; 1984.
- [26] Derakhshan H, Griffith MC, Ingham JM, Out-of-plane behaviour one-way spanning unreinforced masonry walls. *Journal of Engineering Mechanics* 2013, 139(4): 409-417.
- [27] Sorrentino L. Dinamica di muri sollecitati fuori del piano come sistemi di corpi rigidi. PhD thesis, Sapienza University of Rome, Italy; 2003 (in Italian).
- [28] Derakhshan H, Dizhur DY, Griffith MC, Ingham, JM. Seismic Assessment of out-of-plane loaded unreinforced masonry walls in multi-storey buildings, *Bull. New Zealand Society for Earthquake Eng.* 2014; 47(2): 119-138.
- [29] Priestley MJN. Seismic behaviour of unreinforced masonry walls. *Bulletin of the New Zealand National Society for Earthquake Engineering* 1985, 18 No. 2.
- [30] Godio M, Beyer K, Analytical model for the out-of-plane response of vertically spanning unreinforced masonry walls, *Earthquake Engineering & Structural Dynamics*, 2017, DOI: 10.1002/eqe.2929.
- [31] Newmark NM, A method of computation for structural dynamics. *Journal of Engineering Mechanics*, ASCE, 1959, 85 (EM3) 67-94.
- [32] NAM (2015) Hazard and Risk Assessment for Induced Seismicity Groningen. Study 1 Hazard Assessment. (Update 1st May 2015). Available from at: <http://feitenencijfers.namplatform.nl/download/rapportdialog/e2db3b7a-1719-40cb-9002-35f9fcbd1ffd>
- [33] Messali F, Ravenshorst G, Esposito R, Rots J, Large scale testing program for the seismic characterization of Dutch masonry walls. *Proc. 16th World Conf. E. E.*, Santiago, Chile, 2017.

## 5. Modelling energy dissipation in rocking response via equivalent viscous damping

Tomassetti U., Graziotti F., Penna A. Modelling Energy Dissipation in Rocking Response via Equivalent Viscous Damping, *Earthq. Eng. Struct. Dyn.* (to be submitted).

**Abstract.** The assessment of the out-of-plane response of masonry structures has been largely investigated in literature assuming walls respond as rigid or semi-rigid bodies, and relevant equations of motion of single-degree-of-freedom and multi-degree of freedom systems have been proposed. Therein energy dissipation has been usually modelled resorting to the classical hypotheses of impulsive dynamics, delivering a velocity-reduction coefficient of restitution applied at impact. In fewer works a velocity-proportional damping force has been introduced, by means of a viscous coefficient being constant or variable, with constant or stiffness-proportional damping ratio. A review of such models is presented, a criterion for equivalence of dissipated energy is proposed and equations predicting equivalent viscous damping ratios are derived. Finally, equations of motion resorting to equivalent viscous damping ratios are proved effective against experimental responses and large sets of natural ground motions.

### 5.1. Introduction

The out-of-plane (OOP) behaviour of unreinforced masonry (URM) structures subjected to ground motion excitations [1][2][3][4][5] has been extensively investigated by referring to the rocking dynamics of rigid or semi-rigid wall segments. Such an interpretation, confirmed by several experimental tests [6][7][8], could be considered acceptable under specific hypotheses and in case the masonry quality is adequate to avoid disintegration. These rocking bodies impact against each other and the foundation and energy dissipation can be associated to such impact

In a pioneer study, Housner [9], resorting to the classical hypotheses of impulsive dynamics, reduced the velocity of an inverted pendulum by means of a coefficient of restitution (CR) every time it impacted against the foundation.

In the last fifty years the experimental determination of the CR for different masonry block configurations, and interface conditions has been studied [10][11][12][13][14]. The CR was largely adopted for the study of the dynamic behaviour of rigid blocks under trigonometric pulses [15][16][17] and earthquake excitations [18][19][20]. The CR was also employed for simulating the energy dissipation characterising the dynamic response of two-bodies vertical spanning strip walls [21], portal frames [22] and multi block

systems representing potential masonry collapse mechanisms [23]. Moreover, recent studies concerning the derivation of overturning fragility curves of historical masonry façades [24][25], and rocking elements [26][27] also adopted a CR.

In fewer works, the energy dissipation involved in the OOP dynamic response of URM walls has been modelled resorting to a viscous damping force; adopting a constant [28] or a cycle-to-cycle variable [29], damping ratio.

Nevertheless, recent experimental studies on the rocking response of free standing rocking members (i.e. on reinforced-concrete (RC) blocks or steel columns) supported by analytical interpretations highlighted that a significant amount of energy is dissipated continuously other than that lost during impacts [30][31][32][33]. This continuous dissipation can be attributed to flexural response of the main body as well as to the deformation of the rocking interfaces. For example, Kalliontzis and Sritharan [31] have shown that the accuracy of an inverted pendulum model adopting an improved CR (i.e. accounting for physical dimensions of the pivot point [34]) in simulating the rocking response of a RC blocks on a concrete foundation can be significantly improved by integrating the equation of motion with a velocity dependant viscous force and an energy gain coefficient.

This paper presents a methodology to simulate the energy dissipation in the rocking response of URM walls exclusively adopting an equivalent viscous damping (EVD) model. This approach presents several potential advantages over a CR-based framework, such as:

- the rocking problem is formulated in a fashion very similar to that of a classic oscillator, more familiar to engineers;
- its implementation in already available finite-element environments is straightforward and will simplify a comparison with static-equivalent code procedures;
- it allows modelling both the pre-cracking (i.e. before full development of mechanism) and the post-cracking response of walls responding in one-way [35] or two-way bending [36][37];
- the reduced computational effort make the proposed model suitable to perform large numbers of non-linear time-history analyses, such as those necessary to assess the risk for economic and human losses [38].

Hereinafter, a single-degree-of-freedom (SDOF) model for the analysis of the rocking behaviour of parapet wall (PW) and vertical spanning strip walls (VSSW) systems modelling the energy dissipation with different velocity-dependent forces acting on the initial or secant stiffness of the system is presented. Section 2 describes the dynamic behaviour of PW and VSSW mechanisms assuming a rigid body idealisation and the CR as source of damping. Section 3 discusses the assumptions commonly adopted to simulate the OOP behaviour of URM walls accounting for their finite stiffness and strength. EVD models are herein introduced. Tomassetti *et al.* [35] have shown the effectiveness of these damping models in simulating the experimental response of single leaf and cavity VSSW systems [11]. Differences and possible relationships available in literature between EVD-based and CR-based approaches are discussed in Section 4. Section 5 presents the numerical procedure developed in order to propose an equivalence between these damping models. Its validation via comparison with experimental time histories and incremental dynamic analyses is discussed in Section 6.

## 5.2. Dynamic behaviour of rigid body systems

This section reviews the dynamic behaviour of rigid-body systems such as the simple-block and the two-block mechanisms. Initially, the equations of motion for both mechanisms are presented in the form of a classical oscillator. The energy dissipation associated with the two mechanisms is simulated presenting a CR-based approach. Finally, the response given by the numerical model solving the presented equations is validated against existing models in literature.

Figure 5.1 plots a schematic representation of the rocking behaviour of a masonry wall experiencing an OOP excitation. The wall can behave as a single body (of weight  $W$ , mass  $m$ , height  $h$ , thickness  $b$ , and angle  $\alpha$ ) in the case of a PW, rocking about base hinges, or as an assembly of two rigid bodies as in the case of a VSSW. A VSSW responding in rocking is characterised by the formation of pivots at top, bottom and in between. The resulting top and bottom rigid bodies rotate around such pivot points ( $A'-B-C'$  in Figure 1) impacting each other every time the system passes through rest-condition. Angles  $\alpha_2$  and  $\alpha_1$  define the height/thickness ratios of the two bodies,  $h_2$  and  $h_1$  are the related heights,  $W_2$  and  $W_1$  are the corresponding weights and are applied at the bodies' centres of mass,  $m_2$  and  $m_1$  are the related masses,  $O$  is an overburden vertical force (to which no mass is associated) applied with eccentricity  $e$  relative to the centre of the top section. Rotations  $\theta_2$  and  $\theta_1$  are the top and bottom bodies' angular displacements.

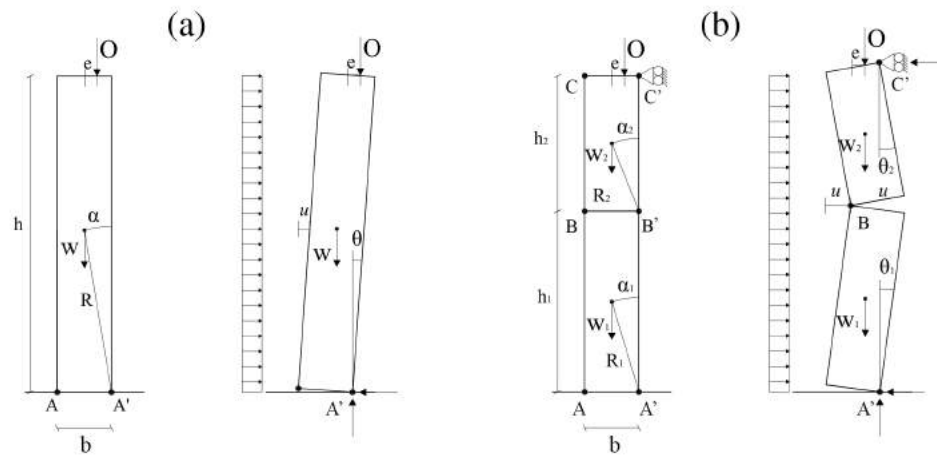


Figure 5.1 Masonry walls in rocking behaviour: geometry at rest and displaced configuration for PW (a) and VSSW (b).

### 5.2.1. Equations of motion

The equation of motion of these rocking systems can be derived directly from Lagrange's equation. Usually the hypotheses of no sliding, no bouncing effect, and simultaneous motion of the supports of the VSSW, are assumed and the corresponding SDOF equations are written in terms of rotations, as done by Housner [9] for a rocking block (representing a PW), or Sorrentino *et al.* [21] and DeJong and Dimitrakopoulos [22] for a VSSW. However, a slender wall allows a piece-wise linearisation of the equation as follows [39]:

$$m_{eff} \cdot \ddot{u}(t) + f_{bi}(u, t) = -\lambda \cdot m_{eff} \cdot \ddot{u}_g(t) \quad (1)$$

where  $u$  represents the horizontal displacement of the wall at mid-height or at intermediate-hinge (shown in Figure 5.1, with  $u \approx \theta \cdot h/2$  or  $u \approx \theta_1 \cdot h_1$ ), for PW and VSSW respectively),  $m_{eff}$  is the effective mass of the system affected by the rotational moment of inertia of the blocks,  $f_{bi}(u, t)$  is the bi-linear rigid-softening restoring force;  $\lambda$  is the parameter that allows exciting the entire mass with the ground acceleration ( $\ddot{u}_g(t)$ ),  $t$  is the time. Table 5.1 identifies these parameters for both mechanisms, assuming a uniformly distributed lateral face load, as a consequence of uniform thickness and density along the wall height. There is experimental evidence that the intermediate hinge is usually located at a non-dimensional height  $h_1/h = 0.5 - 0.7$  [40][11].

**Table 5.1 SDOF parameters for PW and VSSW mechanisms.**

Mechanism	$m_{eff}$	$f_s(u, t)$	$\lambda$
PW	$4/3 \cdot m$	$\frac{2}{h} \cdot W \cdot \left( \frac{b}{2} - u(t) \right) + \frac{2}{h} \cdot O \cdot \left( \frac{b}{2} - e - 2 \cdot u(t) \right)$	3/4
VSSW*	$\frac{2}{3} \cdot (m_1 + m_2)$	$\frac{2}{h_1} \cdot W \cdot (b - u(t)) + \frac{h}{h_1 \cdot h_2} \cdot O \cdot (b + 2e - u(t)) + \frac{2}{h_1} \cdot O \cdot (b - 2e)$	3/2

It is worth emphasising that Equation 1 is undamped. A common approach, relying on the classical hypotheses of the impulse dynamics, is simulating the energy dissipation involved in rocking mechanisms by means of a coefficient of restitution [9][21].

### 5.2.2. Energy dissipation via coefficient of restitution

Aslam *et al.* [41] defined the restitution coefficient  $e$ , as the direct ratio between angular velocities after ( $\dot{\theta}_{n+1}$ ) and before ( $\dot{\theta}_n$ ) the  $n^{th}$  impact. Assuming an infinitesimal impact duration hence instant velocity variation, no displacement during impact and imposing the conservation of angular momentum around the rotational hinge (bottom one for VSSW) by equating the angular momentum after and before the impact, a theoretical coefficient of restitution can be derived as the ratio between the angular velocities after and before the impact for a PW (Equation 2) and VSSW (Equation 3, from [21] assuming homogenous bodies):

$$e_{an, PW} = 1 - \frac{3}{2} \sin^2 \alpha \quad (2)$$

$$e_{an, VSSW} = 1 - 2 \sin^2 \alpha_1 \quad (3)$$

Note that the coefficient of restitution depends on the system slenderness, the squatter the wall (higher  $\alpha$  or  $\alpha_1$ ) the higher the energy dissipation (lower  $e_{an}$ ). Adopting the aforementioned definition, the coefficient of restitution acts by reducing the system velocity at each  $n^{th}$  impact (every time the horizontal displacement  $u$  passes through the null displacement) as follows:

$$\dot{u}_{n+1}(t + dt) = e_{an} \cdot \dot{u}_n(t) \quad (4)$$

### 5.2.3. Validation of the numerical model

The herein presented numerical model solves Equation (1) adopting the Newmark linear acceleration integration scheme implemented in the non-iterative formulation [42]. This reduce the computational effort with respect to event-based procedures which modify the time analysis increment in order to capture instants achieving specific conditions (*e.g.* time of zero displacement, hence, impact). In order to validate the numerical model, Figure 5.2 shows the good match between damped free vibration responses obtained with the implemented SDOF model and the response obtained by Sorrentino *et al.* for PW and VSSW [21].

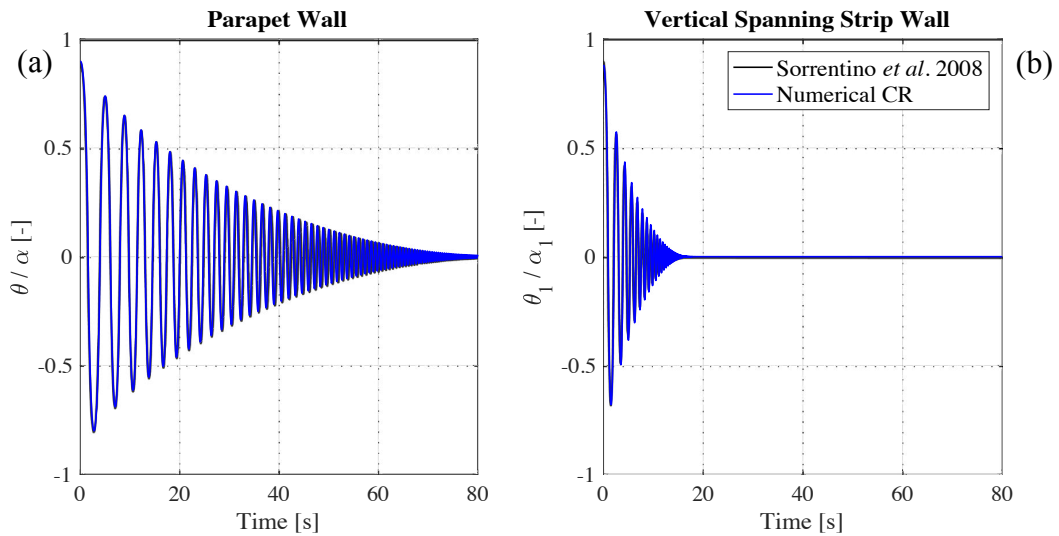


**Figure 5.2 Comparison between damped free vibration response time histories of a PW (a) and VSSW (b) obtained by the presented SDOF and by Sorrentino *et al.* [21]. Details of the walls:  $b=0.4\text{m}$ ,  $h=4.0\text{m}$ ,  $O=0\text{ N}$ ,  $u_0=0.9 \cdot u_{ins}$ ,  $\dot{u}_0=0$ ,  $\ddot{u}_0=0$ ,  $e=0.985$  (PW),  $e=0.955$  (VSSW).**

A further validation of the model is the comparison between the rocking free period of vibration, derived by Housner [9] in closed form solution, and the one obtained from the numerical model. Equation 5 defines the dependence of the time necessary to complete an oscillation to the amplitude of the oscillation itself.

$$T_{PW} = \frac{4}{p} \cosh^{-1} \left( \frac{1}{1 - \theta_0 / \alpha} \right) \quad (5)$$

where  $p$  is the rocking frequency parameter which depends on the block size ( $= \sqrt{3/4} \cdot g/R$  for a single block) while  $\theta_0$  is the initial imposed rotation. Figure 5.3 shows the comparison between the relationship presented in Equation 5 and the periods obtained from undamped free oscillation of the numerical model released from different  $\theta_0$ . Equation 5 and the periods given by the numerical model show good agreement for different block angles ( $\alpha=0.25$ ,  $0.175$  and  $0.1$  rad) and different block sizes ( $p=2$ ,  $3$ ,  $4$ ,  $5$   $\text{s}^{-1}$ ).

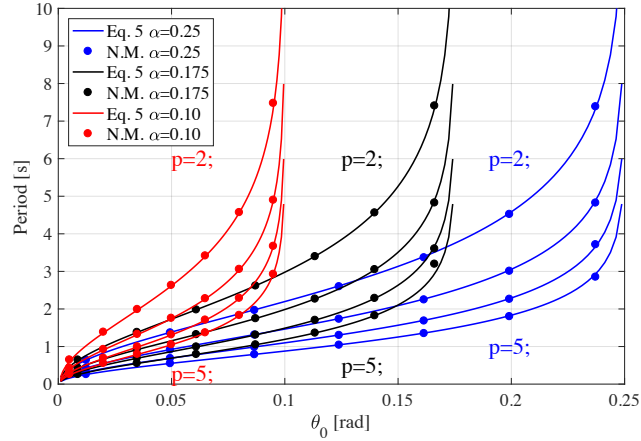


Figure 5.3 Comparison between closed form solution for the dependence of the period on the oscillation amplitude and the results of the numerical model for a PW.

### 5.3. OOP Dynamic behaviour of URM walls

The OOP response of masonry walls has been largely investigated by referring to the rocking dynamics of rigid body systems. Recognising that URM wall segments do not have infinite stiffness and strength, several studies have proposed modifications of the formulation presented in Section 2 in terms of force-displacement relationship and dissipated energy. These aspects will be discussed in section 3.1 and 3.2, respectively.

#### 5.3.1. Force-displacement (F-u) relationship

Before undergoing non-linear rocking behaviour through the development of cracking, URM walls are characterised by a linear response controlled by the masonry flexural strength. A proper consideration of the wall un-cracked response, both in terms of initial stiffness and lateral resistance provided by the tensile strength at the interfaces, may prevent an erroneous estimation of the OOP displacement demand in slender and less slender walls. This has been largely confirmed experimentally [43][44] but also numerically [35].

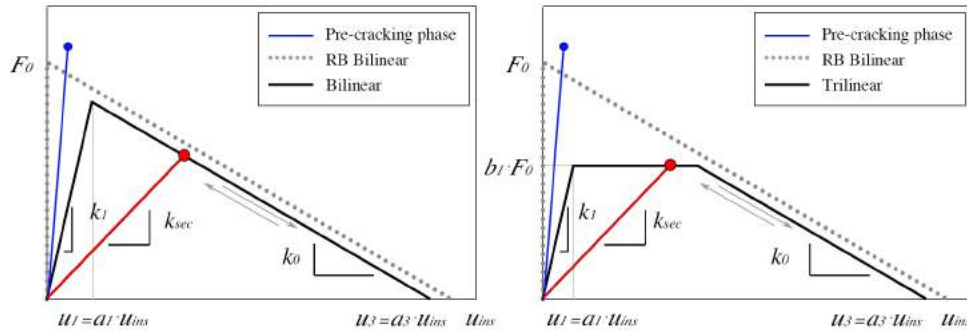
Once the mechanism is triggered, the bi-linear rigid-softening restoring force ( $f_{bi}(u,t)$ ) becomes the reference curve. It relies on the assumption of wall responding as a rigid body or as an assembly of two rigid bodies with an infinite initial stiffness and strength, representing an upper bound of the real OOP static resistance. The bi-linear curve could be identified by the parameters  $F_0$  and  $u_{ins}$  defined according to Table 5.2:

Table 5.2 Rigid body force ( $F_0$ ) and instability displacement ( $u_{ins}$ ) associated with PW and VSSW mechanisms.

Mechanism	$F_0$	$u_{ins}$
PW	$\frac{1}{h}(W+O) \cdot b + \frac{2}{h}O \cdot e$	$\frac{2/h \cdot (W+O) \cdot b/2 - 2/h \cdot O \cdot e}{2/h \cdot (W+2 \cdot O)}$
VSSW	$\frac{2}{h_1}(W+O) \cdot b + \frac{O}{h-h_1}(b+2e)$	$\frac{2/h_1(W+O)b + O \cdot (b+2 \cdot e)/(h-h_1)}{2/h_1(W+O) + 2O/(h-h_1)}$



where  $k_0$  represents the negative stiffness of the system. In order to account for the actual OOP  $F-u$  relationship of a URM wall, different simplified non-linear elastic curves (e.g. bi-linear [45], tri-linear [46][13] and four-branches [47]) constructed from the  $f_{bi}(u,t)$  curve, have been proposed in literature. Figure 5.4 illustrates two commonly assumed idealisations to perform non-linear time history analysis of masonry wall: bilinear and trilinear  $F-u$  relationships. In case of a bilinear  $F-u$  relationship, key parameters are  $u_1$  ( $=a_1 u_{ins}$ ) controlling the wall's initial cracked stiffness and  $u_3$  ( $=a_3 u_{ins}$ ) which, reducing the displacement associated with zero force, may take into account the masonry compressive strength and consequently the physical dimension of the hinges. The trilinear  $F-u$  relationship, is further characterised by  $F_y$  ( $=b_1 F_0$ ) identifies the force plateau; The values for  $a_1$ ,  $a_3$  and  $b_1$  are affected by aspects such as wall thickness, acting vertical overburden force and masonry mechanical properties [48]. Refined works on the characterisation of the  $F-u$  relationship of can be found in [43][13][45][44][48].



**Figure 5.4  $F-u$  relationship implemented: bilinear and trilinear configurations built on the bilinear rigid body idealisation.**

### 5.3.2. Energy dissipation

The overall damping force acting in URM panels or assemblies responding in OOP rocking is given primarily by the energy dissipated through the impact of the wall during rocking in addition to some hysteretic energy dissipation, which both need to be accounted for in the model. The coefficient of restitution experimentally observed for the rocking behaviour of URM elements is lower than  $e_{an}$ , therefore numerical works proposed to replace  $e_{an}$  with an experimental coefficient of restitution  $e_{exp}$  that is  $0.95 \cdot e_{an}$  for PW [12] and  $0.90 \cdot e_{an}$  for VSSW [49]. Graziotti *et al.* observed for a VSSW values of coefficient of restitution ranging between 0.90 and 0.83 with respect to  $e_{an}$  value of 0.99 (specimen slenderness approximately close to 27) [11].

Another option is to model the energy dissipation adopting an EVD approach defining a velocity-dependent damping force through a constant [28], variable (with cycle-to-cycle iterations) [29][43] and stiffness-proportional damping ratio [35].

Despite some studies have shown that the combination of these two different sources of damping (CR and EVD) has shown promising results in simulating the rocking response of RC blocks [31][33], Section 3.2.1 presents several EVD-based damping approaches.

#### 5.3.2.1. EVD models

Three non-iterative EVD-based damping models were investigated, starting from a classical one: the constant damping coefficient (CDC). It assumes a constant damping

ratio ( $\xi$ ) acting on the system initial stiffness ( $\omega_1$ ) of the system [28]. Moreover, two other damping systems have also been investigated and compared in order to capture the dependence of the damping phenomenon on the oscillation amplitude and on the current frequency of vibration. Both damping models act on the instantaneous secant frequency  $\omega(t)$  defined by the instantaneous secant stiffness  $k_{sec}(t)$  of the system (slope of red line in Figure 5.4) and presented in Equation 6:

$$\omega(t) = \sqrt{\frac{k_{sec}(t)}{m_{eff}}} \quad (6)$$

The first one of the two associates a constant damping ratio through all the system frequencies, whereas the second one assumes a stiffness proportional term ( $\xi$ - $\omega$  linear relationship) identified by the damping ratio ( $\xi_{in}$ ) corresponding to the frequency of the first branch of the tri-linear relationship ( $\omega_1$  or  $F_1$ ). The damping coefficient of the three damping models: CDC, constant damping ratio (CDR) and stiffness proportional damping ratio (SDR), is defined by Equations 7, 8, 9 respectively:

$$C_{CDC} = 2 \cdot m_{eff} \cdot \omega_1 \cdot \xi \quad (7)$$

$$C_{CDR}(t) = 2 \cdot m_{eff} \cdot \omega(t) \cdot \xi \quad (8)$$

$$C_{SDR}(t) = 2 \cdot m_{eff} \cdot \omega(t) \cdot \xi(\omega(t)) \quad (9)$$

Figure 5.5 compares the three damping models in terms of the relationship between damping ratio and frequency ( $\xi$ - $\omega$ ) and the one between damping forces (product of the damping coefficients and system velocity) and non-dimensional mid-height displacement (MHD) in matched rocking free vibration decays of a VSSW.

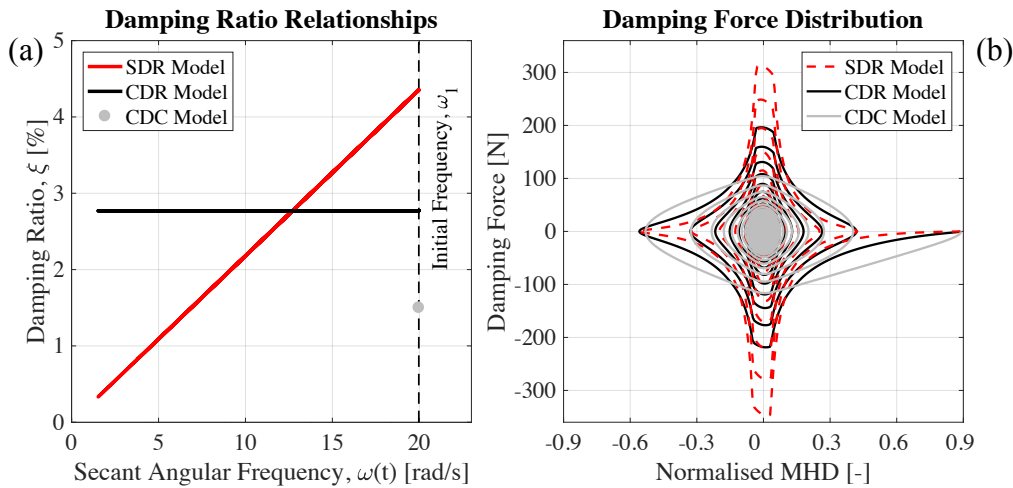


**Figure 5.5 Comparison between  $\xi$ - $\omega$  relationships of the three models (a). Independently from the actual or secant frequency of the system the CDC damp the system proportionally the initial angular frequency. CDR and SDR damping models associate to the current secant frequency a damping ratio according to a constant or a linear (defined by the  $\xi$  value assigned to  $\omega_1$ ) law; distribution of the damping force through the normalised oscillation amplitude of the three damping models: CDC, CDR, SDR (b).**

The wall geometry is the same of the one tested in [11], assuming the same tri-linear parameters ( $a_1=0.04$ ,  $b_1=0.85$  and  $u_3= u_{ins}$ ) for all the three configurations and releasing the systems from an initial normalised displacement equal to 0.9. Independently from the actual or secant frequency the CDC damps the system proportionally to the initial angular frequency. CDR and SDR damping models associate to the current secant frequency a damping ratio according to a constant or a linear law (defined by the  $\xi$  value assigned to  $\omega_1$ ). Both CDR and SDR models, acting on the secant frequency, tend to concentrate the energy dissipation around the zero-oscillations amplitude, which correspond to the impact region, acting in a similar fashion of a coefficient of restitution. The area within the loops in Figure 5.5b representing the dissipated energy is the same for each damping model

#### 5.4. Comparison between CR-based and EVD-based models

CR and EVD are very different damping systems: the former reduces the energy of the system suddenly at each impact, the latter is characterised by a continuous energy loss presenting different distributions according to the selected model (CDC, CDR and SDR, see Figure 5.5b).

Taking as reference a VSSW having geometry  $h=6.0\text{m}$ ,  $b=0.3\text{m}$  (mid-height crack at 4.2m) whose F-u relationship is modelled with a trilinear curve defined by  $a_1=0.04$ ,  $b_1=0.85$  and  $a_3=1.0$ , Figure 5.6 proposes the comparison between matched free vibration responses obtained by releasing the system by an initial displacement equal to 0.9 the instability displacement ( $u_0/u_{ins}$  or  $\theta_0/\alpha$ ) and adopting the CR ( $e=0.875$ ) and a CDR ( $\xi=0.0355$ ) model. The comparison is proposed in terms of normalised MHD time history (Figure 5.6a) and normalised MHD versus normalised MHV (MHV, Figure 5.6b). It is possible to appreciate as the CR acts reducing suddenly the velocity of the block whereas the CDR model decreases smoothly the velocity without inducing a clear discontinuity on it.

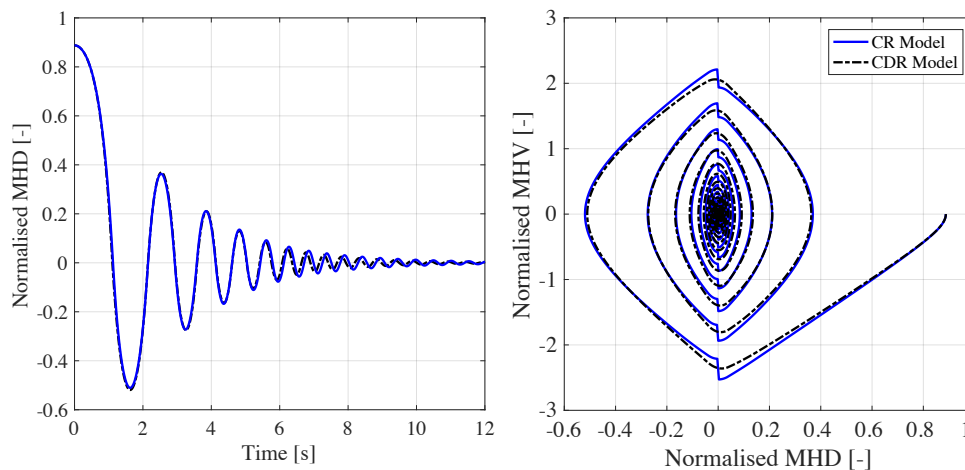


**Figure 5.6 Comparison between matched damped free vibration responses between a CR ( $e=0.875$ ) and a CDR ( $\xi=0.0355$ ) model in terms of normalised MHD time history (a) and normalised MHD versus normalised MHV for a VSSW.**

Priestley *et al.* [50] were the first to study fundamental differences and possible similarities between the classical elastic oscillator (EO) and the rocking block. They tried

to define the EVD ratio associated with the rocking block. This was done by substituting the ratio between peak amplitude displacements in the logarithmic decay of a damped EO with the ratio between maximum rotations after and before the impact derived from Housner [9], which yields in:

$$\xi = \frac{1}{n\pi} \ln \left\{ \frac{\theta_0}{\alpha} \left[ 1 - \sqrt{1 - e^{2n} \left[ 1 - \left( 1 - \frac{\theta_0}{\alpha} \right)^2 \right]} \right]^{-1} \right\} \quad (10)$$

Where  $n$  is the number of impacts experienced (equal to 2 in a full cycle). Priestley *et al.* [50] pointed out as this relation is comparatively insensitive to the initial rotation  $\theta_0/\alpha$ , and number of impacts,  $n$ . Makris and Konstantinidis [18] proposed therefore the following empirical equation to approximate the relation between CR and EVD.

$$\xi = -0.68 \ln(e) \quad (11)$$

Figure 5.7 shows the comparison between free vibrations of a rocking block ( $h=4m$   $b=0.4m$ ) damped by a CR and a EO having period equal to the highlighted cycle. The comparison is proposed for two coefficients of restitution ( $e_{an}=0.985$  and  $e=0.85$ ) while the EVD values associated with the EO are directly calculated from Equation 11. It is possible to see the good match between the damping effect given by the two models as well as the fundamental difference between the two systems: the period of the EO remains constant while the rocking block one is, as expected, oscillation amplitude dependent.

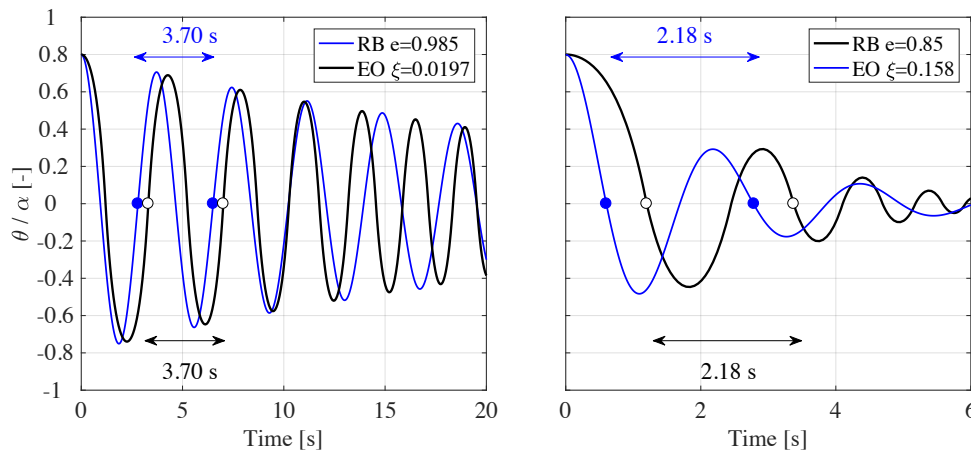


**Figure 5.7 Comparison between matched damped free vibration responses between a CR ( $e=0.875$ ) and a CDR ( $\xi=0.0355$ ) model in terms of normalised MHD time history (a) and normalised MHD versus normalised MHV for a VSSW.**

Nevertheless, modelling the rocking response of a masonry wall having a bi-linear  $F-u$  curve (see Figure 5.4) and adopting the EVD given by Equation 10 or Equation 11, in substitution of a CR, will result in an overdamped response. In other words, the relationship proposed in Equation 10 or 11 might be adopted for linear static procedures and not for performing non-linear time history analysis.

An equivalence between such different damping systems, given a specific  $F-u$  curve configuration, can be carried out by equating the energy losses provided by the different

sources of damping. Generally, the coefficient of restitution, imposing a drop in the velocity at each impact, reduces the kinetic energy of the system. Considering half cycle of displacement between two successive response peaks (positive peak  $u_p^+$  and negative peak  $u_p^-$ ) of a system in free vibration phase, the energy loss due to impact, passing through displacement level equal to zero is given by the difference of kinetic energies after and before the collision:

$$\Delta T = T^+ - T^- = \frac{1}{2} \sum_1^i I_{CMi} \cdot \dot{\theta}_i^{+2} + m_i \cdot v_{CMi}^{+2} - \frac{1}{2} \sum_1^i I_{CMi} \cdot \dot{\theta}_i^{-2} + m_i \cdot v_{CMi}^{-2} \quad (12)$$

where  $\dot{\theta}_i^+$  and  $\dot{\theta}_i^-$  are the bodies angular velocities after and before the impact defined by the rotations according to Figure 5.1, whereas  $v_{CMi}^+$  and  $v_{CMi}^-$  are the centre of mass velocities vectors composed by the two horizontal and vertical components (being the problem defined in 2 dimensions):  $\dot{u}$  and  $\dot{w}$ .

The loss of energy due to an acting viscous damping force can be computed as the work done by the damping force in the considered response and time interval; this yields in the integral of Equation 13:

$$\Delta E = \int_{u_p^+}^{u_p^-} \begin{matrix} C_{CDC} \\ C_{CDR}(t) \\ C_{SDR}(t) \end{matrix} \cdot \dot{u}(t) \cdot du \quad (13)$$

The integral in Equation 14 does not have a trivial solution because the function present several discontinuities corresponding to the  $F-u$  corner points and the law characterising the different damping force depends on the displacement level achieved by the system. Adopting a similar approach, Giannini and Masiani [51] assuming a sine wave displacement rocking response for a rigid block, derived the following equivalence:

$$\xi = \frac{2 \cdot (1 - e)}{\pi \cdot (1 + e)} \quad (14)$$

Therefore, the work will be focused in studying the relationship between these two quantities for the presented EVD models and  $F-u$  relationships.

### 5.5. Derivation of the equivalence between CR and EVD

The work consisted in analysing the damped free vibration response provided by the different damping systems and comparing them. The CR model has been taken as the reference damping systems. This was done with the target of determining a relationship between damping ratio and slenderness of the system via CR. In order to ensure the equivalence between the energy dissipation provided by EVD and CR, satisfying the equivalence between Equations 12 and 13, the damped free vibration decays provided by a velocity dependent acting force (CDC, CDR, SDR) have been matched with the ones provided by a coefficient of restitution.

An error metrics was defined in order to proper select the damping ratio value that allowed to minimise the difference with the coefficient of restitution response for each system.

$$Err = \sum_{j=1}^k (|u_{CR}(j)| - |u_{DAF}(j)|)^2 \quad (15)$$

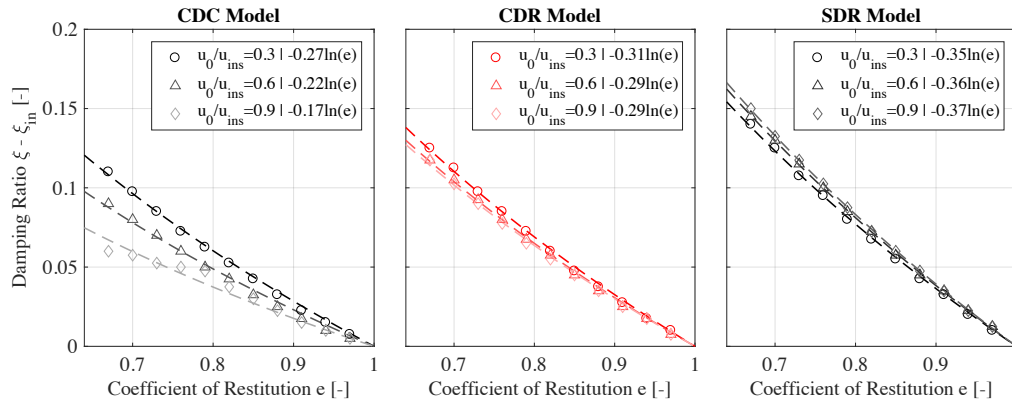
$Err$  represents the summation of absolute difference between the coefficient of restitution decay and the one provided by the models with a damping acting force (CDC, CDR, SDR) at each analysis time step for the entire length of the response ( $k$ ).

Figure 5.8 plots markers indicating the damping ratio values corresponding to each model that minimised the error for a specific PW configuration ( $b=0.4\text{m}$  and  $h=0.4\text{m}$ ) and a defined set of CR (0.67, 0.7, 0.73, 0.76, 0.79, 0.82, 0.85, 0.88, 0.91, 0.94 and 0.97). Releasing the system from an initial imposed displacement equal to 0.9, 0.6 and 0.3 times the instability displacement ( $u_0/u_{ins}$  or  $\theta_0/\alpha$ ), it is also shown the effect of the amplitude of oscillation. The markers are fitted with a logarithmic function as follow:

$$\xi = -x \cdot \ln(e) \quad (16)$$

In general, all the models present a higher dispersion moving towards higher CRs. The equivalence related to the CDC Model is the most sensitive to the oscillation amplitude while CDR and SDR models are only slightly affected by this variable.

In both CDC and CDR models damped high oscillation amplitudes are associated with lower damping ratio values, while for the SDR model the trend is reversed: slightly higher damping ratio values are associated to higher oscillations. This is due to the nature of the SDR model which tend to associate very low damping ratio values to oscillations close to collapse, consequently the request initial damping value to fit the response given by a CR is slightly higher.



**Figure 5.8 EVD values of CDC, CDR and SDR models in matching free vibration responses damped by a CR model. Details of the PW adopted for the comparison:  $a_1=0.06$ ,  $a_3=1.0$ ,  $b=0.4$  and  $h=4\text{m}$ .**

This finding confirm as a CDC model is not a good choice in simulating the energy dissipation involved in rocking mechanism. For the following comparisons, the authors considered as reference  $u_0/u_{ins}$  equal to 0.9. This value is particularly interesting in assessing the behaviour of the system being in vicinity of the static instability (*i.e.*  $u_0/u_{ins}$  equal to 1) and hence the overturning of the element. Figure 5.9 illustrates as the equivalence, once defined a specific bi-linear configuration ( $a_1=0.06$ ,  $a_3=1.0$ ) is insensitive from the block shape reflected by the parameter  $p$  and angle  $\alpha$  (keeping  $b=0.4\text{m}$  and varying  $h$ : 4,6,8 m).

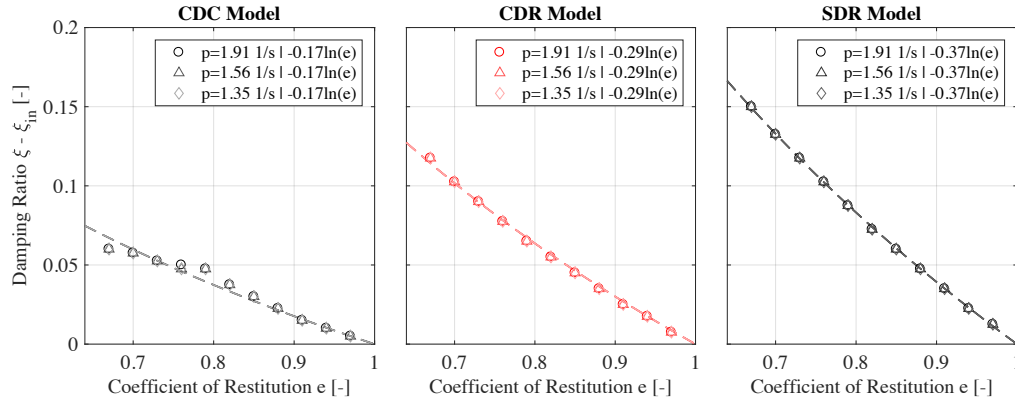


**Figure 5.9** EVD values of CDC, CDR and SDR models in matching free vibration responses damped by a CR model. Details of the PW adopted for the comparison:  $a_I=0.06$ ,  $a_3=1.0$ ,  $u_0/u_{ins}=0.9$ ,  $b=0.4$  and  $h=4,6,8$  m.

On the contrary, the EVD values matching a CR response are strongly affected by the chosen initial stiffness parameter  $a_I$ , which was varied from 0.005 to 0.15 (see Figure 5.10). Again, the most sensitive model to  $a_I$  variations is the CDC one while the less affected is the CDR model. A higher initial stiffness leads to lower values of damping ratio for both CDC and CDR models, the SDR, instead, associates lower damping ratio values to lower  $a_I$  parameters. This is particularly evident for low values of  $e$  that, causing a drop of the oscillation amplitudes, tends to concentrate the free vibration response in low amplitude oscillations, greatly affected by  $a_I$  (linear elastic oscillator type response leading to secant stiffness equal to the initial one); the lower  $a_I$  the quicker the oscillations decay and the higher the requested SDR damping.

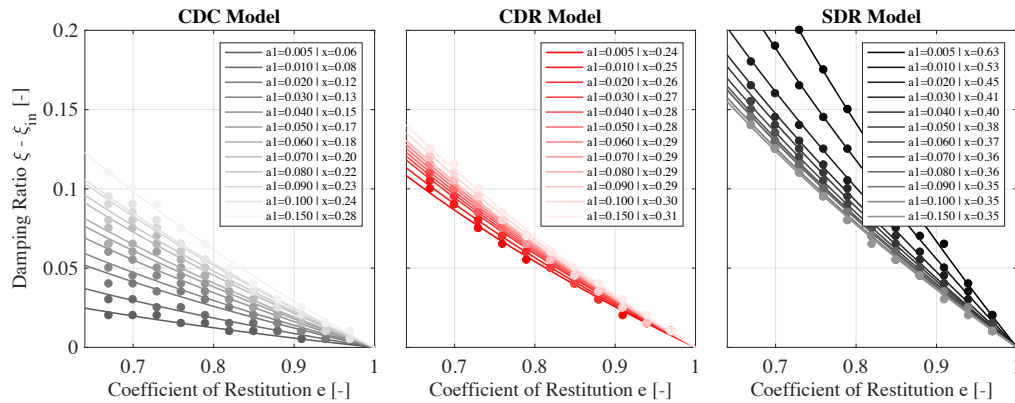


**Figure 5.10** EVD values of CDC, CDR and SDR models in matching free vibration responses damped by a CR model. Details of the PW adopted for the comparison:  $a_I=0.06$ ,  $a_3=1.0$ ,  $u_0/u_{ins}=0.9$ ,  $b=0.4$  and  $h=4$  m.

Results related to the response of VSSW adopting a different F-u curves (e.g. trilinear, see Figure 5.4) are discussed in Tomassetti *et al.* [52]; this study, following a similar approach and modelling the lateral resistance of VSSW with a trilinear curve, has derived very close relationships to the presented one. The equivalence between CR and EVD for same damping models resulted to be insensitive to overburden load on top of the wall and



wall size; on the contrary, EVD values matching the response given by a CR model were affected by amplitude oscillation and strongly affected by the initial stiffness of the wall. Figure 5.11 helps in understanding which one of the models is better in capturing a response damped by a CR. Figure 5.11 plots the minimum errors defined in Equation 15 associated with the best fit considering a specific PW configuration ( $b=0.4\text{m}$ ,  $h=4\text{m}$ ,  $a_1=0.06$ ,  $a_3=1.0$  and  $u_0/u_{ins}=0.9$ ). The errors have been displaced in root due to their wide variation with coefficient of restitution: the higher  $e$ , the higher  $Err$  is.

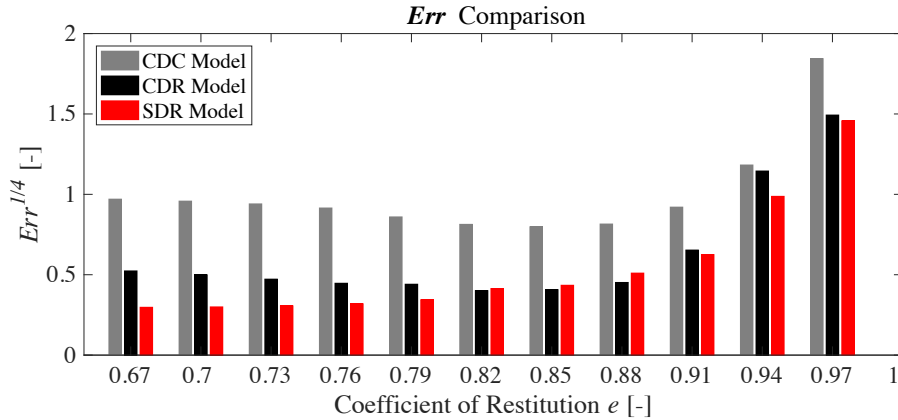


**Figure 5.11** EVD values of CDC, CDR and SDR models in matching free vibration responses damped by a CR model. Details of the PW adopted for the comparison:  $a_1=0.06$ ,  $a_3=1.0$ ,  $u_0/u_{ins}=0.9$ ,  $b=0.4$  and  $h=4$  m.

Both damping models acting on the secant stiffness (CDR and SDR) presented close values of error, both considerably lower than the one associated with a CDC model. The CDR presented the lowest errors in matching free vibration decays controlled by the coefficient of restitution in a range of  $e$  values between 0.91 and 0.8; the remaining coefficient of restitution decays have been simulated more efficaciously by a SDR model. A similar trend was observed for different PW configurations as well as VSSWs.

The previously shown results suggested that the cracked stiffness (controlled by parameter  $a_1$ ) is the system characteristic that more affects the equivalence between velocity dependent acting force models and the coefficient of restitution. In order to derive a relationship describing the dependence of the EVD from the cracked stiffness parameter, a nonlinear regression ( $x(a_1)=m \cdot a_1^k$ ) was performed on the coefficients  $x$  (see Equation 16 and Figure 5.10). Figure 5.12 shows nonlinear regressions of the points obtained from CDC, CDR and SDR models. Finally, substituting in Equation 16 the coefficient  $x$  and the values of CR for the two mechanism (Equations 2 and 3) together with the calibrated  $e_{exp}/e_{an}$  ratio (see Section 3.2), EVD relationships as function of the system geometry are obtained and presented in Equations 17, 18 and 19 for CDC, CDR and SDR models, respectively.

$$\xi_{CDC,PW} = -0.67 \cdot a_1^{0.45} \ln\left(\frac{e_{exp}}{e_{an}} \left[1 - \frac{3}{2} \sin^2 \alpha\right]\right); \quad \xi_{CDC,VSSW} = -0.67 \cdot a_1^{0.45} \ln\left(\frac{e_{exp}}{e_{an}} [1 - 2 \sin^2 \alpha_1]\right) \quad (17)$$

$$\xi_{CDR,PW} = -0.35 \cdot a_1^{0.074} \ln\left(\frac{e_{exp}}{e_{an}} \left[1 - \frac{3}{2} \sin^2 \alpha\right]\right); \quad \xi_{CDR,VSSW} = -0.35 \cdot a_1^{0.074} \ln\left(\frac{e_{exp}}{e_{an}} [1 - 2 \sin^2 \alpha_1]\right) \quad (18)$$

$$\xi_{SDR,PW} = -0.218 \cdot \left(\frac{1}{a_1}\right)^{0.195} \ln\left(\frac{e_{exp}}{e_{an}} \left[1 - \frac{3}{2} \sin^2 \alpha\right]\right); \quad \xi_{SDR,VSSW} = -0.218 \cdot \left(\frac{1}{a_1}\right)^{0.195} \ln\left(\frac{e_{exp}}{e_{an}} [1 - 2 \sin^2 \alpha_1]\right) \quad (19)$$



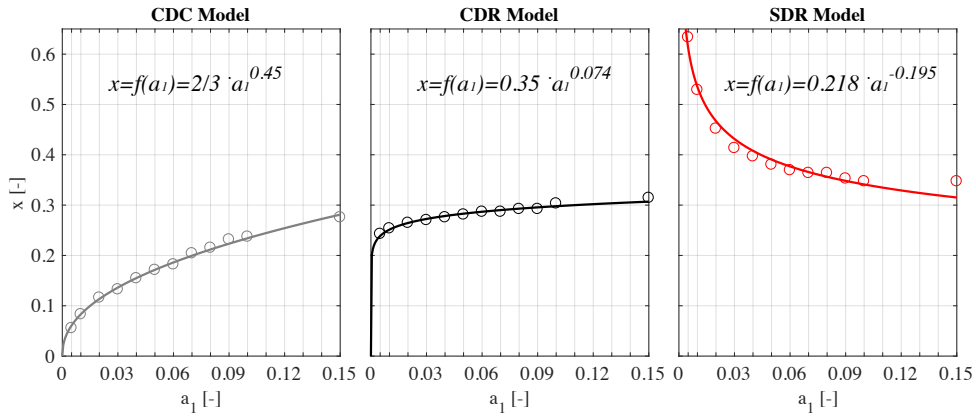


**Figure 5.12** EVD values of CDC, CDR and SDR models in matching free vibration responses damped by a CR model. Details of the PW adopted for the comparison:  $a_1=0.06$ ,  $a_3=1.0$ ,  $u_0/u_{ins}=0.9$ ,  $b=0.4$  and  $h=4$  m.

Figure 5.13 plots these relationships against the slenderness angles  $\alpha$  and  $\alpha_1$  for PW and VSSW, respectively. Assuming a specific bilinear configuration ( $a_1=0.06$ ,  $a_3=1.0$ ), EVD values for CDC, CDR and SDR models are shown considering analytical damping (given purely from geometry,  $e_{exp}/e_{an}=1$ ) and experimental observed damping ( $e_{exp}/e_{an}$  equal to 0.95 for PW and 0.90 for VSSW). Figure 5.13 shows as the difference between geometry-derived damping and experimentally observed one tend to progressively decrease increasing the squatness of the system. Similarly to what observed by Sorrentino *et al.* [21], damping value associated with a VSSW system are generally higher than those associated with PW systems.

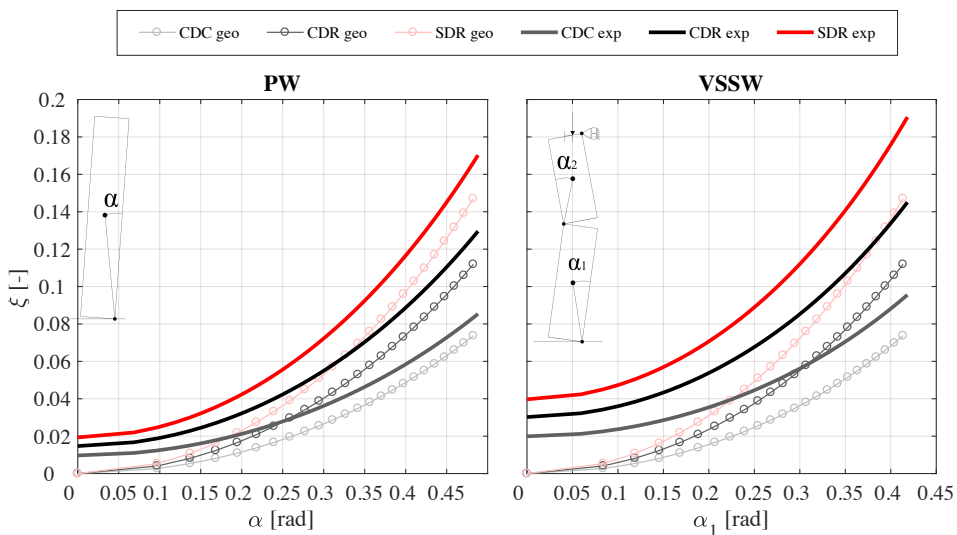


**Figure 5.13** EVD proposed as function of the system geometry for PW and VSSW.

## 5.6. Validation of the proposed EVD relationships

Once derived the equations linking the damping ratio associated with each investigated damping model with the corresponding slenderness angle, their effectiveness is proved against experimental responses and parametric analysis at overturning conditions.

### 5.6.1. Comparison with experimental results

The potential of these damping models in capturing the dynamic rocking response of single leaf and cavity VSSW systems was already discussed by Tomassetti *et al.* [35]. Their numerical simulations adopt a tri-linear configuration with a positive stiffens in the second branch and average  $a_1$  parameter equal to 0.03. The damping ratio values proposed after calibration of the entire sets of tests (low and high amplitudes) for all specimens [35] are compared in Table 5.3 with the ones proposed by Equations 17, 18 and 19 using as input the experimentally measured CR [11]. Regarding the single leaf specimen, the slight difference between calibrated and proposed EVD values (derived for  $u_{max}/u_{ins}=0.9$ ) may be related to the relatively high number of tests of low-moderate peak oscillation amplitude ( $u_{max}/u_{ins}<0.3$ ) and the single one exhibiting the collapse of the specimen. This difference is consistent for the CDC model, which, as discusses in Section 6, is strongly affected by the amplitude of the motion and therefore not recommended. Moreover, Tomassetti *et al.* [35] highlighted that a CDC cannot capture the dependence of the damping phenomenon on the oscillation amplitude underestimating large oscillation peaks. As expected for calibration of tests having low oscillation amplitude response, CDR and SDR, tent to close values of EVD. Regarding the three cavity wall specimens, for which a higher number of tests at high amplitude was observed, the EVD values matching the experimental response are within the range of the proposed values.

**Table 5.3 Comparison between EVD values for CDC, CDR and SDR obtained from calibration of experimental tests and proposed ones (Equations 17, 18, 19).**

	Single leaf wall			Cavity walls		
	Exp. CR [-]	Calibrated $\xi$ [-]	Theoretical $\xi$ [-] (Eq.)	Exp. CR [-]	Calibrated $\xi_{cal}$ [-]	Theoretical $\xi$ [-] (Eq.)
<b>CDC</b>		0.045	0.024-0.019 (17)		0.06	0.068-0.041 (17)
<b>CDR</b>	0.84-0.87	0.06	0.047-0.038 (18)	0.61-0.74	0.10	0.134-0.082 (18)
<b>SDR</b>		0.07	0.075-0.060 (19)		0.15	0.213-0.132 (19)

The performance of these damping models and their comparison with the response given by CR model was further tested against other experimental tests. Parapets tested in as-built condition on the shake-table by Giaretton *et al.* [53] were taken as reference for the following comparisons. The PWs considered for calibration were P4-(B) and P7-(C) both having  $h=1180$  mm,  $b=230$  mm and width equal to 1200 mm. For further details on the tests the interested reader is referred to [53]. Only the tests with harmonic motions as dynamic input and the specimens in already cracked conditions were here considered.

With reference to Section 2, Table 5.4 specifies the modelling parameters adopted to capture the experimental responses in terms of bi-linear  $F-u$  curve and EVD values. The  $F-u$  curves were kept constant, while evaluating the performance of the different damping

models. Table 5.4 provides also the comparison between calibrated EVD and those obtained by using as input the calibrated CR in equations 18 and 19.

**Table 5.4 Modelling parameter for PWs: bi-linear curve parameters, calibrated and proposed EVD values.**

Spec. ID	<i>CR Model</i>					<i>CDR Model</i>			<i>SDR Model</i>		
	$F_0$ [kN]	$u_{ins}$ [mm]	$\alpha_2$ [-]	$\alpha_1$ [-]	$e_{exp}$ [-]	$\alpha_1$ [-]	$\xi_{cal}$ [%]	$\xi_{eq}$ (Eq.18)[-]	$\alpha_1$ [-]	$\xi_{in}$ [-]	$\xi_{eq}$ (Eq.19)[-]
P4-(B)	1.24	115	0.95	0.072	0.935	0.072	0.016	0.019	0.074	0.018	0.024
P7-(C)	1.24	115	0.95	0.070	0.922	0.070	0.022	0.023	0.069	0.026	0.029

Figure 5.14 shows the good match between experimental and numerical non-dimensional displacement histories for the CR, CDR and SDR models. Also in this case, the EVD adopted to obtain a good match with the experimental responses are slightly lower than those proposed in previous sections. This arises, again, because we are analysing response below the level  $u_{max}/u_{ins} < 0.5$ . The overestimation in the initial phases of the response (before second 27) might be attributed to the adoption of a bilinear curve, which at low level of displacement presents a stiffness rather lower than the actual one.

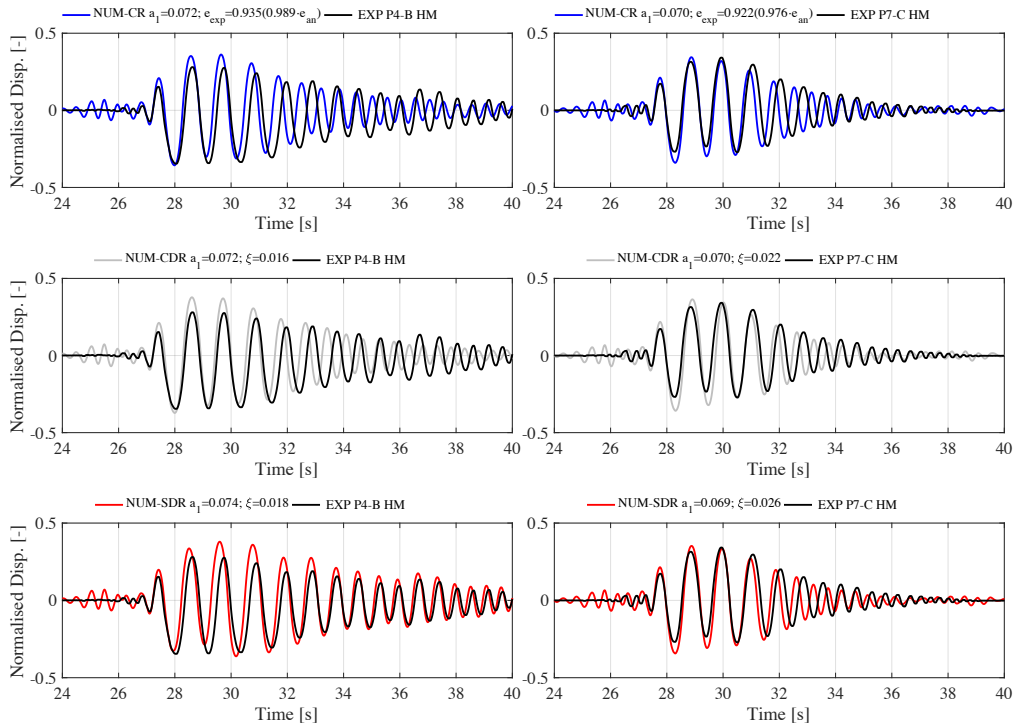


**Figure 5.14 Comparison between exp. and num. non-dimensional disp. histories for CR, CDR and SDR models.**

### 5.6.2. Comparison at overturning condition via IDA analysis

The slight mismatch between calibrated and proposed EVD indicates the need of a further investigation of their performance for oscillation amplitudes inducing overturning, which are the most important ones when interested in assessing risk for human and economic

losses. In order to compare the performance of the proposed damping relationships at overturning conditions of different wall typologies, Incremental Dynamic Analysis (IDA) [54] have been performed. The geometry of the PWs chosen for the comparison is consistent with [45], having values of slenderness (between 5 and 10) and width ( $b=1.2, 0.6, 0.3\text{m}$ ) considered representative of Italian architectonic and/or artistic assets. The comparison between the responses of three more VSSW systems has been also investigated. Table 5.5 lists the analysed walls, their geometry, the associated analytical and experimental CR, and the damping values given by Equations 17, 18 and 19. The walls  $F-u$  was modelled with a bilinear curve with initial stiffness defined by the  $a_1$  parameter [45]. Table 5.5 show also the damping values associated with each block according to Makris and Konstantinidis [18] and Masiani and Giannini [51].

Taking in mind as the risk assessment of the presented block typologies is not the final goal of this specific work, the employed signals were acceleration time-histories selected in the framework of the RINTC project for the city of L'Aquila at 10 different return period levels [55]. The record selection was performed according  $AvgSA$ , defined as the geometric mean of the spectral accelerations within a user-specified range [56].  $AvgSA$ , indeed, represents a good compromise for the characterisation of the structural response in both cases slight damage and collapse [57]. Moreover, its selection, based for the period range 0.2-1.4s (spacing of 0.2s) seems also appropriate for the analysis of rocking structures, in which the oscillation period is amplitude dependant and tend to naturally elongates close to overturning. Therefore, 40 acceleration time-histories (highest between two orthogonal components) corresponding to the IM strips associated with return periods of 500 and 1000 years were employed for the IDA analyses. IDA were, hence, performed by scaling the record  $AvgSA$  till the attainment of overturning condition, here taken when the displacement demand exceeded the static instability displacement,  $u_{max}/u_{ins} > 1$ .

**Table 5.5 Details of the analysed walls and associated damping parameters.**

<i>Wall #</i>	<i>Wall-type</i>	<i>h</i> [m]	<i>b</i> [m]	<i>a<sub>1</sub></i> [-]	<i>e<sub>an</sub></i> [-]	<i>e<sub>exp</sub></i> [-]	$\xi_{CDC}$ Eq. 18 [%]	$\xi_{CDR}$ Eq. 19 [%]	$\xi_{SDR}$ Eq. 20 [%]	$\xi_{M\&K}$ Eq. 12 [%]	$\xi_{M\&G}$ Eq. 15 [%]
1	PW	6.0	1.2	0.0048	0.942	0.895	0.67	2.64	6.83	7.53	3.52
2	PW	1.5	0.3	0.0012	0.942	0.895	0.36	2.38	8.95	7.53	3.52
3	PW	3.0	0.3	0.009	0.985	0.935	0.53	1.65	3.62	4.51	2.11
4	PW	12	1.2	0.036	0.985	0.935	1.00	1.83	2.76	4.51	2.11
5	PW	3.0	0.6	0.0024	0.942	0.895	0.49	2.50	7.82	7.53	3.52
6	PW	6.0	0.6	0.018	0.985	0.935	0.73	1.74	3.16	4.51	2.11
7	VSSW	5.0	0.3	0.02	0.979	0.881	1.46	3.35	5.92	8.62	4.03
8	VSSW	3.75	0.24	0.02	0.976	0.878	1.49	3.43	6.06	8.82	4.12
9	VSSW	3.4	0.36	0.02	0.935	0.842	1.98	4.55	8.04	11.70	5.47

Figure 5.15 shows a very good agreement between collapse empirical cumulative distributions given by the CR and the remaining three damping models (CDC, CDR and SDR) for all the nine walls. The empirical cumulative distributions obtained by adopting the relationship presented by Makris and Konstantinidis present a significant underestimation of the probability of overturning. Beyond the good match between collapse median intensity measures ( $IM^*$ , assuming a lognormal distribution), some consideration regarding the dispersion when  $AvgSA$  is adopted as IM can be done. In general, the dispersion associated with VSSW is lower than PW systems, while

examining PW’s response the lower dispersion is associated with small blocks. This may be related to the nature of the employed accelerograms, very similar for spectral acceleration within the range 0.2-1.4 s within a wide range of secant period for those small blocks fall. Future extension of the presented work may include a proposal for one side rocking mechanisms considering the actual stiffness of the return walls (e.g. [24]). Furthermore, the proposed EVD model may be adopted to perform parametric analysis in order to evaluate the effectiveness of current spectrum-based code prescriptions [28] and eventually propose simplified assessment procedures.

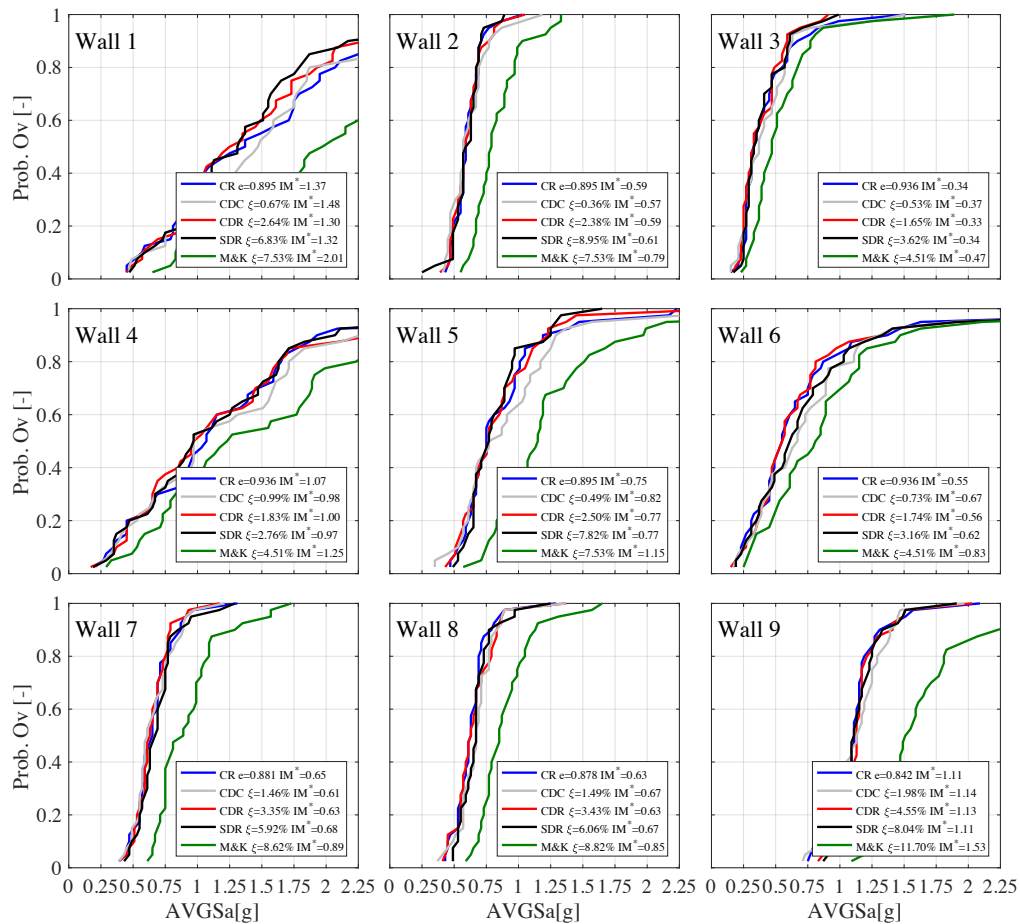


Figure 5.15 Comparison between empirical cumulative distributions obtained with different damping models.

### 5.7. Conclusions

This paper presents a SDOF model for the analysis of the rocking behaviour of parapet wall (PW) and vertical spanning strip wall (VSSW) systems consisting in a bilinear nonlinear elastic oscillator and modelling the energy dissipation with an equivalent viscous damping (EVD) force rather than the most widely used coefficient of restitution. This alternative approach may present several potential advantages over a coefficient of restitution (CR) based approach such as similarities of the damping problem to the

dynamics of classical linear oscillators and easy implementation in already available finite element environments. Moreover, EVD models may model the energy dissipation in both pre-mechanism (during the elastic response) and post-mechanism phases (when the rocking phenomenon take place). This may be particularly important in the case of slightly loaded walls responding in one-way bending or walls in two-way bending.

Several configurations of velocity dependent forces acting on the initial (constant damping coefficient, CDC) or secant stiffness of the system (adopting constant or linear frequency-damping ratio relationships, CDR or SDR) are presented and discussed. The work aimed at defining a relationship between these EVD models and the system slenderness via CR. The response given by CR-based approach was taken as the reference damping system. In order to ensure the equivalence, damped free vibration decays produced by EVD models have been matched with the one provided by a CR.

In general, these equivalences depend on the amplitude of oscillation and the initial stiffness of the systems. Therefore, logarithmic relationships, function of the initial stiffness, were provided to correlate the best damping ratio values associated with the different EVD models with CR values and consequently slenderness angles. The constant damping ratio (CDR) model acting on the system secant stiffness, also considering its reduced dependence on oscillation amplitude and initial stiffness, resulted the most appropriate in simulating free vibration decays damped by a CR. In addition, the stiffness proportional damping ratio (SDR) model has shown rather good performances.

The SDOF model has shown capability of simulating the experimental rocking response of already cracked parapets and the calibrated damping ratio values were very close to the ones proposed by the derived logarithmic relationships. Finally, incremental dynamic analysis adopting damping values provided by the derived relationships were performed on several PWs and VSSWs having slenderness considered representative of Italian architecronic and/or artistic assets. The good match between collapse cumulative distribution functions given by CR and the EVD models confirm the effectiveness of the proposed approach.

## 5.8. Acknowledgments

This work was carried out with the financial support of the Department of Civil Protection, within the 2018 ReLuis research operational project on Masonry Structures.

## 5.9. References

- [1] A. Giuffrè, "A Mechanical Model for Statics and Dynamics of Historical Masonry Buildings," in *Protection of the Architectural Heritage Against Earthquakes*, Vienna: Springer Vienna, 1996, pp. 71–152.
- [2] D. Dizhur *et al.*, "Performance of masonry buildings and churches in the 22 February 2011 Christchurch earthquake," *Bull. New Zeal. Soc. Earthq. Eng.*, vol. 44, no. 4, pp. 279–296, 2011.
- [3] J. Ingham and M. Griffith, "Performance of unreinforced masonry buildings during the 2010 Darfield (Christchurch, NZ) earthquake," *Aust. J. Struct. Eng.*, vol. 11, no. 3, pp. 207–224, 2011.
- [4] A. Penna, P. Morandi, M. Rota, C. F. Manzini, F. da Porto, and G. Magenes, "Performance of masonry buildings during the Emilia 2012 earthquake," *Bull. Earthq. Eng.*, vol. 12, no. 5, pp. 2255–2273, 2014.
- [5] L. Sorrentino, L. Liberatore, D. Liberatore, and R. Masiani, "The behaviour of vernacular buildings in the 2012 Emilia earthquakes," *Bull. Earthq. Eng.*, vol. 12, no. 5, pp. 2367–2382, 2014.
- [6] M. C. Griffith, N. T. K. Lam, J. L. Wilson, and K. Doherty, "Experimental Investigation of Unreinforced Brick Masonry Walls in Flexure," *J. Struct. Eng.*, vol. 130, no. 3, pp. 423–432, 2004.

- [7] O. Penner and K. J. Elwood, "Out-of-plane dynamic stability of unreinforced masonry walls in one-way bending: Shake table testing," *Earthq. Spectra*, vol. 32, no. 3, pp. 1675–1697, 2016.
- [8] P. X. Candeias, A. Campos Costa, N. Mendes, A. A. Costa, and P. B. Lourenço, "Experimental Assessment of the Out-of-Plane Performance of Masonry Buildings Through Shaking Table Tests," *Int. J. Archit. Herit.*, vol. 11, no. 1, pp. 31–58, 2017.
- [9] G. W. Housner, "The behavior of inverted pendulum structures during earthquakes," *Bull. Seismol. Soc. Am.*, vol. 53, no. 2, pp. 403–417, 1963.
- [10] A. A. Costa, A. Arede, A. Penna, and A. Costa, "Free rocking response of a regular stone masonry wall with equivalent block approach: Experimental and analytical evaluation," *Earthq. Eng. Struct. Dyn.*, vol. 42, no. 15, pp. 2297–2319, 2013.
- [11] F. Graziotti, U. Tomassetti, A. Penna, and G. Magenes, "Out-of-plane shaking table tests on URM single leaf and cavity walls," *Eng. Struct.*, vol. 125, 2016.
- [12] L. Sorrentino, O. AlShawa, and L. D. Decanini, "The relevance of energy damping in unreinforced masonry rocking mechanisms. Experimental and analytic investigations," *Bull. Earthq. Eng.*, vol. 9, no. 5, pp. 1617–1642, 2011.
- [13] O. Al Shawa, G. Felice, A. Mauro, and L. Sorrentino, "Out-of-plane seismic behaviour of rocking masonry walls," *Earthq. Eng. Struct. Dyn.*, vol. 41, no. 5, pp. 949–968, Apr. 2012.
- [14] H. Derakhshan, M. C. Griffith, and J. M. Ingham, "Out-of-plane seismic response of vertically spanning URM walls connected to flexible diaphragms," *Earthq. Eng. Struct. Dyn.*, vol. 45, no. 4, pp. 563–580, Apr. 2016.
- [15] J. Zhang and N. Makris, "Rocking response of free-standing blocks under cycloidal pulses," *J. Eng. Mech.*, vol. 127, no. May, pp. 473–483, 2001.
- [16] M. J. DeJong, "Amplification of Rocking Due to Horizontal Ground Motion," *Earthq. Spectra*, vol. 28, no. 4, pp. 1405–1421, 2012.
- [17] E. G. Dimitrakopoulos and M. J. DeJong, "Revisiting the rocking block: Closed-form solutions and similarity laws," in *Proceedings of the Royal Society A: Mathematical, Physical and Engineering Sciences*, 2012, vol. 468, no. 2144, pp. 2294–2318.
- [18] N. Makris and D. Konstantinidis, "The rocking spectrum and the limitations of practical design methodologies," *Earthq. Eng. Struct. Dyn.*, vol. 32, no. 2, pp. 265–289, 2003.
- [19] L. Sorrentino, R. Masiani, and L. D. Decanini, "Overturning of rocking rigid bodies under transient ground motions," *Struct. Eng. Mech.*, vol. 22, no. 3, pp. 293–310, 2006.
- [20] T. Ther and L. P. Kollár, "Overturning of rigid blocks for earthquake excitation," *Bull. Earthq. Eng.*, vol. 16, no. 3, pp. 1607–1631, 2018.
- [21] L. Sorrentino, R. Masiani, and M. C. Griffith, "The vertical spanning strip wall as a coupled rocking rigid body assembly," *Struct. Eng. Mech.*, vol. 29, no. 4, pp. 433–453, 2008.
- [22] M. J. DeJong and E. G. Dimitrakopoulos, "Dynamically equivalent rocking structures," *Earthq. Eng. Struct. Dyn.*, vol. 43, no. 10, pp. 1543–1563, Aug. 2014.
- [23] A. Mehrotra and M. J. DeJong, "A CAD-interfaced dynamics-based tool for analysis of masonry collapse mechanisms," *Eng. Struct.*, vol. 172, no. October 2017, pp. 833–849, 2018.
- [24] L. Giresini and M. Sassu, "Horizontally restrained rocking blocks: evaluation of the role of boundary conditions with static and dynamic approaches," *Bull. Earthq. Eng.*, vol. 15, no. 1, pp. 385–410, 2017.
- [25] L. Giresini, C. Casapulla, R. Denysiuk, J. Matos, and M. Sassu, "Fragility curves for free and restrained rocking masonry façades in one-sided motion," *Eng. Struct.*, vol. 164, no. March, pp. 195–213, 2018.
- [26] E. G. Dimitrakopoulos and T. S. Paraskeva, "Dimensionless fragility curves for rocking response to near-fault excitations," *Earthq. Eng. Struct. Dyn.*, vol. 44, no. 12, pp. 2015–2033, Sep. 2015.
- [27] A. I. Giouvanidis and E. G. Dimitrakopoulos, "Rocking amplification and strong-motion duration," *Earthq. Eng. Struct. Dyn.*, vol. 47, no. 10, pp. 2094–2116, 2018.
- [28] M. C. Griffith, G. Magenes, G. Melis, and L. Picchi, "Evaluation of Out-of-Plane Stability of Unreinforced Masonry Walls Subjected To Seismic Excitation," *J. Earthq. Eng.*, vol. 7, no. sup001, pp. 141–169, 2003.
- [29] N. T. K. Lam, M. Griffith, J. Wilson, and K. Doherty, "Time-history analysis of URM walls in out-of-plane flexure," *Eng. Struct.*, vol. 25, no. 6, pp. 743–754, 2003.
- [30] M. A. Elgawady, Q. Ma, J. W. Butterworth, and J. Ingham, "Effects of interface material on the performance of free rocking blocks," *Earthq. Eng. Struct. Dyn.*, vol. 40, no. 4, pp. 375–392, 2011.
- [31] D. Kalliontzis and S. Sritharan, "Characterizing dynamic decay of motion of free-standing rocking members," *Earthq. Spectra*, vol. 34, no. 2, pp. 843–866, 2018.
- [32] R. Truniger, M. F. Vassiliou, and B. Stojadinović, "An analytical model of a deformable cantilever

- structure rocking on a rigid surface: experimental validation," *Earthq. Eng. Struct. Dyn.*, vol. 44, no. 15, pp. 2795–2815, Dec. 2015.
- [33] J. O'Hagan, K. M. Twigden, and Q. T. Ma, "Sensitivity of post-tensioned concrete wall response to modelling of damping," *NZSEE Conf.*, no. 28, pp. 1–9, 2013.
- [34] D. Kalliontzis, S. Sriharan, and A. Schultz, "Improved Coefficient of Restitution Estimation for Free Rocking Members," *J. Struct. Eng.*, vol. 142, no. June, p. 6016002, 2016.
- [35] U. Tomassetti, F. Graziotti, A. Penna, and G. Magenes, "Modelling one-way out-of-plane response of single-leaf and cavity walls," *Eng. Struct.*, vol. 167, pp. 241–255, Jul. 2018.
- [36] F. Graziotti, U. Tomassetti, S. Sharma, L. Grottoli, and G. Magenes, "Experimental response of URM single leaf and cavity walls in out-of-plane two-way bending generated by seismic excitation," *Constr. Build. Mater.*, vol. (in press), 2018.
- [37] J. Vaculik and M. Griffith, "Out-of-plane load–displacement model for two-way spanning masonry walls," *Eng. Struct.*, vol. 141, pp. 328–343, 2017.
- [38] H. Crowley, B. Polidoro, R. Pinho, and J. van Elk, "Framework for Developing Fragility and Consequence Models for Local Personal Risk," *Earthq. Spectra*, vol. 33, no. 4, pp. 1325–1345, 2017.
- [39] H. Derakhshan, D. Dizhur, M. C. Griffith, and J. M. Ingham, "Seismic Assessment of Out-of-Plane Loaded Unreinforced Masonry Walls," *Bull. New Zeal. Soc. Earthq. Eng.*, vol. 47, no. 2, pp. 119–138, 2014.
- [40] ABK, "Methodology for mitigation of seismic hazards in existing unreinforced masonry buildings: wall testing, out of plane," 1981.
- [41] M. Aslam, W. G. Godden, and D. T. Scalise, "Earthquake Rocking Response of Rigid Bodies," *J. Struct. Div.*, vol. 106, no. 2, pp. 377–392, 1980.
- [42] N. M. Newmark, "A Method of Computation for Structural Dynamics," *Journal of the Engineering Mechanics*, vol. 85, no. 7, pp. 67–94, 1959.
- [43] K. Doherty, "An investigation of the weak links in the seismic load path of unreinforced masonry buildings," no. May, p. 354, 2000.
- [44] H. Derakhshan, M. C. Griffith, and J. M. Ingham, "Airbag testing of multi-leaf unreinforced masonry walls subjected to one-way bending," *Eng. Struct.*, vol. 57, no. December, pp. 512–522, 2013.
- [45] S. Lagomarsino, "Seismic assessment of rocking masonry structures," *Bull. Earthq. Eng.*, vol. 13, no. 1, pp. 97–128, 2015.
- [46] K. Doherty, M. C. Griffith, N. Lam, and J. Wilson, "Displacement-based seismic analysis for out-of-plane bending of unreinforced masonry walls," *Earthq. Eng. Struct. Dyn.*, vol. 31, no. 4, pp. 833–850, 2002.
- [47] T. M. Ferreira, A. A. Costa, R. Vicente, and H. Varum, "A simplified four-branch model for the analytical study of the out-of-plane performance of regular stone URM walls," *Eng. Struct.*, vol. 83, pp. 140–153, 2015.
- [48] H. Derakhshan, M. C. Griffith, and J. M. Ingham, "Out-of-Plane Behavior of One-Way Spanning Unreinforced Masonry Walls," *J. Eng. Mech.*, vol. 139, no. 4, pp. 409–417, 2013.
- [49] L. Sorrentino, "Dinamica di muri sollecitati fuori del piano come sistemi di corpi rigidi," 2003.
- [50] M. J. N. Priestly, "Seismic behaviour of unreinforced masonry walls," *Bull. New Zeal. Natl. Soc. Earthq. Eng.*, vol. 18, no. 2, pp. 191–205, 1985.
- [51] R. Giannini and R. Masiani, "Risposta in frequenza del blocco rigido," in *10th AIMETA Conference*, 1990, pp. 170–174.
- [52] U. Tomassetti, F. Graziotti, A. Penna, and G. Magenes, "Energy dissipation involved in the out-of-plane response of unreinforced masonry walls," in *COMPADYN 2017*, 2017, vol. 2, pp. 2996–3010.
- [53] M. Giaretton, D. Dizhur, and J. M. Ingham, "Dynamic testing of as-built clay brick unreinforced masonry parapets," *Eng. Struct.*, vol. 127, pp. 676–685, 2016.
- [54] D. Vamvatsikos and C. A. Cornell, "Incremental dynamic analysis," *Earthq. Eng. Struct. Dyn.*, vol. 31, no. 3, pp. 491–514, 2002.
- [55] I. Iervolino, A. Spillatura, and P. Bazzurro, "RINTC project - assessing the (implicit) seismic risk of code-conforming structures in Italy," in *COMPADYN 2017*, 2017, pp. 1545–1557.
- [56] M. Kohrangi, P. Bazzurro, D. Vamvatsikos, and A. Spillatura, "Conditional spectrum-based ground motion record selection using average spectral acceleration," *Earthq. Eng. Struct. Dyn.*, vol. 46, no. 10, pp. 1667–1685, Aug. 2017.
- [57] G. J. O'Reilly, M. Kohrangi, P. Bazzurro, and R. Monteiro, "Intensity Measures for the Collapse Assessment of Infilled RC Frames," in *16th Europ. Conf. on Earthq. Eng., 16ECEE*, 2018, no. June.



## 6. Vulnerability of timber roofs supported by unreinforced masonry gables

Tomassetti U., Graziotti F., Correia A.A., Penna A. (2018) Vulnerability of timber roof supported by unreinforced masonry gables, *Earthq. Eng. Struct. Dyn.* (to be submitted).

**Abstract.** Typical low-rise masonry buildings consist unreinforced masonry (URM) walls covered with various timber roof configurations generally supported or finished by masonry gables. Post-earthquake observations and experimental outcomes highlighted the large vulnerability of the URM gables to the development of overturning mechanisms, both due to the inertial out-of-plane excitation and the in-plane timber diaphragm deformability.

This paper presents the static and dynamic experimental seismic performance of three full-scale roofs tested via quasi-static cyclic pushover and shake table tests. Two of them were tested as part of a whole full scale one-storey and two storey building.

A single-degree-of-freedom (SDOF) numerical model, is calibrated against experimental responses and proposed for the analysis of the dynamic behaviour of this roof typology. Several sets of analyses were conducted to assess the vulnerability of these structural components and to study the effect of the characteristics of the whole building (*e.g.* number of storeys and structure strength) on the seismic performance of this roof typology.

### 6.1. Introduction

Collapses of roof structures and gable walls are among the most important vulnerabilities associated with URM structures under seismic loading. Such failures have also been widely confirmed to be an important cause of potential risk for human life by damage observations in the aftermath of recent and past earthquakes [1][2][3]. Roof structures, indeed, tend to be the most fragile elements due to their relatively high flexibility, the low acting overburden load and their location at the top of the building where the floor motion amplification is expected to be the highest. Their damage may be limited to the overturning of the gable wall due to lack of wall-to roof-diaphragm and wall-to-transverse-wall connections (see Figure 6.1a,b,c,d from Darfield 2010 and Gorkha 2015 earthquakes) or involving collapse of the entire roof storey (see Figure 6.1e-f from Emilia 2012 event).

The herein presented experimental and numerical work represents an attempt of assessing the vulnerability and consequently the potential risk for economic and human losses due to the development of a collapse mechanism in the roof structure of terraced houses typical of the Groningen region. This region of the Northern Netherlands has been

exposed to low-intensity shakings due to seismic events induced by gas extraction and consequent reservoir depletion in recent years [4].

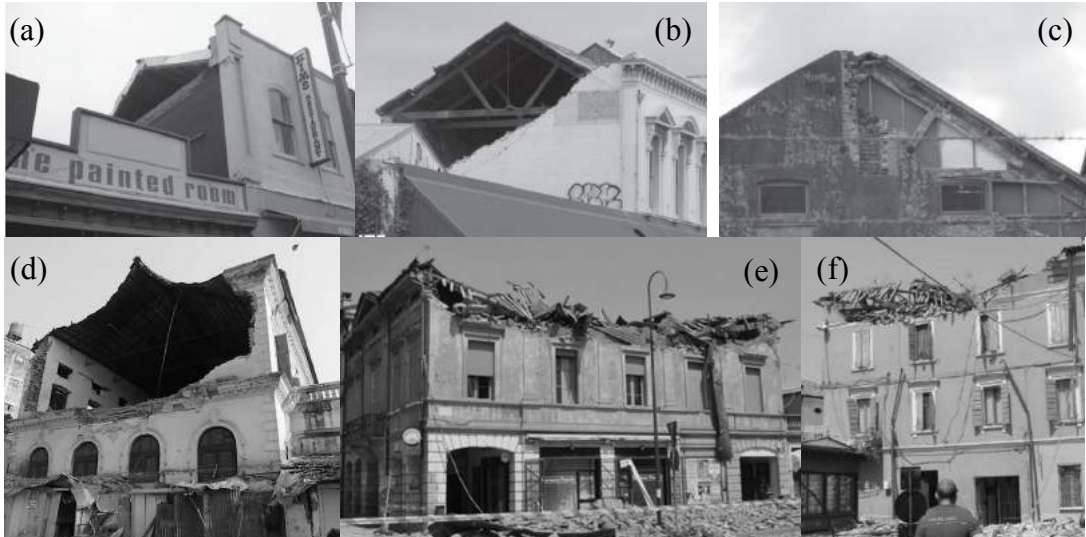


**Figure 6.1 Observations of roof structures damage: overturning of the gable wall (a,g,c [1] and d [3]) and collapse of the roof structure (e,f [2]).**

The shaking table test activities carried out at the EUCENTRE laboratory on a full-scale two-storey building (EUC-1, [5]) and at the LNEC on a full-scale sub-volume (LNEC-1, [6]) of EUC-1 identified in the roof substructure one of the possible causes of damage or local collapse for cavity wall terraced houses. With the aim of characterising the seismic performance of the gable and roof system until the attainment of collapse, a third specimen (LNEC-2) was built and tested at the LNEC laboratory. Complementary information to the one herein presented on this latter specimen are included in [7].

The tests presented in this paper are in fact part of a wide experimental campaign with the aim of improving the analytical and numerical prediction of damage in URM buildings or part of them (e.g. [8][9][10][11]).

Sections 6.2 and 6.3 present geometry and experimental seismic performances of the tested roof configurations, respectively. Section 6.4 introduces a SDOF numerical model for the analysis of their dynamic behaviour while Section 6.5 presents the comparison between experimental and numerical responses. The vulnerability of this roof typology is finally assessed in Section 6.6 considering the roof placed on top of different building configurations in terms of number of storeys and structure lateral strength. The best intensity measure (IM) in predicting their response is also investigated.

## 6.2. Description of the roof structure

The structures object of this study are full-scale timber roofs supported by URM gable walls which lay on a RC slab. All the roofs were approximately 5.85 m long, 5.46 m wide and 2.30 m high with a total mass of 6.5 t (see Figure 6.2). One of the gable wall is made of CS bricks (212×102×71 mm), while the other one is composed of two URM leaves: the inner leaf of CS bricks while the outer leaf of clay bricks (211×100×50 mm). This because the specimen was meant to represent the roof of an end-unit of a set of cavity

wall terraced houses. The two leaves were connected by means of L-shaped steel ties. The roof timber beams were supported by the inner CS leaves, whereas this connection was further reinforced by the presence of L-shaped steel anchors.

Tongue and groove planks with a width equal to 182 mm and a thickness of 18 mm, were nailed at each beam intersection by means of two 60×2 mm nails (100 mm of spacing). In EUC-BUILD-1 specimen the planks were continuous along the entire inclined length while in the other roofs they covered 1/3 and 2/3 of the total length, resulting in an higher number of nailed connections (see detail in Figure 6.2).

The roofs diaphragms were characterised by different opening configurations allowing for access to the floor: EUC-BUILD-1 and LNEC-BUILD-2 presented a single central opening (approximately of dimension 75x110 cm) whereas LNEC-BUILD-1 had four openings (three with dimensions of 54x45 cm, one of 54x72 cm).

The in-plane stiffness of the timber diaphragm was essentially provided by the nailed connections between beams and planks, as well as by the effectiveness of the tongue and groove joints. The roof was completed with the installation of clay tiles. In LNEC-1 and LNEC-2 the horizontal wood profiles (see Figure 6.2d) allowing for the installation of the tiles were directly nailed on the planks whereas in the EUC-1 they were nailed on second order vertical profiles.

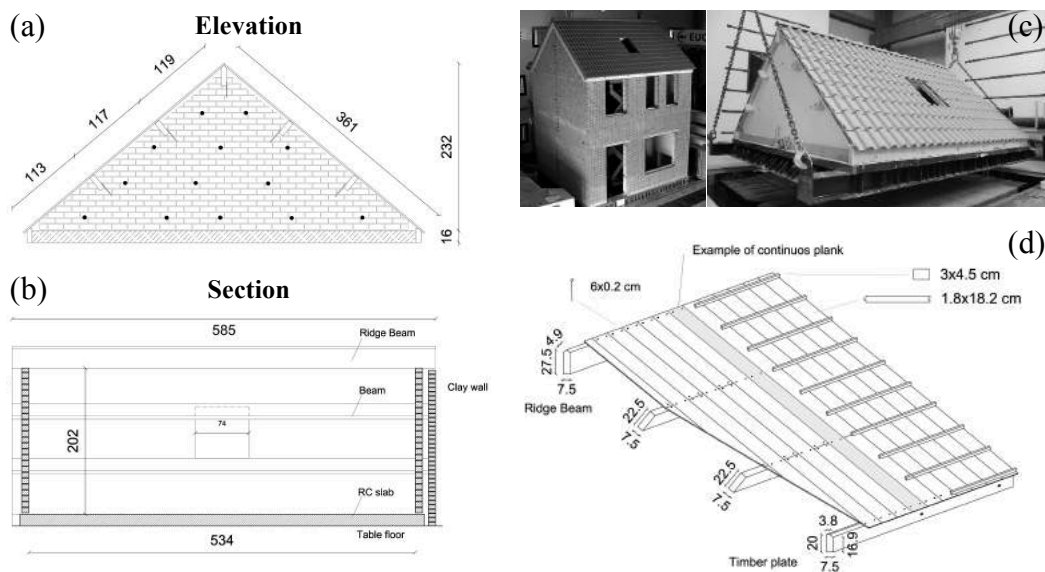


**Figure 6.2** Geometry of the roof: (a) elevation of the CS wall, (b) section; (c) Pictures of EUC-BUILD-1 specimen and LNEC-BUILD-2; (d) details of the construction.

### 6.3. Experimental seismic performance

All the experimental tests have identified this roof typology as a highly flexible sub-structure composed of masonry gables and a timber diaphragm in which the L-shaped connectors facilitate the compatibility of displacement between them [5][6]. For this reason, the dynamic behaviour of the roof system can be analysed as an ensemble in which the lateral resistance is provided by the typical non-linear rocking of the masonry gables together with the highly dissipative timber diaphragm force displacement

behaviour. The timber diaphragm deformation was driven by the induced shear deformation of the board-to-beam connections. The resulting roof structure deformation can be well approximated by a linear function over the roof height with negligible two-way bending deformation of the URM gable as shown by Figure 6.3.

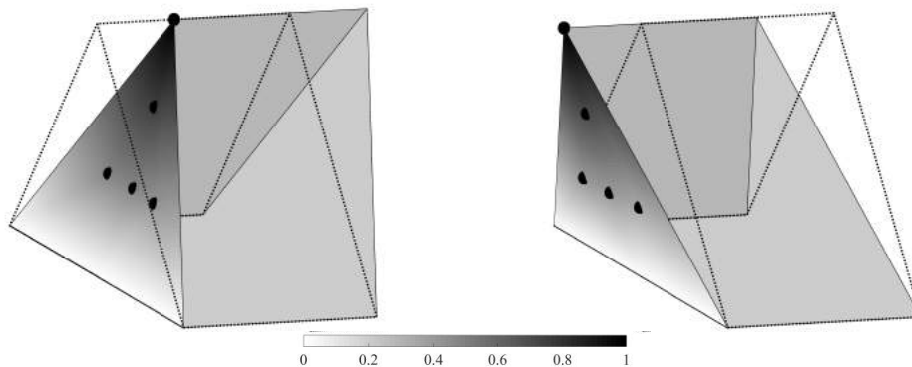


**Figure 6.3** 3d deformation of the East CS gable during FEQ300% at the instant of peak positive (+25 mm) and negative (-34 mm) horizontal displacements. It is constructed by performing linear interpolation between all the points monitored by wire potentiometer and indicated by black spheres.

In all tests, the observed damage was mainly localised at the URM gables whereas the timber diaphragm showed capability of accommodate large deflection without any significant damage as well as stiffness and stress degradation. Cracking at the gable base and at the connection with the L-shaped connectors were the firsts in sight damage. Later on, the elongation of existing cracks and the development of a possible mechanism were observed. Although the collapse of the East gable of EUC-3 achieved at a PTA of 1.14g and a diaphragm drift equal to 5.65%, the roof diaphragm retained load-bearing capacity of its gravity load (see Figure 6.4). Some of the tiles got damaged in this last test.



**Figure 6.4** Frames of the video of LNEC-2 roof taken during F2EQ2-600% test showing the collapse of the gable wall and the final deformation of the timber diaphragm [7].

The experimentally observed damage evolution in all the three specimens allowed for the definition of damage limits (DLs), quantitative boundaries in terms of diaphragm drift between the following damage states (DSs):

- *DS0*, completely undamaged;
- *DS1*, no structural damage: first cracking occurring at the plaster layer;

- *DS2*, minor structural damage; first cracking of the masonry usually located at the base of the URM gables, possible detachment of timber boards;
- *DS3*, moderate structural damage: elongation of existing cracks and development of new ones at the gable-roof beam connection;
- *DS4*, extensive structural damage with the development of a possible OOP mechanism in the gable wall;
- *DS5*, very heavy structural damage, total or local collapse. This level of damage may include a global mechanism of the roof with complete overturning of the system gables-timber framing or the retention of loadbearing capacity associated with a local collapse of a gable. These DS represents potential fall of debris with associated risk for life of the people standing around the building and for building occupants.

Although the three systems had nominally the same geometry, their overall responses differ in terms of dynamic force-displacement backbone curve (see Figure 6.5a) and dissipated energy; the backbone curve is constructed by connecting the peak points of resisted experimental roof base shear and associated diaphragm drift,  $\gamma$  (ridge beam horizontal displacement relative to floor divided by the roof inclined length,  $l_r = 3.61$  m). The last branch of the curves connects the peak resisted base shear with the peak displacement achieved in the last test.

Figure 6.5a illustrates also the different *DLs* while Figure 6.5b shows example of crack pattern associated to each *DS*. Regarding to the dissipated energy, the equivalent viscous damping (*EVD*) values calculated according to the Jacobsen approach [12] for the peak cycle response of LNEC-1 and LNEC-2 are approximately 1.6 time higher than the one associated with EUC-1 specimen one (their hysteretic response will be presented in following sections).

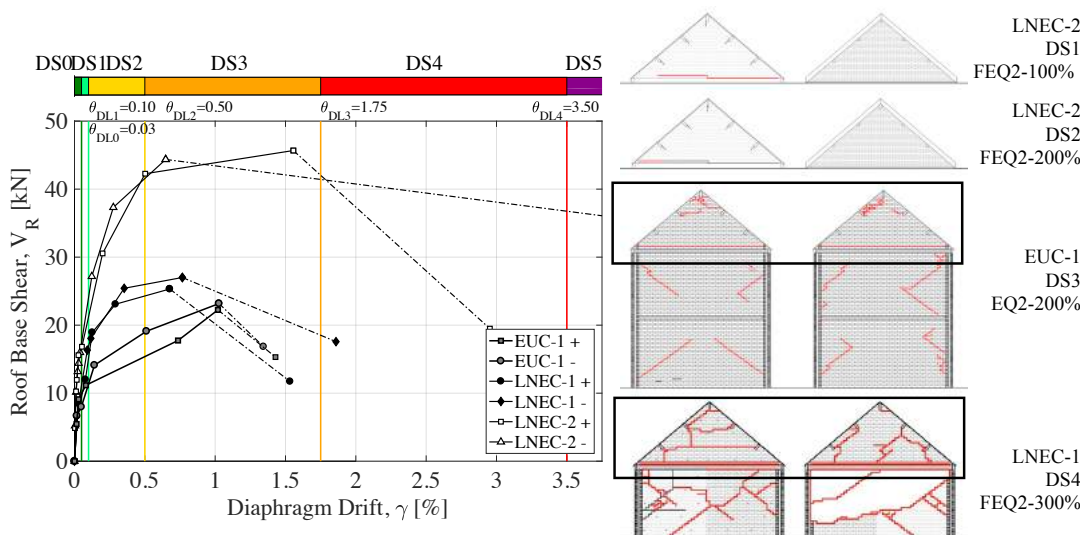


**Figure 6.5 Dynamic backbone curve and identification of DLs (a); the last point of each curve represents the peak displacement achieved in the last test which, due to the dynamic nature of testing, cannot be considered as a strength degradation region; observed crack pattern in EUC-1, LNEC-1 and LNEC-2 and classification of the damage (d).**

These differences could be attributed to the different workmanship of the builders, the mechanical properties and typology of the timber sheeting as well as their positioning, connection with the beam system and the installation technique of the tiles layer. Another fundamental aspect is represented by the different boundary conditions at the base of the gables. For the CS gables, they can be considered somehow similar laying in all the specimens on the RC slab even if placed at different heights: second storey in EUC-1, first-storey in LNEC-1 and shaking table floor for LNEC-2. For the clay gable the situation is quite different: the lower strength exhibited by the EUC-1 and LNEC-1 roofs may be related to the fact that their clay gables stand on a flexible two-storey and one-storey, respectively clay wall connected to the load-bearing structure only by means of the weak ties system. This may compromise the development of the lateral resistance generated by the rocking response of the clay gables. This phenomenon, particularly true for the EUC-1 roof, seems further confirmed by the strength envelopes for  $\gamma$  beyond 1% which, when the  $P-\Delta$  effect significantly reduce the gables re-centring force, tends towards a less marked strength difference.

#### 6.4. Modelling the dynamic response of roof substructures

This section offers an interpretation for modelling the dynamic behaviour of these roof substructures with a simplified single degree of freedom (SDOF) ideal to perform large sets of non-linear time history analysis. The seismic response of these systems relies on the coupled contribution of the typical non-linear rocking behaviour of the masonry gables together with the highly dissipative timber diaphragm hysteretic behaviour. Therefore, the overall lateral resistance of the system can be modelled as two springs in parallel each of them representative of the three URM gables overturning and timber diaphragm force-displacement relationship. The following sections discuss dynamic and static properties of both systems. Figure 6.6 is a two-dimensional idealisation of the roof mechanism showing the assumed linear deflected shape (with  $z$  top displacement), the gables' self-weight ( $W$  or  $W_c$ ) and the roof load transferred to the gables through the wooden beams ( $O_i$ ). Distribution of relative and acceleration at the base of the roof as well as mass per unit length distributions of diaphragm ( $m_{d0}$ ) and gables ( $m_{g0}$ ) are also shown.

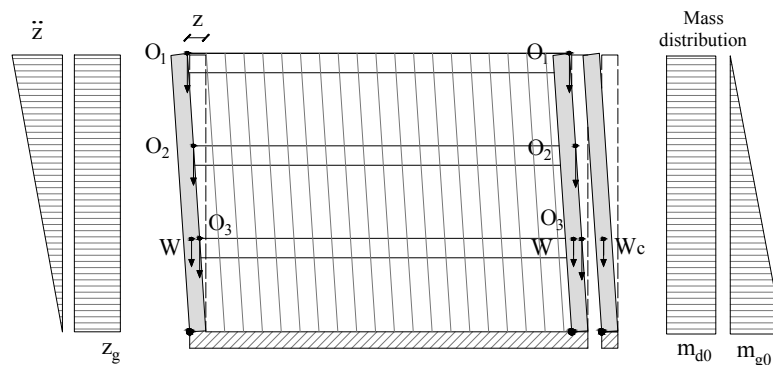


**Figure 6.6 Idealisation of the roof-substructure response when subjected to earthquake excitation: linear deformed shape, relative and ground acceleration profiles and mass distributions for gables and roof diaphragm.**

## 6.4.1. Diaphragm modelling

### 6.4.1.1. Force-displacement relationship

Several experimental works have shown that timber diaphragms are characterised by high flexibility associated with the capability of accommodating large deflection with no indication of structural failure. Wilson *et al.* [13] performing cyclic testing on as built timber diaphragm reached drifts of 3.8% and 5.4% in the parallel to joist and perpendicular to joists directions, respectively, without any insight of damage. The hysteretic behaviour of this diaphragm typology was investigated via cyclic pushover test for the LNEC-2 specimen at the end of the dynamic test and after the removal of the URM gables. Two full cycles at  $\pm 10$  mm,  $\pm 50$  mm,  $\pm 100$  mm and  $\pm 150$  mm were applied as relative displacement between the roof base and the ridge beam (see box in Figure 6.7a). The plot of the force-displacement relationship (Figure 6.7b) shows high non-linearity since ridge beam relative displacements of 1.5 mm (lower than those observed by Wilson *et al.* [13]) and a clear sign of strength degradation only at displacements equal to 150 mm (beyond drift of 4%). This pronounced non-linearity is mainly due to nail yielding and nail slip. Beyond drifts of 2% a clear stiffening effect is detectable.

Similarly to Peralta *et al.* [14], this behaviour can be approximated by a bi-linear idealisation defined by a yield load,  $F_y$ , an initial stiffness  $K_1$  and a secondary stiffness  $K_2$ . A third stiffness  $K_3$  beyond displacement value of 80 mm ( $\Delta_2=2.2\%$ ) is here proposed to model the stiffening phenomenon. Therefore, an elastoplastic relationship with two hardening branches is also proposed to model the diaphragm hysteretic behaviour. The actual  $F$ - $\gamma$  path differs from the idealised one in the unloading region converging to the secondary stiffness  $K_2$  only after the achievement of zero force. This represents one of the approximation of the model herein presented.

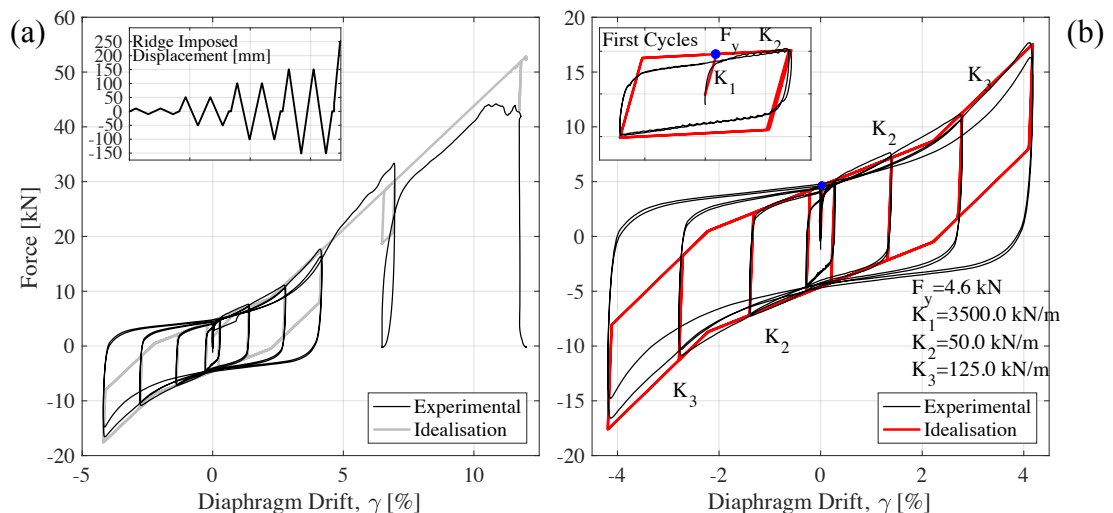


**Figure 6.7 Results of pushover test: imposed displacement and comparison between experimental and idealised hysteretic behaviour (a); zoom of hysteretic behaviour (b).**

An equivalent roof diaphragm shear stiffness  $G_{di}$  can be derived from the assumed tri-linear idealisation by adopting equation 1:

$$G_{di} = \frac{K_i \cdot l_r}{2 \cdot b} \quad (1)$$

where  $b$  represents the roof diaphragm length (5.85 m) and being  $l_r$  the distance from the side of the diaphragm to the first point load. The obtained in-plane strength and stiffness values are compared with the ones obtained from current code assessment procedures such as NZSEE [15], ASCE [16] and the procedure presented in Brignola *et al.* [17]. Table 6.1 compares experimental and analytical values assuming a nail slip equal to 1.1 mm (computed as prescribed by [18]).

**Table 6.1 Comparison between in plane diaphragm stiffness and strength values.**

<i>U.M.</i>	Experimental	NZSEE [15]	ASCE [16]	Brignola <i>et al.</i> [17]
$F_y$ [kN]	4.6	4.5	20.5	-
$\Delta_p$ [mm]	1.31	24.8	14.6	-
$G_d$ [kN/m]	$G_{d1}=1079$ ; $G_{d2}=15.4$ ; $G_{d3}=38.6$ $G_{ds100}=34.3$	55.5	350	36.1

All assessment procedures, including NPR 9998 [19] ( $G_d = 350$  kN/m), underestimate the initial diaphragm stiffness, providing a secant value. The experimental diaphragm secant stiffness at a displacement of 100mm ( $\gamma=2.77\%$ ) is approximately  $G_{ds100} = 34.3$  kN/m, very close to the one proposed by [17]. This is emphasised by Figure 6.1, which plots the experimental secant stiffness values versus the corresponding diaphragm drift as well as the value proposed by the abovementioned assessment procedures. It is worth noting that the stiffness values proposed by NPR 9998 and ASCE underestimate the initial stiffness whereas they provide significantly higher values beyond  $\gamma$  values of 0.15%.

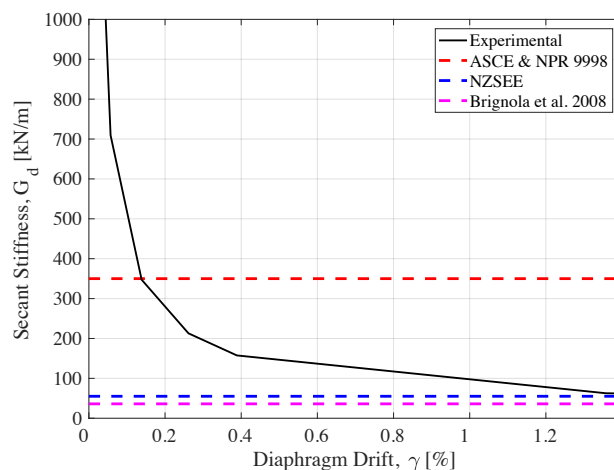


**Figure 6.8 Comparison between experimental diaphragm secant stiffness and values proposed by proposed assessment procedures and national codes.**

Referring to the shake table test on a full-scale house with flexible diaphragms tested by Kallioras *et al.* [20], this value of diaphragm drift corresponds to an inter-storey drift of



approximately 0.20%. Moreover, all assessment procedures do not take into account the stiffening contribution given by the boards wood profiles for the positioning of the tiles as well as the presence of the layer of clay tiles itself.

#### 6.4.1.2. Equation of motion

The dynamic behaviour of a timber diaphragm having distributed mass and elasticity can be approximated as a generalised SDOF [21]. This methodology relays on the definition of a shape function  $\psi(x)$ , which relates the generalised displacement  $z(t)$  with the displacement of any point of the structure  $u(x,t)=\psi(x)z(t)$ , taking into account an approximate shape of fundamental mode of vibration of the system.

The complex deformation pattern characterising the timber diaphragm can be captured by a shear beam idealisation [22]. Therefore, this roof diaphragm can be idealised by a coupled cantilever shear beam having linear shape function ( $\psi(x)=x/h$ ) as experimentally observed. From the selected shape function, the generalised SDOF equation of motion can be written by deriving generalised mass  $\tilde{m}$ , generalised stiffness  $\tilde{k}$  and generalised excitation  $\tilde{L}$ :

$$\tilde{m} = \int_0^{l_r} m(x) \cdot [\psi(x)]^2 dx; \quad \tilde{k} = \int_0^{l_r} GA_t [\psi'(x)]^2 dx; \quad \tilde{L} = \int_0^{l_r} m(x) \cdot \psi(x) dx \quad (2)$$

Assuming a uniformly distributed mass  $m_{d0}$  and adopting the shear stiffness  $G_d$  (achieving independence from diaphragm geometry) the resulting generalised undamped SDOF for the single pitch yields in equation 3:

$$\frac{1}{3} m_{d0} \cdot l_r \cdot \ddot{z}(t) + \frac{G_d b}{l_r} \cdot z(t) = -\frac{1}{2} m_{d0} \cdot l_r \cdot \ddot{z}_g(t) \quad (3)$$

where  $m_{d0} \cdot l_r$  represents half of the total mass of the roof diaphragm  $m_d$  and  $G_d$  in the stiffness term is calibrated according to the idealisation shown in Figure 6.6.

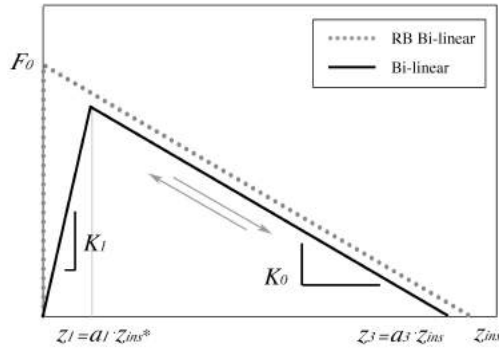
#### 6.4.2. URM gable modelling

URM gables are excited out-of-plane undergoing in non-linear rocking behaviour; their dynamic behaviour can be analysed recurring to a rigid body (RB) idealisation. The gable  $F$ - $z$  relationship can be represented as a simple bi-linear curve constructed from the RB bi-linear one defined by  $F_0$  and  $z_{ins}$  (see equations 4 and 5) [23]. The two parameters depend on the gable self-weight and on the axial load transferred by the beams (with eccentricity equal to  $t/2$ ) at different height of the gable. The initial stiffness is controlled by the parameter  $a_1$  ( $=z_1/z_{ins}$ ) whereas the position of the descending branch by  $a_3$  ( $=z_1/z_{ins}$ ). Both curves are shown in Figure 6.9.

With reference to Figure 6.6 regarding mass and acceleration distributions and adopting D'Alembert's principle the undamped equation of motion for the masonry gables can be written as follow:

$$\frac{1}{4} m_{g0} \cdot h \cdot \ddot{z}(t) + f_{bi}(z(t)) = -\frac{1}{2} m_{g0} \cdot h \cdot \ddot{z}_g(t) \quad (6)$$

where  $m_{d0} \cdot h/2$  represents the total mass of the gable  $m_g$ .



$$F_0 = \frac{W \left( \frac{t}{2} - \frac{z}{3} \right) + \sum O_i \left( t - z \frac{h_i}{h} \right)}{h/3} \quad (4)$$

$$z_{ins} = \frac{(W/2 + \sum O_i) t}{(W/3 + \sum O_i \cdot h_i/h)} \quad (5)$$

Figure 6.9  $F$ - $z$  relationship of URM gables subjected to OOP excitation: RB idealisation and assumed bi-linear curve.

### 6.4.3. Implemented numerical model

The numerical model adopts the Newmark ‘linear acceleration method’ integration scheme implemented in the non-iterative formulation version [24]. The implemented SDOF equation describing the roof structure dynamic response as function of the ridge displacement is defined by equation 7:

$$\begin{aligned} & \left[ \frac{1}{3} m_d + n_g \cdot \frac{1}{2} m_g \right] \cdot \ddot{z}(t) + 2 \left[ \frac{1}{3} m_d + n_g \cdot \frac{1}{2} m_g \right] \cdot \omega_{in} \cdot \xi \cdot \dot{z}(t) + \\ & f_{tri}(z(t)) + n_g \cdot f_{bi}(z(t)) = - \left[ \frac{1}{2} m_d + n_g \cdot m_g \right] \cdot \ddot{z}_g(t) \end{aligned} \quad (7)$$

Where  $n_g$  is the number of gable participating to the motion,  $\omega_{in}$  the initial angular frequency of the system,  $\xi$  the system damping ratio.  $f_{tri}(z(t))$  is the elastoplastic  $F$ - $z$  curve with two hardening branch presented in Figure 6.7 while  $f_{bi}(z(t))$  is the elastic bi-linear curve of Figure 6.9.

### 6.5. Comparison with experimental results

This section presents experimental and numerical results in terms of acceleration capacity and hysteretic behaviour of the tested roof structures. Their experimental responses have been simulated through their entire testing sequence by adopting as input accelerations the one recorded on the RC slab at their base. While parameters related to diaphragm strength and stiffness were kept constant, the increasing damage observed in the gable walls was simulated by increasing the  $a_i$  value (reducing the gable stiffness).

The lateral contribution provided by the URM gables was taken as sum of the single gable contribution (two CS gables and a clay one). The stabilising effect given by the axial load ( $O_i$  in Figure 6.6) transferred by the beams was associated only with the inner CS gable walls. In order to take into account the different boundary conditions characterising the clay gable in the specimens, its lateral resistance was neglected in the EUC-1 case and halved in LNEC-1. The total gable force  $F_0^*$ , defined as sum of the single gable contributions  $F_0$  is presented in Table 6.2. In the case of LNEC-2 the total force  $F_0^*$  has been slightly amplified (15%) to take into account the ties coupling force

contribution [10]. The global instability displacement of the gables has been set equal to the instability of the load-bearing CS gable. Regarding to the energy dissipation, the selected damping ratio for the EUC-1 specimen has been amplified by 1.6 in order to take into account the highest energy dissipation showed by analysing the area within the main response cycle associated with LNEC-1 and LNEC-2 [6]. Table 6.2 lists the parameters adopted for simulating the dynamic response.

**Table 6.2 Modelling parameters adopted for the simulation of the experimental response.**

		<i>EUC-1</i>	<i>LNEC-1</i>	<i>LNEC-2</i>
<b>Test #</b>		9	11	12
$F_0$	[kN]	3.77	4.38	5.06
$z_{ins}$	[m]	0.16	0.16	0.16
$a_1$	[-]	0.03, 0.06 (T#1-8, 9)	0.03, 0.1 (T#1-10,11)	0.03, 0.1, 0.2, 0.9 (T#1-9, 10, 11, 12)
$a_3$	[-]	1	1	1
$F_v$	[kN]	4.8	5.8	6.6
$G_{d1}$	[kN/m]	600	900	1400
$G_{d2}$	[kN/m]	55	18	18
$G_{d3}$	[kN/m]	55	41.1	41.1
$\xi$	[%]	5.5	8.9	8.9

Stiffness and strength assumed to capture the dynamic response of EUC-2 are slightly higher than those directly observed from the cyclic test. In particular,  $F_y$  and  $G_{d1}$  have been increased from the experimental ones by 35% and 30%, respectively. The roofs incremental dynamic testing sequences expressed in terms of acceleration at the roof base vs peak diaphragm drift compared with the numerical responses show a good agreement in Figure 6.10. Beside this, the saturation of the acceleration amplification at the roof base level due to damage occurring at the structure is particularly visible for EUC-1 and only marginal for LNEC-1. For a detailed description of the testing protocol as well as test by test damage report we remind to [5][6][7] for EUC-1, LNEC-1 and LNEC-2, respectively. Figure 6.11 shows the comparison between experimental and numerical hysteretic responses for all the calibrated specimens during relevant tests. To allow for a direct comparison between experimental and numerical responses the roof base shear has been approximated by assigning one-half of the diaphragm mass and one-third of the mass of the gables (total mass of 2600 kg) to the average ridge beam acceleration and the remaining masses (3900 kg) to the slab acceleration. This approximation showed a rather small difference with a more refined calculation of the roof base shear, justifying its adoption [7]. The agreement between numerical and experimental responses is very good.

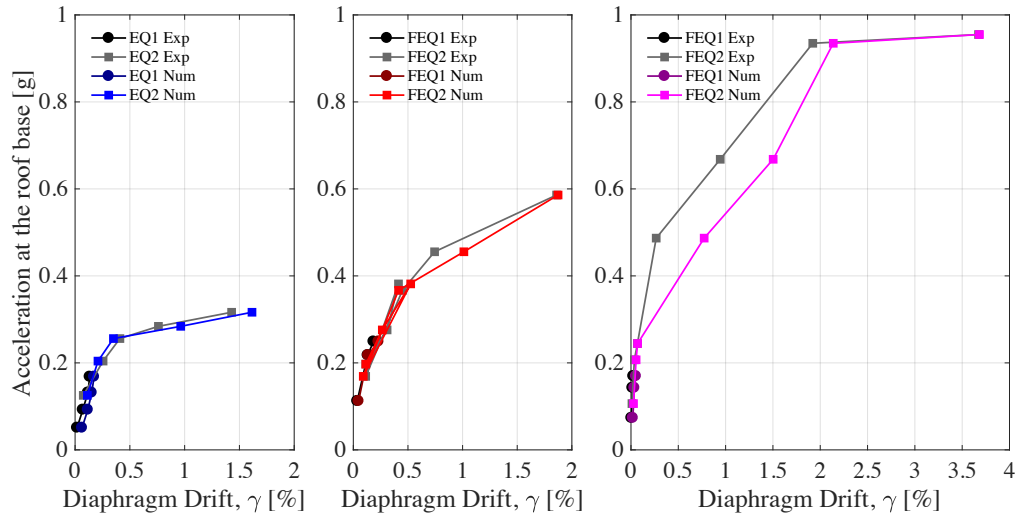


Figure 6.10 Comparison between experimental and numerical incremental dynamic testing sequences.

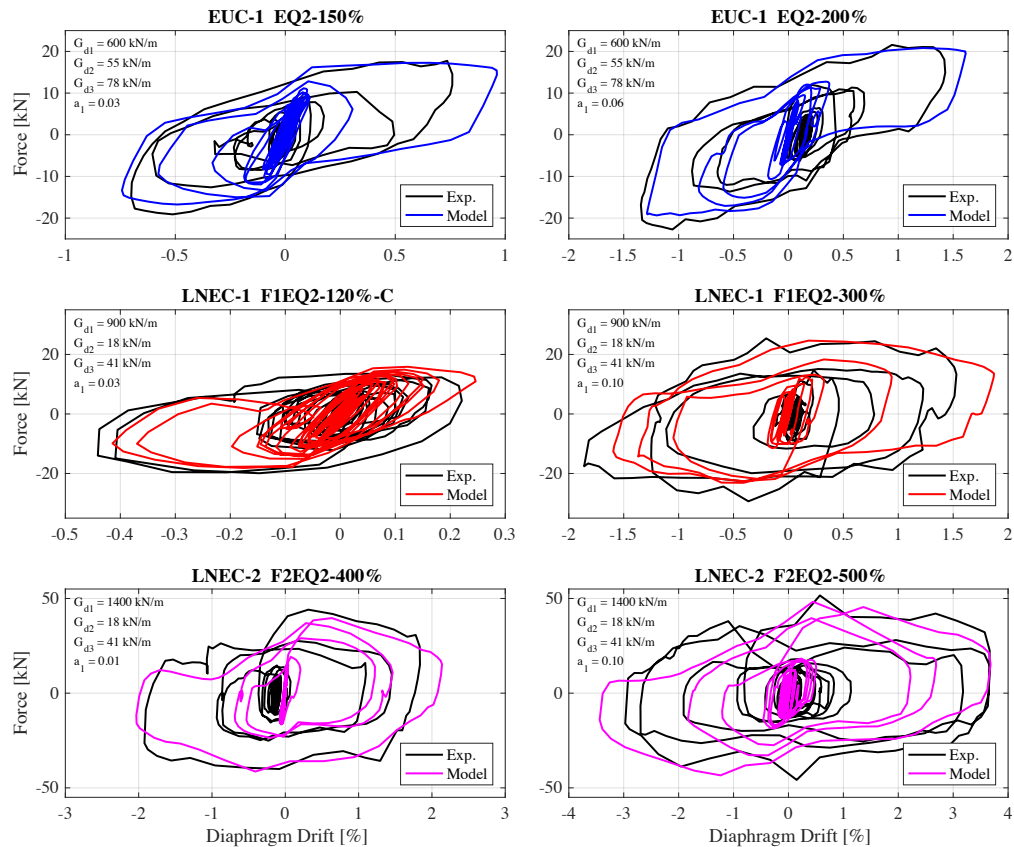


Figure 6.11 Comparison between experimental and numerical hysteretic response for relevant tests.

### 6.6. Vulnerability of roof structures

Once validated against experimental results, this simplified model for the analysis of the response of roof structures was used to determine the vulnerability of these structural typologies. A seismic assessment of these architectural elements can only be performed by taking the filtering effect given by the structure into account, since these elements are located at the top of the building where the floor dynamic amplification is expected to be highest. This was initially done by defining a primary SDOF model representative of the global response of URM buildings. Signals filtered by this primary SDOF system's response were utilised to investigate the secondary SDOF system's response, representative of the roof response. The dynamic interaction between these two systems was neglected as the mass of the roof is generally less than 10% of the whole building mass.

Although the adoption of SDOF systems presents several shortcomings (e.g. neglect higher modes of vibrations), in the case of residential URM structures having small regular plans and a reduced number of storeys (1, 2 or 3) they may capture quite well the overall response.

#### 6.6.1. Primary SDOF (URM building's response)

The SDOF presented by Graziotti *et al.* [25] was adopted to model the global response of the URM structures. The SDOF system, implemented in the software TREMURI [26], [27], adopted a suitable nonlinear spring comprised of two macroelements in parallel allowing for an appropriate calibration between flexure-dominated and shear-dominated responses. The model has shown promising capability to replicate the nonlinear response of URM multi-degree of freedom (MDOF) systems. In particular, the configuration assuming a contribution of 20% of the responding in shear macroelement over the total resisting force (model designation 20 in [28]) together with the associated limited hysteretic energy ( $\xi_{hyst} = 14.9\%$ ) dissipation was adopted to model the response of Dutch cavity wall buildings. As largely documented by experimental tests [5][6], their in-plane seismic response is indeed controlled by flexure.

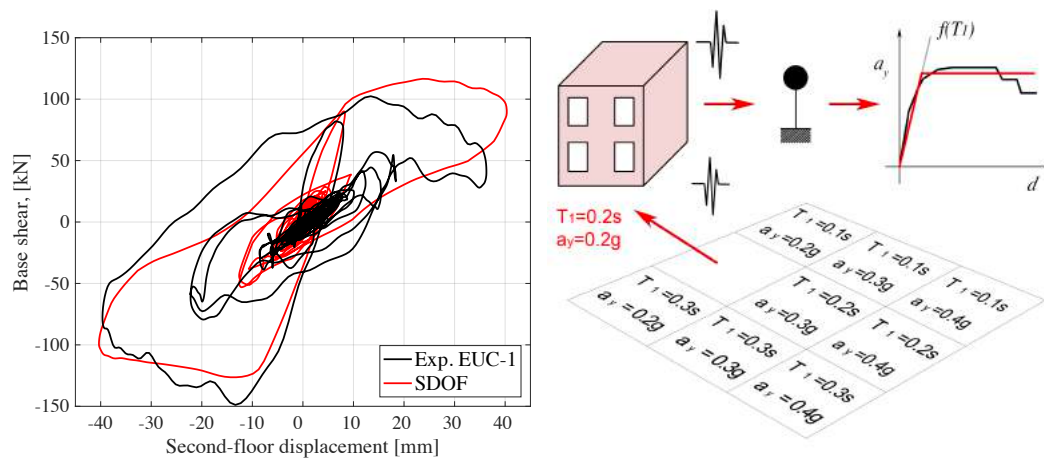


Figure 6.12 Comparison between experimental and SDOF hysteretic response for EQ2-200% test ( $\Gamma=1.18$ ;  $T_1=0.31$ ;  $a^*=0.21g$ )

Figure 6.12a shows the comparison in terms of base shear vs second-floor displacement between experimental response and associated equivalent SDOF system for EUC-1.

With the objective of investigating the variability of the roof response when placed on top of different structural configurations, a set of primary SDOF systems were defined according to different building height and strengths. Figure 6.12b is a schematic representation of the set of primary buildings investigated. Taking as reference the commonly adopted force-displacement elastoplastic idealisation [30], this building variability was defined in terms of initial idealised elastic period and yield pseudo-acceleration plateau,  $a_y$ . Three different initial elastic periods (0.1 s, 0.2 s and 0.3 s) representative of building heights of one, two and three storeys ( $\Gamma=1, 1.19$  and  $1.27$ ) associated each of them with three yield pseudo-accelerations ( $a_y$  equal to 0.2 g, 0.3 g and 0.4 g) were considered to cover realistic ranges for residential URM buildings. Table 6.3 lists the characteristics of the considered set of primary structures.

**Table 6.3 Characteristics of the considered set of buildings: fundamental period, modal shape, mass vector, modal participation factor, SDOF pseudo accelerations resistance and associated yield displacement.**

<i>Storey</i>	<i>T<sub>1</sub></i>	<i>ϕ</i>	<i>M</i>	<i>Γ</i>	<i>a<sub>y</sub></i>	<i>d<sub>y</sub></i>
[#]	[s]	[-]	[t]	[-]	Range [g]	[mm]
1	0.1	[1]	[30]	1	0.2 0.3 0.4	0.6 0.8 1.0
2	0.2	[0.56 1.0]	[24.5 24.5]	1.19	0.2 0.3 0.4	2.0 3.0 4.0
3	0.3	[0.39 0.69 1.0]	[24.5 24.5 24.5]	1.27	0.2 0.3 0.4	4.6 6.8 9.1

The primary structure seismic performance was evaluated through the DLs proposed on the basis of dynamic experimental tests by Tomassetti *et al.* [6] for URM cavity wall buildings and expressed in terms of inter-storey drift ratio. The DLs are 0.1%, 0.15%, 0.35%, and 0.90% defining the thresholds limits between DS1, DS2, DS3, DS4 and DS5.

### 6.6.2. Secondary SDOF (Roofs' response)

Three sets of modelling parameters of roof structure were obtained by the calibration procedure presented in section 6.5. However, the vulnerability study of this roof typology was assessed by considering the actual geometry of these structures: the average width of cavity wall buildings was reported to be approximately 8 m with an associated roof mass of 9920 kg. This corresponds to changes only in gable OOP  $F-u$  parameters which strictly depend on the structure geometry. Parameters such as the diaphragm strength (depending on the joists span) and stiffness were kept the same as obtained from the calibration process. As in the case of EUC-1 specimen, the gable wall was modelled in all cases simply as an added mass (not providing any lateral resistance) and no tie contribution force was considered. Table 6.4 identifies these parameters.

**Table 6.4 Modelling parameters adopted for assessing the vulnerability of roof structures.**

	<i>EUC-1 type</i>	<i>LNEC-1 type</i>	<i>LNEC-2 type</i>
$F_0$ [kN]	6.79	6.79	6.79
$z_{ins}$ [m]	0.16	0.16	0.16
$a_1$ [-]	0.03	0.03	0.03
$F_y$ [kN]	4.8	5.8	6.4
$G_{d1}$ [kN/m]	600	900	1200
$G_{d2}$ [kN/m]	55	15	15
$G_{d3}$ [kN/m]	55	41.1	41.1
$\xi$ [%]	5.5	8.9	8.9
$T_r$ [s]	0.25	0.22	0.20

A comprehensive seismic assessment of this roof typology can be carried out only accounting for a possible development of a local mechanism in the URM gables. Therefore, the attainment of global or partial collapse may be assessed both by looking at the roof diaphragm drift with the methodology here presented or at the mid-height out-of-plane displacement of the gables considering a one-way bending mechanism. Although the lateral support provided by the connection with the timber structure, the development of such mechanism can be facilitated from the extensive cracking occurring from earlier stage of testing at the location of L-connectors (see cracking pattern in Figure 6.5). The SDOF model presented by Tomassetti *et al.* [10], assuming top and bottom supports moving simultaneously and successfully calibrated on the experimental tests, was adopted to analyse the development of this possible mechanism. The allowed OOP displacement was limited by the achieved global diaphragm drift [31]. A better idealisation of this mechanism is provided by the simplified numerical model developed by Derakhshan *et al.* [32] accounting for top diaphragm flexibility and differential acceleration and displacements of the top and bottom supports.

Furthermore, advanced numerical simulations adopting the discrete elements approach for the evaluation of the seismic performance of a terraced-houses (considering their actual geometry) discourage the possibility of a local mechanism in the gables [33][11].

### 6.6.3. Employed accelerograms and response of primary SDOFs

A set of 3506 accelerograms (1753 in EW and NS components) including records from NGA1 [34], European [35] and Groningen databases [36] specifically selected for the derivation of the fragility functions and the computation of the probabilistic risk assessment for the Groningen field [37], has been used for the nonlinear dynamic analyses of the SDOF systems. In particular, the magnitude range has been taken to be between 3.5 and 6.5, and epicentral distances up to 60 km have been used.

Figure 6.13a is a histogram showing the distribution of the predominant period (the one associated with the highest spectral acceleration) over the entire record set. Buildings with fundamental period within the range of 0.1~0.2 s are the most exposed to high spectral accelerations for this record set. Figure 6.13b is instead one of the outcome of the nonlinear time history analysis (NLTH) of the primary SDOF: the ratio between median acceleration amplification at the last floor and PGA. The highest amplifications are observed for the two-storey buildings. Figure 6.13c is instead the comparison between normalised by PGA median ground and floor acceleration spectra for the entire set. The median ground acceleration spectrum shows the highest spectral acceleration within the

period range of 0.15~0.2 s. As expected, the median floor spectra show amplification (proportional to the building strength) at the fundamental period of the structure. The fundamental periods associated with the three analysed roof structures are also shown.

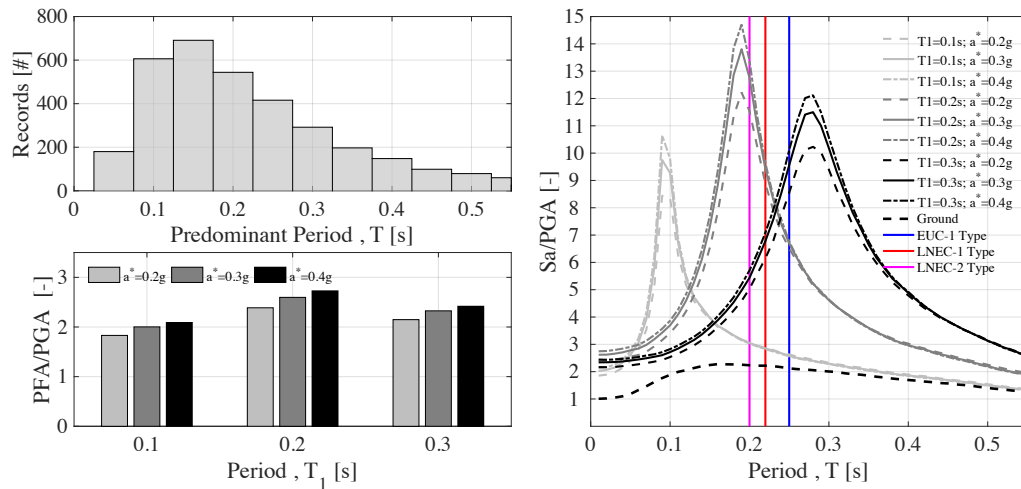


**Figure 6.13** Histogram of the predominant period (a), ratio between top storey PFA and PGA (b), comparison between ground and floor normalised by PGA median acceleration spectra (c).

#### 6.6.4. Results of NLTH analysis

In order to evaluate the response of the roofs to the input floor accelerations, the drift diagram defined by the ridge beam horizontal displacements divided by the inclined length of the roof,  $\gamma$ , was chosen as the engineering demand parameter. While this EDP is typically related to the in-plane damage, this was adopted here as the EDP to describe the roof damage due to OOP response since it was observed experimentally to correspond quite well also in this case.

Figure 6.14 plots the results of a specific set of floor motion analysis (two-storey building  $T_1=0.2s$  and  $a_y=0.3g$ ) for the three roof typologies against three different intensity measures (IMs): PGA, ground spectral acceleration at the fundamental period of the primary structure ( $SAT_1$ ) and ground average spectral acceleration ( $AvgSA$ ). This latter IM is defined as the geometric mean of spectral accelerations within a user-specified range of periods [38]. The period range considered in this study includes spectral accelerations associated with the minimum primary or secondary structure fundamental periods  $T_1$  or  $T_r$  (0.1s or 0.2s) and with elongated maximum primary or secondary structure periods  $1.5 \cdot T_1$  or  $1.5 \cdot T_r$  (0.45s or 0.375s) within the entire set of considered configurations. Consequently, the period range selected for the assessment of the entire portfolio of structural configurations was 0.1-0.45s with 0.05s of spacing.



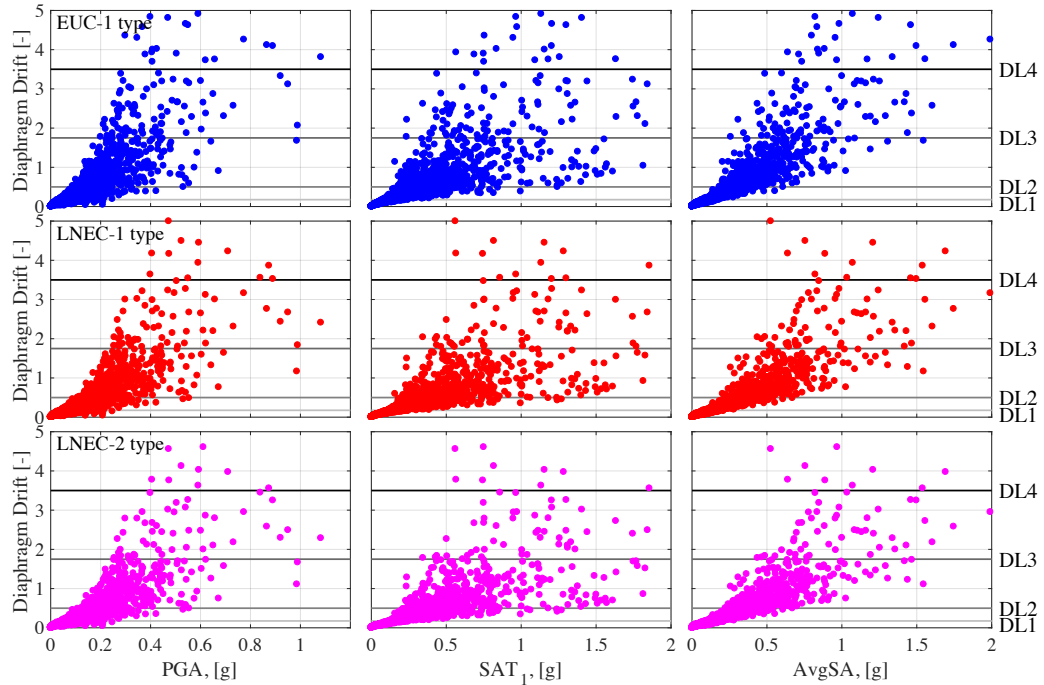


**Figure 6.14** Seismic response of different roof structure typologies placed on a two-storey building ( $T_1=0.2s$   $a_y=0.3g$ ) evaluated against different IMs: PGA,  $SAT_1$  and AvgSA.

The highest responses in terms of diaphragm drift are shown by the EUC-1 roof typology whereas LNEC-1 and mainly LNEC-2 roof type resulted not particularly vulnerable to heavy damage and collapse presenting very few realisations exceeding  $DL4$ . This is related to the low displacement demand associated with the employed accelerograms and mainly due to saturation of the floor acceleration amplification transferred from the primary SDOF systems at the base of the roof structures. Among the three IMs investigated,  $SAT_1$  appears to be the most disperse approaching high displacement demand of the roof structure (beyond  $DL2$ ), whereas  $AvgSA$  seems to perform very well especially for  $DL1$  and  $DL2$ . This is particularly true for this building typology ( $T_1=0.2s$  and  $a_y=0.3g$ ) where primary and secondary structure periods of vibration are quite close. The analysis of the local mechanism occurring in the gable walls resulted in zero realisations of collapse.

### 6.6.5. Fragility curves of roof structures

This section focuses on the calculation of the conditional probability that a ground motion of a given intensity measure ( $IM=x$ ) will cause the exceedance a given DL which, can be expressed via the usual lognormal distribution [39]:

$$P_{ex} = P(D > DLi | IM = x) = \Phi\left(\frac{\ln x - \mu}{\beta}\right) \quad (8)$$

where  $\Phi$  is the standard normal cumulative distribution function,  $\mu$  is the median value of the demand (the IM level with 50% probability of exceedance) and  $\beta$  is the dispersion of the demand conditioned on the IM.

The numerical simulation results (such as those shown in Figure 6.14), grouped in strips according to the selected IM, provided at each IM stripe the fraction of ground motions out of the total causing the exceedance of the considered LS. Maximum likelihood estimation (MLE) method was then used to fit the observed data, allowing for the determination of the  $\mu$  and  $\beta$  fragility function parameters (equation 8) which gives the highest probability of producing the data obtained from the structural analysis [40][41][42].  $\mu$  and  $\beta$  were evaluated through the maximisation of the following likelihood function:

$$L = \prod_{i=1}^n P_{ex}^{y_i} (1 - P_{ex})^{1-y_i} \quad (9)$$

where  $y_i$  is the binomial distribution variable equal to unity when the DS is reached, and null otherwise and  $P_{ex}$  is the probability of exceeding a DL at a given IM presented in equation 8.

Figure 6.15 show the three roofs' fragility functions (for all the considered LSs) as function of the earlier presented IMs and assuming as primary structure still a two-storey building ( $T_1=0.2s$  and  $a_y=0.3g$ ).

Before analysing their performance in terms of dispersion, it has to be stated that the fragility function related to *DS4* cannot be considered as much reliable as the others due to the few realisations beyond the DL4 threshold drift (see Figure 6.14). As earlier mentioned this is due to saturation of the acceleration amplification at the last storey which induces a lower demand in the roof structure. As a consequence, the fragility functions show that exceedance of first DLs (DL1 and DL2) are 'quite likely' event while the attainment of heavy damage and collapse seems very rare possibilities.

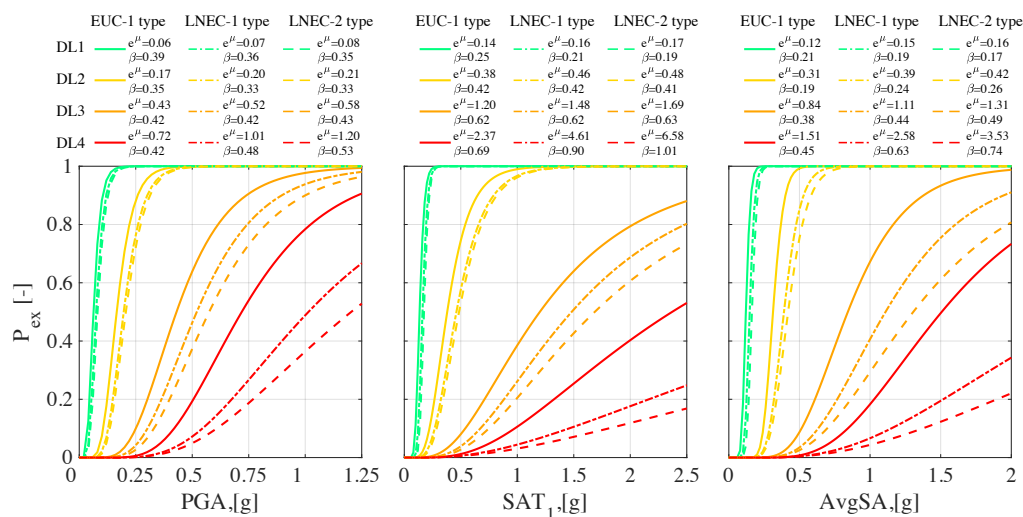


**Figure 6.15 Fragility curves of three roof structure typologies (EUC-1, LNEC-1, LNEC-2) placed on top of a two-storey building ( $T_1=0.2s$   $a_y=0.3g$ ).**

*AvgSA* is the best IM, as far as this building configuration is considered, due to a reduced dispersion for the fragility function associated with DS1, DS2 and DS3. While  $SAT_1$  performed well only for DS1, it results that PGA, when DS2 and DS3 are considered, is

not a bad IM with dispersion value only slightly higher than *AvgSA*. Moreover, if only the fragility functions related to DS4 are considered PGA is the best IM.

Once fragility functions for a specific building typology have been presented, the next step is discussing how their median and dispersion may vary when different building configurations and different DLs are considered.

Figure 6.16 represents a contour map of the median PGA causing exceedance of the considered DL for the three roof typologies as function of building height and building strength. The whiter the surface, the higher the vulnerability of the corresponding structural configuration (lower median PGA). The colour scale is kept constant for the three roof typologies and considered DL.

Generally, a reader expert of structural dynamics may think that the vulnerability of a roof structure depends on the building height, a longer period will cause a higher acceleration demand on the roof substructure and on the building strength, a higher “yielding” force will transmit a higher acceleration at the roof base. These are expected results of this study, particularly evident when looking at the surfaces interpolating median PGA values for DL3 and DL4. The one-storey building with low strength ( $T_f=0.1s$   $a_y=0.2g$ ) associated with dark colours results as an example the least vulnerable for roof structures.

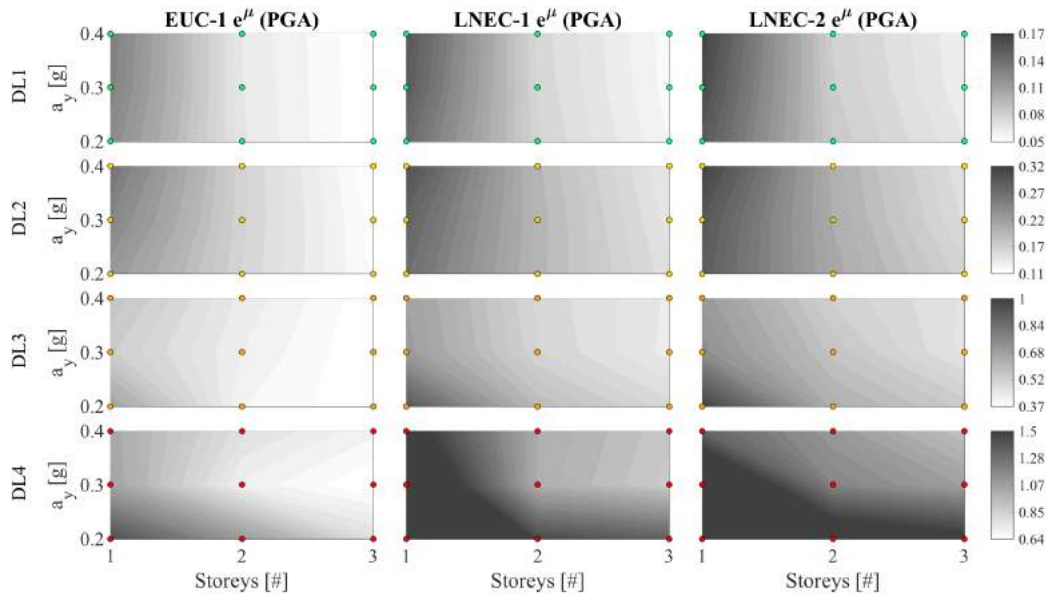
For DL1 and DL2 limit states, when the fraction of primary structure undergoing in nonlinear response is rather lower, the building strength is not a significant parameter when attempting to describe the variability of the median PGA (almost vertical trend lines between 0.2g and 0.4g  $a_y$  values at a given number of storey).

However, for this record set, the distribution of the median PGA with the number of storeys cannot be considered linear due to a region with almost constant colour between two and three storey buildings ( $T_1=0.2s$  and  $T_1=0.3s$ , respectively) that is particularly evident for DL1 and slightly less for DL2. This may be related to the ground motion characteristics of the employed record set (see Figure 6.13) which tend to excite periods close to the two-storey building one and due to amplification of the roof responses which have fundamental periods close to this structure typology.

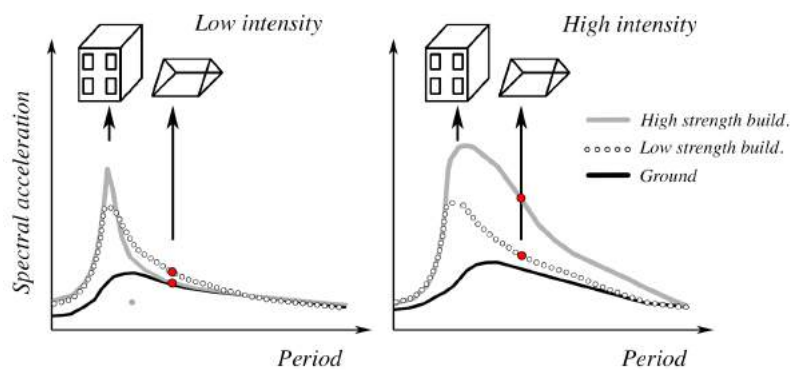
The ratios between highest and lowest median PGA (less and most vulnerable configurations) causing exceedance of the given LS for EUC-1 roof assume values of 2.96 for DL1 ( $T_f=0.1s$   $a_y=0.4g$  and  $T_f=0.3s$   $a_y=0.2g$ ), 2.35 for DL2 ( $T_f=0.1s$   $a_y=0.4g$  and  $T_f=0.3s$   $a_y=0.4g$ ) and 1.83 for DL3 ( $T_f=0.1s$   $a_y=0.2g$  and  $T_f=0.3s$   $a_y=0.4g$ ). The other roof typologies exhibited similar ratios.

Figure 6.16 shows also a quite interesting phenomenon highlighted by the darker colours associated with higher strength (lower vulnerability of  $a_y=0.4g$  with respect to  $a_y=0.2g$ ) for DL1 and DL2 (most likely to occur) and one-storey building structures; this trend, which may sound quite unusual (given a period higher vulnerability of the weakest structure), can be explained by the schematic representation of Figure 6.17. In the case of low intensity ground motions and a structure having fundamental mode of vibration shorter than the roof one, low strength buildings, although lower values of PFA, undergoes easily in nonlinear response producing most severe floor spectrum for the higher period roof. However, when the ground motion intensity is strong enough to induce nonlinearity in both structures (low and high strength) the situation is reversed and high strength buildings become the most dangerous for roof structure (DL3 and DL4 in Figure 6.16).

This remarks as the roof response is strongly affected by the global structure response and that an assessment of these architectural assets can only be performed by analysing also the primary structure performance. Moreover, a combined evaluation of global and local performances can better identify the critical scenario for computation of economic and human losses.



**Figure 6.16** 3d Distribution of median PGA causing exceeding of the considered LS for the three roof typologies. The median values of the fragility functions shown in Figure 6.15 are located in the midpoint of the surfaces.



**Figure 6.17** Acceleration demand in roof structure with period larger than the primary structure one for low and high ground motion intensity.

Figure 6.18 plots the conditional probability of achieving a specific DS in the roof structure given the occurrence of a specific DS in the primary structure for all the considered building configurations.

In other words, the bars were produced by applying statistics on the fraction of realisations inducing a specific DS in the primary structure (classified according to the building inter-storey drift), therefore the sum of the bin values within each box is equal to

one. This may help readers and decision-makers in understanding which is the nonlinear demand and consequently the damage state associated with the roof structure given the primary structure DS.

As expected, damage occurring in the roof structure is strongly dependent from the number of storeys while the building strength seems to play a secondary role.

Figure 6.18 shows clearly how for no or slight structural damage in the primary structure (DS1 and DS2) a higher damage state is expected in the roof structure due to acceleration amplification and high flexibility of these architectural elements. On the other hand, for high non-linear demand in the primary structure (DS4 and DS5) the DS associated with the roof substructure tend to be lower compared to the global one. Therefore, roof structures are expected to achieve slight or moderate level of damage for low level of seismic demand and damage of the primary structure while their heavy damage and collapse is unlikely to occur, even for high level of distress achieved in the primary structure.

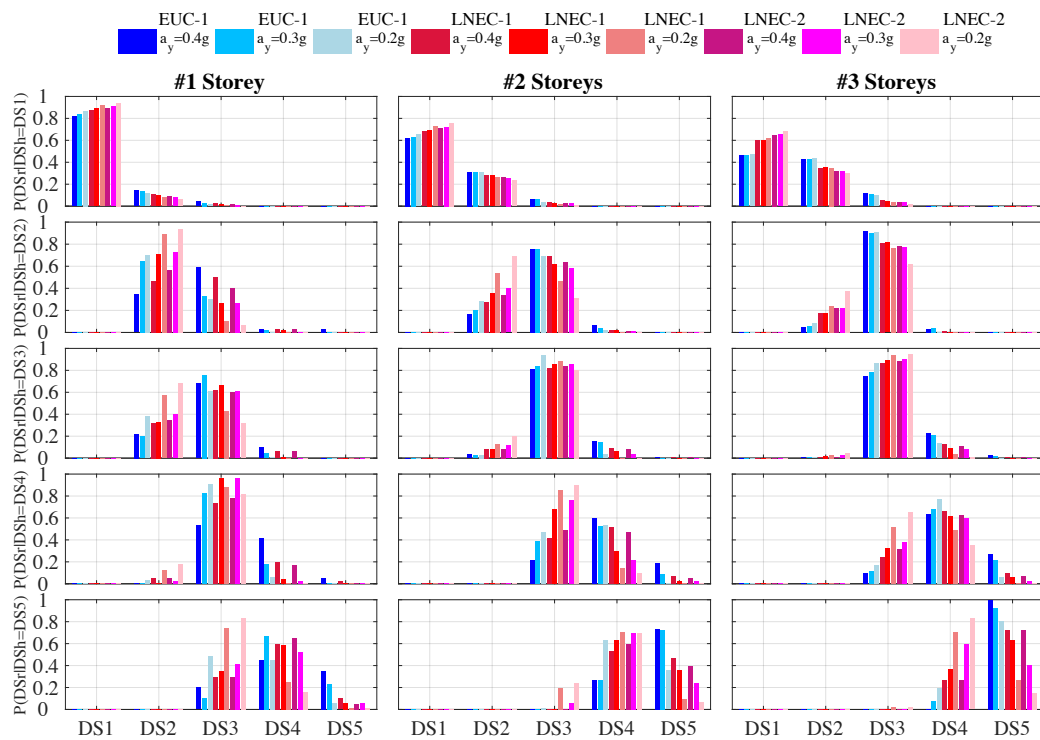


**Figure 6.18** Conditional probability of achieving a specific DS in the roof structure given the attainment of a specific DS in the building for all the structural configuration considered.

The distribution of the fragility function dispersion over the set of considered building configurations and different DLs is another interesting aspect to analyse. Figure 6.19 is contour map of the distribution of the dispersion according to the three IMs earlier introduced. This may allow to evaluate the performance of each IM in characterising the structural performance for the entire set of buildings under consideration. The whiter the surface is, the lower the dispersion of the corresponding structural configuration is. The colour scale is kept constant for the three roof typologies and considered DL.

In general, an increase in dispersion for all the IMs is associated (particularly evident for DL3 and DL4) with buildings experiencing high nonlinear behaviour (e.g. moving towards one-storey low-strength structure) resulting in a lower demand for the roof substructure.

When looking at a specific IM, PGA presented for DL1 and DL2 a rather significant increase in dispersion moving towards taller buildings (e.g. structures with higher fundamental period of vibration); SAT1 on the other hand, showed a reduction in dispersion when the roof is placed on tallest buildings.

Summarising, SAT1 appears to perform well at low level of ductility demand of the primary structure (DL1) whereas PGA is a good IM for high level of ductility demand in both primary and secondary structures. *AvgSA* remains the most efficient IM (whiter surfaces), however when non-linearity become very pronounced PGA and *AvgSA* tend to close values of dispersion. In the remaining cases PGA presented only moderate higher value of dispersion with respect *AvgSA*. For this reason, considering also the reduced effort in the computation of the hazard model, the choice of PGA seems reasonable.

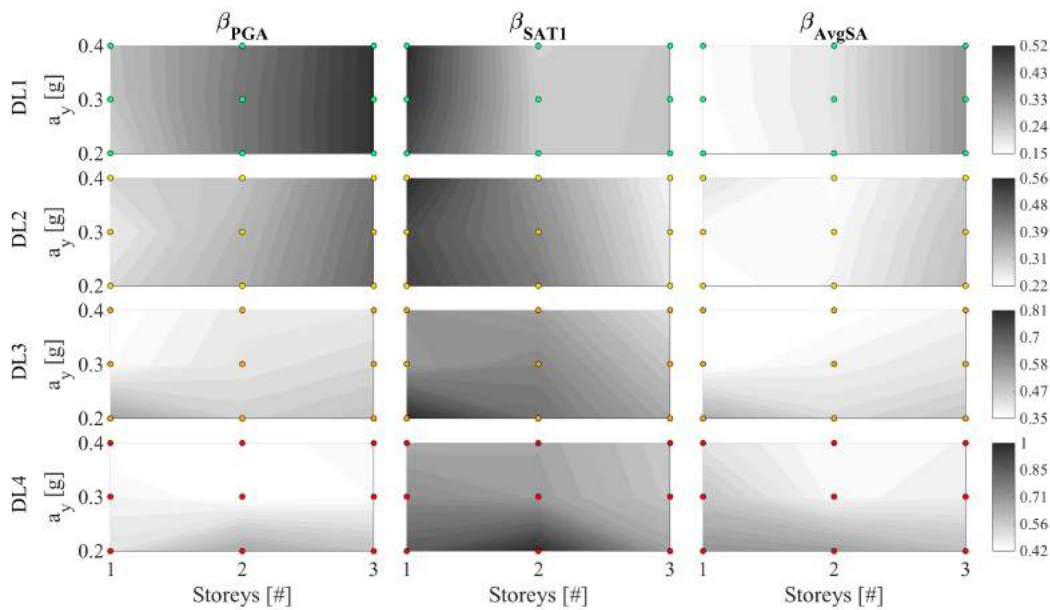


**Figure 6.19 3d Distribution of fragility function dispersion over different building configurations and different IMs: PGA, SAT<sub>1</sub> and AvgSA.**

## 6.7. Conclusions

Dynamic testing of building prototype representative of typical Dutch terraced houses and observations from post-earthquake surveys addressed the roof structures as one of the potential causes of damage and collapse. This specific roof typology composed of URM gables supporting a timber diaphragm have shown over different shaking table tests similar behaviour in terms of damage and deflected shapes. The presence of L-shaped connectors between roof beams and masonry gables ensured compatibility of displacement between URM gables and timber diaphragm associated with a linear

deflected shape over the roof height. In this case the diaphragm drift (ridge beam horizontal displacement divided by the roof inclined length) has been identified as a good EDP for describing the roof damage.

The paper shows as their dynamic behaviour can be well captured by a SDOF system composed of two springs in parallel: a bi-linear elastic one for the simulation of the typical non-linear rocking behaviour of the masonry gables and an elastoplastic one with two hardening branches for simulating the highly dissipative timber diaphragm hysteretic behaviour. The low computational demanding numerical model, calibrated on the basis of experimental tests, has been used to perform a seismic assessment of roof structures taking the ground motion filtering effect given by the structure into account.

For this purpose, a set of SDOF systems, specifically calibrated to simulate the in-plane global response of low-rise URM buildings, was employed. Signals filtered by this primary SDOF system's response were utilised to investigate the response of roof structures. This allowed for the investigation of the roof response variability when placed on top of different structural configurations, which may vary in number of storeys and strength.

The vulnerability study suggested that, when compatibility of displacement between URM gable and timber diaphragm is ensured, attainment of heavy damage, partial and global collapse of the roof are very rare scenarios. This is mainly due to saturation of the floor acceleration amplification transferred from the global structure at the base of the roof. On the other hand, being such structures very flexible, attainment of slight damage resulted possible scenarios even for low intensity ground motions. Conditional probability of achieving a specific damage state in the roof sub-structure given the damage level associated with different configuration of primary structures and for different roof configurations are calculated.

In order to identify the most appropriate IM, the distribution of the roof fragility function dispersion over the different building configurations analysed was evaluated. Generally, *AvgSA* resulted as the most efficient IM, whereas PGA tended to *AvgSA* values of dispersion only for high levels of nonlinear demand in both global and roof structures. As expected, SAT1, instead performed well for first damage levels of the roof structure.

## 6.8. Acknowledgments

This paper describes an activity that is part of the project entitled “Study of the vulnerability of masonry buildings in Groningen” at EUCENTRE, undertaken within the framework of the research program for hazard and risk of induced seismicity in Groningen sponsored by the Nederlandse Aardolie Maatschappij BV. The authors would like to thank all the parties involved in this project: LNEC Lab and EUCENTRE Lab, together with NAM, Arup and TU Delft. The useful advices of R. Pinho, are gratefully acknowledged. Special thanks, go also to J. Uilenreef, G. Magenes, A. Campos Costa, H. Crowley, A. I. Marques, M. Mandirola, L. Grottoli, P.X. Candeias, for their support in the different phases of the experimental campaign.

## 6.9. References

- [1] J. Ingham and M. Griffith, “Performance of unreinforced masonry buildings during the 2010 Darfield (Christchurch, NZ) earthquake,” *Aust. J. Struct. Eng.*, vol. 11, no. 3, pp. 207–224, 2011.
- [2] A. Penna, P. Morandi, M. Rota, C. F. Manzini, F. da Porto, and G. Magenes, “Performance of

- masonry buildings during the Emilia 2012 earthquake,” *Bull. Earthq. Eng.*, vol. 12, no. 5, pp. 2255–2273, 2014.
- [3] D. Dizhur, R. P. Dhakal, J. Bothara, and J. M. Ingham, “Building typologies and failure modes observed in the 2015 Gorkha (Nepal) earthquake,” *Bulletin of the New Zealand Society for Earthquake Engineering*, vol. 49, no. 2, pp. 211–232, 2016.
- [4] S. J. Bourne, S. J. Oates, J. J. Bommer, B. Dost, J. Van Elk, and D. Doornhof, “A Monte Carlo method for probabilistic hazard assessment of induced seismicity due to conventional natural gas production,” *Bull. Seismol. Soc. Am.*, vol. 105, no. 3, pp. 1721–1738, 2015.
- [5] F. Graziotti, U. Tomassetti, S. Kallioras, A. Penna, and G. Magenes, “Shaking table test on a full scale URM cavity wall building,” *Bull. Earthq. Eng.*, vol. 15, no. 12, 2017.
- [6] U. Tomassetti *et al.*, “Two-way bending out-of-plane collapse of a full-scale URM building tested on a shake table,” *Bull. Earthq. Eng.*, vol. (in press), 2018.
- [7] A. A. Correia, U. Tomassetti, A. Campos Costa, A. Penna, G. Magenes, and F. Graziotti, “Collapse shake-table test on a URM-timber roof structure,” in *16th European Conference on Earthquake Engineering*, 2018, pp. 1–12.
- [8] S. Kallioras, “Numerical Simulation of Shaking Table Tests on a URM Cavity-Wall Building,” *J. Int. Mason. Soc.*, vol. 30, no. 2, p. 39, 2017.
- [9] C. Avenas, C. Fusco, A. Mooneghi, Y. Huang, M. Palmieri, and R. Sturt, “LS-DYNA Numerical Simulation of Full Scale Masonry Cavity Wall Terraced House Tested Dynamically,” in *16th Europ. Conf. on Earthq. Eng., 16ECEE*, 2018.
- [10] U. Tomassetti, F. Graziotti, A. Penna, and G. Magenes, “Modelling one-way out-of-plane response of single-leaf and cavity walls,” *Eng. Struct.*, vol. 167, pp. 241–255, Jul. 2018.
- [11] D. Malomo, R. Pinho, and A. Penna, “Using the applied element method for modelling calcium silicate brick masonry subjected to in-plane cyclic loading,” *Earthq. Eng. Struct. Dyn.*, vol. 47, no. 7, pp. 1610–1630, 2018.
- [12] L. Jacobsen, “Steady Forced Vibrations as Influenced by Damping,” *Transactions of the American Society of Mechanical Engineers*, vol. 1, no. 1, pp. 169–181, 1930.
- [13] A. Wilson, P. J. H. Quenneville, and J. M. Ingham, “In-Plane Orthotropic Behavior of Timber Floor Diaphragms in Unreinforced Masonry Buildings,” *J. Struct. Eng.*, vol. 140, no. 1, p. 4013038, 2014.
- [14] D. F. Peralta, J. M. Bracci, and M. B. D. Hueste, “Seismic behavior of wood diaphragms in pre-1950s unreinforced masonry buildings,” *J. Struct. Eng.*, vol. 130, no. 12, pp. 2040–2050, 2004.
- [15] NZSEE, “Assessment and Improvement of the Structural Performance of Buildings in Earthquakes,” 2006.
- [16] ASCE, “Seismic rehabilitation of existing buildings,” ASCE/SEI 41-06, Reston, VA, 2007.
- [17] A. Brignola, S. Podestà, and S. Pampanin, “In-plane stiffness of wooden floor,” *2008 NZSEE Conf. Pap.* 49, no. 49, pp. 1–19, 2008.
- [18] European Committee for Standardization, *EN 1995-1-1: Design of timber structures: General – Common rules and rules for buildings*. CEN, Brussels, 2004.
- [19] Nederlands Normalisatie Instituut (NEN), *NEN NPR 9998:2017 Assessment of structural safety of buildings in case of erection, reconstruction and disapproval – Basic rules for seismic actions: induced earthquakes*. 2017.
- [20] S. Kallioras *et al.*, “Experimental seismic performance of a full-scale unreinforced clay-masonry building with flexible timber diaphragms,” *Eng. Struct.*, vol. 161, no. November 2017, pp. 231–249, Apr. 2018.
- [21] A. Chopra, “Dynamics of Structures,” 2007.
- [22] A. Wilson, P. Quenneville, and J. Ingham, “Natural period and seismic idealization of flexible timber diaphragms,” *Earthq. Spectra*, vol. 29, no. 3, pp. 1003–1019, 2013.
- [23] S. Lagomarsino, “Seismic assessment of rocking masonry structures,” *Bull. Earthq. Eng.*, vol. 13, no. 1, pp. 97–128, 2015.
- [24] N. M. Newmark, “A Method of Computation for Structural Dynamics,” *Journal of the Engineering Mechanics*, vol. 85, no. 7, pp. 67–94, 1959.
- [25] F. Graziotti, A. Penna, and G. Magenes, “A nonlinear SDOF model for the simplified evaluation of the displacement demand of low-rise URM buildings,” *Bull. Earthq. Eng.*, vol. 14, no. 6, pp. 1589–1612, 2016.
- [26] S. Lagomarsino, A. Penna, A. Galasco, and S. Cattari, “TREMURI program: An equivalent frame model for the nonlinear seismic analysis of masonry buildings,” *Eng. Struct.*, vol. 56, pp. 1787–1799, 2013.
- [27] A. Penna, S. Lagomarsino, and A. Galasco, “A nonlinear macroelement model for the seismic analysis of masonry buildings,” *Earthq. Eng. Struct. Dyn.*, vol. 43, pp. 159–179, 2014.



- 
- [28] G. Guerrini, F. Graziotti, A. Penna, and G. Magenes, "Improved evaluation of inelastic displacement demands for short-period masonry structures," *Earthq. Eng. Struct. Dyn.*, vol. 46, no. 9, pp. 1411–1430, Jul. 2017.
- [29] U. Tomassetti *et al.*, "Dynamic collapse testing of a full-scale URM cavity-wall structure," *XVII ANIDIS*, pp. 83–93, 2017.
- [30] Ministry of Infrastructures and Transport (MIT), *Norme tecniche per le costruzioni, DM 14/01/2008*. 2008.
- [31] K. Beyer and F. Lucca, "Effect of static and kinematic boundary conditions on the out-of-plane response of brick masonry walls," *Proc. 16th Int. Brick Block Mason. Conf.*, pp. 1439–1446, 2016.
- [32] H. Derakhshan, M. C. Griffith, and J. M. Ingham, "Out-of-plane seismic response of vertically spanning URM walls connected to flexible diaphragms," *Earthq. Eng. Struct. Dyn.*, vol. 45, no. 4, pp. 563–580, Apr. 2016.
- [33] R. Pinho, D. Malomo, and E. Brunesi, "Nonlinear dynamic analysis of index buildings for v5 fragility and consequence models," 2017.
- [34] B. Chiou, R. Darragh, N. Gregor, and W. Silva, "NGA project strong-motion database," *Earthq. Spectra*, vol. 24, no. 1, pp. 23–44, 2008.
- [35] S. Akkar *et al.*, "Reference database for seismic ground-motion in Europe (RESORCE)," *Bull. Earthq. Eng.*, vol. 12, no. 1, pp. 311–339, 2014.
- [36] J. J. Bommer *et al.*, "Developing an application-specific ground-motion model for induced seismicity," *Bull. Seismol. Soc. Am.*, vol. 106, no. 1, pp. 158–173, 2016.
- [37] H. Crowley, B. Polidoro, R. Pinho, and J. van Elk, "Framework for Developing Fragility and Consequence Models for Local Personal Risk," *Earthq. Spectra*, vol. 33, no. 4, pp. 1325–1345, 2017.
- [38] M. Kohrangi, P. Bazzurro, D. Vamvatsikos, and A. Spillatura, "Conditional spectrum-based ground motion record selection using average spectral acceleration," *Earthq. Eng. Struct. Dyn.*, vol. 46, no. 10, pp. 1667–1685, Aug. 2017.
- [39] C. A. Cornell, F. Jalayer, R. O. Hamburger, and D. A. Foutch, "Probabilistic Basis for 2000 SAC Federal Emergency Management Agency Steel Moment Frame Guidelines," *J. Struct. Eng.*, vol. 128, no. 4, pp. 526–533, Apr. 2002.
- [40] P. Gehl, D. M. Seyedi, and J. Douglas, "Vector-valued fragility functions for seismic risk evaluation," *Bull. Earthq. Eng.*, vol. 11, no. 2, pp. 365–384, 2013.
- [41] J. W. Baker, "Efficient analytical fragility function fitting using dynamic structural analysis," *Earthq. Spectra*, vol. 31, no. 1, pp. 579–599, 2015.
- [42] E. G. Dimitrakopoulos and T. S. Paraskeva, "Dimensionless fragility curves for rocking response to near-fault excitations," *Earthq. Eng. Struct. Dyn.*, vol. 44, no. 12, pp. 2015–2033, Sep. 2015.



## 7. Probabilistic seismic assessment of URM chimneys and parapets

Tomassetti U., Graziotti F., Penna A. Probabilistic seismic assessment of URM chimneys and parapets, *Earthquake Spectra* (to be submitted).

**Abstract.** Unreinforced masonry (URM) parapets and chimneys are typical architectural components of low-rise commercial and residential URM buildings. These elements are free standing components located above the perimeter walls or the roofline, subjected, hence, to the highest amplification of ground motion during an earthquake. Their damage and collapse may represent a significant hazard for building occupants and pedestrians, as well as, losses in terms of building repair cost. For these reasons, a single-degree-of-freedom (SDOF) model is presented and calibrated on several experimental dynamic tests on parapets and chimneys. The model is then adopted to assess the vulnerability of opportunely selected secondary elements placed on top of different primary structure and roof configurations. Further SDOFs are used to simulate the responses of primary structures and roofs when subjected to a large set of natural ground motions. Their acceleration output is used as acceleration input for chimneys and parapets. Overturning fragility curves are obtained from the cloud results. Moreover, focus is also placed in establishing which intensity measure result as the most efficient one and how the median collapse intensity is affected by the characteristics of the primary structure. The numerical fragility functions are finally compared with empirical ones.

### 7.1. Introduction

Unreinforced masonry (URM) parapets and chimneys are typical architectural components of low-rise commercial and residential URM buildings. These elements are free standing components located above the perimeter walls or the roofline and characterised with several typologies of connection details with the primary structure. Due to their location on top of conventional buildings parapets and chimneys are subjected to the highest amplification of ground motion during an earthquake resulting as a significant hazard for building occupants and pedestrians. Their high seismic vulnerability has been pointed out by several last-event post-earthquake reconnaissance reporting a large number of damaged and toppled parapets and chimneys (Canterbury sequence 2010-2011 [1][2][3], Emilia 2012 [4], Kaikoura 2016 [5]).

The surveys after the Canterbury 2010-2011 events concluded that approximately 65% of the URM chimney stock in the Central Business District collapsed while 20% underwent damage and only 15% remained completely undamaged [6]. The same sequence caused significant damage and collapse of URM walls and parapets due to the activation of out-of-plane (OOP) mechanisms [2]. The damage was mainly associated with flexural-rocking and rocking-sliding mechanisms and often located at the connection with floor and roof timber diaphragm due to interaction with the primary structure.

Cracking at the roofline (Figure 7.1c) associated with sliding and/or rotation after intense rocking (Figure 7.1d), disintegration due to weak mortar and dislodged bricks (Figure 7.1e), toppling (Figure 7.1f), detachment of the stack (Figure 7.1h) were the most frequently encountered chimney failures [5]. Initiation of cracking or fallen debris at the ground level (Figure 7.1a-b) were observed in case of damaged parapets. Figure 7.1 shows some these observed failures. Failures of the brace-to-masonry connections were also observed in the case of restrained parapets and chimneys [3].

While masonry walls and parapets were observed to collapsed almost universally in the outward direction representing a threat for pedestrians and passers-by [3], chimneys often were seen to topple inward compromising the structural integrity of roof and ceiling structures and representing a significant hazard for building occupants [6].

The risk represented by these secondary elements is not only related to fatality and injuries as documented by [4] but also to economic and financial losses. Giaretton *et al.* [6], indeed, estimate that 90% of all 15400 insurance claims for residential buildings following the 2010-2011 Canterbury sequence were associated with URM chimneys with a total repair cost exceeding US\$ 54 million.

While in high seismicity areas the mitigation of this risk was carried out by removing these elements or through the application of specific code guidelines (*e.g.* bracing them to the roof structure) [7][8][9][10][11], the communities of areas such as the Groningen region, not naturally subjected to earthquakes, have been recently potentially exposed to the hazard above described due to human induced earthquakes.

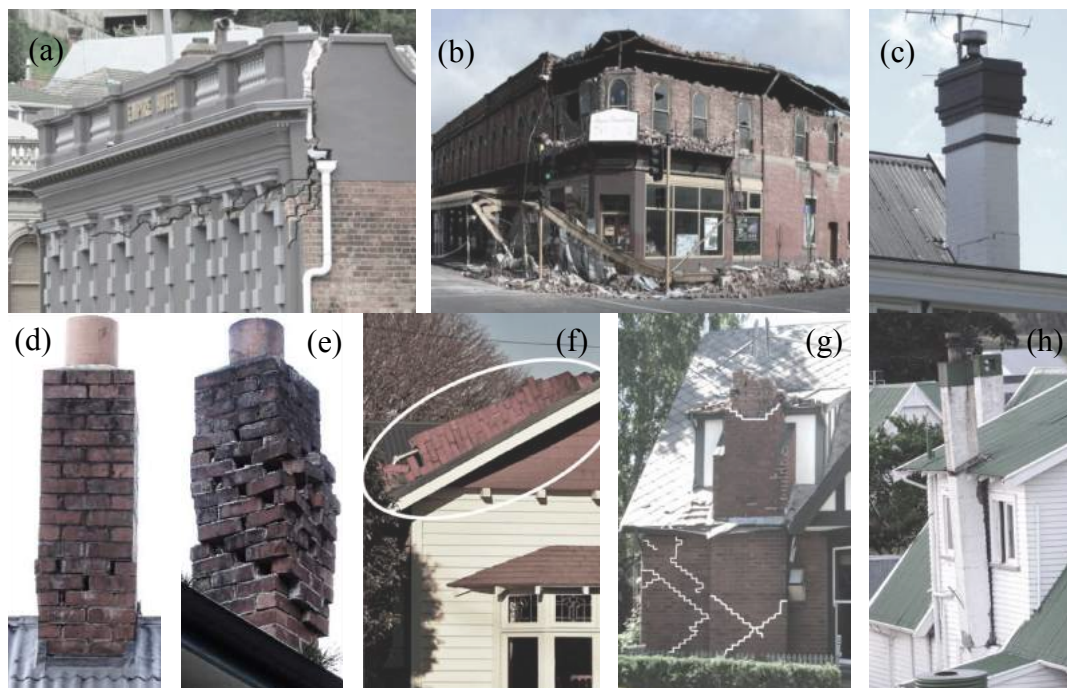


**Figure 7.1 Observations of damaged parapets and chimneys: pictures from[1][2][3][4][5].**

Generally when interested in probabilities of damage and collapse of chimneys and parapets, researchers and practitioners currently refer to fragility functions based on collected empirical data [12][13], which presents several shortcomings. Analytical

overturning fragilities of these secondary elements modelling the response of the primary structure are limited to few studies, mainly focused on overturning of rigid blocks [14].

With the goal of understanding the seismic behaviour of these non-structural elements in as-built and retrofitted conditions, static and dynamic in-situ and laboratory tests were carried out in literature [6][15][16][17]. These experimental tests may represent also a reliable reference for the development and calibration of numerical models simulating the static and dynamic behaviour of structures

This paper presents a single-degree-of-freedom (SDOF) numerical model for the analysis of their rocking dynamic behaviour discussing limitations and advantages of the employed approach. The response of the numerical model is, then, calibrated on several experimental dynamic tests on parapets and chimneys. The model is finally adopted to assess the vulnerability of this secondary elements placed on top of different primary structure and roof configurations (in terms of number of storeys and structure lateral strength). SDOFs for the simulation of the global response of the primary structure and roof were adopted to produce chimney and parapets input motions. The best ground and floor intensity measures (IM) in predicting their response are also evaluated and discussed.

## 7.2. Modelling the dynamic response of parapets and chimneys

Post-event damage observations and experimental tests have shown that the governing mechanism for parapets and chimneys, in the vast majority of cases, is related to flexure leading, in case the masonry quality is good enough to ensure the formation of such mechanism, to rocking behaviour.

Of course, their dynamic response may result rather complex involving mortar disintegration and dislodged bricks, one-side rocking [18] and two-way bending mechanisms [19] in the case of parapets while sliding phenomena associated with rocking, rotations and three dimensional motions were observed in the case of chimneys. In both cases the nature of the construction detail and the dynamic interaction between the element and the primary structure may play a significant role (*e.g.* connections with floor and roof framing) and represent a complex variable to model.

The herein adopted numerical model is a SDOF system for the analysis of the two-dimensional dynamic behaviour of these non-structural elements able to capture both their initial elastic phase and the following rocking phase [20]. The model relies on the assumption of these elements responding dynamically as rigid bodies. Sliding and rocking-sliding effects cannot be captured by the adopted model and a reader interested in such phenomenon is referred to [21].

### 7.2.1. Equation of motion

The SDOF equation of motion governing the dynamic rocking behaviour of masonry elements such as chimneys and parapets based on their force-displacement relationship is the defined by equation 1 [22][23]. Equation 1 is equivalent to those proposed by Housner [24] and many other researchers describing the rigid block dynamics as function of the rotation of the rigid body.

$$m^* \cdot a^*(t) + C(t) \cdot v^*(t) + F^*(d^*(t)) = m^* \cdot a_g(t) \quad (1)$$

where  $t$  is the time,  $a^*(t)$  the system equivalent acceleration,  $a_g(t)$  the acceleration excitation at the base  $v^*(t)$ , the equivalent velocity,  $d^*(t)$  the equivalent displacement,  $c(t)$  is the system damping coefficient and  $F^*(d^*(t))$  the equivalent nonlinear spring force expressed as a function of  $d^*(t)$ . According to standard modal analysis,  $m^*$  and  $d^*$ , equivalent modal mass and displacement can be calculated dividing the walls into  $n$  finite elements each with mass  $m_i$  and horizontal displacement  $\delta_i$  as follow:

$$m^* = \frac{(\sum_{i=1}^n m_i \cdot \delta_i)^2}{\sum_{i=1}^n m_i \cdot \delta_i^2}; \quad d^* = \frac{\sum_{i=1}^n m_i \cdot \delta_i^2}{\sum_{i=1}^n m_i \cdot \delta_i} \quad (2)$$

In the case of rocking response of these URM free-standing elements characterized by a linear displacement profile with top displacement equal to unity and uniformly distributed mass,  $m^*$  and  $d^*$  are  $3/4m$  (total mass) and  $2/3d_i$  (top displacement). If interested in modelling the pre-activation mechanism phase (e.g. linear elastic response), the displacement profile is better characterized by a second order polynomial relationship, which leads to values of  $m^*$  and  $d^*$  approximately equal to  $3/5m$  and  $5/8d_i$ .

### 7.2.2. Force-displacement relationship

Before undergoing non-linear rocking behaviour through the development of cracking URM walls are characterised by a linear response controlled by the masonry flexural strength (see schematic representation of Figure 7.2). A proper consideration of the uncracked response, both in terms of initial stiffness and lateral resistance provided by the tensile strength at the interfaces, may better characterise the performance of these masonry elements avoiding the overestimation or underestimation in peculiar cases of their displacement demand. This has been observed for the OOP behaviour of masonry walls experimentally [25][26] and numerically [20]. Figure 7.2 shows the idealisation of a chimney as a rocking block characterised by the radius vector  $R$ , defining the position of the centre of mass with respect to the corner  $O$  and the slenderness angle  $\alpha$ : arctangent of the ratio thickness  $t$  to height  $h$ .

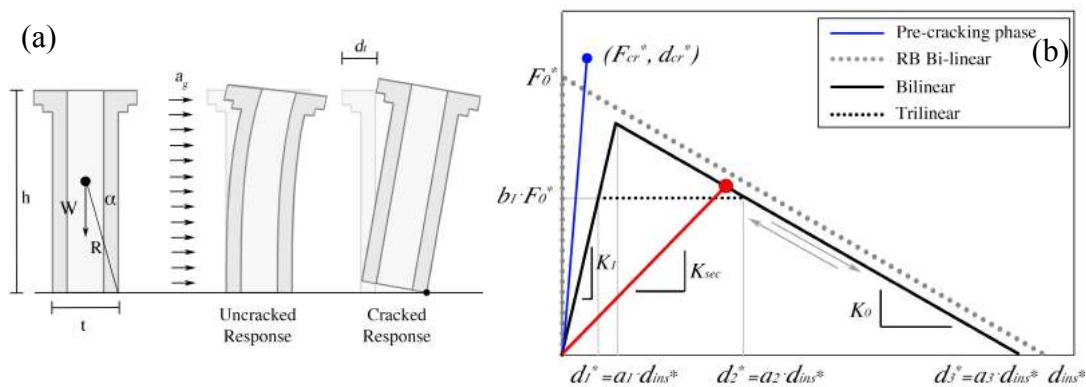


**Figure 7.2 Schematisation of a chimney as a rocking block, un-cracked and rocking responses (a).  $F$ - $u$  relationship implemented: linear elastic response followed by bilinear and trilinear configurations built on the bi-linear rigid body idealisation ( $F_0^* - d_{ins}^*$ ).**

Recognising that the URM wall segments do not have infinite stiffness, several researchers proposed relationships such as bi-linear [27], tri-linear [22] and quadri-linear [28] constructed from the associated rigid-body force-displacement curve ( $F_0^* - d_{ins}^*$ ), to

model the actual rocking  $F^*-d^*$  curve. According to the equivalent mass and displacement described in Section 7.2.1, equations 3 and 4 define the rigid body curve:

$$F_0^* = m^* \cdot g \cdot t/h = m^* \cdot g \cdot \tan(\alpha) \quad (3)$$

$$d_{ins}^* = h/h_G \cdot R \cdot \sin(\alpha) \cong \frac{2}{3}t \quad (4)$$

$K_0 (=F_0^*/d_{ins}^*)$  represents the negative stiffness of the system while  $m^*$  is 3/4 of the total mass.  $h_G$  is the height of the centre of gravity.

In case of a bilinear  $F^*-d^*$  relationship, key parameters are  $d_1^*(=a_1 d_{ins}^*)$  controlling the wall's initial cracked stiffness and  $d_3^*(=a_3 d_{ins}^*)$  which, reducing the displacement associated with zero force, may take into account the masonry compressive strength and consequently the physical dimension of the hinges [20][29].  $F_1^*(=(a_3 d_{ins}^* - a_1 d_{ins}^*)/K_0)$  depends on the other parameters. The trilinear  $F^*-d^*$  relationship, is further characterised by  $F_y^*(=b_1 F_0^*)$  identifying the force plateau while  $d_2^*$  is defined by the other parameters ( $=a_3 d_{ins}^* - F_y^*/K_0$ ).

Similarly to Tomassetti *et al.* [20], the pre-activation mechanism phase, was taken into account by adopting an initial elastic branch until exceeding of the point having coordinates  $F_{cr}^*$  and  $d_{cr}^*$ . By assuming a uniformly distributed lateral face load (considering uniform thickness and density along the element height), the equivalent inertial force necessary to trigger the rocking mechanism (*e.g.* cracking at the element base) can be estimated as follow:

$$F_{cr}^* = m^* \cdot g \cdot \frac{I_g}{t \cdot h} \left( f_w + \frac{W}{A} \right) \quad (5)$$

where  $I_g$  is the section moment of inertia,  $A$  the section area,  $f_w$  the masonry flexural strength,  $W$  the weight of the element and  $m^*$  3/5 of the total mass. For a parapet wall a width of 1 meter can be considered.  $d_{cr}^*$  was instead defined according to calibration of experimental tests.

### 7.2.3. Energy dissipation

The overall damping force acting during the rocking response of these URM elements is given primarily by the energy dissipated through impacts in addition to a small contribution from the hysteretic energy dissipation. These two sources of damping have been modelled by Tomassetti *et al.* [20], recurring to two different typologies of damping coefficient, both acting on the instantaneous secant stiffness of the system updated at each analysis step ( $\omega(t) = \sqrt{K_{sec}(t)}/m^*$ , see  $K_{sec}(t)$  in Figure 7.2b). The first one,  $C_{CDR}(t)$ , associates a constant damping ratio (CDR) through all the system frequencies, whereas the second one,  $C_{SDR}(t)$ , assumes a stiffness proportional term (linear  $\xi-\omega$  relationship, SDR) identified by the damping ratio ( $\xi_m$ ) corresponding to the frequency of the elastic branch of the bi-linear or tri-linear relationship ( $\omega_1$ ). Both  $C_{CDR}$  and  $C_{SDR}$  models, acting on the secant frequency, tend to concentrate the energy dissipation around the zero-oscillations amplitude region, where the secant stiffness matching the initial one is higher. The most widely used approach, relying on the classical hypothesis of the impulse dynamics (*e.g.* inelastic impacts, no sliding), is simulating the energy dissipation involved in such mechanisms through a coefficient of restitution. The analytical coefficient of restitution, defined by equation 6 and depending on the block geometry, acts by reducing

the system velocity at each impact event (e.g. when the horizontal displacement  $u$  passes through the null displacement).

$$e_{an} = 1 - \frac{3}{2} \sin^2 \alpha \quad (6)$$

The coefficient of restitution experimentally observed for URM walls is lower than  $e_{an}$ , therefore numerical works proposed an experimental coefficient of restitution  $e_{exp}$  that is  $0.95 \cdot e_{an}$  [30].

#### 7.2.4. The numerical model

The numerical model adopts the Newmark ‘linear acceleration method’ [31] integration scheme implemented in the non-iterative formulation version. The model solves equation 1 considering two distinct: pre-and-post activation mechanisms (see also [20]). The former is violated at the attainment of the cracking force  $F_{cr}^*$  with the model that initially assumes pre-mechanism stiffness (given by  $F_{cr}^*$  and  $d_{cr}^*$ ) and  $m^*$  equal to  $3/5 \cdot m$  then switching to rocking analysis with  $F^*-d^*$  relationship represented by the bilinear or trilinear configuration and  $m^*$  equal to  $3/4 \cdot m$ . During the pre-mechanism phase, the damping coefficient ( $C_{lin}$ ) adopted is independent of the damping system adopted (since the  $F^*-d^*$  displacement is simply linear elastic) and it is constant during all the analysis steps.

### 7.3. Simulation of the experimental response of parapets and chimneys

In order to prove the capability of the simplified numerical model to capture the seismic behaviour of these URM elements, several experimental tests were calibrated adopting all the damping models aforementioned. The reference experimental tests and the characteristics of the specimens are listed in Section 7.3.1 whereas the results of the calibration process are discussed in Section 7.3.2 and Section 7.3.3 for parapets and chimneys, respectively.

#### 7.3.1. Reference experimental campaigns

Parapets and chimneys tested in as-built condition on the shake-table by Giaretton *et al.* [6][15] were taken as reference for calibration and model validation. Both specimen typologies were built with vintage solid clay bricks (of size 230x110x75) with 15 mm thick mortar bed-joints.

The parapets considered for calibration were P4-(B) and P7-(C), both 1180 mm high, 1200 mm wide and 230 mm thick. Their masonry flexural bond strength was 0.07 and 0.02 MPa, whereas the masonry compressive strength 10.7 and 7.4 MPa for P4-(B) and P7-(C), respectively.

The dynamic response of chimneys C1-(A) and C2-(B), having both geometry 470x470x1870 mm (flue of 250x250x1870 mm) and a total weight of approximately 518 kg, has been simulated with the simplified numerical model. The two specimens presented different mortar mixes with mortar compressive strength of 2.1 and 0.5 MPa and masonry compressive strength of 11.1 and 7.4 MPa for C1(A) and C2(B), respectively. A timber frame, intended to replicate a detail of the chimney-roof connection, was constructed around them.



The parapet specimens were tested under two different input typologies: the first one was a ground motion (GM) recorded during the 22 February 2011 Christchurch earthquake applied with increasing intensity up to attainment of cracking and rocking. The second dynamic input was an increasing amplitude harmonic motion (HM) applied during the post-cracking phase [15]. URM Chimneys were, instead, tested under a HM input [6].

The response of a URM chimney tested as architectural element of a one-storey full-scale house on the LNEC shake table was also calibrated [32][33]. The building prototype was made of clay solid bricks (size 208×100×50mm) and 10-mm-thick mortar bed joints with average masonry compressive and flexural strengths equals to 11.45 MPa and 0.36 MPa, respectively. The masonry density was 1912 kg/m<sup>3</sup>. The 540x540 mm chimneys with a 340x340 mm flue was interlocked with an in-plane excited wall up to the first-floor level (height of 2.72m) extending for approximately 2.3 m above the roofline for a total height of 5.28 m. The calibration of the aforementioned tests allowed for the identification of parameters in terms of  $F^*-d^*$  relationship and damping properties that resulted in an efficient simulation of the experimental response

### 7.3.2. Calibration of parapet responses

The experimental response of parapet specimens was captured adopting all the aforementioned damping models, coefficient of restitution, CDR and SDR and a bilinear  $F^*-d^*$  model. The calibration process confirmed the rocking behaviour to be highly nonlinear and consequently very sensitive to small changes of dynamic input or  $F^*-d^*$  curve as well as damping properties. The rocking frequency parameter  $p$  of the associated idealised rocking block was approximately 3.5 1/s.

Table 7.1 presents the calibrated tests including the specimen name, the input typology (GM or HM), the initial status of the specimen (cracked or uncracked, CR or UN) and the parameters that best simulated the experimental response of the different tests. These parameters have been selected to be consistent with the test by test observed damage and to maintain as much as possible uniformity among all the tests.

**Table 7.1 SDOF parameters adopted to simulate the experimental response in the different testing phases for parapets**

Spec. ID	Input	Initial Status	$F_{cr}^*$ [kN]	$a_{cr}$ [-]	$F_0^*$ [kN]	$d_{ins}^*$ [mm]	$a_3$ [-]	SDR Model		CDR Model		CoR Model	
								$a_1$ [-]	$\xi_{in}$ [%]	$a_1$ [-]	$\xi$ [%]	$a_1$ [-]	$e_{exp}$ [-]
P4-(B)	GM	UN	2.19	0.017	0.93	153	0.95	0.077	3.0	0.06	2.0	0.06	0.908
P4-(B)	HM	CR	-	-	0.93	153	0.95	0.074	1.8	0.061	1.5	0.07	0.936
P7-(C)	GM	UN	1.15	0.040	0.93	153	0.95	0.055	3.0	0.055	2.0	0.05	0.936
P7-(C)	HM	CR	-	-	0.93	153	0.95	0.069	2.6	0.057	1.9	0.07	0.917

Figure 7.3 shows the general good match between experimental and calibrated-numerical normalised displacement histories ( $d^*/d_{ins}^*$ ) for P4-(B) and P7-(C) specimens. The displacement histories are interrupted at the instant of the impact with the protection barriers placed in proximity of the static instability ( $d_{ins}^*$ ). In particular, for the two tests in which the parapets were initially undamaged (GM inputs) the responses of the numerical model assuming initially un-cracked and cracked configurations having same bilinear  $F^*-d^*$  curve are shown. These two responses show the importance of accounting for the initial elastic strength of the parapet. In the P4-(B) case, the numerical damaged

history presented an initial overestimation of the displacement demand (around second 14) leading for coefficient of restitution and CDR damping models to a premature collapse. Both CDR and SDR models in the initially undamaged configuration were able to capture the experimental response until the impact (second 24), while the coefficient of restitution did not attain collapse. In both cases the calibrated  $F_{cr}^*$  values resulted almost double than those obtained from equation 5 (1.0 kN and 0.46 kN using a flexural bond of 0.07 MPa and 0.02 MPa for P4(B) and P7(C), respectively).

The adopted  $a_1$  values well agree with the value of 0.06 proposed by Lagomarsino [27] while the  $e_{exp}/e_{an}$  ratios used by the coefficient of restitution damped model (0.91-0.94) are only slightly lower than 0.95 suggested by Sorrentino *et al.* [30]. Among the three damping models the SDR appeared to be the most appropriate one.

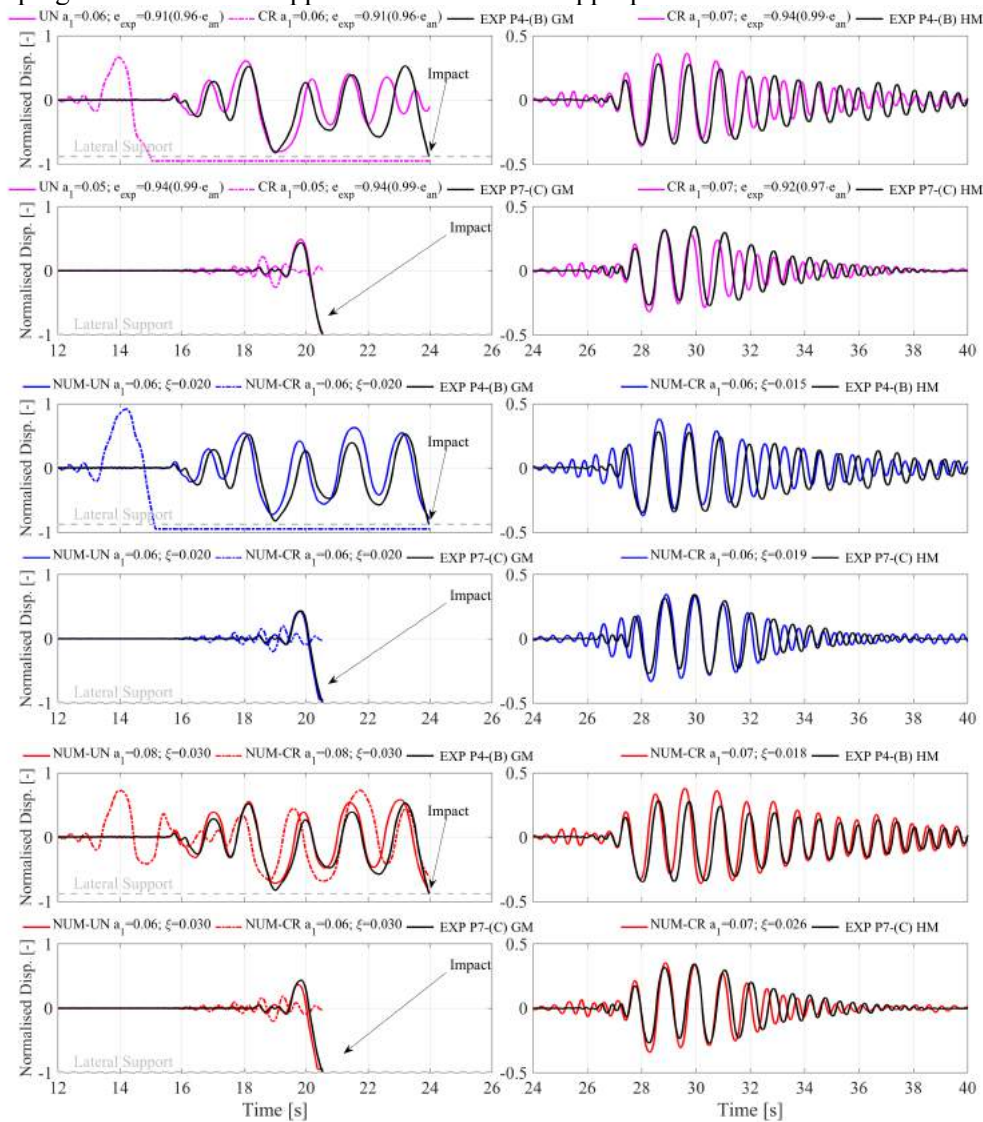


**Figure 7.3 Comparison between experimental and numerical normalized displacement histories for P4-(B) and P7-(C) specimens adopting three damping models: coefficient of restitution (pink), CDR (blue), SDR (red).**

### 7.3.3. Calibration of chimney responses

Very little research about the numerical simulation of the dynamic response of URM chimneys by means of simplified models is currently available in literature. This is because these elements were considered of secondary importance until a few years ago but also due to the lack of reference experimental tests for calibration purposes. Nevertheless, the calibration procedure and the derivation of SDOF parameters followed strictly the procedure discussed for parapet specimens (see parameters in Table 7.2).

**Table 7.2 SDOF parameters adopted to simulate the experimental response in the different testing phases for chimneys**

Spec. ID	Input	Initial Status	$F_{cr}^*$ [kN]	$a_{cr}$ [-]	$F_0^*$ [kN]	$d_{ins}^*$ [mm]	$a_3$ [-]	$b_1$ [-]	SDR Model		CDR Model		CoR Model	
									$a_1$ [-]	$\xi_{in}$ [%]	$a_1$ [-]	$\xi$ [%]	$a_1$ [-]	$e_{exp}$ [-]
C1-(A)	HM	UN	2.77	0.063	0.96	313	0.95	-	0.063	15.5	0.063	12.8	0.051	0.69
C2-(B)	HM	UN	-	-	0.96	313	0.75	0.50	0.048	5.00	0.046	4.00	0.046	0.81
LNEC	SC2-250%	UN	3.13	0.015	1.33	360	0.95	-	0.056	15.5	0.056	12.5	0.054	0.68
LNEC	SC2-300%	UN	3.13	0.015	1.33	360	0.95	-	0.056	15.5	0.056	12.5	0.054	0.68
LNEC	SC2-400%	CR	-	-	1.33	360	0.95	-	0.058	8.0	0.058	6.00	0.058	0.77
LNEC	SC2-500%	CR	-	-	1.33	360	0.95	-	0.058	13.0	0.058	10.0	0.058	0.69

The two chimneys tested by Giaretton *et al.* [6] exhibited rocking behaviour with a substantial difference. The C1(A) specimen, having stronger flexural bond, has shown a classical rocking behaviour with a migration of the bottom interface (see Figure 7.4a) whereas C2(B) presented a rocking response associated with bulging effect and consequently diffuse propagation of cracking due to mortar disintegration (see Figure 7.4b). In both specimen, the mechanism engaging only the portion above the roofline connection of the chimney stack, in particular an height of 1.44 m (16 courses,  $p=3.11$  l/s) and 1.35 m (15 courses,  $p=3.21$  l/s) for C1(A) and C2(B), respectively.



**Figure 7.4 Frames of the dynamic response of URM chimneys (taken from Giaretton *et al.* [6]): progression of rocking for C1(A) (a) and rocking associated with disintegration of mortar for C2(B) (b).**

Figure 7.5 shows the comparison between experimental and numerical (initially undamaged and damaged) normalised displacement histories for the C1(A) chimney adopting the three discussed damping models. The good match of Figure 7.5 was obtained recurring to a flexural bond of 0.20 MPa for the determination of  $F_{cr}^*$  (equation 5), a bilinear  $F^*-d^*$  curve with  $a_1$  values close to 0.06 and  $e$  values ( $e_{exp}/e_{an}=0.81$ ) as well

as  $\xi$  (above 0.10) considerably higher than those generally associated to OOP rocking masonry walls ( $e_{exp}/e_{an}=0.95$  [30]). The flexibility of rocking body and rocking interface, the reduced slenderness and eventual bouncing phenomena might nullify the assumption of conservation of angular momentum. More refined models accounting for these effects may better interpret their dynamic behaviour; however, this is beyond the scope of this work which aims at assessing their probabilistic performance.

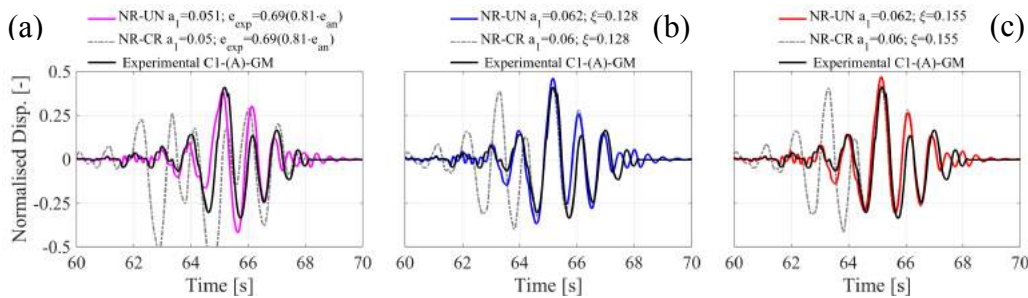


**Figure 7.5 Comparison between experimental and numerical normalised displacement histories for C1(A) specimen adopting coefficient of restitution (pink), CDR (blue), SDR (red) damping models.**

The weak bond of the C2(B) specimen did not allow the development of a lateral strength close to the rigid body one leading to a trilinear  $F^*-d^*$  curve with a force plateau limited to 50% of  $F_0^*$ . Moreover, initial elastic stiffness fell on the first branch of the tri-linear idealisation and the damage at the rocking interface limited the capacity curve at a static instability displacement of  $0.75 d_{ins}^*$ . Despite the inability of the numerical model to capture the asymmetric experimental response, the match is still satisfactory. Damping parameters were in this case considerably lower than those adopted for C2(B).

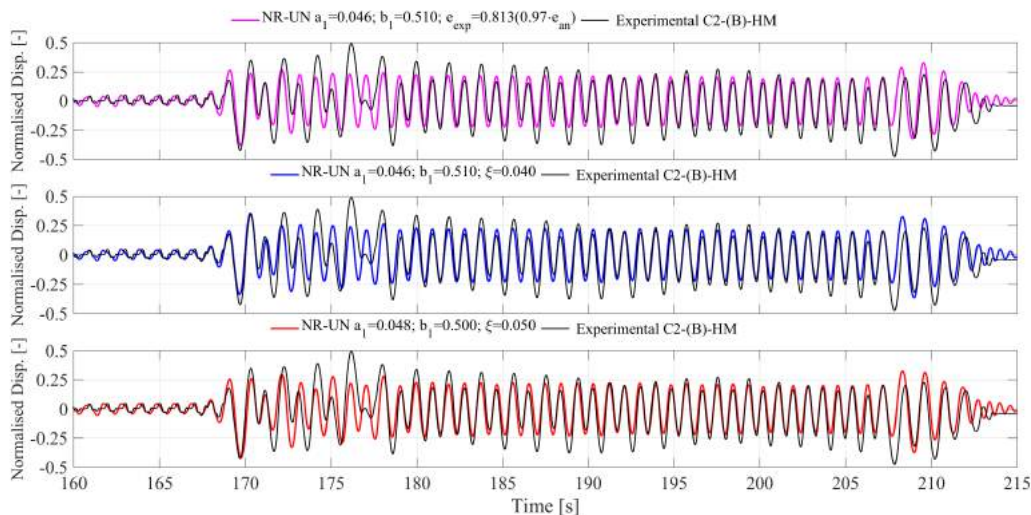


**Figure 7.6 Comparison between experimental and numerical normalised displacement histories for C2(B) specimen adopting coefficient of restitution (pink), CDR (blue), SDR (red) damping models.**

The LNEC South chimney exhibited cracking and rocking response at the first-floor level during test SC2-300% ( $PGA = 0.58g$ , see Figure 7.7a). The chimney top displacement was measured by a wire potentiometer attached to the strong reaction wall of the laboratory while an accelerometer recorded the acceleration at the location of the crack.

During test SC2-350% ( $PGA = 0.61 g$ ), a new crack developed several centimetres above the roofline, following a possible collision between the chimney stack and the roof sheathing. In this test and in the following ones, the chimney stack has shown rocking oscillations as a two-rigid-block system with quasi-stable displacement amplitude that reached a maximum of nearly  $0.5 d/d_{ins}$  (see Figure 7.7b). Displacements of the chimney top and mid-height crack location as well as accelerations at the same levels were retrieved from the video recordings of the last two tests: SC2-400% ( $PGA = 0.68 g$ ) and SC2-500% ( $PGA = 1.00 g$ ).

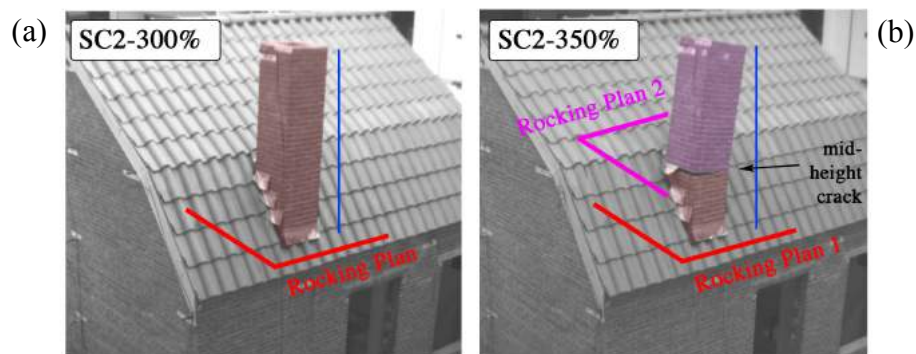


**Figure 7.7** Frames of the dynamic response of South URM chimney (adapted from [32]) : one-body rocking behaviour during SC2-300% test (a), formation of mid-height crack and two-bodies rocking system during SC2-350% test (b).

In order to characterise pre-and-post mechanism phases with same SDOF parameters, the chimney experimental response of tests SC-250% (linear elastic response) and SC2-300% (occurring of cracking) was calibrated. The height of the rocking chimney stack was approximately 2.76 m. The acceleration recorded close to the crack location at the first-floor level was used as input one and a bi-linear relationship was used to characterise the element  $F^*-d^*$  curve. A bond of 0.29 MPa was plugged in equation 5 to determine  $F_{cr}^*$  with respect to the 0.36 MPa value observed from characterisation tests (see).

The results of the calibration procedure presented in Figure 7.8 shows overestimation of the displacement demand in the pre-cracking test (SC-250%), this may be partially attributed to underestimation of experimental response due to friction of the wire potentiometer for low amplitude response (few millimetres). Overestimation of the low displacement demand was also observed for the test in which the rocking mechanism was triggered (SC-300%), especially for the first response cycle. SDOF  $F^*-d^*$  and damping parameters were consistent with those adopted for C1(A).



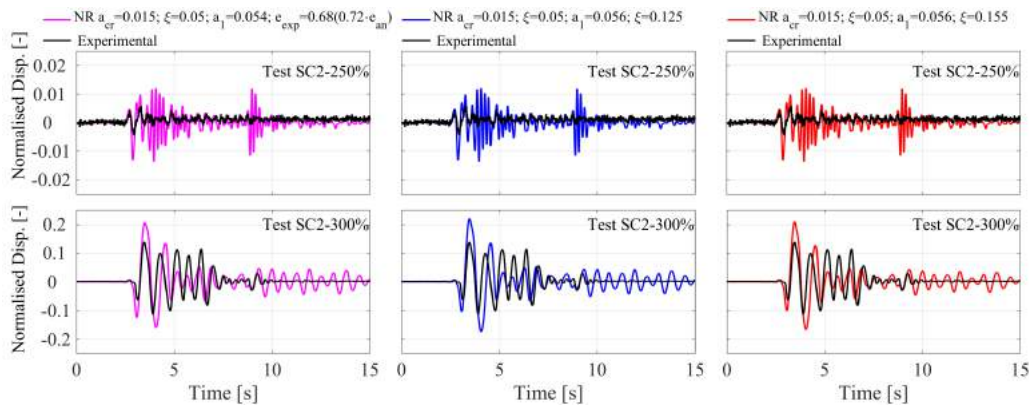


**Figure 7.8 Comparison between experimental and numerical normalised displacement histories for the LNEC chimney adopting coefficient of restitution (pink), CDR (blue), SDR (red) damping models.**

Despite the rocking motion of two bodies and a certain degree of uncertainty related to experimental data (retrieved from video recordings) the response of the upper body of the chimney stack was also simulated with the presented model. This was done with the purpose of assessing somehow the robustness of the adopted SDOF parameters more than a mere calibration of the experimental response as for previous tests. Given the abovementioned limitations, the match between experimental and numerical responses shown by Figure 7.9 seems satisfactory in terms of amplitude oscillation and energy dissipation.

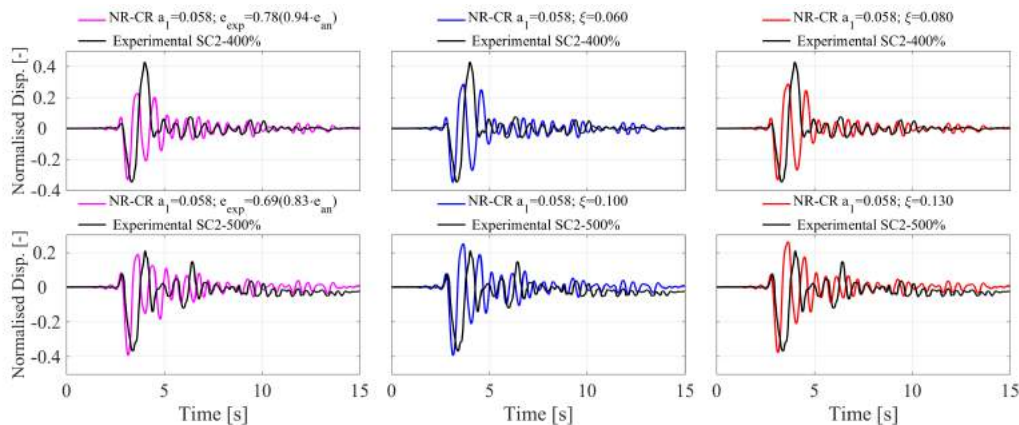


**Figure 7.9 Comparison between experimental and numerical normalised displacement histories for C2(B) specimen adopting coefficient of restitution (pink), CDR (blue), SDR (red) damping models.**

#### 7.4. Seismic vulnerability of parapet and chimney

Once validated against experimental results, the simplified model was used to assess the vulnerability of URM parapets and chimneys in the Groningen building stock. A seismic assessment of these architectural elements can only be performed by taking the filtering effect given by the structure into account, since these elements are located on top of

perimeter walls or above the roofline where the floor dynamic amplification is expected to be highest.

This was done by defining SDOF systems representative of both the global response of a URM building (primary structure) and the response of the roof structure (secondary structure). Both SDOFs, discussed in Sections 7.4.1 and 7.4.2, have been validated against experimental results. Signals filtered by the primary structure SDOF system's response were adopted to obtain a secondary SDOF system's response, or as input acceleration for the assessment of specific elements such as parapets or tall chimneys anchored to the perimeter walls. Furthermore, the secondary structure SDOF system's response was used as input to assess the performance of the masonry elements usually located on top of roof structures (squat chimneys). Figure 7.10 is a schematic representation of the SDOF adopted for the assessment of parapet and chimney elements. The dynamic interaction between these primary and secondary systems was neglected as the mass of the roof is generally less than 10% of the whole building mass. In these simulations, it is assumed that strength and stiffness of the chimney-building connection are sufficient to avoid any relative translation between the chimney and the building. Thus, toppling, as for parapets, can occur only at the top level. This modelling approach can only capture damage related to the portion of the chimney extending above the roof line (perhaps the most common damage mode). Any possible dynamic local effect such as impacts between chimney stack and roof framing is also not considered.

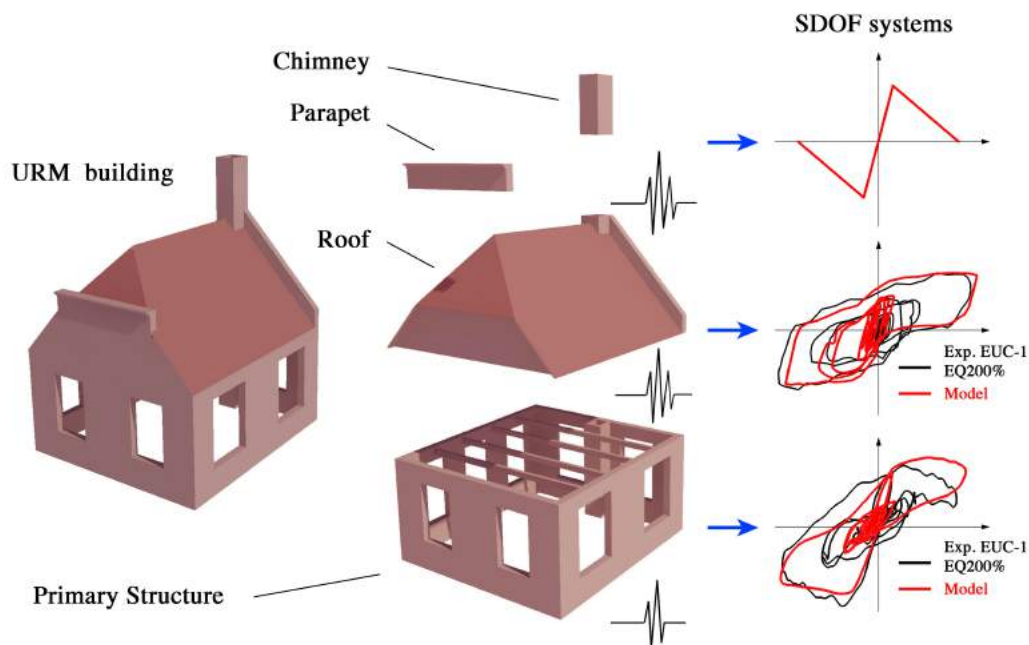


**Figure 7.10** Schematic representation of the assessment procedure performed through the definition of different typologies of SDOF systems.

#### 7.4.1. Primary SDOF (URM building's response)

The SDOF presented by Graziotti *et al.* [34] was adopted to model the global response of the URM structures. The SDOF system, implemented in the software TREMURI

[35][36], adopted a suitable nonlinear spring comprised of two macroelements in parallel allowing for an appropriate calibration between flexure-dominated and shear-dominated responses. Despite already known shortcomings related to SDOF systems, the model has shown promising capability to replicate the nonlinear response of URM multi-degree of freedom (MDOF) systems as well as experimental responses. Figure 7.10 show also the simulation of the hysteretic behaviour of a Dutch URM terraced house tested on a shake table ( test EQ2-200% [37]). In particular, the configuration assuming a contribution of 20% of the responding in shear macroelement over the total resisting force (model designation 20 in [38]) together with the associated limited hysteretic energy ( $\xi_{hyst}=14.9\%$ ) dissipation was adopted to model the response of Dutch cavity wall buildings. As largely documented by experimental tests [37][39][40], their in-plane seismic response is indeed controlled by flexure.

With the objective of investigating the variability of parapet and chimneys when placed on top of different structural configurations, a set of primary SDOF systems were defined according to different building height and strengths. Taking as reference the commonly adopted force-displacement elastoplastic idealisation [41], this building variability was defined in terms of initial idealised elastic period and yield pseudo-acceleration plateau,  $a_y$ . Three different initial elastic periods (0.1 s, 0.2 s and 0.3 s) representative of building heights of one, two and three storeys ( $\Gamma=1, 1.19$  and  $1.27$ ) associated each of them with three yield pseudo-accelerations ( $a_y$  equal to 0.2 g, 0.3 g and 0.4 g) were considered to cover realistic ranges for residential URM buildings. Table 7.3 lists the characteristics of the considered set of primary structures.

**Table 7.3 Characteristics of the considered set of buildings: fundamental period, modal shape, mass vector, modal participation factor, SDOF pseudo accelerations resistance and associated yield displacement.**

<i>Storey</i>	$T_1$	$\phi$	$M$	$\Gamma$	$a_y$	$d_y$
<i> [#]</i>	<i> [s]</i>	<i> [-]</i>	<i> [t]</i>	<i> [-]</i>	<i> Range [g]</i>	<i> [mm]</i>
1	0.1	[1]	[30]	1	0.2 0.3 0.4	0.6 0.8 1.0
2	0.2	[0.56 1.0]	[24.5 24.5]	1.19	0.2 0.3 0.4	2.0 3.0 4.0
3	0.3	[0.39 0.69 1.0]	[24.5 24.5 24.5]	1.27	0.2 0.3 0.4	4.6 6.8 9.1

The primary structure seismic performance was evaluated through the DLs proposed on the basis of dynamic experimental tests by Tomassetti *et al.* [40] for URM cavity wall buildings and expressed in terms of inter-storey drift ratio. The DLs are 0.1%, 0.15%, 0.35%, and 0.90% defining the thresholds limits between DS1, DS2, DS3, DS4 and DS5.

#### 7.4.2. Secondary SDOF (Roof building's response)

The SDOF presented by Tomassetti *et al.* [42] was adopted to model the response of roof structures. This SDOF system couples a bi-linear elastic spring typical of the non-linear rocking behaviour of the masonry gables (see  $F^*-d^*$  relationship of Figure 7.2b) with an elastoplastic having two hardening branches spring simulating the highly dissipative timber diaphragm hysteretic behaviour. The model assuming a linear deflected shape was validated against the results of three experimental tests on Dutch roofs. Figure 7.10 shows also the simulation of the hysteretic behaviour of a Dutch roof tested as component of a full-scale house ( test EQ2-200% [37], details of the simulation [42]).



In order to limit the number of analysis, only a specific roof configuration having period of 0.25 s, mass of 9920 kg and  $a_y$  of approximately 0.10 g was adopted for this work. For further details on the adopted numerical model see configuration EUC-1 in [42].

**7.4.3. Employed accelerograms and response of primary and secondary SDOFs**

A set of 3506 accelerograms (1753 in EW and NS components) including records from NGA1 [43], European [44] and Groningen databases [45] specifically selected for the derivation of the fragility functions and the computation of the probabilistic risk assessment for the Groningen field [46], has been used for the nonlinear dynamic analyses of the SDOF systems. In particular, the magnitude range has been taken to be between 3.5 and 6.5, and epicentral distances up to 60 km have been used. Figure 7.11a is a histogram showing the distribution of the predominant period (the one associated with the highest spectral acceleration) over the entire record set. Buildings with fundamental period within the range of 0.1~0.2 s are the most exposed to high spectral accelerations for this record set. Figure 7.11b is instead one of the outcome of the nonlinear time history analysis (NLTH) of the primary SDOF: median acceleration amplification ratios between last floor and PGA and roof and PGA. In general, the obtained values are consistent with those experimentally observed [37][39][40], and among the studied configurations highest amplifications are expected for the two-storey buildings.

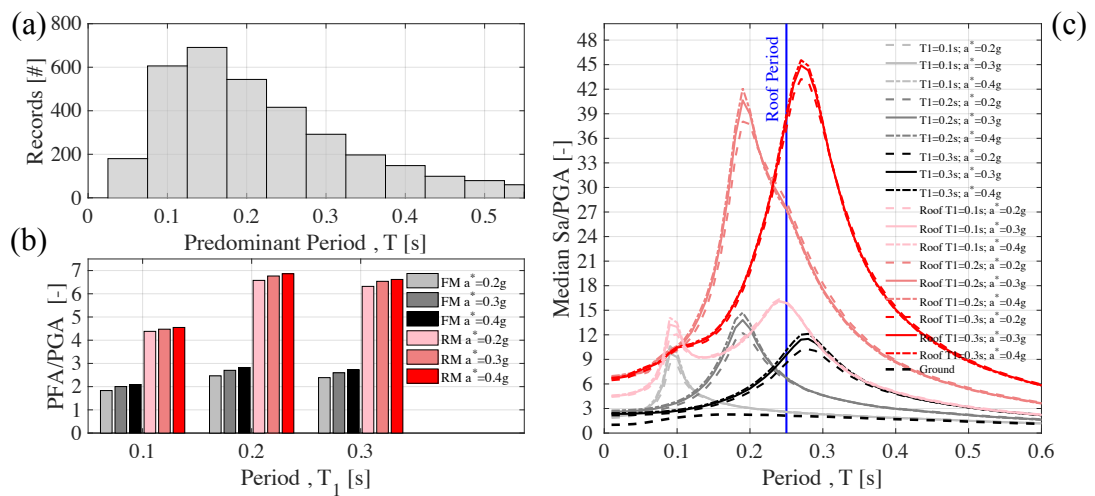


**Figure 7.11 Histogram of the predominant period (a), ratio between top storey PFA and PGA (b), comparison between ground and floor normalised by PGA median acceleration spectra (c).**

Figure 7.11c is instead the comparison between normalised by PGA median ground, floor and roof acceleration spectra for the entire set. The median ground acceleration spectrum shows the highest spectral acceleration within the period range of 0.15~0.2 s. As expected, the median floor spectra show amplification at the fundamental period of the structure. All median roof spectra are instead characterised by a double spike: at the fundamental period of the primary structure and at the period of the period of the roof structure. While highest amplification is expected at the floor level for the two-storey buildings, the most demanding roof motions (RM) are expected for three-storey houses due to dynamic interaction with the roof structure.

#### 7.4.4. Adopted intensity measures

Chimneys and parapets, as mentioned above, are subjected to a ground motion shaking filtered by primary structure and roof substructure, reason why their seismic performance was evaluated by adopting both ground and floor motion intensity measures (GIM and FIM). A desirable intensity measure (IM) ought to be: practical, IMs for which robust and modern ground motion prediction equations are available, efficient, structural response should exhibit relatively low variability for the parameters of interest, sufficient: important record-specific seismological parameters such as magnitude, distance, epsilon are represented without introducing any bias in results [47].

Part of the focus of this study was on the second point above relating to the IM efficiency with respect to the overturning of URM non-structural components. Focus was placed not only in establishing which IM resulted as the most efficient one, but also in investigating the performance of ground motion intensity measures (GMIMs) with respect to floor or roof motion ones (FMIMs or RMIMs), differences between damaged and undamaged elements and finally assessing how they are affected by primary structure characteristics and variability. Table 7.4 lists the selected IM parameters generally adopted to assess rocking behaviour and their corresponding equation.

**Table 7.4 Intensity measures adopted for the fragility curves.  $a(t)$ ,  $v(t)$ ,  $d(t)$  are absolute acceleration, velocity and displacement time histories,  $t$  is the signal duration while the subscripts  $g$  and  $f$  indicate ground and floor or eventually roof.**

<i>GMIM</i>	<i>Equation</i>	<i>FMIM/RMIM</i>	<i>Equation</i>
PGA	$\max  a_g(t) $	PFA	$\max  a_f(t) $
Sa( $T_1$ )	$Sa(T_1)$	FSa( $T_1$ )	$FSa(T_1)$
AvgSa	$\left[ \prod_{i=1}^n Sa(T_i) \right]^{1/n}$	AvgFSa	$\left[ \prod_{i=1}^n FSa(T_i) \right]^{1/n}$
PGV	$\max  v_g(t) $	PFV	$\max  v_f(t) $
PGD	$\max  d_g(t) $	PFD	$\max  d_f(t) $
HI	$\int_{0.1}^{2.5} Sv(T_i) dT$	FHI	$\int_{0.1}^{2.5} FSv(T_i) dT$
IA	$\frac{\pi}{2g} \int_0^{\infty} a_g(t)^2 dt$	FIA	$\frac{\pi}{2g} \int_0^{\infty} a_f(t)^2 dt$
CAV	$\int_0^{t_g}  a_g(t)  dt$	FCAV	$\int_0^{t_f}  a_f(t)  dt$
RMSA	$\left( \frac{1}{t_g} \int_0^{t_g} a_g(t)^2 dt \right)^{\frac{1}{2}}$	FRMSA	$\left( \frac{1}{t_g} \int_0^{t_g} a_f(t)^2 dt \right)^{\frac{1}{2}}$

They include peak ground and floor time history parameters such as acceleration (*PGA* and *PFA*), velocity (*PGV* and *PFV*) and displacement (*PGD* and *PFD*); Floor and ground spectral acceleration at the fundamental period of the wall,  $Sa(T_1)$ , and structure,  $Sa(T_h)$ , and average spectral acceleration, *AvgSA*, were also considered. This latter IM is defined as the geometric mean of spectral accelerations within a user-specified range of periods [48]. The period range considered in this study includes spectral accelerations associated with the parapet/chimney cracked initial period ( $T_1$ , see Table 7.5) and elongated secant

period corresponding to a displacement of  $0.25 d_{ins}^*$  (suggested by Derakhshan [49] for the assessment of rocking walls). Consequently, the selected period ranges for the assessment of the entire portfolio of parapets and chimneys was 0.35-1.10s and 0.45-1.40s (with 0.05s of spacing), respectively. Other ground and floor intensity measures were cumulative absolute velocity,  $CAV$  and  $FCAV$ , Arias intensity [50],  $IA$  and  $FIA$ , root-mean-square acceleration,  $RMSA$  and  $FRMSA$  and Housner intensity [51],  $HI$  and  $FHI$ .

#### 7.4.5. Geometries and modelling parameters

The geometries selected for the vulnerability study cover the dimensions of the majority of local architectural elements according to the on-field survey performed by [52]. While for parapets a width of 1 metre and thicknesses of one two and three masonry leaves were considered, the geometries selected for chimneys refer to Figure 7.12.

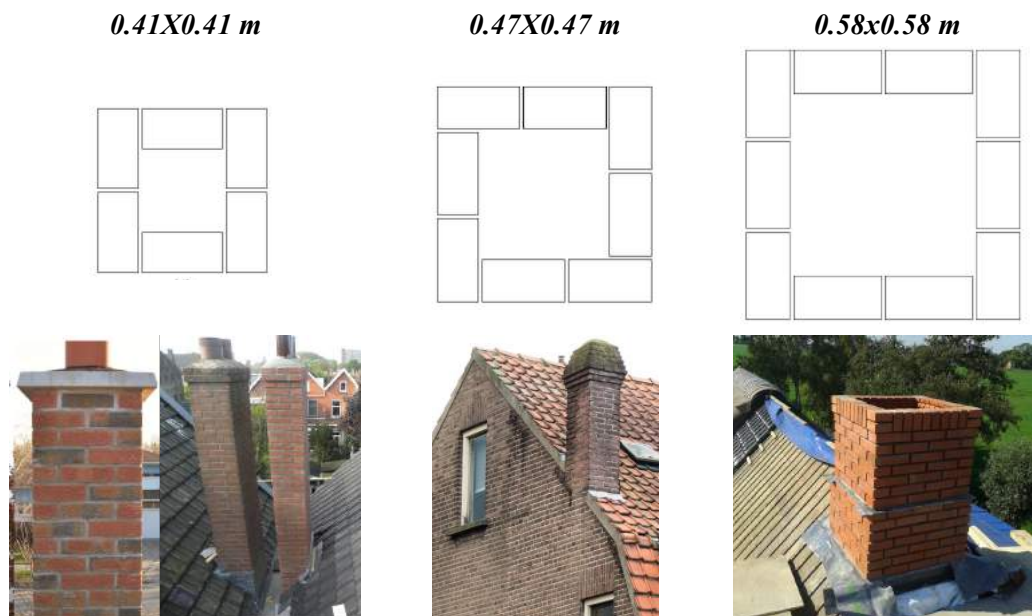


Figure 7.12 Plan view and pictures of selected chimney configurations.

A masonry density of  $1750 \text{ kN/m}^3$  and a flexural bond of  $0.15 \text{ MPa}$  (lower bound of the in-situ flexural bond [53]) were adopted. In order to study the effect of considering the flexural bond leading to cracking accelerations higher than those triggering rocking [6], analyses were performed in both initially undamaged and damaged configurations. The rocking  $F^*-d^*$  relationship was modelled with a bilinear relationship whereas a SDR model was adopted to simulate the energy dissipation. Table 7.5 presents the selected geometries and the adopted modelling parameters for parapets (P#) and chimneys (C#). Table 7.5 specifies also the set of signals adopted for the vulnerability study: ground motions, GM, floor motions, FM and roof motions, RM. Note that specific chimney configuration such as 2.2 metres tall chimneys are not subjected to RMs since they are typically connected to perimeter walls (see also Figure 7.12).

Table 7.5 Geometries and modelling parameters adopted for parapets.

<i>P-ID</i>	<i>t</i>	<i>h</i>	$\alpha$	$e_{an}$	$F_{cr}^*$	$T_{cr}$	$T_1$	$a_{cr}$	$a_1$	$a_3$	$\xi_{in}$	<i>Input</i>
	[m]	[m]	[-]	[-]	[kN]	[s]	[s]	[-]	[-]	[-]	[%]	[-]
<i>P1-60</i>	0.10	0.60	0.16	0.96	0.51	0.10	0.34	0.03	0.06	0.90	3.9	<i>GM-FM</i>
<i>P1-90</i>	0.10	0.90	0.11	0.98	0.35	0.14	0.41	0.03	0.06	0.90	3.0	<i>GM-FM</i>
<i>P1-120</i>	0.10	1.20	0.08	0.99	0.27	0.19	0.48	0.03	0.06	0.90	2.7	<i>GM-FM</i>
<i>P2-60</i>	0.21	0.60	0.34	0.83	2.27	0.10	0.33	0.03	0.06	0.95	9.1	<i>GM-FM</i>
<i>P2-90</i>	0.21	0.90	0.23	0.92	1.56	0.14	0.40	0.03	0.06	0.95	5.4	<i>GM-FM</i>
<i>P2-120</i>	0.21	1.20	0.17	0.95	1.20	0.19	0.47	0.03	0.06	0.95	4.0	<i>GM-FM</i>
<i>P3-60</i>	0.32	0.60	0.49	0.67	5.26	0.10	0.33	0.03	0.06	0.97	17.5	<i>GM-FM</i>
<i>P3-90</i>	0.32	0.90	0.34	0.83	3.62	0.14	0.40	0.03	0.06	0.97	9.3	<i>GM-FM</i>
<i>P3-120</i>	0.32	1.20	0.26	0.90	2.80	0.19	0.46	0.03	0.06	0.97	6.3	<i>GM-FM</i>

Table 7.6 Geometries and modelling parameters adopted for chimneys.

<i>C-ID</i>	<i>t</i>	<i>w</i>	<i>h</i>	$\alpha$	<i>p</i>	$e_{an}$	$F_{cr}^*$	$T_{cr}$	$T_1$	$a_{cr}$	$a_1$	$a_3$	$\xi_{in}$	<i>Input</i>
	[m]	[m]	[m]	[-]	[-]	[-]	[kN]	[s]	[s]	[-]	[-]	[-]	[%]	[-]
<i>C1-120</i>	0.41	0.41	1.20	0.33	3.41	0.84	1.73	0.24	0.42	0.05	0.05	0.97	14.4	<i>GM-FM-RM</i>
<i>C1-220</i>	0.41	0.41	2.20	0.18	2.56	0.95	1.04	0.41	0.56	0.05	0.05	0.97	9.8	<i>GM-FM</i>
<i>C2-120</i>	0.47	0.47	1.20	0.37	3.38	0.80	2.57	0.24	0.42	0.05	0.05	0.98	16.4	<i>GM-FM-RM</i>
<i>C2-220</i>	0.47	0.47	2.20	0.21	2.56	0.93	1.55	0.41	0.56	0.05	0.05	0.98	10.4	<i>GM-FM</i>
<i>C3-120</i>	0.58	0.58	1.40	0.39	3.11	0.78	3.94	0.26	0.45	0.05	0.05	0.98	17.4	<i>GM-FM-RM</i>
<i>C3-220</i>	0.58	0.58	2.20	0.23	2.44	0.92	2.52	0.43	0.59	0.05	0.05	0.98	11.1	<i>GM-FM</i>

#### 7.4.6. Analyses results

The seismic performance was evaluated by means of a simple engineering demand parameter (EDP): the absolute peak displacement normalised with respect to the reduced instability displacement,  $d^*/(a_3 \cdot d_{ins}^*)$ . The architectural element is in the elastic phase with cracked or uncracked stiffness for outcome values of  $d^*/(a_3 \cdot d_{ins}^*)$  lower than  $a_1$ , while  $d^*/(a_3 \cdot d_{ins}^*)$  values equal or larger than unity were considered as overturning. The values of displacement demand exceeding  $a_3 \cdot d_{ins}^*$  were, indeed, automatically set to the static instability limit by the numerical model. The remaining  $d^*/(a_3 \cdot d_{ins}^*)$  values ranging from  $a_1$  and unity represent rocking realisations without overturning.

Once obtained the response of a given parapet or chimney from  $n$  GM or FM signals, each displacement demand is plotted against a scalar IM. Generally, a power law relationship between median demand and considered IM is adopted to analyse clouds of rocking elements [54][55][56]. This can be rearranged to perform a linear regression of the logarithms of IM and displacement demand quantity to establish a demand model of the following form:

$$\ln(D) = b \cdot \ln(IM) + \ln(a) \quad (7)$$

where  $a$ ,  $b$  are regression coefficients.

Figure 7.13 shows clouds of the P2-90 parapet in both initially damaged (grey) and undamaged (light blue) configurations subjected to GM signals and adopting  $PGA$ ,  $Sa(T_1)$  or  $Sa(T_{cr})$  and  $PGV$  (generally related to overturning) as IMs.

The clouds show that a simple linear regression cannot effectively describe the EDP-IM relationship due to a sudden change in slope after  $a_1$ . This phenomenon is more

pronounced for lower values of  $a_1$  (higher values of initial stiffness). Several works, analysing cloud results of rocking elements, highlighted that a distinction can be made between realisations before and beyond 1.3 the triggering rocking acceleration in order to perform bilinear regressions [54][56]. In this case, distinct linear regressions for realisations before and beyond  $a_1$  (censuring observations with  $d^*/d_{ins}^*$  equal to unity) were performed employing maximum likelihood technique [57].

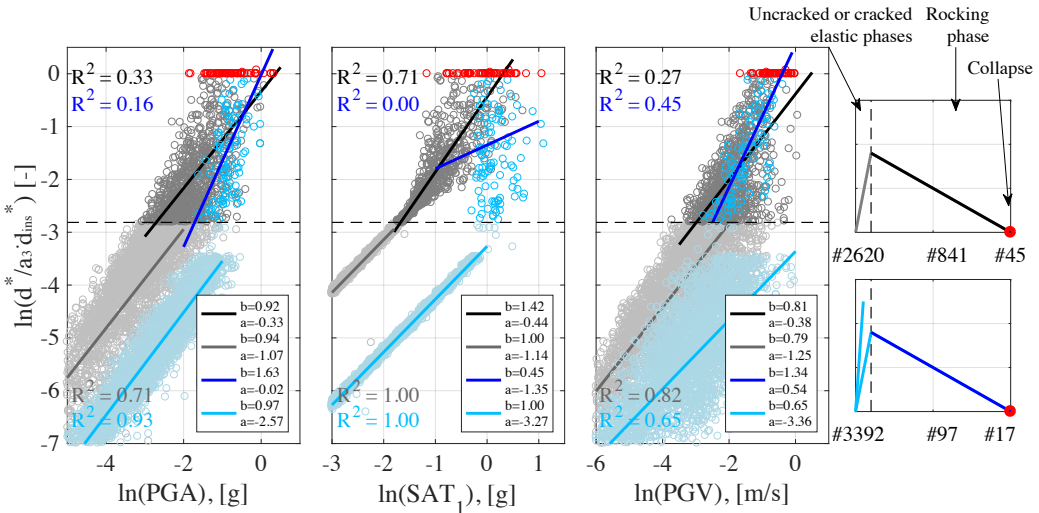


**Figure 7.13 Clouds and distinct linear regressions for realisations after and before  $a_1$  for P2-90 subjected to GM signals ( $R$ , coefficient of determination).**

Of course, when interested in probability of overturning we refer to the linear regression of the safe rocking realisations (blue and black lines).

Looking at PGA and PGV regression lines, a paradoxical conclusion may arise: an undamaged parapet results as more vulnerable than an initially damaged one (lower abscissa at  $\ln(d^*/d_{ins}^*)$  equal to 0). This is because the regression lines were performed on a different set of realisations, which are associated with a different level of spectral acceleration demand necessary to induce rocking in the two cases. Being the cracking spectral acceleration significantly higher, the number of observations inducing rocking and collapse in the uncracked parapet is much lower (light blue dots). Despite this, the collapse ratio, defined as number of overturning divided by total number of rocking observations, (17.5%) is higher than the one associated with a cracked parapet (5.4%).

Indeed, the response of systems having initially higher strength than the rocking one, when this initial inertial force is exceeded, are subjected to a sudden increase in the displacement demand compromising part of the isolation effect given by a pure rocking behaviour. This behaviour has been observed experimentally [19] and numerically [20] in the out-of-plane response of masonry walls. The consideration of the initial elastic strength may significantly affect the response suggesting for a deep investigation of the dynamic behaviour of these systems, in which rocking behaviour represents only the residual capacity (e.g. out-of-plena two-way bending response of walls [58])

Moreover, the analysis of residuals related to rocking realisations suggest strong non-linearity even in log-log space. Taking in mind as the scope of this work is not investigating which IM is more linearly correlated in log-log space with rocking demand,

but proposing realistic fragility curves for these architectural elements, a different approach was employed for the fragility models.

**7.4.7. Floor rocking spectra**

In order to investigate the influence of the building characteristics, expressed in terms of strength and stiffness, on the rocking response, rocking spectra have been computed adopting GM and FM signals. The rocking spectrum is a plot of the peak absolute rotation sustained by a rigid rocking body having given slenderness (associated with the energy dissipated) and frequency parameter  $p$ , inversely proportional to the block size in the case of homogeneous body [59].

Figure 7.14 shows the comparison between rocking spectra associated with GM and FM signals for three different records of increasing ductility demand on the primary structure.

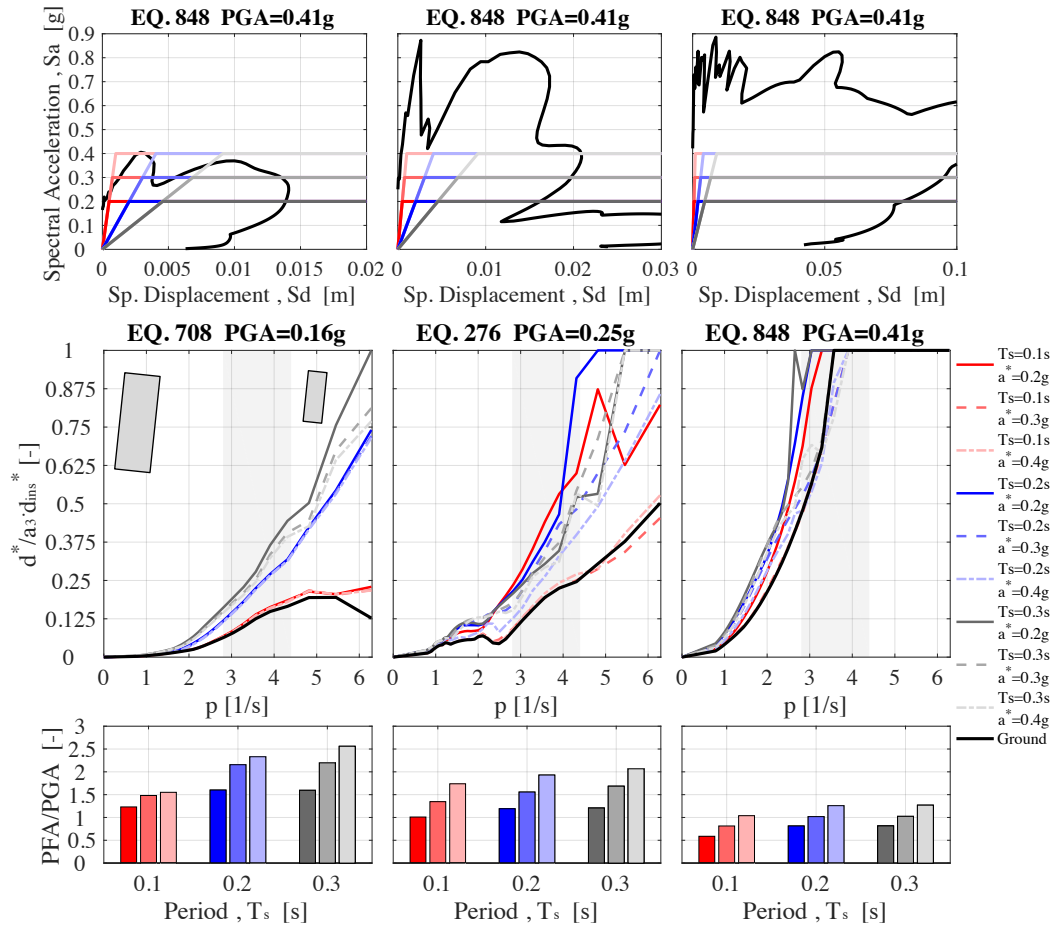


**Figure 7.14 Ductility demand of the selected earthquakes on the studied building configurations (top). Comparison between ground and floor rocking spectra (centre). Peak floor amplification for the different building configurations under study (bottom).**

Since the object of the present study are masonry elements, similarly to [60], the rocking spectra were calculated assuming a bi-linear  $F^*-d^*$  curve with  $a_1$  equal to 0.06 and  $a_3$  equal to 1 (neglecting the initial elastic phase). The considered slenderness angle was  $0.175rad$  and a reduced coefficient of restitution ( $0.95 \cdot e_{an}$ ) was employed for the

analyses. The shaded area represents the range of frequencies of interest for these masonry elements.

In some spectra, rotations are not strictly monotonically increasing due to the non-linear nature of the rocking dynamic. Besides the well-known “scale effect”, the larger the block the lower the response [24][61], no amplifications for specific block sizes are detectable. Figure 7.14 shows as for low ductility demand the building strength does not play a role in the rocking amplification (EQ 708) as the input acceleration; moving towards more severe earthquakes (EQ 276) rocking amplification tends to be much more consistent for the buildings having lower strength ( $a_y=0.2g$ , solid lines); this behaviour is emphasised for very rare event (EQ 848) when low strength buildings, despite the clear de-amplification effect at the floor level, can induce overturning for  $p$  values around 3 when normalised peak rotations from the GM signal are limited to 0.5. Still for rare events, it has to be noted that the range of variation of floor spectra with respect to ground rocking spectra is rather reduced. In the light of the above discussion, it can be concluded as rocking elements are subjected to higher displacement demand when placed on lower strength buildings associated with early saturation of acceleration amplification and increase in floor velocity.

#### 7.4.8. Fragility curves

This section focuses on the calculation of the conditional probability that a GM or FM of a given intensity measure ( $IM=x$ ) will cause overturning which, can be expressed via the usual lognormal distribution [62]:

$$P_{ov} = P(D > C | IM = x) = \Phi\left(\frac{\ln x - \mu}{\beta}\right) \quad (8)$$

where  $\Phi$  is the standard normal cumulative distribution function,  $\mu$  is the median value of the demand (the IM level with 50% probability of exceedance) and  $\beta$  is the dispersion of the demand conditioned on the IM. The numerical simulation results, grouped in strips according to the selected IM, provided at each IM stripe the fraction of signals out of the total causing overturning (vertical stripes in Figure 7.13). Maximum likelihood estimation method was then used to fit the observed data, allowing for the determination of the  $\mu$  and  $\beta$  fragility function parameters (equation 8) which gives the highest probability of producing the data obtained from the structural analysis [63][64][54].  $\mu$  and  $\beta$  were evaluated through the maximisation of the following likelihood function:

$$L = \prod_{i=1}^n P_{ov}^{y_i} (1 - P_{ov})^{1-y_i} \quad (9)$$

where  $y_i$  is the binomial distribution variable equal to unity when overturning is reached, and null otherwise and  $P_{ov}$  is the probability of overturning at a given IM presented in equation 8.

For the sake of comparison overturning fragility functions have been produced by assuming parapet and chimneys located at the ground level, at top of several building configurations and at the roofline.

#### 7.4.8.1. Analysis of the different IMs efficiency

This section investigates the performance of GMIMs and FMIMs (presented in section 7.4.4) in terms of dispersion of the overturning fragility curve,  $\beta_{IM}$ , for parapet walls and chimneys. Overturning fragility curves have been computed for all studied elements in cracked and uncracked configurations subjected to GM, FM and RM signals (see Table 7.5). Looking at parapet walls, the  $\beta_{IM}$  values presented in Figure 7.15 refer to ground (gray bars) and floor motion inputs (blue and red bars) by adopting both GMIMs and FMIMs. Figure 7.15 shows only  $\beta_{IM}$  values associated with a set of analysis in which at least 0.5% cases attained overturning (e.g. cracked P3-60 subjected to GMs did not show any collapses), while the dispersion values associated with FM inputs are the average of the nine values obtained from the analysis of the parapet performance placed on top of each specific building configuration. Note also that the values adopting the spectral acceleration as GMIM for GM and FM inputs are not directly comparable since they refer to spectral acceleration at the fundamental period of the wall ( $Sa(T_{cr})$  or  $Sa(T_I)$ ) for GM inputs and spectral acceleration at the building fundamental period ( $Sa(T_s)$ ) for FM inputs.

When GMIMs are considered to predict overturning of elements subjected to FM inputs (blue bars), the dispersion did not increase with respect to values obtained from GM signals (grey bars). On the contrary, for specific GMIMs such as PGA, AvgSa, IA and CAV a slight reduction (95%) is observed. The possible increase in dispersion associated with adopting an IM not directly related to the input of the parapets (e.g. PGA instead of PFA) seems to be compensated by the filtering effect given by the primary structure. Regardless of the GM, the filtering effect of the primary structure tends to homogenize the entire set of input signals.

Figure 7.15 highlights also differences between the response of cracked and uncracked systems. The most efficient GMIMs for cracked parapets are *AvgSa*, *HI*, *PGV* and *CAV*, these latter three have been already identified as good predictor of rocking response by several researchers [54][55]. The same GMIMs, were observed as the most efficient also for undamaged parapets but associated with a slightly higher dispersion. The only exceptions are *PGA RMSA* and  $Sa(T_s)$ , for which a decrease in dispersion is observed.

The performance of PGV/PGA ratio was also investigated to show very less correlation with the rocking demand. However, it has been addressed as highly efficient when adopted in bivariate fragility functions together with PGA and PGV [54]. Duration IMs have also shown very low correlation for the considered induced seismicity scenario. This could be explained by the reduced duration characterising all employed accelerograms which are representative of induced earthquakes.

Looking at FMIM the most efficient IM appears to be PFA followed by PFV and *AvgFSa*. Nevertheless, PFA, due to its saturation with increasing earthquake intensity, is not recommended as IM.

Chimneys exhibited almost zero overturning when subjected to GM excitations, therefore the corresponding fragility curves have not been constructed. The analysis of GMIMs, FMIMs and RMIMs efficiency (see Figure 7.16) have shown results similar to those observed for parapets, highlighting the good performances of *AvgSa*, *PFV* and *PRV*.



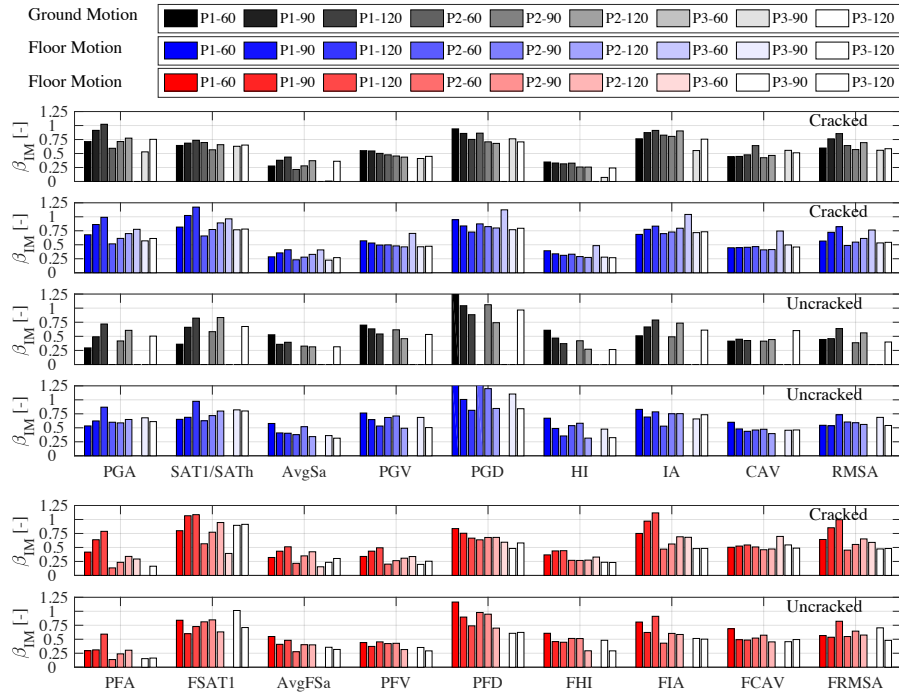


Figure 7.15 Dispersion of the overturning fragility curves associated with GM (gray) and FM (blue/red) inputs expressed in terms of GMIM and FMIM for parapet walls.

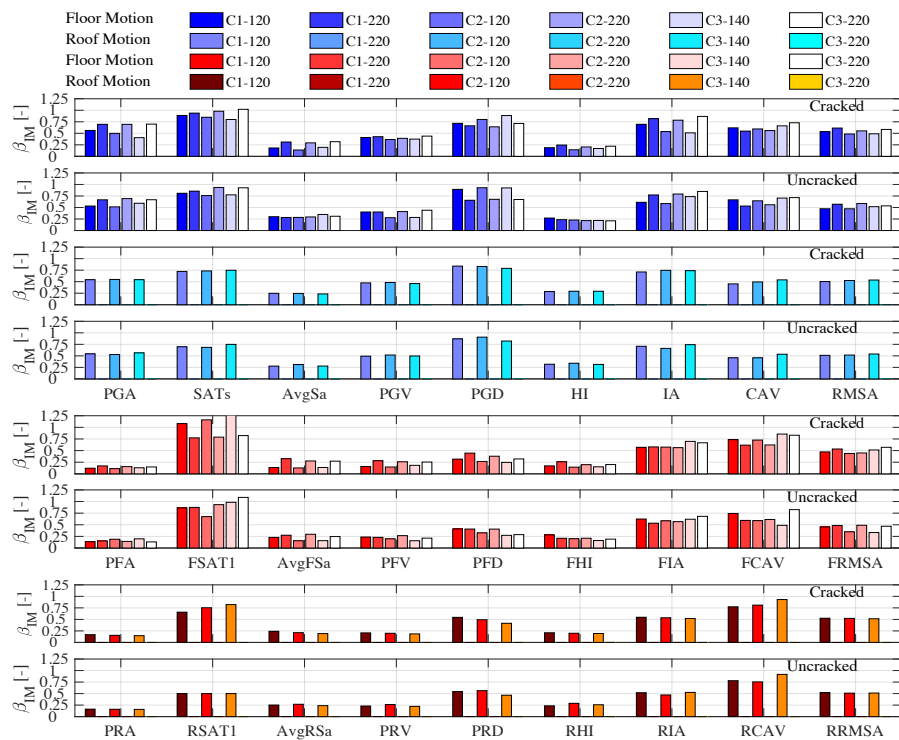


Figure 7.16 Dispersion of the overturning fragility curves associated with FM and RM inputs and expressed in terms of GMIM (blue bars) and FMIM/RMIM (red bars) for chimneys.

Cracked and uncracked chimneys, on the contrary with respect to parapets, have shown very little differences in terms of fragility curve dispersion. Moreover, the decrease in dispersion phenomenon described for parapets subjected to FMs seems to be emphasised when the double filtering effect of primary and secondary structures is taken into account.

**7.4.8.2. Proposed fragility curves for parapets**

This section presents overturning fragility curves expressed in terms of GMIM and FMIM for parapet walls. *AvgSa* was selected as GMIM (see Figure 7.17) while PFV (see Figure 7.19) as best FMIM.

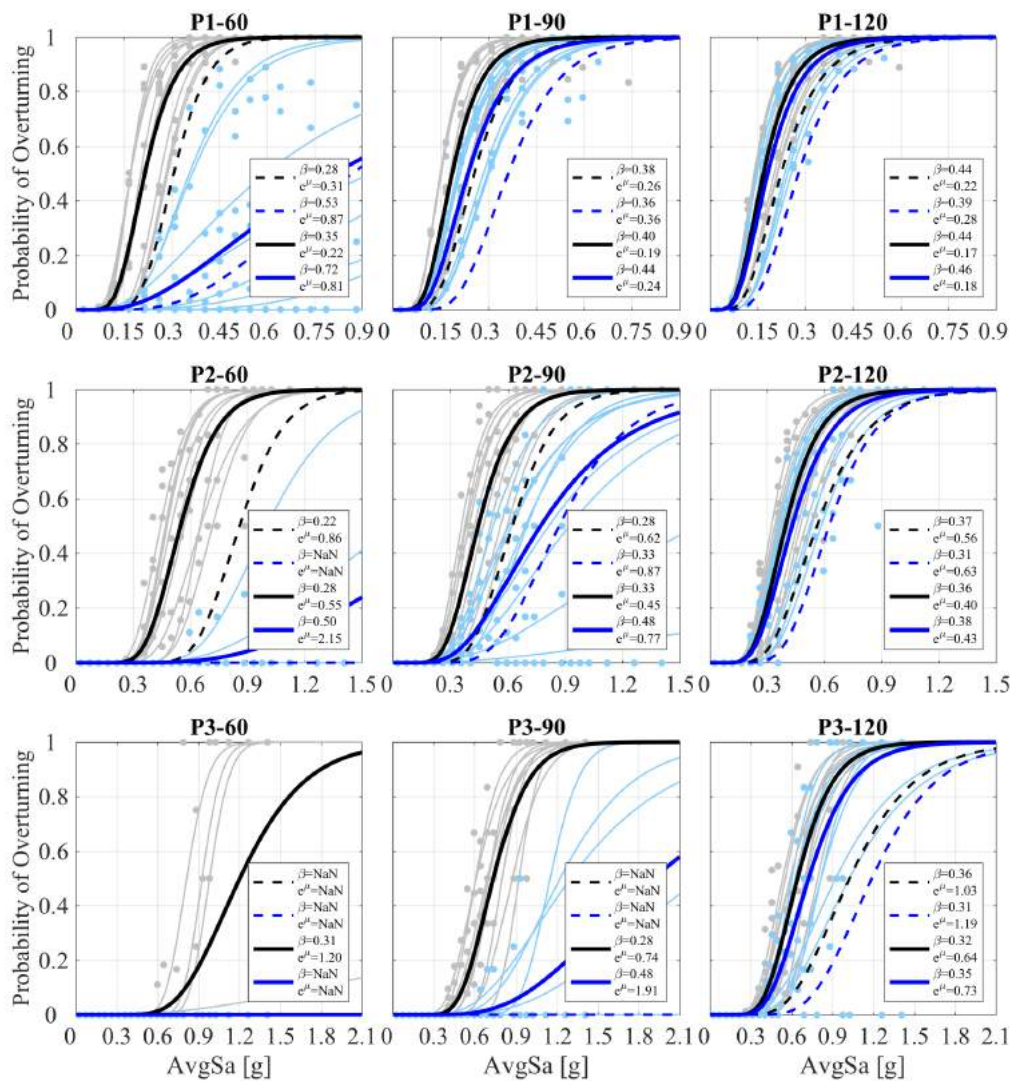


Figure 7.17 Overturning fragility curves adopting *AvgSa* as GMIM: parapet placed on a generic building configuration in cracked (black line) and uncracked (blue lines) conditions. Parapet placed at the ground level in cracked (dashed black line) and uncracked (dashed blue lines) conditions.

Each box of Figure 7.17 presents probabilities of collapse associated with a specific parapet configuration. Grey and light-blue fragility curves are related to the specific

parapet placed on top of a specific building configuration in cracked and uncracked conditions, respectively. On the contrary, black and blue lines are fragility curves of the same parapet placed on top of a generic building configuration. These curves, fitting statistics (fraction of overturning out of total signals in the bin) of the parapet placed on top of all building typologies, assume a uniformly distributed population of buildings of one two and three storeys and 0.2, 0.3 and 0.4g of yield strength (total of 9 building configurations). For the sake of comparison, the fragility curves of the same parapet subjected to GM signals in cracked and uncracked conditions are also shown in black and blue dashed lines.

Figure 7.17 illustrates how, if only the rocking phase is analysed (cracked parapets, black lines), the vulnerability of these elements is primarily related to their thickness and, secondly, to their height. On the other hand, the performance of undamaged parapets (blue lines) highlights that neglecting pre-mechanism phase and tensile strength of masonry may lead to a significant underestimation of the median collapse intensity. With decreasing the height of the parapet this underestimation became more pronounced: from 5% for P1-120 to almost 400% for P1-60. The undamaged P3-60 did not show any overturning. When these fragility curves are compared with those obtained by assuming parapets located at the ground level an average decrease of the median AvgSa is observed, quantified in approximately 0.70 for cracked parapets and 0.66 for initially uncracked ones.

Fragility curves associated with a parapet placed on top of a specific building show quite a consistent variability in terms of median overturning intensity. Maximum and minimum median intensities for the same parapet may present ratio values of 2 for cracked parapets and much higher ones for uncracked parapets. This may be related to the case in which only specific building typologies are able to transfer accelerations sufficient to crack and overturn the element (see P3-90 in Figure 7.17). This is confirmed by Figure 7.18 which is a contour map plot showing the variation of the median overturning AvgSa with the characteristics of the primary structure. Whiter colours indicate higher vulnerability.

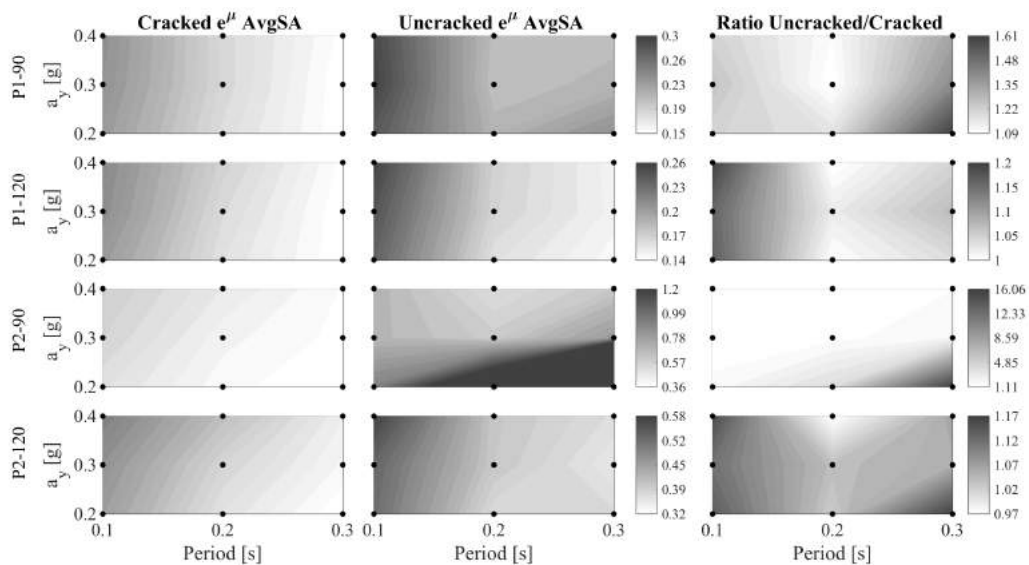


**Figure 7.18** Variation of the median overturning AvgSa with the primary building characteristics for cracked and uncracked parapets.

Two legends are provided: the first one shows the range of median AvgSa variation for both cracked and uncracked elements whereas the second one the variability of their ratio values. As abovementioned, initially cracked parapets tends to be more vulnerable when placed on low strength ( $a_y=0.2g$ ) three-storey buildings ( $T_s=0.3s$ ) as shown by the inclined contour lines of the first column in Figure 7.18. The response of initially uncracked parapets is instead affected by the amplification at the last floor level of the spectral acceleration corresponding to the parapet undamaged period (see whiter colours around 0.2s period structures in the third column). On the contrary with respect to damaged parapets, low strength three storey buildings may result very little vulnerable (see P2-90).

Regarding the dispersion, as expected, Figure 7.17 illustrates also that the dispersions associated with the overturning fragility curve related to a generic building are higher than those associated with a specific building. Figure 7.19 presents fragility functions of the same parapets adopting as IM PFV.

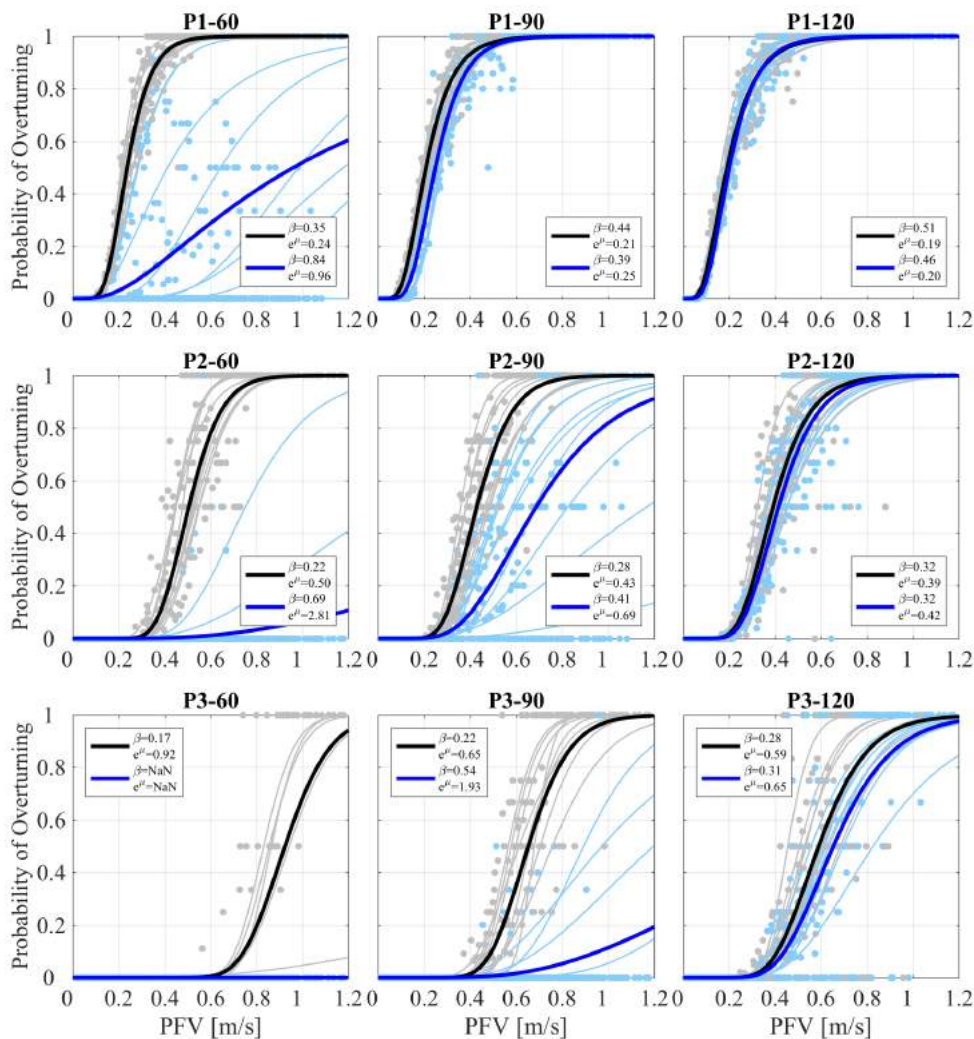


**Figure 7.19** Overturning fragility curves adopting PFV as FMIM: parapet placed on a generic building configuration in cracked (black line) and uncracked (blue lines) conditions.

Table 7.7 and Table 7.8 present the overturning fragility curves parameters related to parapets in initially cracked and uncracked conditions assuming as IM ground and floor motion parameters.

**Table 7.7 Overturning fragility curve parameters adopting GMIM.**

P#	PGA [g]		Sa(T <sub>j</sub> ) [g]		AvgSa [g]		PGV [m/s]		PGD [m]		HI [m]		IA [m/s]		CAV [m/s]		RMSA [g]	
	$\beta$	$e^{\mu}$	$\beta$	$e^{\mu}$	$\beta$	$e^{\mu}$	$\beta$	$e^{\mu}$	$\beta$	$e^{\mu}$	$\beta$	$e^{\mu}$	$\beta$	$e^{\mu}$	$\beta$	$e^{\mu}$	$\beta$	$e^{\mu}$
P1-60*	0.73	0.27	0.83	0.60	0.35	0.22	0.62	0.24	0.99	0.047	0.45	0.51	0.74	0.38	0.49	4.89	0.61	0.30
P1-90*	0.89	0.25	1.01	0.55	0.40	0.19	0.57	0.19	0.87	0.033	0.39	0.41	0.81	0.32	0.48	4.19	0.75	0.27
P1-120*	1.02	0.23	1.14	0.52	0.44	0.17	0.53	0.16	0.76	0.027	0.36	0.36	0.86	0.29	0.48	3.78	0.84	0.25
P2-60*	0.56	0.65	0.67	1.58	0.28	0.55	0.53	0.63	0.90	0.171	0.36	1.24	0.77	1.77	0.48	10.78	0.51	0.69
P2-90*	0.65	0.56	0.77	1.37	0.33	0.45	0.51	0.49	0.87	0.120	0.33	0.98	0.79	1.23	0.43	8.50	0.58	0.59
P2-120*	0.73	0.52	0.88	1.30	0.36	0.40	0.49	0.41	0.83	0.095	0.31	0.85	0.83	1.00	0.43	7.61	0.64	0.55
P3-60*	0.62	1.73	0.87	6.17	0.31	1.20	0.57	1.61	1.01	0.711	0.40	2.81	0.92	8.91	0.69	33.25	0.68	2.16
P3-90*	0.61	0.96	0.75	2.56	0.28	0.74	0.50	0.85	0.81	0.237	0.32	1.61	0.79	3.10	0.50	14.42	0.56	1.01
P3-120*	0.65	0.84	0.79	2.17	0.32	0.64	0.51	0.71	0.84	0.193	0.31	1.37	0.83	2.37	0.49	12.25	0.58	0.87
P1-60	0.77	0.84	1.01	2.50	0.72	0.81	0.91	0.99	1.41	0.350	0.80	1.95	1.11	2.58	0.68	13.84	0.73	0.91
P1-90	0.66	0.27	0.70	0.59	0.44	0.24	0.67	0.26	1.03	0.051	0.52	0.55	0.73	0.39	0.50	5.11	0.57	0.30
P1-120	0.92	0.24	0.98	0.51	0.46	0.18	0.58	0.18	0.85	0.031	0.42	0.40	0.83	0.31	0.48	4.03	0.78	0.26
P2-60	0.74	3.28	0.85	9.32	0.50	2.15	0.84	4.09	1.56	4.88	0.64	5.95	0.72	10.51	0.61	38.95	0.74	3.65
P2-90	0.58	0.81	0.67	1.96	0.48	0.77	0.65	0.88	1.10	0.295	0.53	1.74	0.75	2.42	0.45	12.21	0.56	0.88
P2-120	0.69	0.54	0.80	1.30	0.38	0.43	0.52	0.46	0.88	0.110	0.36	0.93	0.81	1.11	0.41	7.92	0.60	0.56
P3-60	-	-	-	-	-	-	-	-	-	-	-	-	-	-	-	-	-	-
P3-90	0.86	3.94	0.96	10.76	0.48	1.91	0.75	3.08	1.20	1.657	0.51	4.23	0.92	14.23	0.58	34.41	0.83	4.13
P3-120	0.64	0.93	0.78	2.46	0.35	0.73	0.53	0.81	0.85	0.227	0.35	1.56	0.80	2.75	0.47	13.15	0.57	0.95

\*initially cracked parapets

**Table 7.8 Overturning fragility curve parameters adopting FMIM.**

P#	PFA [g]		FSa(T <sub>j</sub> ) [g]		AvgFSA [g]		PFV [m/s]		PFD [m]		FHI [m]		FIA [m/s]		FCAV [m/s]		FRMSA [g]	
	$\beta$	$e^{\mu}$	$\beta$	$e^{\mu}$	$\beta$	$e^{\mu}$	$\beta$	$e^{\mu}$	$\beta$	$e^{\mu}$	$\beta$	$e^{\mu}$	$\beta$	$e^{\mu}$	$\beta$	$e^{\mu}$	$\beta$	$e^{\mu}$
P1-60*	0.51	0.41	1.66	2.55	0.33	0.36	0.35	0.24	0.85	0.047	0.37	0.73	0.82	1.81	0.51	11.50	0.65	0.70
P1-90*	0.67	0.39	1.24	1.26	0.44	0.31	0.44	0.21	0.77	0.035	0.44	0.61	1.01	1.57	0.53	10.13	0.84	0.68
P1-120*	0.81	0.38	1.60	2.02	0.52	0.28	0.51	0.19	0.68	0.029	0.45	0.54	1.15	1.41	0.56	9.32	0.98	0.66
P2-60*	0.41	0.69	1.68	14.50	0.25	0.98	0.22	0.50	0.65	0.143	0.27	1.72	0.70	5.48	0.56	24.96	0.53	1.37
P2-90*	0.47	0.64	1.10	3.52	0.36	0.81	0.28	0.43	0.69	0.112	0.27	1.38	0.74	4.33	0.50	19.45	0.62	1.27
P2-120*	0.53	0.63	1.49	7.71	0.43	0.72	0.32	0.39	0.69	0.094	0.28	1.22	0.83	3.97	0.51	17.77	0.70	1.24
P3-60*	0.19	0.75	1.98	171.8	0.16	1.77	0.17	0.92	0.55	0.331	0.24	3.56	0.63	13.60	0.56	47.94	0.54	2.81
P3-90*	0.41	0.84	1.26	10.05	0.30	1.34	0.22	0.65	0.51	0.180	0.23	2.28	0.73	8.46	0.58	33.41	0.56	1.84
P3-120*	0.47	0.82	1.59	21.75	0.36	1.19	0.28	0.59	0.61	0.164	0.25	1.96	0.76	7.04	0.56	27.83	0.58	1.66
P1-60	0.71	1.07	1.53	11.64	1.01	2.03	0.84	0.96	1.35	0.352	0.94	3.49	1.40	14.53	0.92	43.81	0.94	2.58
P1-90	0.41	0.39	0.68	0.85	0.44	0.39	0.39	0.25	0.90	0.052	0.47	0.79	0.70	1.80	0.51	11.80	0.56	0.68
P1-120	0.65	0.37	0.75	0.52	0.49	0.30	0.46	0.20	0.76	0.033	0.45	0.58	0.95	1.42	0.49	9.58	0.82	0.64
P2-60	0.54	1.96	1.13	36.49	0.69	5.40	0.69	2.81	1.20	2.034	0.86	14.49	0.99	44.65	0.69	88.00	0.76	6.33
P2-90	0.36	0.72	0.77	3.65	0.47	1.35	0.41	0.69	0.87	0.235	0.50	2.50	0.66	6.54	0.50	26.22	0.57	1.68
P2-120	0.47	0.62	0.68	1.52	0.42	0.77	0.32	0.42	0.71	0.105	0.30	1.31	0.73	3.95	0.48	18.07	0.63	1.21
P3-60	-	-	-	-	-	-	-	-	-	-	-	-	-	-	-	-	-	-
P3-90	0.43	1.42	1.19	31.10	0.56	3.84	0.54	1.93	0.85	0.772	0.61	7.76	0.80	25.95	0.51	52.91	0.71	5.16
P3-120	0.41	0.80	0.73	3.16	0.38	1.33	0.31	0.65	0.64	0.192	0.31	2.24	0.70	7.40	0.52	28.26	0.54	1.69

\*initially cracked parapets



### 7.4.8.3. Proposed fragility curves for chimneys

This section, similarly to the previous one, presents overturning fragility curves expressed in terms of GMIM and FMIM for chimneys. Also in this case  $AvgSa$  was selected as GMIM (see Figure 7.20) while PFV and PRV (see Figure 7.21) as best FMIM and RMIM. Grey and light-red fragility curves are related to a specific chimney (in cracked and uncracked conditions) extending above the roof line from a perimeter walls, therefore damage at the chimney stack is associated with a specific building top floor acceleration. Silver and pink fragility curves represent instead probability of overturning of the same chimney extending above the roof line from the roof ridge and subjected consequently to RMs of a specific building configuration.

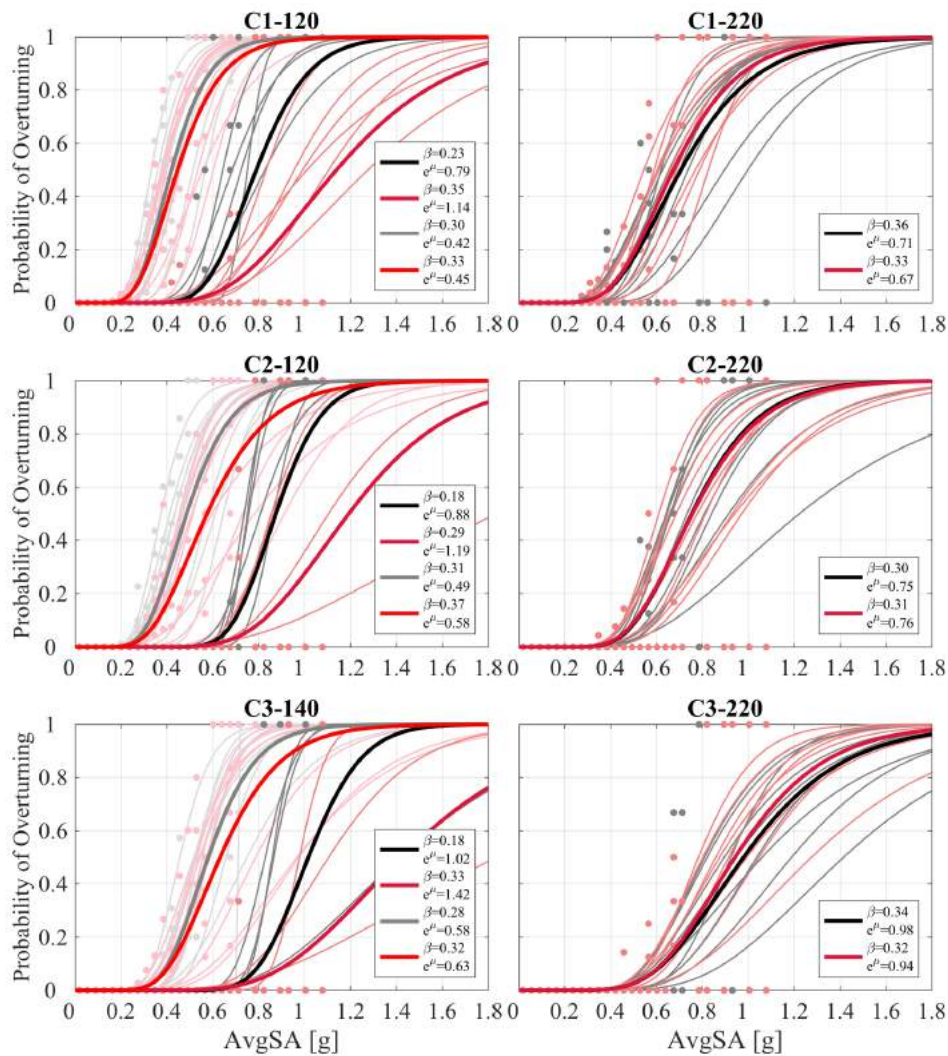


Figure 7.20 Overturning fragility curves adopting  $AvgSa$  as GMIM: chimneys placed on a generic building configuration in cracked (black line) and uncracked (dark red lines) conditions. C1-120, C2-120 and C3-120 chimneys were subjected to RMs in cracked (grey lines) and un-cracked (red lines).

In general, the most vulnerable chimneys are short ones located above the roof ridge. Accounting for the pre-mechanism phase for the selected geometries seems to have a minor importance with respect to parapet cases, especially when chimneys are subjected to roof motions. Considering the initial elastic phase affect mainly short chimneys subjected to FMs. In some cases, when the number of observed collapses is rather low, undamaged chimneys may result slightly more vulnerable (see C1-120) due to amplification at chimney un-cracked period and ‘explosive’ phenomenon earlier discussed. The average ratio between median overturning intensities of chimneys subjected to FMs and those subjected to RMs is approximately 1.8 for cracked chimneys and 2.3 for undamaged ones.

Figure 7.19 presents fragility functions of the same chimneys adopting as IM PFV and PRV. It is interesting to observe how the floor velocity required to overturn a chimney at the floor level is lower than the required PRV at the roof ridge level. Table 7.9 to Table 7.12 present the chimneys overturning fragility curves parameters.

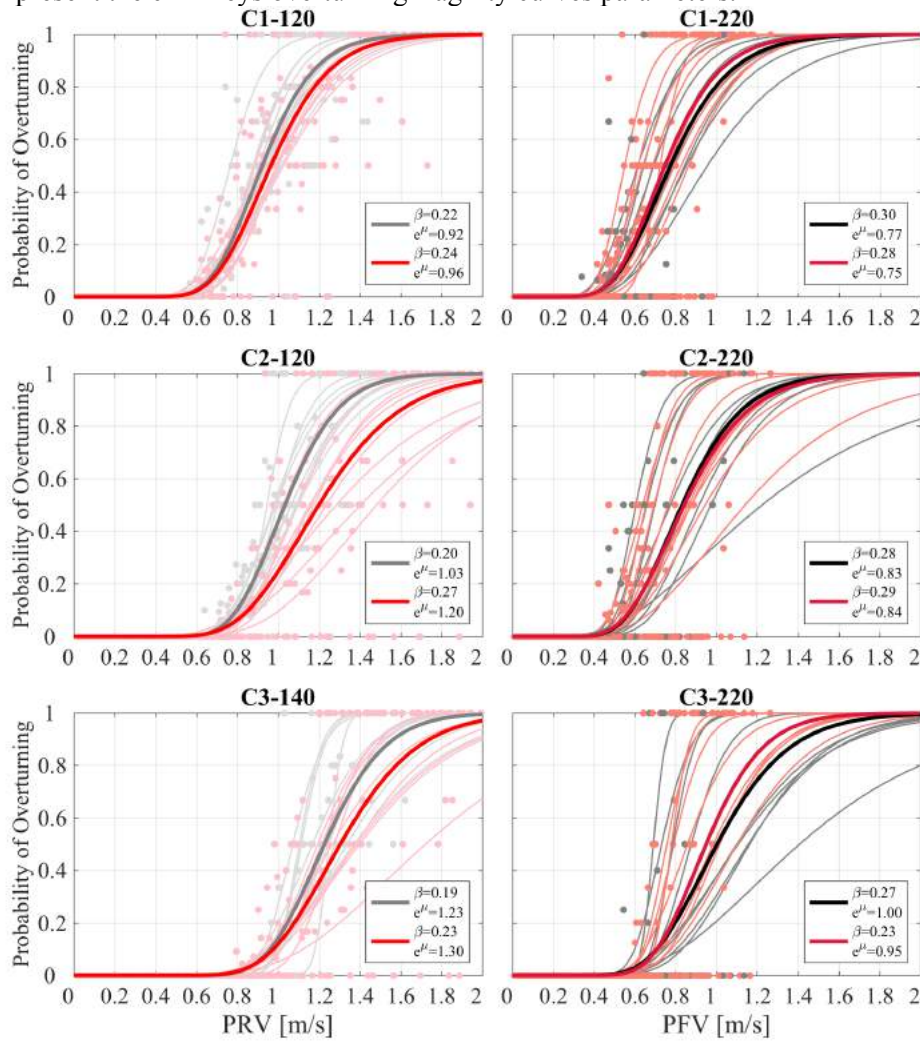


Figure 7.21 Overturning fragility curves adopting PFV and PRV as FMIM: chimneys subjected to FMs in cracked (black lines) and uncracked (dark red lines) conditions, chimneys subjected to RMs in cracked (grey lines) and uncracked (red lines) conditions.

Table 7.9 Fragility curve parameters of chimneys at top floor level adopting GMIMs.

C#	PGA [g]		Sa(T <sub>s</sub> ) [g]		AvgSa [g]		PGV [m/s]		PGD [m]		HI [m]		IA [m/s]		CAV [m/s]		RMSA [g]	
	$\beta$	$e^{\mu}$	$\beta$	$e^{\mu}$	$\beta$	$e^{\mu}$	$\beta$	$e^{\mu}$	$\beta$	$\beta$	$e^{\mu}$	$\beta$	$e^{\mu}$	$\beta$	$e^{\mu}$	$\beta$	$e^{\mu}$	$\beta$
C1-120*	0.61	1.45	0.86	4.94	0.23	0.79	0.44	1.14	0.74	0.34	0.23	2.09	0.75	5.28	0.60	23.95	0.57	1.51
C1-220*	0.73	1.35	0.93	4.08	0.36	0.71	0.46	0.94	0.69	0.24	0.29	1.81	0.89	4.35	0.54	17.29	0.65	1.33
C2-120*	0.60	1.70	0.88	6.37	0.18	0.88	0.42	1.30	0.76	0.44	0.15	2.23	0.66	5.92	0.62	29.30	0.52	1.66
C2-220*	0.70	1.47	0.93	4.77	0.30	0.75	0.42	1.00	0.65	0.26	0.23	1.92	0.81	4.75	0.54	19.37	0.59	1.39
C3-140*	0.55	2.00	0.94	10.00	0.18	1.02	0.44	1.62	0.86	0.71	0.13	2.44	0.68	8.23	0.69	42.07	0.60	2.43
C3-220*	0.74	2.14	1.01	8.03	0.34	0.98	0.43	1.27	0.70	0.38	0.25	2.35	0.92	8.38	0.71	33.80	0.66	2.03
C1-120	0.63	2.10	0.83	6.88	0.35	1.14	0.50	1.65	0.94	0.76	0.33	2.91	0.75	8.22	0.67	37.30	0.59	2.15
C1-220	0.71	1.27	0.86	3.49	0.33	0.67	0.45	0.90	0.69	0.23	0.28	1.75	0.85	3.97	0.53	16.71	0.61	1.23
C2-120	0.63	2.50	0.87	9.20	0.29	1.19	0.40	1.60	1.00	1.07	0.25	2.88	0.67	8.79	0.68	44.00	0.50	2.10
C2-220	0.72	1.52	0.90	4.57	0.31	0.76	0.44	1.02	0.68	0.27	0.25	1.93	0.84	4.94	0.55	19.68	0.63	1.46
C3-140	0.63	3.01	0.85	10.91	0.33	1.42	0.34	1.62	1.04	1.53	0.25	3.14	0.78	13.63	0.76	64.57	0.58	2.92
C3-220	0.70	1.93	0.94	6.73	0.32	0.94	0.43	1.26	0.67	0.35	0.23	2.29	0.87	7.59	0.69	32.05	0.61	1.83

\*initially cracked parapets

Table 7.10 Fragility curve parameters for roof chimneys adopting GMIMs.

C#	PGA [g]		Sa(T <sub>s</sub> ) [g]		AvgSa [g]		PGV [m/s]		PGD [m]		HI [m]		IA [m/s]		CAV [m/s]		RMSA [g]	
	$\beta$	$e^{\mu}$	$\beta$	$e^{\mu}$	$\beta$	$e^{\mu}$	$\beta$	$e^{\mu}$	$\beta$	$\beta$	$e^{\mu}$	$\beta$	$e^{\mu}$	$\beta$	$e^{\mu}$	$\beta$	$e^{\mu}$	$\beta$
C1-120*	0.59	0.65	0.73	1.66	0.30	0.42	0.51	0.61	0.88	0.16	0.33	1.19	0.78	1.74	0.47	10.46	0.53	0.69
C2-120*	0.61	0.77	0.73	1.96	0.31	0.49	0.53	0.71	0.88	0.20	0.35	1.38	0.84	2.33	0.51	12.35	0.57	0.84
C3-140*	0.59	0.94	0.75	2.55	0.28	0.58	0.50	0.85	0.83	0.25	0.32	1.63	0.82	3.20	0.54	15.42	0.57	1.02
C1-120	0.59	0.68	0.71	1.69	0.33	0.45	0.53	0.64	0.91	0.18	0.37	1.27	0.79	1.87	0.48	10.97	0.53	0.73
C2-120	0.59	0.86	0.70	2.18	0.37	0.58	0.55	0.83	0.91	0.25	0.39	1.60	0.79	2.76	0.49	13.46	0.56	0.94
C3-140	0.61	1.02	0.77	2.79	0.32	0.63	0.53	0.92	0.85	0.27	0.35	1.76	0.84	3.57	0.55	16.37	0.58	1.10

Table 7.11 Fragility curve parameters of chimneys at top floor level adopting FMIMs.

C#	PFA [g]		FSa(T <sub>s</sub> ) [g]		AvgFSa [g]		PFV [m/s]		PFD [m]		FHI [m]		FIA [m/s]		FCAV [m/s]		FRMSA [g]	
	$\beta$	$e^{\mu}$	$\beta$	$e^{\mu}$	$\beta$	$e^{\mu}$	$\beta$	$e^{\mu}$	$\beta$	$\beta$	$e^{\mu}$	$\beta$	$e^{\mu}$	$\beta$	$e^{\mu}$	$\beta$	$e^{\mu}$	$\beta$
C1-120*	0.39	1.00	1.14	13.28	0.19	1.21	0.19	0.85	0.33	0.21	0.17	3.03	0.83	16.08	0.72	60.98	0.56	2.57
C1-220*	0.50	1.06	0.80	3.71	0.36	1.12	0.30	0.77	0.47	0.20	0.27	2.65	0.84	11.92	0.65	42.65	0.62	2.31
C2-120*	0.31	0.94	1.16	18.02	0.18	1.35	0.17	0.93	0.27	0.22	0.15	3.37	0.80	18.66	0.73	72.92	0.51	2.64
C2-220*	0.51	1.19	0.85	4.63	0.31	1.20	0.28	0.83	0.38	0.20	0.21	2.83	0.86	14.40	0.68	50.46	0.57	2.34
C3-140*	0.25	0.93	1.31	35.01	0.19	1.58	0.15	1.05	0.28	0.26	0.12	3.75	0.90	31.30	0.71	83.39	0.56	3.53
C3-220*	0.50	1.37	0.98	8.09	0.36	1.57	0.27	1.00	0.32	0.23	0.24	3.51	1.07	31.13	0.91	108.49	0.66	3.54
C1-120	0.27	0.93	1.03	21.88	0.30	1.66	0.25	1.10	0.41	0.30	0.32	4.35	0.80	22.37	0.70	78.35	0.52	2.97
C1-220	0.50	1.06	0.99	6.86	0.33	1.07	0.28	0.75	0.44	0.19	0.25	2.56	0.84	11.49	0.65	42.04	0.60	2.20
C2-120	0.21	0.87	0.85	16.32	0.18	1.62	0.13	1.07	0.33	0.28	0.22	4.26	0.61	18.44	0.55	60.06	0.34	2.29
C2-220	0.48	1.10	1.03	9.04	0.34	1.23	0.29	0.84	0.40	0.21	0.23	2.87	0.87	14.60	0.67	49.16	0.60	2.45
C3-140	0.22	0.94	0.87	21.94	0.17	1.76	0.08	1.11	0.25	0.28	0.15	4.33	0.67	25.05	0.47	53.34	0.36	2.61
C3-220	0.41	1.12	1.16	16.37	0.32	1.47	0.23	0.95	0.30	0.22	0.22	3.40	0.98	25.02	0.83	88.09	0.59	3.04

Table 7.12 Fragility curve parameters for roof chimneys adopting RMIMs.

C#	PRA [g]		RSa(T <sub>s</sub> ) [g]		AvgRSa [g]		PRV [m/s]		PRD [m]		RHI [m]		RIA [m/s]		RCAV [m/s]		RRMSA [g]	
	$\beta$	$e^{\mu}$	$\beta$	$e^{\mu}$	$\beta$	$e^{\mu}$	$\beta$	$e^{\mu}$	$\beta$	$\beta$	$e^{\mu}$	$\beta$	$e^{\mu}$	$\beta$	$e^{\mu}$	$\beta$	$e^{\mu}$	$\beta$
C1-120*	0.27	1.00	0.50	0.30	0.26	1.41	0.22	0.92	0.57	0.31	0.22	3.19	0.78	1.74	0.47	10.46	0.53	0.69
C2-120*	0.26	1.06	0.50	0.30	0.23	1.62	0.20	1.03	0.51	0.34	0.21	3.69	0.84	2.33	0.51	12.35	0.57	0.84
C3-140*	0.26	1.19	0.50	0.30	0.22	1.97	0.19	1.23	0.43	0.38	0.20	4.53	0.82	3.20	0.54	15.42	0.57	1.02
C1-120	0.26	1.01	0.50	0.30	0.27	1.48	0.24	0.96	0.57	0.32	0.25	3.39	0.79	1.87	0.48	10.97	0.53	0.73
C2-120	0.25	1.12	0.50	0.30	0.29	1.89	0.27	1.20	0.56	0.40	0.30	4.43	0.79	2.76	0.49	13.46	0.56	0.94
C3-140	0.26	1.22	0.50	0.30	0.25	2.10	0.23	1.30	0.46	0.41	0.25	4.89	0.84	3.57	0.55	16.37	0.58	1.10



#### 7.4.9. Relationship between global and local damage

This section focus on the computation of the conditional probability of achieving a specific performance in the parapet or chimney given the occurrence of a specific damage state (DS) in the primary structure for all the considered building configurations. In other words, the bars were produced by applying statistics on the fraction of realisations inducing a specific DS in the primary structure (classified according to the building inter-storey drift), therefore the sum of the bin values within each box is equal to one. For simplicity, only buildings having 0.2g of yield strength were considered. Primary structure DSs were evaluated according to the drift level discussed in 7.4.1, while with reference to Figure 7.13, the masonry elements performance was classified as elastic, rocking and collapse. This may help readers and decision-makers in understanding the performance of these non-structural elements alongside with the damage of the primary structure. It has to be clear that, for initially uncracked masonry elements, realisations falling in the ‘Rocking’ bin represent damaged parapets and chimneys.

Figure 7.22 presents the conditional probabilities of elastic, rocking and overturning realisations given the occurrence of a specific DS in the primary structure for initially cracked (grey bars) and uncracked (coloured bars) parapets.

While statistics of initially cracked, parapets confirm what observed in sections 7.4.7 and 7.4.8.2, the results of undamaged parapets suggest that especially squat elements (P1-60 P2-60 and P3-60) remained undamaged in two and three storey buildings regardless the level of damage experienced by the structure. On the other hand, these elements experienced damage and collapse when placed on top of one-storey buildings due to spectral acceleration amplification.

The conditional probabilities of the chimney performance, shown in Figure 7.23, highlight the vulnerability of chimneys extending from the roof ridge with respect to those connected to perimeter walls and hence subjected to FMs. Only initially undamaged chimneys are shown. For a building in DS2 almost 100% of the roof chimneys attained cracking regardless the number of storeys of the primary structure. At the attainment of DS3 the firsts overturning of roof chimneys are observed. Two storeys buildings seem to be the most demanding for chimneys anchored to the perimeter walls

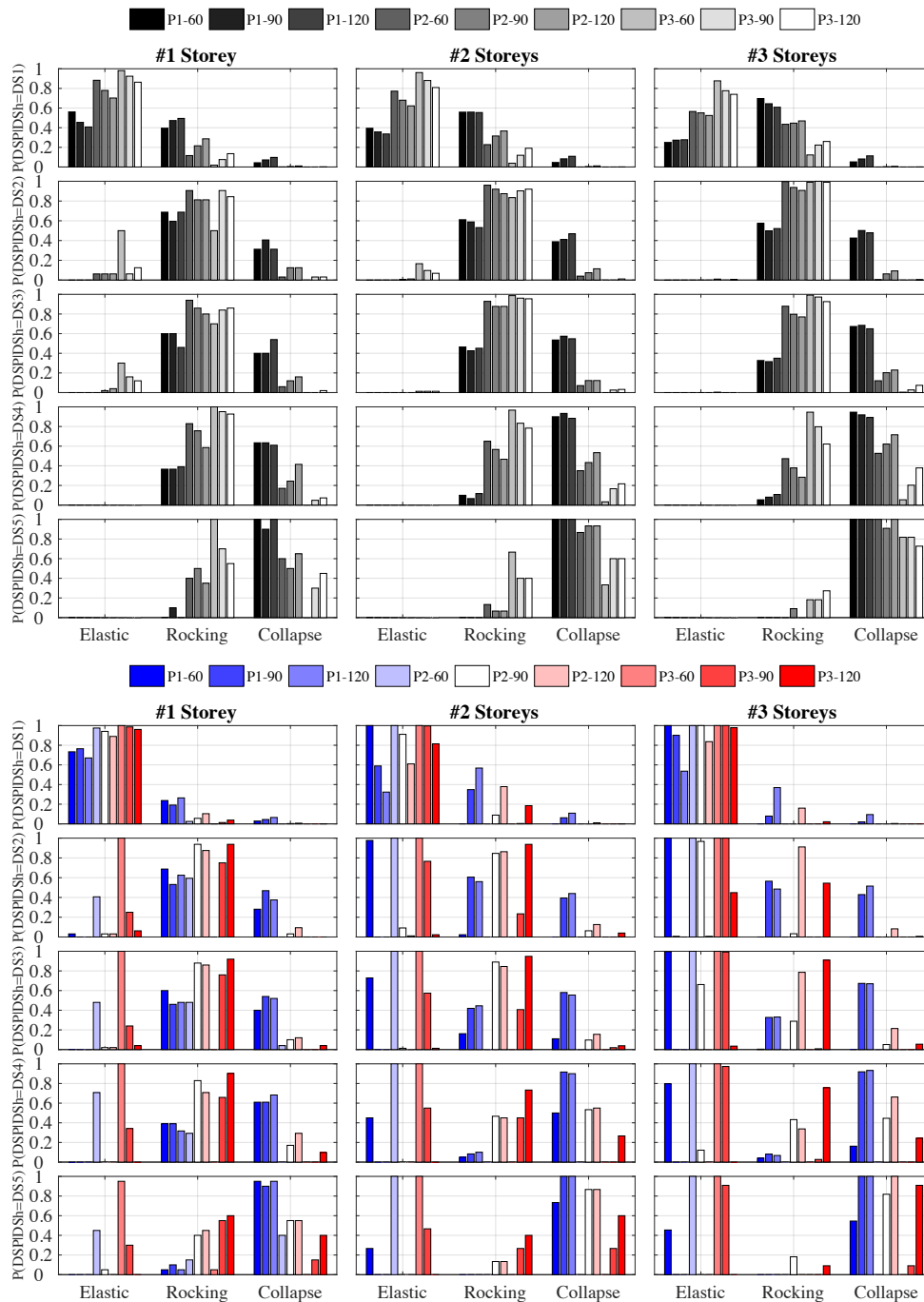
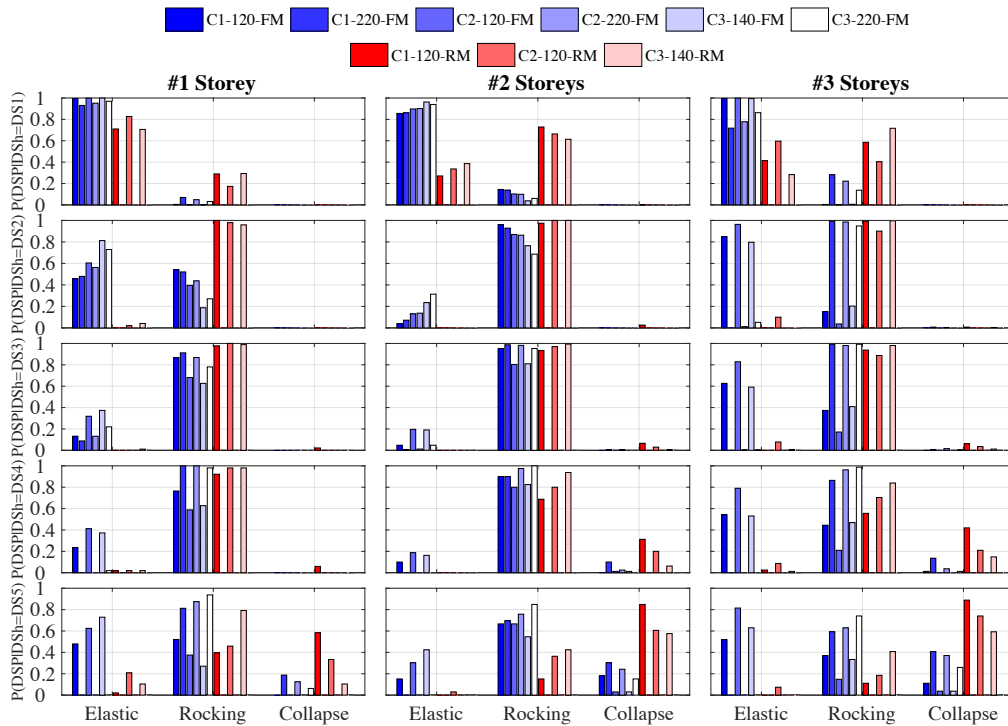


Figure 7.22 Conditional probabilities of achieving specific DS of the parapets given the primary structure damage state for initially cracked (grey bars) and uncracked elements (coloured bars).



**Figure 7.23** Conditional probabilities of achieving specific DS in the chimneys given the primary structure damage state for initially uncracked elements subjected to FMs (blue bars) and RMs (red bars).

**7.4.10. Comparison with empirical fragility functions**

Generally when interested in probabilities of damage and collapse of chimneys and parapets, researchers and practitioners currently refer to fragility functions based on collected empirical data [12][13][65], which presents several shortcomings. The main shortcomings associated with the empirical data are related to a binary and non-homogenous classification of damage associated with a lack of information in the type of or extent of damage [12]. This in addition to the strong dependence of the observed performance to the considered area in terms of hazard and exposure make quite difficult the use of these curves. On the other hand, the analytical fragility functions herein presented, despite the promising ability in simulating experimental responses, adopts several abovementioned simplifications (*e.g.* neglecting vertical accelerations and local effect like pounding, damage concentration only in the portion of the chimney stack above the roofline etc.).

Recognising the considerable diversity of the two approaches, Figure 7.24 compares the obtained overturning fragility (considering a generic building) curves with empirical ones available in literature. Both chimneys and parapets’ fragilities adopt PGA as IM. The empirical fragility function are based on inspection data following San Fernando, Northridge, Nisqually and San Simeon events for chimneys [12] and Loma Prieta and Northridge events for parapets [65]. In general, all numerical fragility curves present rather high values of dispersions, however, compatible with those observed for rocking rigid bodies when PGA is adopted as IM [54]. Shaded areas represent the variability of

each specific fragility curves with the characteristics of the primary structure. All numerical fragility curves, with the only exception of single leaf parapets (P1-120 and P1-90), result as less vulnerable than empirical ones. According to the author's opinion, this might be related to two main reasons: analytical curves refer to overturning of the element while empirical one to a generic damage, the low demanding employed set of ground motions, being representative of induced earthquakes.

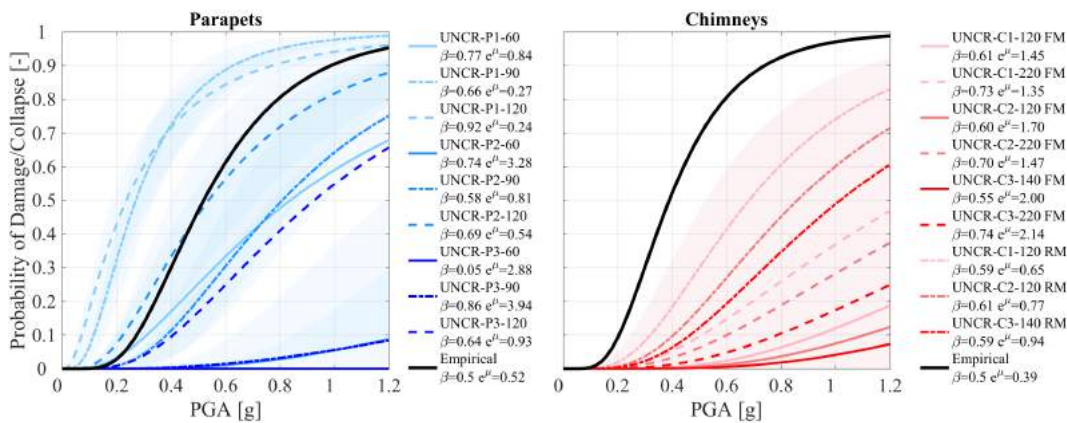


**Figure 7.24 Comparison between analytical and empirical fragility curves. Shaded areas represent the range of variation of fragility curves for the element placed on top of specific structure configuration.**

## 7.5. Conclusions

Observations from post-earthquake surveys addressed Unreinforced masonry (URM) parapet and chimneys as one of the most vulnerable elements in low-rise commercial and residential buildings. Due to their location on top of conventional buildings these elements are subjected, hence, to the highest amplification of ground motion during an earthquake. Their damage and collapse may represent a significant hazard for building occupants and pedestrians, as well as, losses in terms of building repair cost.

The paper shows that the dynamic behaviour of parapets and chimneys can be modelled with a single-degree-of-freedom (SDOF) system which take into account both pre-and-post mechanism phases. Its force-displacement ( $F-d$ ) relationship is characterised by a linear elastic curve having strength and stiffness governed by the masonry flexural strength followed by a residual capacity consisting in a bi-linear curve constructed on the rigid body  $F-d$  idealisation.

Calibration of several experimental dynamic tests allowed for the determination of reliable parameters in terms of  $F-d$  curve and dissipated energy for the simulation of their seismic response. A bilinear curve having a corner displacement expressed as fraction of the instability displacement and equal to 0.06 for parapets and 0.05 for chimneys was proposed. The energy dissipation was modelled via coefficient of restitution by reducing the theoretical value by 0.94 for parapets and 0.80 for chimneys and also recurring to velocity dependant equivalent viscous damping forces. This latter source of damping, proportional to the secant stiffness of the system, has been employed adopting damping ratio values between 1.5-3% for parapets and 12-15% for chimneys.

The SDOF model was then adopted to assess the vulnerability of opportunely selected secondary elements placed on top of different primary structure and roof configurations. The buildings differ in terms of number of storeys and structure lateral strength. SDOF systems, representative of the structure global response and the roof where subjected to a large set of natural ground motions representative of induced earthquakes. Their acceleration output was used as acceleration input for chimneys and parapets.

The cloud analyses were discussed analysing differences in response between initially damaged elements, undergoing directly in rocking behaviour, and undamaged systems where rocking is triggered only at the attainment of cracking. The influence of the substructure characteristics on parapets and chimneys was also discussed.

Overtuning fragility curves were obtained from the cloud results and focus was also placed in establishing which intensity measure (IM) resulted as the most efficient one.

Primary structure and roof filtering effects resulted in a slight decrease of the response dispersion. The most efficient ground motion IMs were, consistently with other works in literature, *AvgSa*, *HI*, *PGV* and *CAV* for both initially damaged and undamaged systems (associated with slightly higher dispersion). When floor motions IMs were considered, PFV resulted as the most efficient one.

Recognising the considerable diversity of the two approaches, the obtained overturning fragility curves for parapet and chimneys were compared with empirical ones available in literature and expressed in PGA. Analytical fragility curves resulted as less vulnerable than empirical ones. This might be related to two main reasons: analytical curves refer to overturning of the element while empirical one to a binary classification of damage associated with lack of information, the low demanding employed set of ground motions, being representative of induced earthquakes.

## 7.6. Acknowledgments

The useful advice of Dr. G. Guerrini, S. Sharma, L. Rottoli is gratefully acknowledged.

## 7.7. References

- [1] J. Ingham and M. Griffith, "Performance of unreinforced masonry buildings during the 2010 Darfield (Christchurch, NZ) earthquake," *Aust. J. Struct. Eng.*, vol. 11, no. 3, pp. 207–224, 2011.
- [2] D. Dizhur *et al.*, "Performance of masonry buildings and churches in the 22 February 2011 Christchurch earthquake," *Bull. New Zeal. Soc. Earthq. Eng.*, vol. 44, no. 4, pp. 279–296, 2011.
- [3] L. Moon *et al.*, "The demise of the URM building stock in Christchurch during the 2010-2011 Canterbury earthquake sequence," *Earthquake Spectra*, vol. 30, no. 1, pp. 253–276, 2014.
- [4] A. Penna, P. Morandi, M. Rota, C. F. Manzini, F. da Porto, and G. Magenes, "Performance of masonry buildings during the Emilia 2012 earthquake," *Bull. Earthq. Eng.*, vol. 12, no. 5, pp. 2255–2273, 2014.
- [5] D. Dizhur, M. Giaretton, and J. Ingham, "Performance of early masonry, cob and concrete buildings in the 14 November 2016 Kaikoura earthquake," *Bull. New Zeal. Soc. Earthq. Eng.*, vol. 50, no. 2, pp. 194–205, 2017.
- [6] M. Giaretton, J. M. Ingham, and D. Dizhur, "Experimental validation of seismic retrofit solutions for URM chimneys," *Bull. Earthq. Eng.*, vol. 16, no. 1, pp. 295–313, 2018.
- [7] FEMA-E-74, *Reducing the risks of nonstructural earthquake damage a practical guide*. Federal Emergency Management Agency, (USA), Washington, 2011.
- [8] FEMA DR-4193-RA1, *Repair of earthquake-damaged masonry fireplace chimneys*. Federal Emergency Management Agency, (USA), Washington, 2015.
- [9] NZHPT, *Repairing and rebuilding historic chimneys after an earthquake. Sustainable management of historic heritage guidance series*. New Zealand Historic Places Trust, Wellington, 2010.
- [10] AS-3826, *Strengthening existing buildings for earthquake*. Australia: Australian Standard, 1998.

- [11] ASCE/SEI-41, *Seismic evaluation and retrofit of existing buildings*. USA: American Society of Civil Engineers, 2013.
- [12] FEMA P-58/BD-3.9.7, *Fragility of masonry chimneys*. Federal Emergency Management Agency, (USA), Washington, 2010, p. 30.
- [13] D. B. Booth, R. E. Wells, and R. W. Givler, "Chimney damage in the greater Seattle area from the Nisqually earthquake of 28 February 2001," *Bull. Seismol. Soc. Am.*, vol. 94, no. 3, pp. 1143–1158, 2004.
- [14] M. D. Purvance, A. Anooshehpour, and J. N. Brune, "Freestanding block overturning fragilities: Numerical simulation and experimental validation," *Earthq. Eng. Struct. Dyn.*, vol. 37, no. 5, pp. 791–808, Apr. 2008.
- [15] M. Giaretton, D. Dizhur, and J. M. Ingham, "Dynamic testing of as-built clay brick unreinforced masonry parapets," *Eng. Struct.*, vol. 127, pp. 676–685, 2016.
- [16] D. Dizhur, M. Giaretton, H. Derakhshan, J. Ingham, and M. Griffith, "In-situ earthquake testing and securing of domestic URM chimneys," in *10th Australasian Masonry Conference - AMC*, 2018.
- [17] H. Derakhshan, W. D. Lucas, and M. C. Griffith, "In-situ seismic verification of non-structural components of unreinforced masonry buildings," *Aust. J. Struct. Eng.*, vol. 19, no. 1, pp. 44–58, 2018.
- [18] L. Sorrentino, S. Kunnath, G. Monti, and G. Scalora, "Seismically induced one-sided rocking response of unreinforced masonry façades," *Eng. Struct.*, vol. 30, no. 8, pp. 2140–2153, 2008.
- [19] F. Graziotti, U. Tomassetti, S. Sharma, L. Grottoli, and G. Magenes, "Experimental response of URM single leaf and cavity walls in out-of-plane two-way bending generated by seismic excitation," *Constr. Build. Mater.*, vol. (in press), 2018.
- [20] U. Tomassetti, F. Graziotti, A. Penna, and G. Magenes, "Modelling one-way out-of-plane response of single-leaf and cavity walls," *Eng. Struct.*, vol. 167, pp. 241–255, Jul. 2018.
- [21] P. R. Lipscombe and S. Pellegrino, "Free Rocking of Prismatic Blocks," *J. Eng. Mech.*, vol. 119, no. 7, pp. 1387–1410, Jul. 1993.
- [22] K. Doherty, M. C. Griffith, N. Lam, and J. Wilson, "Displacement-based seismic analysis for out-of-plane bending of unreinforced masonry walls," *Earthq. Eng. Struct. Dyn.*, vol. 31, no. 4, pp. 833–850, 2002.
- [23] L. Sorrentino, D. D'Ayala, G. de Felice, M. C. Griffith, S. Lagomarsino, and G. Magenes, "Review of Out-of-Plane Seismic Assessment Techniques Applied To Existing Masonry Buildings," *Int. J. Archit. Herit.*, vol. 11, no. 1, pp. 2–21, 2017.
- [24] G. W. Housner, "The behavior of inverted pendulum structures during earthquakes," *Bull. Seismol. Soc. Am.*, vol. 53, no. 2, pp. 403–417, 1963.
- [25] H. Derakhshan, M. C. Griffith, and J. M. Ingham, "Airbag testing of multi-leaf unreinforced masonry walls subjected to one-way bending," *Eng. Struct.*, vol. 57, no. December, pp. 512–522, 2013.
- [26] K. Doherty, "An investigation of the weak links in the seismic load path of unreinforced masonry buildings," no. May, p. 354, 2000.
- [27] S. Lagomarsino, "Seismic assessment of rocking masonry structures," *Bull. Earthq. Eng.*, vol. 13, no. 1, pp. 97–128, 2015.
- [28] T. M. Ferreira, A. A. Costa, R. Vicente, and H. Varum, "A simplified four-branch model for the analytical study of the out-of-plane performance of regular stone URM walls," *Eng. Struct.*, vol. 83, pp. 140–153, 2015.
- [29] H. Derakhshan, M. C. Griffith, and J. M. Ingham, "Out-of-Plane Behavior of One-Way Spanning Unreinforced Masonry Walls," *J. Eng. Mech.*, vol. 139, no. 4, pp. 409–417, 2013.
- [30] L. Sorrentino, O. AlShawa, and L. D. Decanini, "The relevance of energy damping in unreinforced masonry rocking mechanisms. Experimental and analytic investigations," *Bull. Earthq. Eng.*, vol. 9, no. 5, pp. 1617–1642, 2011.
- [31] N. M. Newmark, "A Method of Computation for Structural Dynamics," *Journal of the Engineering Mechanics*, vol. 85, no. 7, pp. 67–94, 1959.
- [32] S. Kallioras, A. A. Correia, A. I. Marques, P. X. Candeias, and F. Graziotti, "LNEC-BUILD-3: Experimental investigation of the seismic response of a Dutch URM detached house with chimneys." *Tech. Report, EUCENTRE, Pavia, Italy*, 2018.
- [33] S. Kallioras, A. A. Correia, F. Graziotti, A. Penna, and G. Magenes, "Experimental seismic performance of an unreinforced clay-masonry building with chimneys up to collapse conditions," *V. e Giardini*, no. (to be submitted), 2018.
- [34] F. Graziotti, A. Penna, and G. Magenes, "A nonlinear SDOF model for the simplified evaluation of the displacement demand of low-rise URM buildings," *Bull. Earthq. Eng.*, vol. 14, no. 6, pp. 1589–

- 1612, 2016.
- [35] S. Lagomarsino, A. Penna, A. Galasco, and S. Cattari, "TREMURI program: An equivalent frame model for the nonlinear seismic analysis of masonry buildings," *Eng. Struct.*, vol. 56, pp. 1787–1799, 2013.
- [36] A. Penna, S. Lagomarsino, and A. Galasco, "A nonlinear macroelement model for the seismic analysis of masonry buildings," *Earthq. Eng. Struct. Dyn.*, vol. 43, pp. 159–179, 2014.
- [37] F. Graziotti, U. Tomassetti, S. Kallioras, A. Penna, and G. Magenes, "Shaking table test on a full scale URM cavity wall building," *Bull. Earthq. Eng.*, vol. 15, no. 12, 2017.
- [38] G. Guerrini, F. Graziotti, A. Penna, and G. Magenes, "Improved evaluation of inelastic displacement demands for short-period masonry structures," *Earthq. Eng. Struct. Dyn.*, vol. 46, no. 9, pp. 1411–1430, Jul. 2017.
- [39] S. Kallioras *et al.*, "Experimental seismic performance of a full-scale unreinforced clay-masonry building with flexible timber diaphragms," *Eng. Struct.*, vol. 161, no. November 2017, pp. 231–249, Apr. 2018.
- [40] U. Tomassetti *et al.*, "Two-way bending out-of-plane collapse of a full-scale URM building tested on a shake table," *Bull. Earthq. Eng.*, vol. (in press), 2018.
- [41] Ministry of Infrastructures and Transport (MIT), *Norme tecniche per le costruzioni, DM 14/01/2008*. 2008.
- [42] U. Tomassetti, "Tools and strategies for combined local and global seismic vulnerability assessment of URM structures," Ph.D. Thesis, University of Pavia, 2018.
- [43] B. Chiou, R. Darragh, N. Gregor, and W. Silva, "NGA project strong-motion database," *Earthq. Spectra*, vol. 24, no. 1, pp. 23–44, 2008.
- [44] S. Akkar *et al.*, "Reference database for seismic ground-motion in Europe (RESORCE)," *Bull. Earthq. Eng.*, vol. 12, no. 1, pp. 311–339, 2014.
- [45] J. J. Bommer *et al.*, "Developing an application-specific ground-motion model for induced seismicity," *Bull. Seismol. Soc. Am.*, vol. 106, no. 1, pp. 158–173, 2016.
- [46] H. Crowley, B. Polidoro, R. Pinho, and J. van Elk, "Framework for Developing Fragility and Consequence Models for Local Personal Risk," *Earthq. Spectra*, vol. 33, no. 4, pp. 1325–1345, 2017.
- [47] J. E. Padgett, B. G. Nielson, and R. DesRoches, "Selection of optimal intensity measures in probabilistic seismic demand models of highway bridge portfolios," *Earthq. Eng. Struct. Dyn.*, vol. 37, no. 5, pp. 711–725, Apr. 2008.
- [48] M. Kohrangi, P. Bazzurro, D. Vamvatsikos, and A. Spillatura, "Conditional spectrum-based ground motion record selection using average spectral acceleration," *Earthq. Eng. Struct. Dyn.*, vol. 46, no. 10, pp. 1667–1685, Aug. 2017.
- [49] H. Derakhshan, D. Y. Dizhur, M. C. Griffith, and J. M. Ingham, "Seismic assessment of out-of-plane loaded unreinforced masonry walls in multi-storey buildings," *Bull. New Zeal. Soc. Earthq. Eng.*, vol. 47, no. 2, pp. 119–138, 2014.
- [50] A. Arias, "A measure of earthquake intensity," in *Seismic Design for Nuclear Power Plants*, 1970, pp. 438–483.
- [51] G. W. Housner, "Intensity of Ground Motion During Strong Earthquakes.," *Calif. Inst. Technol.*, 1952.
- [52] T. Taig and F. Pickup, "Risk assessment of falling hazards in earthquakes in the Groningen region," Nam platform, 2016.
- [53] M. Tondelli, F. Graziotti, A. Rossi, and G. Magenes, "Characterization of masonry materials in the Groningen area by means of in-situ and laboratory testing," *Tech. Report, Eucentre, Pavia, Italy.*, 2015.
- [54] E. G. Dimitrakopoulos and T. S. Paraskeva, "Dimensionless fragility curves for rocking response to near-fault excitations," *Earthq. Eng. Struct. Dyn.*, vol. 44, no. 12, pp. 2015–2033, Sep. 2015.
- [55] L. Giresini, C. Casapulla, R. Denysiuk, J. Matos, and M. Sassu, "Fragility curves for free and restrained rocking masonry façades in one-sided motion," *Eng. Struct.*, vol. 164, no. March, pp. 195–213, 2018.
- [56] A. I. Giouvanidis and E. G. Dimitrakopoulos, "Rocking amplification and strong-motion duration," *Earthq. Eng. Struct. Dyn.*, vol. 47, no. 10, pp. 2094–2116, 2018.
- [57] P. J. Stafford, "Conditional prediction of absolute durations," *Bull. Seismol. Soc. Am.*, vol. 98, no. 3, pp. 1588–1594, 2008.
- [58] J. Vaculik and M. Griffith, "Out-of-plane load–displacement model for two-way spanning masonry walls," *Eng. Struct.*, vol. 141, pp. 328–343, 2017.
- [59] N. Makris and D. Konstantinidis, "The rocking spectrum and the limitations of practical design

- methodologies,” *Earthq. Eng. Struct. Dyn.*, vol. 32, no. 2, pp. 265–289, 2003.
- [60] L. Sorrentino, L. Liberatore, D. Liberatore, and R. Masiani, “The behaviour of vernacular buildings in the 2012 Emilia earthquakes,” *Bull. Earthq. Eng.*, vol. 12, no. 5, pp. 2367–2382, 2014.
- [61] L. Sorrentino, R. Masiani, and L. D. Decanini, “Overturning of rocking rigid bodies under transient ground motions,” *Struct. Eng. Mech.*, vol. 22, no. 3, pp. 293–310, 2006.
- [62] C. A. Cornell, F. Jalayer, R. O. Hamburger, and D. A. Foutch, “Probabilistic Basis for 2000 SAC Federal Emergency Management Agency Steel Moment Frame Guidelines,” *J. Struct. Eng.*, vol. 128, no. 4, pp. 526–533, Apr. 2002.
- [63] P. Gehl, D. M. Seyed, and J. Douglas, “Vector-valued fragility functions for seismic risk evaluation,” *Bull. Earthq. Eng.*, vol. 11, no. 2, pp. 365–384, 2013.
- [64] J. W. Baker, “Efficient analytical fragility function fitting using dynamic structural analysis,” *Earthq. Spectra*, vol. 31, no. 1, pp. 579–599, 2015.
- [65] H. Krawinkler, J. D. Osteraas, B. M. McDonald, and J. P. Hunt, “Development of damage fragility functions for URM chimneys and parapets,” in *15th World Conference on Earthquake Engineering*, 2012.



## Conclusions

Meaningful and reliable advances in the field of earthquake engineering applied to unreinforced masonry structures can be made only by co-ordinating large scale experimental campaigns along with the contemporary development of numerical models calibrated to the experimental data. Keeping this in mind, this thesis attempts to answer several questions that have arisen due to an increasing interest in understanding as well as predicting the risk associated with seismic events from both an experimental as well as numerical standpoint:

Chapter 1 presented the results of an OOP shaking table test campaign on cavity wall and single-leaf components. All test specimens collapsed in one-way vertical bending/rocking behaviour, exhibiting the classical top, bottom and mid-height hinges. Despite the negligible flexural stiffness of the metal ties connecting the leaves of the cavity walls and poor mechanical characteristics of the CS wall mortar, the connections still ensured a horizontal displacement compatibility between the two leaves' even in the case of low tie densities (i.e. 2 ties/m<sup>2</sup>). All the tested cavity wall specimens showed lower capacities when compared to the single-leaf specimen loaded with the same axial force. The experimental work confirmed that the specimen capacity is strongly influenced by the vertical stress acting on the walls, also for cavity walls. The number of ties connecting the two walls also was discovered to significantly affect the cavity wall response in terms of capacities as well as the ability to withstand a larger number of dynamic tests.

Such coupled response allowed the analysis of the OOP seismic behaviour of cavity walls by simplified SDOF models. Investigations were performed into the force-displacement relationship and the dynamic energy dissipation involved in the mechanism. Regarding the  $F-\Delta$  relationship, the cavity components showed capacities that could be modelled using RB mechanisms of the two walls considered independently and summing the response. Energy dissipation was estimated assuming two damping models: 1) impulsive dynamics with the coefficient of restitution and 2) classical dynamics theory with the damping ratio. For the single leaf specimen, the coefficient of restitution was assessed to be around 0.90 with a ratio between theoretical and experimental values of around 91%. Cavity components exhibited much lower values of the coefficient of restitution around 0.7 as a result of dynamic interaction between the component leaves. Equivalent viscous damping ratio values of 5 to 10% were observed for the single-leaf specimen while much larger values going up to 30% were observed for the cavity wall components.

Chapter 2 presented the results of a unidirectional shaking table test performed on a full-scale specimen representative of a Dutch two-storey URM building with cavity walls and a timber roof. The building specimen was intended to represent the end-unit of a terraced house of the late '70s, without any specific seismic detailing. The loadbearing walls were built with a 10-cm-thick calcium silicate URM, while three out of the four façades were completed by a clay veneer connected to the calcium silicate walls by means of steel ties.

All construction materials were characterized mechanically and their properties were found to be compatible with the ones found in the existing building stock of Groningen.

The loadbearing structure exhibited a box-type global response due to the presence of rigid concrete floor slabs which engaged the longitudinal walls and prevented the occurrence of local out-of-plane failure mechanism until a PGA of 0.31g. No torsional response of the building was recorded, leading to full exploitation of in-plane capacity of the longitudinal walls. Four damage states were identified and found to be in good agreement with theoretical proposals available in literature. The building withstood the input motion with a PGA of 0.17g with little damage (maximum first inter-storey drift  $\theta_1 = 0.12\%$ ) and was in the near-collapse state at a PGA of 0.31g ( $\theta_1 = 0.88\%$ ).

No significant shear damage occurred in the masonry piers, which were in general quite slender and their response was mainly governed by rocking. Sliding occurred at the top of masonry walls parallel to the table motion. Substantial compatibility of displacements was observed between the inner and outer walls up to the near collapse state. During the last run (PGA = 0.31g), the loadbearing structure and the veneer moved almost independently. The stiffness contribution of the external clay masonry was reduced and consequently the displacement demand of the internal structure increased. The fundamental period of the structure after the tests was discovered to be almost 3.5 larger than the initial undamaged one. Some diagonal stepped cracks were also observed in the transversal load bearing walls due to the out-of-plane excitation.

The structure was characterized by a very flexible roof. A study of the dynamic behaviour of the roof substructure is proposed in this chapter and is in fact also accomplished experimentally in Chapter 3 and Chapter 6. Despite the high flexibility and the consequent vulnerability of the roof system, the shaking table tests were able to fully exploit the strength of the loadbearing structure with a maximum base shear coefficient of almost 0.25 being calculated.

Chapter 3 presented the results of a bi-axial (horizontal and vertical excitation) shake table test performed on a one-storey full-scale specimen representative of a Dutch URM building with cavity walls and timber roof. This specimen also reproduced a sub-structure (*i.e.* the second floor and roof) of the building prototype reported in Chapter 2. The specimen was subjected to incremental input motions adopting as horizontal component the first-floor accelerograms recorded during the tests performed on the two-storey building tests and following also the same testing protocol in order to allow for a realistic comparison with the experiment reported in Chapter 2.

This sub-structure also exhibited a box-type global response like that of the structure reported in Chapter 2. Despite the large flexibility and the consequent vulnerability of the roof system, the collapse of the specimen at a PGA of 0.63 g was driven by the out-of-plane failure of the East wall. A pronounced rocking mechanism developed by the slender longitudinal piers combined with the vertical input motion led to an uplift of the RC slab causing a loss of restraint at the top of the East transverse wall, making it much more vulnerable to out-of-plane actions. The RC slab, after the failure of the East load-bearing wall, rested, at the end of the test, on the outer veneer wall with a significant residual displacement (beyond 60 mm).

Such an observed failure mechanism highlighted the importance of considering eventual variations of the structural elements' boundary conditions (*e.g.* acting axial load) while assessing their seismic performance. Simplified analytical formulation was also proposed

to take into account the interaction between the boundary condition of the out-of-plane panel (collapsed in the test) and the uplift of the slab due to flange effect caused by the returning walls.

Chapter 4 presented a numerical SDOF model for the OOP analysis of masonry walls capable of successfully simulating the OOP one-way bending dynamic response of single leaf and cavity wall URM specimens tested and presented in Chapter 1. The calibration of the model provided valuable insights on the force displacement relationship and the damping properties of these wall typologies in both pre-and-post mechanism activation phases. A simplified analytical formulation was proposed to estimate cracking force and initial stiffness of the wall typologies.

Two tri-linear configurations corresponding to different levels of vertical overburden were proposed and consequently used to successfully model the rocking behaviour of single leaf CS walls. Stiffness and strength degradation of the specimens were also modelled by reducing the tri-linear plateau.

The tri-linear rocking relationships of cavity systems (assuming the same parameters found for the two single leaf configurations) were built on rigid bi-linear curves obtained by simply summing the forces associated with the rigid body mechanism of the two leaves considered independently. A further contribution to the lateral resistance was discovered to originate from the forces of the tie coupling system. Three stages of degradation of the cavity specimen were identified. A methodology for modelling the dynamic behaviour of cavity walls accounting for the contribution of the ties as well as the degree of connection between the two leaves was also presented.

Finally, the efficiency of different damping models in simulating the experimental responses was also tested. It was discovered that a classical EVD damping model (constant damping coefficient) cannot capture the dependence of the damping phenomenon on the oscillation amplitude and underestimates large oscillation peaks. Damping models acting on the system's current secant stiffness were shown to better simulate the experimental dynamic response. A stiffness-proportional damping model (SDR), assuming  $\zeta_{in}$  values equal to 7% and 15% for single leaf and cavity wall specimens respectively, was seen to have the best performance for the simulation of response peaks of both wall typologies. Adopting a constant damping ratio (CDR) also showed good performance in simulating the experimental behaviour.

Chapter 5 presented a SDOF model for the analysis of the rocking behaviour of parapet wall (PW) and vertical spanning strip wall (VSSW) systems consisting of a bilinear nonlinear elastic oscillator. Energy dissipation was modelled with an equivalent viscous damping (EVD) force rather than the more widely used coefficient of restitution.

This alternative approach presented several potential advantages over a coefficient of restitution based approach such as similarities of the damping problem to the dynamics of classical linear oscillators and easy implementation in already available finite element environments. Moreover, EVD models may model the energy dissipation in both pre-mechanism (during the elastic response) and post-mechanism phases (when the rocking phenomenon take place). This is particularly important in the case of slightly loaded walls responding in one-way bending or walls in two-way bending.

Several configurations of velocity dependent forces acting on the initial (constant damping coefficient, CDC) or secant stiffness of the system (adopting constant or linear

frequency-damping ratio relationships, CDR or SDR) were presented and discussed. The work aimed at defining a relationship between these EVD models and the system slenderness via coefficient of restitution. The response given by the coefficient of restitution approach was taken as the reference damping system. In order to ensure the equivalence, damped free vibration decays produced by EVD models were matched with the one provided by a coefficient of restitution.

Logarithmic relationships, function of the initial stiffness, were provided to correlate the best damping ratio values associated with the different EVD models with coefficient of restitution values and consequently slenderness angles. The constant damping ratio (CDR) model acting on the system secant stiffness, also considering its reduced dependence on oscillation amplitude and initial stiffness, resulted to be the most appropriate in simulating free vibration decays damped by a coefficient of restitution. In addition, the stiffness proportional damping ratio (SDR) model also showed a rather good performance.

The SDOF model showed capability of simulating the experimental rocking response of already cracked parapets and the calibrated damping ratio values were very close to the ones proposed by the derived logarithmic relationships. Finally, incremental dynamic analysis adopting damping values provided by the derived relationships were performed on several PWs and VSSWs having slenderness considered representative of Italian architectonic and/or artistic assets. The good match between collapse cumulative distribution functions given by coefficient of restitution and the EVD models confirmed the effectiveness of the proposed approach.

Chapter 6 initially presents the results of a shake table test performed on a Dutch roof substructure un to collapse conditions. This specific roof typology (tested also in the experimental campaigns of Chapter 2 and 3) composed of URM gables supporting a timber diaphragm have shown over different shaking table tests similar behaviour in terms of damage and deflected shapes. The presence of L-shaped connectors between roof beams and masonry gables ensured compatibility of displacement between URM gables and timber diaphragm associated with a linear deflected shape over the roof height. In this case the diaphragm drift (ridge beam horizontal displacement divided by the roof inclined length) has been identified as a good EDP for describing the roof damage. Chapter 6 presented also a SDOF model capable of capturing the dynamic behaviour of these roof typologies. The SDOF system was composed of two springs in parallel: a bi-linear elastic one for the simulation of the typical non-linear rocking behaviour of the masonry gables and an elastoplastic one with two hardening branches for simulating the highly dissipative timber diaphragm hysteretic behaviour. This second spring was calibrated on the basis of a cyclic quasi-static test performed on the roof diaphragm after the end of the dynamic shake table test. The low computational demanding numerical model, calibrated on the basis of experimental tests, was used to perform a seismic assessment of roof structures taking the ground motion filtering effect given by the structure into account.

For this purpose, a set of SDOF systems, specifically calibrated to simulate the in-plane global response of low-rise URM buildings, was employed. Signals filtered by this primary SDOF system's response were utilised to investigate the response of roof structures. This allowed for the investigation of the roof response variability when placed on top of different structural configurations, which may vary in number of storeys and

strength. The vulnerability study suggested that, when compatibility of displacement between URM gable and timber diaphragm is ensured, attainment of heavy damage, partial and global collapse of the roof are very rare scenarios. This is mainly due to saturation of the floor acceleration amplification transferred from the global structure at the base of the roof. On the other hand, such structures being very flexible, attainment of slight damage resulted possible scenarios even for low intensity ground motions. Conditional probability of achieving a specific damage state in the roof sub-structure given the damage level associated with different configuration of primary structures and for different roof configurations were calculated.

In order to identify the most appropriate IM, the distribution of the roof fragility function dispersion over the different building configurations analysed was evaluated. Generally, *AvgSA* resulted as the most efficient IM, whereas PGA tended to *AvgSA* values of dispersion only for high levels of nonlinear demand in both global and roof structures. As expected, SAT1, instead performed well for first damage levels of the roof structure. Diaphragm drift (ridge beam horizontal displacement divided by the roof inclined length) which has already been identified as a good EDP for describing the roof damage in typical Dutch terraced houses from both dynamic testing (reported in this thesis) as well as post-earthquake surveys was used.

Chapter 7 presents an interpretation to model the dynamic behaviour of parapets and chimneys with a single-degree-of-freedom (SDOF) system which take into account both pre-and-post mechanism phases. Its force-displacement ( $F-d$ ) relationship is characterised by a linear elastic curve having strength and stiffness governed by the masonry flexural strength followed by a residual capacity consisting in a bi-linear curve constructed on the rigid body  $F-d$  idealisation.

Calibration of several experimental dynamic tests allowed for the determination of reliable parameters in terms of  $F-d$  curve and dissipated energy for the simulation of their seismic response. A bilinear curve having a corner displacement expressed as fraction of the instability displacement and equal to 0.06 for parapets and 0.05 for chimneys was proposed. The energy dissipation was modelled via coefficient of restitution by reducing the theoretical value by 0.94 for parapets and 0.80 for chimneys and also recurring to velocity dependant equivalent viscous damping forces. This latter source of damping, proportional to the current secant stiffness of the system, has been employed adopting damping ratio values between 1.5-3% for parapets and 12-15% for chimneys.

The SDOF model was then adopted to assess the vulnerability of opportunely selected secondary elements placed on top of different primary structure and roof configurations. The buildings differ in terms of number of storeys and structure lateral strength. SDOF systems, representative of the structure global response and the roof where subjected to a large set of ground motions representative of induced earthquakes. Their acceleration output was used as acceleration input for chimneys and parapets.

The cloud analyses were discussed analysing differences in response between initially damaged elements, undergoing directly in rocking behaviour, and undamaged systems where rocking is triggered only at the attainment of cracking. The influence of the substructure characteristics on parapets and chimneys response was also discussed.

Overturning fragility curves were obtained from the cloud results and focus was also placed in establishing which intensity measure (IM) resulted as the most efficient one.

Primary structure and roof filtering effects resulted in a slight decrease of the response dispersion. The most efficient ground motion IMs were, consistently with other works in

literature,  $AvgSa$ ,  $HI$ ,  $PGV$  and  $CAV$  for both initially damaged and undamaged systems (associated with slightly higher dispersion). When floor motion IMs were considered, PFV resulted as the most efficient one. Recognising the considerable diversity of the two approaches, the obtained overturning fragility curves for parapet and chimneys were compared with empirical ones available in literature and expressed in PGA. Analytical fragility curves resulted as less vulnerable than empirical ones. This might be related to two main reasons: analytical curves refer to overturning of the element while empirical one to a binary classification of damage associated with lack of information, the low demanding employed set of ground motions, being representative of induced earthquakes.

### Future development

The following topics also require further research attention:

- Dynamic testing and numerical simulation of URM walls subjected to out-of-plane one way bending with top support having finite stiffness and consequently imposing an OOP drift. This is in order to investigate the role of diaphragm flexibility in the OOP response of walls.
- Dynamic testing of a full-scale terraced house in bi-axial (horizontal and vertical) excitation evaluating possible development of local mechanisms in the slender piers of the upper storey; a further shake table test may also assess the effectiveness of retrofit solution based on the adoption of working in-plane and out-of-plane timber strong backs.
- Enhance the presented SDOF model for the analysis of the OOP response of URM walls in one-way bending including time history variation of the acting overburden axial stress during the analysis. This is in order to properly consider eventual variation of boundary conditions (see Chapter 3).
- Development of a SDOF model for the analysis of the dynamic OOP two-way bending behaviour of URM walls taking into account peak strength, relying on the masonry torsional resistance, and residual capacity associated with combined rocking and torsional friction resistance.
- Extension of the proposed EVD slenderness-angle relationships to the case of one sided rocking mechanisms considering the actual stiffness of the return walls.
- Performing parametric analysis of URM walls in forced OOP excitation damped by EVD models in order to evaluate the effectiveness of current spectrum-based code prescriptions and eventually propose simplified assessment procedures.
- Calibration of the dynamic response of roofs typical of Dutch detached houses in which gable walls are not loadbearing the timber diaphragm. This is in order to consider a wider variability of primary and roof structures in the vulnerability analyses.
- Dynamic testing of chimneys in order to better characterise their performance in terms of initiation of cracking, damage propagation and collapse.
- Improving modelling of roof chimneys accounting for possible sliding and sliding-rocking effects, as well as considering eventual multi-body mechanisms.
- In the framework of a combined multiscale approach, the development of a light computational numerical model having few degree of freedoms and allowing for simultaneously analysing global, local, roof and secondary elements performances.